

Oceanologia

Official Journal of the Polish Academy of Sciences: Institute of Oceanology and Committee on Maritime Research



EDITOR-IN-CHIEF

Janusz Pempkowiak
Institute of Oceanology Polish Academy of Sciences, Sopot, Poland

MANAGING EDITOR

Agata Bielecka - abielecka@iopan.gda.pl

Editorial Office Address

Institute of Oceanology Polish Academy of Sciences (IO PAN)
Powstańców Warszawy 55
81-712 Sopot, Poland
Mail: pempa@iopan.gda.pl

THEMATIC EDITORS

Alicja Kosakowska – Institute of Oceanology Polish Academy of Sciences, Sopot, Poland
Stanisław Massel – Institute of Oceanology Polish Academy of Sciences, Sopot, Poland
Jan Marcin Węśławski – Institute of Oceanology Polish Academy of Sciences, Sopot, Poland
Marek Zajączkowski – Institute of Oceanology Polish Academy of Sciences, Sopot, Poland
Tymon Zieliński – Institute of Oceanology Polish Academy of Sciences, Sopot, Poland

ADVISORY BOARD

Prof. Jerzy Dera

Institute of Oceanology Polish Academy of Sciences (IO PAN), Sopot, Poland

Prof. Howard Gordon

Dept. of Physics, University of Miami, USA

Prof. Genrik Sergey Karabashev

P.P. Shirshov Institute of Oceanology RAS, Moscow, Russia

Prof. Zygmunt Kowalik

Institute of Marine Science, School of Fisheries and Ocean Sciences, University of Alaska Fairbanks (UAF), USA

Prof. Matti Leppäranta

Department of Physics, University of Helsinki, Finland

Prof. Gennady Matishov

Murmansk Marine Biological Institute KSC, Russian Academy of Sciences (MMBI KSC RAS), Russia

Prof. Sergej Olenin

Coastal Research and Planning Institute, Klaipeda University CORPI, Lithuania

Prof. Anders Omstedt

University of Gothenburg, Dept. Earth Sciences: Oceanography, Gothenburg, Sweden

Prof. Marcin Pliński

Institute of Oceanography, University of Gdańsk, Gdynia, Poland

Prof. Xosé Antón Álvarez Salgado

Department of Oceanography, Marine Research Institute, Spanish Research Council (CSIC), Spain

Prof. Tarmo Soomere

Institute of Cybernetics, Tallinn University of Technology, Tallinn, Estonia

Prof. Hans von Storch

Institute for Coastal Research, Helmholtz Zentrum Geesthacht, Germany

Prof. Dariusz Stramski

Marine Physical Laboratory, Scripps Institution of Oceanography, University of California, San Diego, USA

Prof. Juergen Suendermann

Institut für Meereskunde, Universität Hamburg, Hamburg, Germany

Prof. Piotr Szefer

Department of Food Sciences, Medical University of Gdańsk, Gdańsk, Poland

Prof. Antoni Śliwiński

Institute of Experimental Physics, University of Gdańsk, Gdańsk, Poland

Prof. David Turner

Department of Chemistry and Molecular Biology, University of Gothenburg, Sweden

Prof. Bogdan Woźniak

Institute of Oceanology Polish Academy of Sciences (IO PAN), Sopot, Poland

Prof. Ronald Zaneveld

Western Environmental Technology Laboratories, Philomath, USA

This journal is supported by the Ministry of Science and Higher Education, Warsaw, Poland

Indexed in: ISI Journal Master List, Science Citation Index Expanded, Scopus, Current Contents, Zoological Record, Thomson Scientific SSCI, Aquatic Sciences and Fisheries Abstracts, DOAJ

IMPACT FACTOR ANNOUNCED FOR 2015 IN THE 'JOURNAL CITATION REPORTS' IS 0.935; 5-year IF – 1.116

Publisher

Elsevier Sp. z o.o. 4/59,
02-796 Warsaw, Poland
Tel. +48 22 546 38 20, Fax. +48 22 546 38 21

Director of Journals Publishing

Ewa Kittel-Prejs

Publishing Manager

Agnieszka Pawłowska
a.pawlowska@elsevier.com

Marketing & Promotion Manager

Anna Szkolut
a.szkolut@elsevier.com
48 22 546 38 40, 48 515 090 174

Publishing Editor

Joanna Lewczuk
j.lewczuk@elsevier.com
48 515 082 585, 48 22 546 38 24

Subscription and Distribution Manager

Jacek Sołtyk
prenumerata@elsevier.com
48 22 546 38 27, 48 510 134 282

Advertising Pharma Solutions

Monika Giergiełewicz
m.giergielewicz@elsevier.com
48 519 130 280

ISSN 0078-3234



ORIGINAL RESEARCH ARTICLE

Epibenthic diversity and productivity on a heavily trawled Barents Sea bank (Tromsøflaket)

Monika Kędra^{a,*}, Paul E. Renaud^{b,c}, Hector Andrade^b

^a *Institute of Oceanology, Polish Academy of Sciences, Sopot, Poland*

^b *Akvaplan-niva; Fram Centre for Climate and the Environment, Tromsø, Norway*

^c *University Centre in Svalbard, Longyearbyen, Norway*

Received 12 August 2016; accepted 13 December 2016

Available online 24 December 2016

KEYWORDS

Epibenthos;
Benthic secondary
production;
Shallow banks;
Trawling impacts

Summary Shallow Arctic banks have been observed to harbour rich communities of epifaunal organisms, but have not been well-studied with respect to composition or function due to sampling challenges. In order to determine how these banks function in the Barents Sea ecosystem, we used a combination of video and trawl/dredge sampling at several locations on a heavily trawled bank, Tromsøflaket – located at the southwestern entrance to the Barents Sea. We describe components of the benthic community, and calculate secondary production of dominant epifaunal organisms. Forty-six epibenthic taxa were identified, and sponges were a significant part of the surveyed benthic communities. There were differences in diversity and production among areas, mainly related to the intensity of trawling activities. Gamma was the most diverse and productive area, with highest species abundance and biomass. Trawled areas had considerably lower species numbers, and significant differences in epifaunal abundance and biomass were found between all trawled and untrawled areas. Trawling seems to have an impact on the sponge communities: mean individual poriferan biomass was higher in untrawled areas, and, although poriferans were observed in areas subjected to more intensive trawling, they were at least five times less frequent than in untrawled areas.

© 2016 Institute of Oceanology of the Polish Academy of Sciences. Production and hosting by Elsevier Sp. z o.o. This is an open access article under the CC BY-NC-ND license (<http://creativecommons.org/licenses/by-nc-nd/4.0/>).

* Corresponding author at: Institute of Oceanology, Polish Academy of Sciences, Powstańców Warszawy 55, 81-712 Sopot, Poland. Tel.: +48 58 73 11 779; fax: +48 58 551 21 30.

E-mail address: kedra@iopan.gda.pl (M. Kędra).

Peer review under the responsibility of Institute of Oceanology of the Polish Academy of Sciences.



Production and hosting by Elsevier

<http://dx.doi.org/10.1016/j.oceano.2016.12.001>

0078-3234/© 2016 Institute of Oceanology of the Polish Academy of Sciences. Production and hosting by Elsevier Sp. z o.o. This is an open access article under the CC BY-NC-ND license (<http://creativecommons.org/licenses/by-nc-nd/4.0/>).

1. Introduction

The Barents Sea is one of the most productive marginal seas of the world's oceans (Carmack and Wassmann, 2006; Sakshaug, 1997; Sakshaug and Slagstad, 1991). The estimated average annual primary productivity in the Barents Sea is about $100 \text{ g C m}^{-2} \text{ y}^{-1}$, but can be up to three times higher on the shallow banks (Sakshaug et al., 2009). Those shallow water regions make up more than one-third of the Barents Sea area (Jakobsson, 2002) and are characterized by strong depth gradients and dynamic physical processes, including turbulent currents which interact to generate seasonally high productivity. Shallow depths encourage rapid settlement of newly fixed organic carbon to the sea floor, and together with strong near-bottom currents, support rich filter-feeding communities (Kędra et al., 2013). Shallow banks are significant biodiversity hot spots in the larger ecosystem, and their ecosystem functioning may be particularly significant since carbon cycling, benthic secondary production, and food-web subsidies are enhanced (Grebmeier et al., 2006; Piepenburg et al., 1997; Piepenburg and Schmid, 1996, 1997).

Tromsøflaket, located at the southern entrance of the Barents Sea, is similar to other Barents Sea banks as it supports rich communities of epifaunal organisms, including long-lived and potentially vulnerable sponges and corals (Buhl-Mortensen et al., 2012; Jørgensen et al., 2011; Zenkevich, 1963). It is also an important spawning and harvesting area for some species of commercial fish (Loeng and Drinkwater, 2007; Olsen et al., 2010; Winsnes and Skjoldal, 2009). Benthic secondary productivity in this region has recently been estimated, and high values have been suggested for some biotopes (Buhl-Mortensen et al., 2012). Some areas are heavily fished, with bottom trawls being one of the most common gears employed, but potential impacts on ecological function, including future fisheries, have not been assessed.

Dredging and trawling activities can have serious impacts on the bottom communities, and marine ecosystems in general (Callaway et al., 2007; De Juan et al., 2011; Handley et al., 2014; Hiddink et al., 2006; Hinz et al., 2009; Kaiser et al., 2006; Olsgaard et al., 2008). These effects include habitat alteration (Mangano et al., 2013) and shifts in benthic communities towards smaller, short-lived and fast-growing species, which can cause system shifts from high to low diversity and from a high biomass – low turnover to a low biomass – high turnover system (Dannheim et al., 2014). This has wider ecosystem implications: affecting marine food webs by altering the quality of food available to commercially important species as well as affecting their size (Hinz et al., 2009; Shephard et al., 2014; Smith et al., 2013).

Despite their potential for having high ecosystem value, many shallow areas represent a challenge for researchers. The coarse substrate and strong currents make the use of traditional quantitative sampling gears (grabs) difficult or impossible. However, an underwater video has been used effectively to assess epifaunal community structure and function in a variety of shallow water habitats, and can identify areas with evidence of trawling activities (Buhl-Mortensen et al., 2009, 2012; Lindholm et al., 2004). Moreover, since it is a non-destructive sampling methodology, visual surveys are valuable for examining potentially vulnerable or sensitive seabed areas (Kilgour et al., 2014).

We, therefore, use underwater video to investigate epibenthic communities in the Tromsøflaket area. We ask what the characteristic values for diversity, biomass, and secondary production of epibenthic fauna on this Arctic bank are, and discuss how trawling may affect those parameters. These results provide important data for future studies of benthic fauna and ecosystem functioning.

2. Material and methods

2.1. Study area

Tromsøflaket is located in the southwestern Barents Sea with a depth plateau between 150–200 m (Buhl-Mortensen et al., 2009). The oceanography here is influenced by two major current systems. The southern part is dominated by the north-flowing Norwegian Coastal Current, with relatively cold, low-salinity coastal water while the rest of the bank is influenced by the Norwegian Atlantic Current, bringing relatively warm, saline water to the north (Bellec et al., 2008; Dijkstra et al., 2013; Skarðhamar and Svendsen, 2005). Bottom temperature and salinity average are 4.8°C (± 1.5 standard deviation) and 35.1‰ (± 0.3), respectively (Jørgensen et al., 2015). Most of the bank sediments are glacially derived. Coarse sediments are found on ridges and shallow parts of the bank while finer sediments concentrate in depressions, on the slopes, and in the deeper areas (Bellec et al., 2008). The bank is ecologically and economically important since it supports vulnerable sponge habitats which account for about 90% of the benthic biomass (Buhl-Mortensen et al., 2009; Jørgensen et al., 2015), and is a spawning area for commercial fish. In addition, it is a retention area for eggs and larvae (Olsen et al., 2010), which are then preyed upon by breeding and overwintering seabirds. Long-line, Danish seine, and bottom-trawling fishers are highly active on the east side of the bank (Jørgensen et al., 2016; Olsen et al., 2010; Winsnes and Skjoldal, 2009).

2.2. Sampling and data analysis

A combination of video and trawl/dredge sampling was used to describe components of the benthic community, and to calculate secondary production of dominant epifaunal organisms. The sea-bed conditions and epifauna were recorded and photographed in summer 2008 using a SUB-fighter 4500 ROV equipped with zoom- and wide-angle video cameras (Fig. 1). Lasers on the ROV permitted the size estimation of objects detected. Differential GPS (in relation to the support ship *Olympic Poseidon*) was used for positioning. A transponder mounted on the ROV confirmed $\pm 5 \text{ m}$ accuracy in the depth and positioning. Videos were taken at the depths of: 177–213 m in Alke Nord, 160–173 m in Alke Sør, and about 190 m in the Gamma areas. The video survey was conducted under contract to the oil and gas company ENI, and raw video files were provided for the purposes of these analyses.

Five to ten-minute-long video transects were taken in each area. In all, 24 video transects from Alke Nord, 21 from Alke Sør, and 23 from Gamma were analyzed in detail using frame captures approximately every 30 s ($n = 10\text{--}20$ frames per transect). To complement underwater video information, epifauna were collected at several locations (7 from Alke and

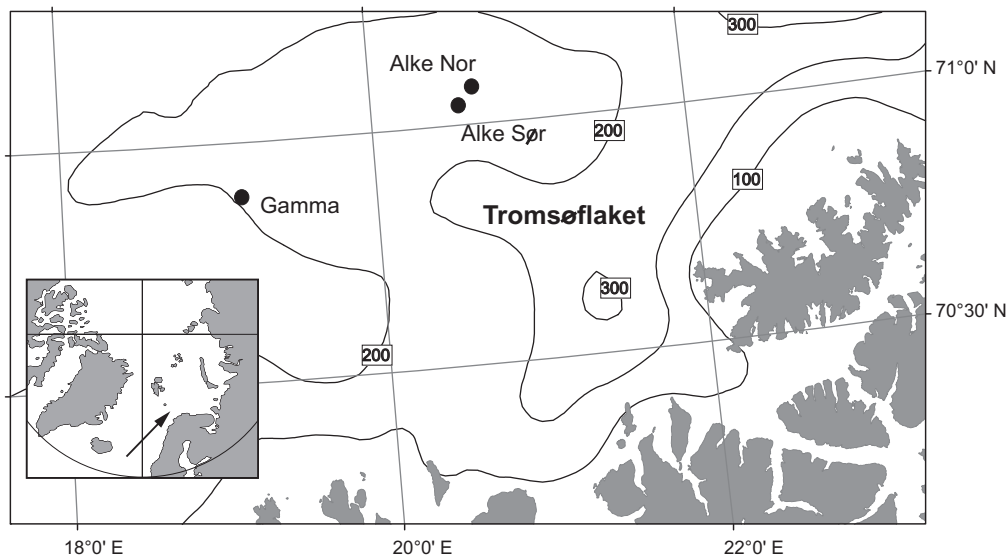


Figure 1 Map indicating the location of Tromsøflaket and positions of sampling sites.

6 from Gamma fields) with dredges and trawls in August 2008 aboard the r/v Oceania. Benthic epifaunal organisms collected by dredge were sorted onboard and fixed in buffered 10% formalin. Later in the laboratory, material was identified to the lowest possible taxonomic level, dried and weighed (dry weight; a selection of different sizes of organisms was made). For each species, the size–biomass relationship was established. On the basis of this information, species (or lowest identifiable taxonomic level) identities observed on the video were confirmed, counted from each snapshot and measured. Biomass (dry weight) was determined using the empirical relationships calculated from dredge samples. Secondary production was calculated according to Brey (2001). In order to convert biomass [$\text{g dry weight m}^{-2}$] into energy [kJ] and thereafter to production values [kJ y^{-1}], data were first transformed using published conversion factors (Brey, 2001). Subsequently, production/biomass (P B^{-1}) ratios were calculated for up to three size categories (large, medium and small, depending upon how much the P B^{-1} ratio varied with organism size) for each species by employing a multiple regression model incorporating habitat (e.g., water temperature, depth) and taxon-specific (e.g., phylum level, motility) data (Bolam et al., 2010; Brey, 2001). To calculate secondary production, the biomass per area of each

organism/size class was multiplied by the respective P B^{-1} ratio. Total production values for each replicate were then calculated as the sum of production values for each individual, and thereafter aggregated at the phylum level. Production at each area was represented as the average of the replicates but one individual transect outlier was excluded from further analysis. Finally, average production values were transformed to carbon using the conversion factor $45.7 \text{ J} = 1 \text{ mg C}$ (Salonen et al., 1976), and all the calculated values were standardized to a per m^2 basis.

For each snapshot, the presence of trawling tracks was noted (Photo 1) and, later, those results were used to contrast the effects of trawling on biodiversity, total abundance, total biomass, and poriferan biomass. Mean values are given with standard errors. Differences in taxonomic richness, abundance, and biomass among sampling areas (Alke Nord, Alke Sør and Gamma) were tested using the nonparametric Kruskal–Wallis test and Dunn's post hoc multiple comparisons test while differences between trawled and untrawled areas were tested with the corrected Mann–Whitney U test (sample size larger than 20 and ties occurred across both samples; Sokal and Rohlf, 1981). Nonparametric tests were chosen since normality could not be obtained even after data transformation. The number of taxa observed and estimated total

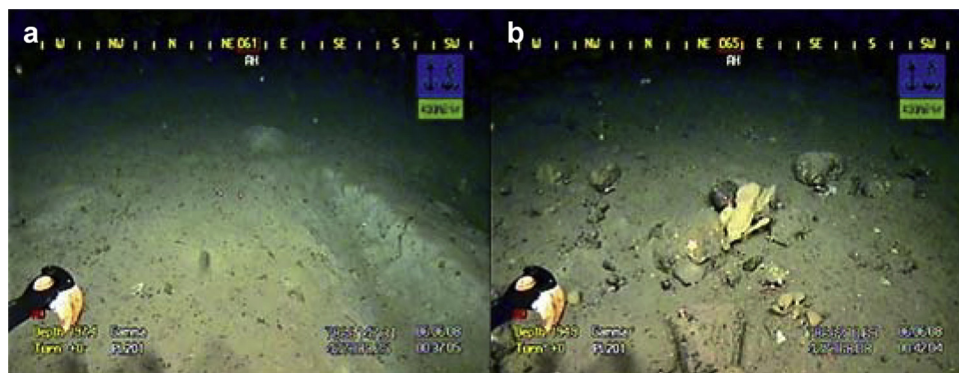


Photo 1 Snapshots of underwater video showing trawled areas (a) versus untrawled areas (b).

richness [Chao2] with 95% confidence intervals for each area were computed according to Colwell et al. (2004). Data analyses were performed using the Excel, EstimateS (Colwell, 2009) and Statsoft software STATISTICA v. 6.

3. Results

3.1. Diversity

Altogether, 46 epibenthic taxa and 7 fish taxa were identified across all surveyed areas (Fig. 2, Table 1). Estimated richness [Chao2] was 88 species with 95% confidence intervals from 46 to 106. In Alke Nord the mean number of observed taxa was 26 while Chao2 gave the estimate of 38 species (95% CI 29–79). In Alke Sør the mean number of observed taxa was 21, with Chao2 of 27 (95% CI 22–51), and in Gamma the mean number of observed taxa was 28, with Chao2 of 40 (95% CI 30–96). Mean number of taxa per snapshot was 0.5 ± 0.03 in Alke Nord, 0.3 ± 0.03 in Alke Sør and 1.5 ± 0.1 in Gamma. Alke Nord and Alke Sør were characterized by a gravel and soft sediment bottom; and Gamma had muddy and sandy sediments, with some crushed stones. In areas with heterogeneous bottoms, i.e. with both soft and hard substrate, more taxa were found.

3.2. Productivity, abundance and biomass

Gamma was the most productive area, with total production of $0.5 \text{ g C m}^{-2} \text{ y}^{-1} \pm 0.44$, Alke Nord's total production was $0.33 \text{ g C m}^{-2} \text{ y}^{-1} \pm 0.77$ (with an exception of one video transect, where production of mainly poriferans and echinoderms reached $5.6 \text{ g C m}^{-2} \text{ y}^{-1}$; however, this video was excluded from further analysis as an outlier) and Alke Sør had the lowest total production of only $0.07 \text{ g C m}^{-2} \text{ y}^{-1} \pm 0.12$ (Fig. 3). Poriferans contributed the most to the total production in all areas, followed by echinoderms (Fig. 3).

In Alke Nord and Alke Sør there were no organisms present on most of the snapshots (60–67%), while in Gamma only 10% of the photographs showed no macroscopic organisms. Mean epifaunal total abundance in Alke Nord reached $0.7 \text{ ind. m}^{-2} \pm 0.3$, $1.6 \text{ ind. m}^{-2} \pm 0.8$ in Gamma and only $0.1 \text{ ind. m}^{-2} \pm 0.02$ in Alke Sør (Fig. 4A). There were significant

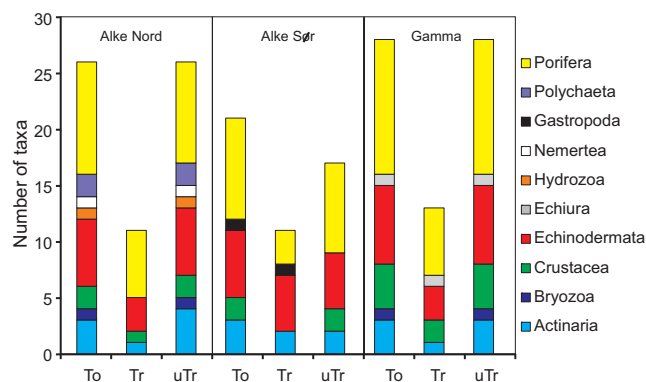


Figure 2 Total (To) taxa number in different taxonomic groups in trawled (Tr) and untrawled (uTr): Alke Nord, Alke Sør and Gamma.

Table 1 Most common taxa arranged in biomass (per m^2) order for trawled and untrawled areas in Alke Nord, Alke Sør and Gamma. A – Actinaria, B – Bryozoa, C – Crustacea, E – Echinodermata, Ec – Echiura, H – Hydrozoa, P – Porifera. Poriferan species that occurred only once are marked with *. Taxa identified to higher level than family and single taxa other than poriferans are not included.

Trawled	Untrawled
Alke Nord	
<i>Ceramaster granularis</i> (E)	<i>Geodia barretti</i> (P)
* <i>Phakellia ventilabrum</i> (P)	Chalinidae indet. (P)
* <i>Geodia barretti</i> (P)	<i>Ceramaster granularis</i> (E)
<i>Leptychaster arcticus</i> (E)	<i>Crisia eburnea</i> (B)
<i>Stylocordyla borealis</i> (P)	<i>Bolocera tuediae</i> (A)
<i>Polymastia</i> sp. (P)	<i>Phakellia ventilabrum</i> (P)
<i>Stichastrella</i> sp. (E)	<i>Actinostola callosa</i> (A)
<i>Bolocera tuediae</i> (A)	<i>Stylocordyla borealis</i> (P)
* <i>Asbestopluma pennatula</i> (P)	<i>Cerianthus</i> sp. (A)
<i>Munida</i> sp. (C)	<i>Leptychaster arcticus</i> (E)
	<i>Henricia</i> sp. (E)
	Hexactinellida (P)
	<i>Axinella infundibuliformis</i> (P)
	* <i>Asbestopluma pennatula</i> (P)
	<i>Munida</i> sp. (C)
	* <i>Mycale lingua</i> (P)
Alke Sør	
<i>Phakellia ventilabrum</i> (P)	<i>Phakellia ventilabrum</i> (P)
<i>Stichastrella</i> sp. (E)	<i>Geodia barretti</i> (P)
<i>Ceramaster granularis</i> (E)	<i>Ceramaster granularis</i> (E)
<i>Hippasteria phrygiana</i> (E)	* <i>Aplysilla sulfurea</i> (P)
<i>Poraniomorpha</i> sp. (E)	<i>Stichastrella</i> sp. (E)
* <i>Antho dichotoma</i> (P)	<i>Leptychaster arcticus</i> (E)
	<i>Bolocera tuediae</i> (A)
	<i>Axinella infundibuliformis</i> (P)
	<i>Poraniomorpha</i> sp. (E)
	<i>Asbestopluma pennatula</i> (P)
	<i>Hyas</i> sp. (C)
	* <i>Polymastia</i> sp. (P)
	* <i>Stylocordyla borealis</i> (P)
	<i>Munida</i> sp. (C)
Gamma	
<i>Geodia barretti</i> (P)	<i>Geodia barretti</i> (P)
<i>Parastichopus tremulus</i> (E)	<i>Parastichopus tremulus</i> (E)
<i>Geodia macandrewii</i> (P)	<i>Geodia macandrewii</i> (P)
* <i>Phakellia ventilabrum</i> (P)	<i>Phakellia ventilabrum</i> (P)
<i>Ceramaster granularis</i> (E)	<i>Aplysilla sulfurea</i> (P)
<i>Munida</i> sp. (C)	<i>Mesothuria intestinalis</i> (E)
* <i>Hymedesmia</i> sp. (P)	<i>Lithodes maja</i> (C)
<i>Bonellia viridis</i> (Ec)	<i>Axinella infundibuliformis</i> (P)
* <i>Mycale lingua</i> (P)	<i>Bolocera tuediae</i> (A)
	<i>Stichastrella</i> sp. (E)
	<i>Hymedesmia</i> sp. (P)
	<i>Ceramaster granularis</i> (E)
	<i>Reniera</i> sp. (P)
	<i>Bonellia viridis</i> (Ec)
	<i>Munida</i> sp. (C)
	<i>Henricia</i> sp. (E)
	* <i>Chalinidae</i> indet. (P)

Table 1 (Continued)

Trawled	Untrawled
	<i>Hyas</i> sp. (C)
	<i>Mycale lingua</i> (P)
	*Hexactinellida (P)
	<i>Stylocordyla borealis</i> (P)

differences in epifaunal total abundance among those three areas (Kruskal–Wallis test: $p < 0.05$; Dunn's test: $p < 0.05$; Table 2). Mean epifaunal total biomass (dry weight) in Alke Nord reached $10.1 \text{ g m}^{-2} \pm 4.0$, $20.8 \text{ g m}^{-2} \pm 5.3$ in Gamma and only $1.1 \text{ g m}^{-2} \pm 0.3$ in Alke Sør (Fig. 4B). There were significant differences in epifaunal total biomass among areas (Kruskal–Wallis test: $p < 0.05$; Dunn's test: $p < 0.05$; Table 2).

3.3. Trawled versus untrawled areas

Tracks from trawling were registered at all surveyed areas. Trawled areas had considerably lower taxonomic richness: in Alke Nord 26 taxa were found in untrawled areas versus 11 taxa noted in trawled areas. In Alke Sør 17 taxa and 11 taxa were found in untrawled and trawled areas, respectively. In the Gamma 28 taxa were found in untrawled versus 13 taxa found in trawled areas (Fig. 2). Mean number of taxa per snapshot reached in Alke Nord: 0.5 ± 0.04 and 0.2 ± 0.05 , in Alke Sør: 0.4 ± 0.04 and 0.2 ± 0.05 and in Gamma: 1.5 ± 0.1 and 0.9 ± 0.1 in untrawled and trawled areas, respectively. There were significant differences in taxonomic richness per photograph between trawled and untrawled area at each study site (Mann–Whitney U test, $p < 0.01$; Table 2). Poriferans dominated in terms of the number of taxa, production, and biomass in all regions (Figs. 2 and 3). Hydrozoans, bryozoans and annelids (filtering feeding Sabeliidae) were only present in untrawled areas. Actinarians, echinoderms, crustaceans and poriferans were present in both trawled and untrawled areas, but each group was more diverse in untrawled areas (Table 1). Gastropods were recorded only in trawled sites of Alke Sør. Sponge diversity was higher in untrawled areas (porifera *Axinella infundibuliformis* only present there).

Mean epifaunal abundance reached $0.9 \pm 0.4 \text{ ind. m}^{-2}$ and $0.1 \pm 0.03 \text{ ind. m}^{-2}$ in Alke Nord, $1.8 \pm 0.9 \text{ ind. m}^{-2}$ and $0.6 \pm 0.2 \text{ ind. m}^{-2}$ in Gamma, and only $0.1 \pm 0.02 \text{ ind. m}^{-2}$

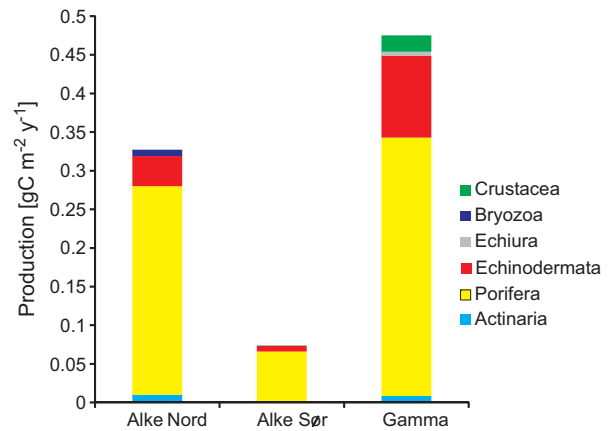


Figure 3 Total epibenthic production [$\text{g C m}^{-2} \text{ y}^{-1}$] per dominating taxa in areas: Alke Nord, Alke Sør and Gamma.

m^{-2} and $0.06 \pm 0.02 \text{ ind. m}^{-2}$ in Alke Sør, in untrawled and trawled areas, respectively (Fig. 4A). Mean epifaunal biomass in Alke Nord reached: $13.0 \pm 5.2 \text{ g m}^{-2}$ and $0.5 \pm 0.16 \text{ g m}^{-2}$, in Alke Sør: $1.4 \pm 0.4 \text{ g m}^{-2}$ and $0.3 \pm 0.09 \text{ g m}^{-2}$ and in Gamma: $23.3 \pm 6.3 \text{ g m}^{-2}$ and $6.3 \pm 2.5 \text{ g m}^{-2}$ in untrawled and trawled areas, respectively (Fig. 4B). There were significant differences in epifaunal abundance and biomass between all untrawled and trawled areas (Mann–Whitney U test, $p < 0.05$; Table 2; Fig. 4A and B). Sponges mean individual biomass in untrawled areas was higher: $32.2 \pm 57.0 \text{ g m}^{-2}$ and $19.1 \pm 54.7 \text{ g m}^{-2}$ in Alke Nord, $18.5 \pm 31.8 \text{ g m}^{-2}$ and $8.2 \pm 8.6 \text{ g m}^{-2}$ in Alke Sør and $53.5 \pm 59.8 \text{ g m}^{-2}$ and $46.2 \pm 49.1 \text{ g m}^{-2}$ in Gamma, untrawled and trawled areas respectively. Although poriferans were also observed in areas subjected to more intensive trawling they were at least five times less frequent (and 18 times less in Gamma) than in untrawled areas.

4. Discussion

In the Barents Sea, banks are recognized as important diversity and productivity “hot spots” (Cochrane et al., 2012; Kędra et al., 2013). Indeed, 46 taxa were found in this study in Tromsøflaket, which was equal to the lower *Chao2* 95% confidence interval. Nevertheless, this value is lower than other findings for this bank: Buhl-Mortensen et al. (2012)

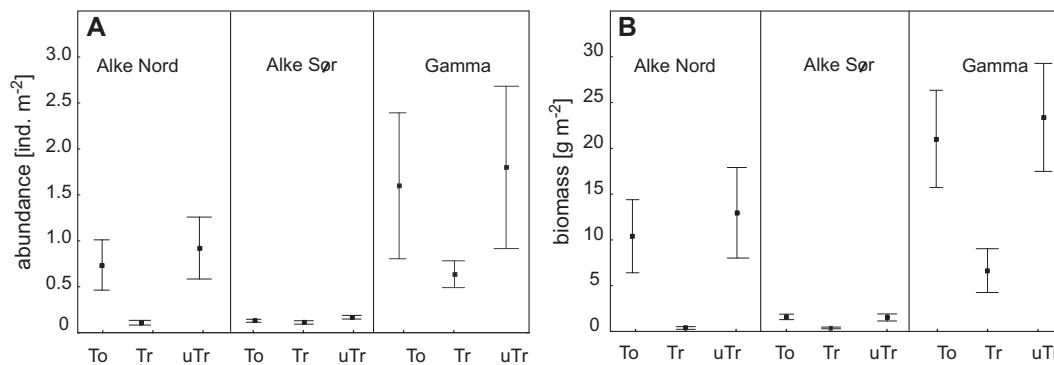


Figure 4 (A) Mean abundance [ind. m^{-2}] and (B) mean total epibenthic biomass [g m^{-2}] (dry weight) with standard error for Alke Nord, Alke Sør and Gamma per total area (To) and in trawled (T) and untrawled (uTr) areas.

Table 2 Results of statistical tests: K-W – Kruskal–Wallis, D – Dunn's post hoc multiple comparisons, U – corrected Mann–Whitney U, used to assess differences in abundance, biomass and taxonomic richness (number of taxa), among sampling areas (Alke Nord, Alke Sør and Gamma) and between trawled and untrawled areas. Test results are given (stat) and significance level (p). Significant differences are marked with *.

	Test		Abundance		Biomass		Taxonomic richness	
			stat	p	stat	p	stat	p
Area	K-W	H	249.77*	<0.01	216.27*	<0.01	293.32*	<0.01
Alke Nord vs. Alke Sør	D	z	4.03*	<0.05	2.90*	<0.05	1.13	>0.05
Alke Nord vs. Gamma	D	z	11.07*	<0.05	10.83*	<0.05	13.50*	<0.05
Alke Sør vs. Gamma	D	z	14.15*	<0.05	12.87*	<0.05	13.73*	<0.05
Trawled vs. untrawled								
Alke Nord	U	Z_{cor}	-4.31*	<0.01	-4.10*	<0.01	-3.95*	<0.01
Alke Sør	U	Z_{cor}	-2.08*	0.037	-1.97*	0.048	-1.98*	0.047
Gamma	U	Z_{cor}	-2.95*	<0.01	-4.06*	<0.01	-3.55*	<0.01

reported about 180 taxa; another study showed over 100 taxa in Tromsøflaket area (Buhl-Mortensen et al., 2009). Our values were lower; however, those two studies were conducted on a larger area, in a wider range of habitats, and with higher sampling effort than in the current study. Also, the reported average number of taxa was only about 30 for depths under 200 m in Tromsøflaket (Buhl-Mortensen et al., 2012). Where the same sediment types were sampled, Buhl-Mortensen et al. (2009) reported many of the same dominant poriferan (*Asbestopluma pennatula*, *Geodia* spp., *Stylodordyla borealis*, *Phakellia* sp., *Axinella* sp. and *Polymastia* sp.) and asteroidean taxa (*Ceramaster granularis* and *Poraniomorpha* spp.) as found here. Buhl-Mortensen et al. (2012) reported higher diversity and production in regions with heterogeneous bottom sediments, where gravel and/or stones were present.

In general, Arctic shallow banks are characterized by high biomass of epifaunal communities, especially when compared to deeper areas (Grebmeier et al., 2006; Kędra et al., 2013; Piepenburg et al., 1997; Piepenburg and Schmid, 1996, 1997). Although Tromsøflaket epifaunal diversity was relatively high, its biomass (less than 20 g m⁻² dry weight in all fields on average) and production (below 0.5 g C m⁻² y⁻¹, but above 5 g C m⁻² y⁻¹ in one Alke Nord location) were lower compared to epibenthos in other parts of the Barents Sea. However, the biomass and production estimation in this study might be biased due to the chosen method (video analysis) and more extensive dredge sampling may reveal higher values. In deep parts of the Barents Sea, benthic biomass is on average about 100 g m⁻² wet weight (Gulliksen et al., 2009), while on the most productive bank (Svalbard Bank) it averages about 600 g m⁻² (Idelson, 1930; Kędra et al., 2013). Buhl-Mortensen et al. (2012) reported similar or lower (to our results) epifaunal production values for some biotopes. Lower primary production and greater depths at Tromsøflaket (compared to Svalbard Bank) likely result in lower organic matter input to the sea floor, and may be reflected by the lower epifaunal biomass there. However, this pattern is not necessary reflected for epifauna at all deeper (about 200 m) banks in the Barents Sea (Jørgensen et al., 2016). Moreover, Tromsøflaket is subjected to intensive fishing through its whole area (Jørgensen et al., 2016), influencing standing stocks of benthic epifauna. Epifaunal

contribution to benthic productivity at other sites of approximately 200 m in the Barents Sea is believed to be minor (about 4%; Piepenburg, 2005), but since we only focused on the epifauna and no infaunal samples were taken, we cannot estimate the bank's total benthic production.

In our study trawling tracks were registered at all surveyed regions. Fishing intensity at Tromsøflaket is high, particularly in both Alke fields (<http://kart.fiskeridir.no/>; Jørgensen et al., 2016). This is reflected in significantly lower biomass and productivity in those fields compared to Gamma, where fishing pressure is lower. Although we designated particular fields in each snapshot as trawled or untrawled, lack of trawling marks on analyzed videos at Gamma (and other areas) does not preclude their presence nearby and their influence on epifauna there. Bottom trawling is known to have direct influence on bottom communities through dislocation, damage and mortality of benthic organisms (Bergman and Hup, 1992; Bergman and van Santbrink, 2000; Collie et al., 2016; Jennings and Kaiser, 1998), but also indirect effects through sediment disturbance and resuspension (Jennings et al., 2001; Watling et al., 2001). Sessile filter-feeders and large-bodied animals, such as sponges (dominant taxa in this study), hydroids, soft corals and bryozoans, are more sensitive to such disturbance but can survive in lightly trawled areas (Boulcott and Howell, 2011; Kaiser et al., 2002, 2006; Løkkeborg, 2005; Tillin et al., 2006). Heavily trawled areas in our study were less diverse, but all functional groups were present, including the sessile poriferans (although filter-feeding hydrozoans, bryozoans and polychaetes were absent). Intensively trawled areas are often characterized by a higher relative biomass of mobile animals and scavenging invertebrates (Collie et al., 1997; Rumohr and Kujawski, 2000; Tillin et al., 2006) which might have been the case of gastropods presence in Alke Sør. The high abundance of the opportunist crustaceans *Munida* sp. and *Hyas* sp. was also noted in the Gamma and Alke Sør, but in both trawled and untrawled areas.

Trawling impacts on sessile organisms are particularly high, and in the case of large sponges, the removal rate is estimated to reach about 20% of initial biomass per single trawl (Pitcher et al., 2000). Although the removal process is fast and effective, the time needed for recovery is long and the success of recovery uncertain. Studies on the recovery

rate of benthic populations in fished areas suggest a steady recovery of the benthic megafauna within at least 5 years after cessation of trawling and dredging activities (Hermsen et al., 2003). Benthic infaunal communities are reported to need at least 18 months to recover (Desprez, 2000; Sarda et al., 2000; Tuck et al., 1998), but the recovery of large sessile fauna will more likely take years to decades (Ragnarsson et al., 2015). Sponges, in particular, needed 8 years to recover (based on meta-analysis of about 100 different fishing impact manipulations, mainly from north Europe and northeast America; Kaiser et al., 2006), but there are some indications that large sponges and corals recovery might take even more than 15 years (on tropical shelves in Australia, Pitcher et al., 2000). Islandic scallop needed about 20 years to initiate population recovery, after heavy fishing on the Svalbard Bank was ceased due to stock depletion; yet, the current densities and biomass are still lower than in the 1920s, before the fisheries had started (Idelson, 1930; Kędra et al., 2013). In this study, sponge diversity was lower in trawled areas and specimens observed in trawled areas had lower individual biomass than ones outside the trawling tracks. Although some, even large, sponges were found in this study in old trawling tracks, it is more likely that those individuals were dislocated and moved by recent fishing activities, so it is questionable whether they survived.

The impact of chronic bottom trawling on benthic fauna depends on the natural disturbance levels to which benthic communities are adapted. In general, biomass and production of fauna on poorly-sorted, gravelly or muddy sediments, as found in our study, were more sensitive to chronic trawling than well-sorted sandy habitat substrates (Bolam et al., 2014; Queiros et al., 2006). Removal or disturbance of habitat-forming species like corals and sponges can have a serious effect on biodiversity and ecosystem functioning. For example, lower benthic production in regions of high importance for fisheries may reduce fish growth and reproduction since bottom fishing may affect diet composition and prey quality (Collie et al., 2016; Johnson et al., 2015; Shephard et al., 2014; Smith et al., 2013). It is important to note, however, that we only evaluated epibenthic megafauna in this study, and we cannot be certain to what extent these results are mirrored in other community components.

5. Conclusions

Our results suggest some impact of trawling on the epifaunal biomass and productivity in Tromsøflaket that are not unequivocal. More unambiguous results could be obtained if large areas with no trawling impacts were sampled. Increasing anthropogenic pressure in the area, including continued trawling and potential oil drilling, as well as accelerating climate change, will strongly affect vulnerable epifauna and habitats of Tromsøflaket. Thus, further studies on diversity and productivity of epifauna, and their links with infaunal components, in this area are required.

Acknowledgements

This study was funded in large part by ENI as part of the Arctic Seas Biodiversity (ASBD) project, with additional financial support from the Polish Ministry of Science and Higher Educa-

tion (382/W-Akvaplan-niva/2009/0), the Fram Centre flagship “Environmental impacts of industrial activity in the north” (MIKON), the Polish National Science Centre (2015/19/B/NZ8/03945), Akvaplan-niva and Institute of Oceanology PAN. We would like to express our deep thanks to the r/v Oceania crew, and Capt. Dag Mollan and the m/v Arian. We thank E. Bjørnbom and ENI for providing the ROV video footage.

References

- Bellec, V., Wilson, M., Bøe, R., Rise, L., Thorsnes, T., Buhl-Mortensen, L., Buhl-Mortensen, P., 2008. Bottom currents interpreted from iceberg plough marks revealed by multibeam data at Tromsøflaket, Barents Sea. *Mar. Geol.* 249 (3), 257–270, <http://dx.doi.org/10.1016/j.margeo.2007.11.009>.
- Bergman, M.J.N., Hup, M., 1992. Direct effects of beam trawling on macrofauna in a sandy sediment in the southern North Sea. *ICES J. Mar. Sci.* 49 (1), 5–11, <http://dx.doi.org/10.1093/icesjms/49.1.5>.
- Bergman, M.J.N., van Santbrink, J.W., 2000. Mortality in megafaunal benthic populations caused by trawl fisheries on the Dutch continental shelf in the North Sea in 1994. *ICES J. Mar. Sci.* 57 (5), 1321–1331, <http://dx.doi.org/10.1006/jmsc.2000.0917>.
- Bolam, S.G., Barrio-Frojan, C.R.S., Eggleton, J.D., 2010. Macrofaunal production along the UK continental shelf. *J. Sea Res.* 64, 166–179, <http://dx.doi.org/10.1016/j.seares.2010.02.003>.
- Bolam, S.G., Coggan, R.C., Diesing, M., Stephens, D., 2014. Sensitivity of macrobenthic secondary production to trawling in the English sector of the Greater North Sea: a biological trait approach. *J. Sea Res.* 85, 162–177, <http://dx.doi.org/10.1016/j.seares.2013.05.003>.
- Boulcott, P., Howell, T.R.W., 2011. The impact of scallop dredging on rocky-reef substrata. *Fish. Res.* 110, 415–420, <http://dx.doi.org/10.1016/j.fishres.2011.05.006>.
- Brey, T., 2001. Population Dynamics in Marine Benthic Invertebrates. A Virtual Handbook, Version 01.2. Alfred Wegener Institute for Polar and Marine Research, Germany, 200 pp., <http://www.thomas-brey.de/science/virtualhandbook>.
- Buhl-Mortensen, L., Buhl-Mortensen, P., Dolan, M.F.J., Dannheim, J., Bellec, V., Holte, B., 2012. Habitat complexity and bottom fauna composition at different scales on the continental shelf and slope of northern Norway. *Hydrobiologia* 685 (1), 191–219, <http://dx.doi.org/10.1007/s10750-011-0988-6>.
- Buhl-Mortensen, P., Dolan, M., Buhl-Mortensen, L., 2009. Prediction of benthic biotopes on a Norwegian offshore bank using a combination of multivariate analysis and GIS classification. *ICES J. Mar. Sci.* 66 (9), 2026–2032, <http://dx.doi.org/10.1093/icesjms/66.9.2026>.
- Callaway, R., Engelhard, G.H., Dann, J., Cotter, J., Rumohr, H., 2007. A century of North Sea epibenthos and trawling: comparison between 1902–1912, 1982–1985 and 2000. *Mar. Ecol.-Prog. Ser.* 346, 27–43, <http://dx.doi.org/10.3354/meps07038>.
- Carmack, E., Wassmann, P., 2006. Food webs and physical-biological coupling on pan-Arctic shelves: unifying concepts and comprehensive perspectives. *Prog. Oceanogr.* 71 (2–4), 446–477, <http://dx.doi.org/10.1016/j.pocean.2006.10.004>.
- Cochrane, S.K.J., Pearson, T.H., Greenacre, M., Costelloe, J., Ellingsen, I.H., Dahle, S., Gulliksen, B., 2012. Benthic fauna and functional traits along a Polar Front transect in the Barents Sea – advancing tools for ecosystem-scale assessments. *J. Mar. Syst.* 94, 204–217, <http://dx.doi.org/10.1016/j.jmarsys.2011.12.001>.
- Collie, J.S., Escanero, G.A., Valentine, P.C., 1997. Effects of bottom fishing on the benthic megafauna of Georges Bank. *Mar. Ecol.-Prog. Ser.* 155, 159–172, <http://dx.doi.org/10.3354/meps155159>.

- Collie, J., Hiddink, J.G., van Kooten, T., Rijnsdorp, A.D., Kaiser, M.J., Jennings, S., Hilborn, R., 2016. Indirect effects of bottom fishing on the productivity of marine fish. *Fish Fish.*, <http://dx.doi.org/10.1111/faf.12193>.
- Colwell, R.K., 2009. EstimateS: Statistical estimation of species richness and shared species from samples. Version 8.2. User's Guide and application published at <http://purl.oclc.org/estimates>.
- Colwell, R.K., Mao, C.X., Chang, J., 2004. Interpolating, extrapolating, and comparing incidence-based species accumulation curves. *Ecology* 85, 2717–2727, <http://dx.doi.org/10.1890/03-0557>.
- Dannheim, J., Brey, T., Schroder, A., Mintenbeck, K., Knust, R., Arntz, W.E., 2014. Trophic look at soft-bottom communities – short-term effects of trawling cessation on benthos. *J. Sea Res.* 85, 18–28, <http://dx.doi.org/10.1016/j.seares.2013.09.005>.
- De Juan, S., Demestre, M., Sanchez, P., 2011. Exploring the degree of trawling disturbance by the analysis of benthic communities ranging from a heavily exploited fishing ground to an undisturbed area in the NW Mediterranean. *Sci. Mar.* 75 (3), 507–516, <http://dx.doi.org/10.3989/scimar.2011.75n3507>.
- Desprez, M., 2000. Physical and biological impact of marine aggregate extraction along the French coast of the Eastern English Channel: short and long-term post-dredging restoration. *ICES J. Mar. Sci.* 57 (5), 1428–1438, <http://dx.doi.org/10.1006/jmsc.2000.0926>.
- Dijkstra, N., Junttila, J., Carroll, J., Husum, K., Hald, M., Elvebakk, G., Godtliessen, F., 2013. Baseline benthic foraminiferal assemblages and habitat conditions in a sub-Arctic region of increasing petroleum development. *Mar. Environ. Res.* 92, 178–196, <http://dx.doi.org/10.1016/j.marenvres.2013.09.014>.
- Grebmeier, J.M., Cooper, L.W., Feder, H.M., Sirenko, B.I., 2006. Ecosystem dynamics of the Pacific-influenced northern Bering and Chukchi seas in the Amerasian Arctic. *Prog. Oceanogr.* 71 (2–4), 331–361, <http://dx.doi.org/10.1016/j.pocean.2006.10.001>.
- Gulliksen, B., Hop, H., Nielsens, M., 2009. Benthic life. In: Sakshaug, E., Johnsen, G., Kovacs, K. (Eds.), *Ecosystem Barents Sea*. Tapir Acad. Press, Trondheim, 339–372.
- Handley, S.J., Willis, T.J., Cole, R.G., Bradley, A., Cairney, D.J., Brown, S.N., Carter, M.E., 2014. The importance of benchmarking habitat structure and composition for understanding the extent of fishing impacts in soft sediment ecosystems. *J. Sea Res.* 86, 58–68, <http://dx.doi.org/10.1016/j.seares.2013.11.005>.
- Hermesen, J.M., Collie, J.S., Valentine, P.C., 2003. Mobile fishing gear reduces benthic megafaunal production on Georges Bank. *Mar. Ecol.-Prog. Ser.* 260, 97–108, <http://dx.doi.org/10.3354/meps260097>.
- Hiddink, J.G., Jennings, S., Kaiser, M.J., Queiros, A.M., Duplisea, D.E., Piet, G.J., 2006. Cumulative impacts of seabed trawl disturbance on benthic biomass, production, and species richness in different habitats. *Can. J. Fish. Aquat. Sci.* 63 (4), 721–736, <http://dx.doi.org/10.1139/f05-266>.
- Hinz, H., Prieto, V., Kaiser, M.J., 2009. Trawl disturbance on benthic communities: chronic effects and experimental predictions. *Ecol. Appl.* 19 (3), 761–773, <http://dx.doi.org/10.1890/08-0351.1>.
- Idelson, M.S., 1930. A preliminary quantitative evaluation of the bottom fauna of the Spitzbergen bank. *Ber. Wissenschaftlichen Meeresinstitut.* 4, 27–46.
- Jakobsson, M., 2002. Hypsometry and volume of the Arctic Ocean and its constituent seas. *Geochem. Geophys. Geosyst.* 3 (5), 1–18, <http://dx.doi.org/10.1029/2001GC000302>.
- Jennings, S., Dinmore, T.A., Duplisea, D.E., Warr, K.J., Lancaster, J.E., 2001. Trawling disturbance can modify benthic production processes. *J. Anim. Ecol.* 70 (3), 459–475, <http://dx.doi.org/10.1046/j.1365-2656.2001.00504.x>.
- Jennings, S., Kaiser, M.J., 1998. The effects of fishing on marine ecosystems. *Adv. Mar. Biol.* 34, 201–212, [http://dx.doi.org/10.1016/S0065-2881\(08\)60212-6](http://dx.doi.org/10.1016/S0065-2881(08)60212-6).
- Johnson, A.F., Gorelli, G., Jenkins, S.R., Hiddink, J.G., Hinz, H., 2015. Effects of bottom trawling on fish foraging and feeding. *P. R. Soc. B* 282 (1799), 20142336, <http://dx.doi.org/10.1098/rspb.2014.2336>.
- Jørgensen, L.L., Ljubin, P., Skjoldal, H.R., Ingvaldsen, R.B., Anisimova, N., Manushin, I., 2015. Distribution of benthic megafauna in the Barents Sea: baseline for an ecosystem approach to management. *ICES J. Mar. Sci.* 72 (2), 595–613, <http://dx.doi.org/10.1093/icesjms/fsu106>.
- Jørgensen, L.L., Planque, B., Thangstad, T.H., Certain, G., 2016. Vulnerability of megabenthic species to trawling in the Barents Sea. *ICES J. Mar. Sci.* 73 (1), i84–i97, <http://dx.doi.org/10.1093/icesjms/fsv107>.
- Jørgensen, L.L., Renaud, P.E., Cochrane, S.K., 2011. Improving benthic monitoring by combining trawl and grab surveys. *Mar. Pollut. Bull.* 62 (6), 1183–1190, <http://dx.doi.org/10.1016/j.marpolbul.2011.03.035>.
- Kaiser, M.J., Clarke, K.R., Hinz, H., Austen, M.C.V., Somerfield, P.J., Karakassis, I., 2006. Global analysis of response and recovery of benthic biota to fishing. *Mar. Ecol.-Prog. Ser.* 311, 1–14, <http://dx.doi.org/10.3354/meps311001>.
- Kaiser, M.J., Collie, J.S., Hall, S.J., Jennings, S., Poiner, I.R., 2002. Modification of marine habitats by trawling activities: prognosis and solutions. *Fish Fish.* 3 (2), 1–24, <http://dx.doi.org/10.1046/j.1467-2979.2002.00079.x>.
- Kędra, M., Renaud, P.E., Andrade, H., Goszczko, I., Ambrose Jr., W.G., 2013. Benthic community structure, diversity and productivity in the shallow Barents Sea bank (Svalbard Bank). *Mar. Biol.* 160 (4), 805–819, <http://dx.doi.org/10.1007/s00227-012-2135-y>.
- Kilgour, M.J., Auster, P.J., Packer, D., Purcell, M., Packard, G., Dessner, M., Sherrell, A., Rissolo, D., 2014. Use of AUVs to inform management of deep-sea corals. *Mar. Technol. Soc. J.* 48 (1), 21–27, <http://dx.doi.org/10.4031/MTSJ.48.1.2>.
- Lindholm, J., Auster, P., Valentine, P., 2004. Role of a large marine protected area for conserving landscape attributes of sand habitats on Georges Bank (NW Atlantic). *Mar. Ecol.-Prog. Ser.* 269, 61–68, <http://dx.doi.org/10.3354/meps269061>.
- Loeng, H., Drinkwater, K.F., 2007. An overview of the ecosystems of the Barents and Norwegian Seas and their response to climate variability. *Deep-Sea Res. Pt. II* 54 (23–26), 2478–2500, <http://dx.doi.org/10.1016/j.dsr2.2007.08.013>.
- Løkkeborg, S., 2005. Impacts of trawling and scallop dredging on benthic habitats and communities, *FAO Fisheries Technical Paper* 472. FAO, Rome, 58 pp.
- Mangano, M.C., Kaiser, M.J., Porporato, E.M.D., Spano, N., 2013. Evidence of trawl disturbance on mega-epibenthic communities in the Southern Tyrrhenian Sea. *Mar. Ecol.-Prog. Ser.* 475, 101–117, <http://dx.doi.org/10.3354/meps10115>.
- Olsen, E., Aanes, S., Mehl, S., Holst, J.C., Aglen, A., Gjøsæter, H., 2010. Cod, haddock, saithe, herring, and capelin in the Barents Sea and adjacent waters: a review of the biological value of the area. *ICES J. Mar. Sci.* 67 (1), 87–101, <http://dx.doi.org/10.1093/icesjms/fsp229>.
- Olsgaard, F., Schaanning, M.T., Widdicombe, S., Kendall, M.A., Austen, M.C., 2008. Effects of bottom trawling on ecosystem functioning. *J. Exp. Mar. Biol. Ecol.* 366 (1–2), 123–133, <http://dx.doi.org/10.1016/j.jembe.2008.07.036>.
- Piepenburg, D., 2005. Recent research on Arctic benthos: common notions need to be revised. *Polar Biol.* 28 (10), 733–755, <http://dx.doi.org/10.1007/s00300-005-0013-5>.
- Piepenburg, D., Ambrose Jr., W.G., Brandt, A., Renaud, P.E., Ahrens, M.J., Jensen, P., 1997. Benthic community patterns reflect water column processes in the Northeast Water polynya (Greenland). *J. Mar. Syst.* 10 (1–4), 467–482, [http://dx.doi.org/10.1016/S0924-7963\(96\)00050-4](http://dx.doi.org/10.1016/S0924-7963(96)00050-4).
- Piepenburg, D., Schmid, M.K., 1996. Brittle star fauna (Echinodermata: Ophiuroidea) of the Arctic northwestern Barents Sea:

- composition, abundance, biomass and spatial distribution. *Polar Biol.* 16 (6), 383–392, <http://dx.doi.org/10.1007/BF02390420>.
- Piepenburg, D., Schmid, M.K., 1997. A photographic survey of the epibenthic megafauna of the Arctic Laptev Sea shelf: distribution, abundance, and estimates of biomass and organic carbon demand. *Mar. Ecol.-Prog. Ser.* 147, 63–75, <http://dx.doi.org/10.3354/meps147063>.
- Pitcher, C.R., Poiner, I.R., Hill, B.J., Burrige, C.Y., 2000. Implications of the effects of trawling on sessile megazoobenthos on a tropical shelf in northeastern Australia. *ICES J. Mar. Sci.* 57, 1359–1368, <http://dx.doi.org/10.1006/jmsc.2000.0911>.
- Queiros, A.M., Hiddink, J.G., Kaiser, M.J., Hinz, H., 2006. Effects of chronic bottom trawling disturbance on benthic biomass, production and size spectra in different habitats. *J. Exp. Mar. Biol. Ecol.* 335 (1), 91–103, <http://dx.doi.org/10.1016/j.jembe.2006.03.001>.
- Ragnarsson, S.Á., Thorarinsdóttir, G.G., Gunnarsson, K., 2015. Short and long-term effects of hydraulic dredging on benthic communities and ocean quahog (*Arctica islandica*) populations. *Mar. Environ. Res.* 109, 113–123, <http://dx.doi.org/10.1016/j.marenvres.2015.05.003>.
- Rumohr, H., Kujawski, T., 2000. The impact of trawl fishery on the epifauna of the southern North Sea. *ICES J. Mar. Sci.* 57, 1389–1394, <http://dx.doi.org/10.1006/jmsc.2000.0930>.
- Sakshaug, E., 1997. Biomass and productivity distributions and their variability in the Barents Sea. *ICES J. Mar. Sci.* 54 (3), 341–350, <http://dx.doi.org/10.1006/jmsc.1996.0170>.
- Sakshaug, E., Johnsen, G., Kristiansen, S., von Quillfeldt, C., Rey, F., Slagstad, D., Thingstad, F., 2009. *Phytoplankton and primary production*. In: Sakshaug, E., Johnsen, G., Kovacs, K. (Eds.), *Ecosystem Barents Sea*. Tapir Acad. Press, Trondheim, Norway, 167–208.
- Sakshaug, E., Slagstad, D., 1991. Light and productivity of phytoplankton in polar marine ecosystems: a physiological view. *Polar Res.* 10 (1), 69–85, <http://dx.doi.org/10.1111/j.1751-8369.1991.tb00636.x>.
- Salonen, J., Sarvala, J., Hakala, I., Viljanen, M.J., 1976. The relation of energy and organic carbon in aquatic invertebrates. *Limnol. Oceanogr.* 21 (5), 724–730, <http://dx.doi.org/10.4319/lo.1976.21.5.0724>.
- Sarda, R., Pinedo, S., Gremare, A., 2000. Changes in the dynamics of shallow sandy-bottom assemblages due to sand extraction in the Catalan Western Mediterranean Sea. *ICES J. Mar. Sci.* 57 (5), 1446–1453, <http://dx.doi.org/10.1006/jmsc.2000.0922>.
- Shephard, S., Minto, C., Zolck, M., Jennings, S., Brophy, D., Reid, D., 2014. Scavenging on trawled seabeds can modify trophic size structure of bottom-dwelling fish. *ICES J. Mar. Sci.* 71 (2), 398–405, <http://dx.doi.org/10.1093/icesjms/fst134>.
- Skarðhamar, J., Svendsen, H., 2005. Circulation and shelf–ocean interaction off North Norway. *Cont. Shelf Res.* 25 (12–13), 1541–1560, <http://dx.doi.org/10.1016/j.csr.2005.04.007>.
- Smith, B.E., Collie, J.S., Lengyel, N.L., 2013. Effects of chronic bottom fishing on the benthic epifauna and diets of demersal fishes on northern Georges Bank. *Mar. Ecol.-Prog. Ser.* 472, 199–217, <http://dx.doi.org/10.3354/meps10031>.
- Sokal, R.R., Rohlf, F.J., 1981. *Biometry*, 2nd edn. W.H. Freeman and Company, San Francisco, 859 pp.
- Tillin, H.M., Hiddink, J.G., Jennings, J., Kaiser, M.J., 2006. Chronic bottom trawling alters the functional composition of benthic invertebrate communities on a sea-basin scale. *Mar. Ecol. Prog. Ser.* 318, 31–45, <http://dx.doi.org/10.3354/meps318031>.
- Tuck, I.D., Hall, S.J., Robertson, M.K., Armstrong, E., Basford, D.J., 1998. Effects of physical trawling disturbance in a previously un-fished sheltered Scottish sea loch. *Mar. Ecol.-Prog. Ser.* 162, 227–242, <http://dx.doi.org/10.3354/meps162227>.
- Watling, L., Findlay, R.H., Mayer, L.M., Schick, D.F., 2001. Impact of a scallop drag on the sediment chemistry, microbiota, and faunal assemblages of a shallow subtidal marine benthic community. *J. Sea Res.* 3–4 (46), 309–324, [http://dx.doi.org/10.1016/S1385-1101\(01\)00083-1](http://dx.doi.org/10.1016/S1385-1101(01)00083-1).
- Winsnes, I., Skjoldal, H.R., 2009. Management plan for the Norwegian part of the Barents Sea Ecosystem. In: Bianchi, G., Skjoldal, H.R. (Eds.), *The Ecosystem Approach to Fisheries*. CABI, Cambridge, MA, 228–245.
- Zenkevich, L.A., 1963. *The Biology of the Seas of the USSR*. Acad. Sci. USSR, Moscow, 955 pp.



Available online at www.sciencedirect.com

ScienceDirect

journal homepage: www.journals.elsevier.com/oceanologia/



ORIGINAL RESEARCH ARTICLE

Wave-induced bottom shear stress estimation in shallow water exemplified by using deep water wind statistics

Dag Myrhaug*

Department of Marine Technology, Norwegian University of Science and Technology (NTNU), Trondheim, Norway

Received 9 June 2016; accepted 16 September 2016

Available online 4 October 2016

KEYWORDS

Random waves;
Bottom friction;
Large bed roughness;
Erosion and deposition
of mud;
Wind statistics

Summary The paper provides a simple and analytical method which can be used to give estimates of the wave-induced bottom shear stress for very rough beds and mud beds in shallow water based on wind statistics in deep water. This is exemplified by using long-term wind statistics from the northern North Sea, and by providing examples representing realistic field conditions. Based on, for example, global wind statistics, the present results can be used to make estimates of the bottom shear stress in shallow water.

© 2016 Institute of Oceanology of the Polish Academy of Sciences. Production and hosting by Elsevier Sp. z o.o. This is an open access article under the CC BY-NC-ND license (<http://creativecommons.org/licenses/by-nc-nd/4.0/>).

1. Introduction

Simple and effective descriptions of transport mechanisms in operational estuarine, coastal and ocean circulation models

* Correspondence to: Department of Marine Technology, Otto Nielsens vei 10, NO-7491 Trondheim, Norway. Tel.: +47 73 59 55 27; fax: +47 73 59 55 28.

E-mail address: dag.myrhaug@ntnu.no.

Peer review under the responsibility of Institute of Oceanology of the Polish Academy of Sciences.



Production and hosting by Elsevier

are often required, in which the bottom shear stress represents an important component in finite water depths. In estuarine and coastal zones, at shallow and intermediate water depths, the water particle movements induced by surface waves have a strong effect in the entire water column from the surface to the bottom of the sea. The flow in this region is generally induced by surface waves and currents, where the bottom wave boundary layer is a thin flow region at the seabed dominated by friction arising from the bottom roughness. The wave boundary layer flow determines the bottom shear stress, which affects, e.g. the sediment transport and assessment of the stability of scour protections in the marine environment. The boundary layer flow regime is most commonly rough turbulent, although the flow regime over mud beds is mostly laminar and smooth turbulent depending on the bottom sediments and wave activity.

<http://dx.doi.org/10.1016/j.oceano.2016.09.002>

0078-3234/© 2016 Institute of Oceanology of the Polish Academy of Sciences. Production and hosting by Elsevier Sp. z o.o. This is an open access article under the CC BY-NC-ND license (<http://creativecommons.org/licenses/by-nc-nd/4.0/>).

The rough turbulent flow regime considered here corresponds to very rough beds. The results in this flow regime are relevant for assessing, e.g. the stability of scour protection in the coastal environment for relative large stone sizes compared to the near-bed random wave activity.

Laminar flow near mud beds, where clays and silt are referred to as mud, is of practical interest. The movement of mud within coastal and estuarine waters might have large economical and ecological impact in the development of new engineering works and maintenance of existing installations, e.g. related to necessary routine dredging required for ports' accessibility to shipping. The capability to predict the movement of the mud is also essential to understand the distribution of certain pollutants adsorbed to mud, as cohesive sediments are often contaminated. It appears that organic (polychlorinated biphenyl (PCBs), etc.) pollutants adhere easily to the clay particles and organic materials of the sediments. The results for laminar flow are relevant for assessing erosion and deposition of mud beneath random waves.

Further details on the background and complexity of the flow, as well as reviews of the problems are found in the textbooks of, e.g. Nielsen (1992), Fredsøe and Deigaard (1992), Soulsby (1997), Whitehouse et al. (2000), Winterwerp and van Kesteren (2004).

The purpose of this study is to demonstrate how wind statistics in deep water can be used to provide the wave-induced bottom shear stress in shallow water. Results are given for the bottom shear stress beneath random surface waves at beds with very large roughness and for laminar flow applied to mud beds, and are primarily based on the previous work by Myrhaug and Holmedal (2010) who provided the seabed shear stress spectrum for very rough beds and for laminar flow. Examples of results representing realistic field conditions are given.

2. Bottom shear stress beneath random waves in shallow water

2.1. Spectrum of bottom shear stress

Following Myrhaug and Holmedal (2010) (hereafter referred to as MH10) the bottom shear stress spectrum for laminar flow in shallow water ($kh \ll 1$) is obtained as (see Eq. (A12) in the Appendix)

$$S_{(\tau/\rho)(\tau/\rho)}(\omega, h) = \frac{\nu_f \omega^3}{(kh)^2} \frac{\omega^2 h}{2g} S_{\zeta\zeta}(\omega). \quad (1)$$

Here τ is the bottom shear stress, ρ is the fluid density, ω is the cyclic wave frequency, h is the water depth, ν_f is the kinematic viscosity of the fluid, k is the wave number determined from the dispersion relationship $\omega^2 = gk \tanh kh$ which in shallow water reduces to $\omega^2 = k^2 gh$, g is the acceleration due to gravity, and $S_{\zeta\zeta}(\omega)$ is the deep water wave spectrum.

The bottom shear stress spectrum for rough turbulent flow over a bed with very large roughness in shallow water is obtained as (see Eq. (A16) in the Appendix)

$$S_{(\tau/\rho)(\tau/\rho)}(\omega, h) = \frac{c^2 z_0^2 \omega^4}{4(kh)^2} \frac{\omega^2 h}{2g} S_{\zeta\zeta}(\omega). \quad (2)$$

Here z_0 is the average bottom roughness, and c is a constant with the two values 9 and 18 reflecting that c depends strongly on the geometry of the large roughness elements (see the Appendix for more details). The first term on the right hand side of Eqs. (1) and (2) represents the square of the magnitude of the transfer function between the bottom shear stress τ/ρ and the free surface elevation ζ ; the second term represents the depth correction factor in shallow water, i.e. a correction factor which is used to transform the deep water wave spectrum $S_{\zeta\zeta}(\omega)$ to shallow water (see the Appendix for more details).

By substituting $k^2 = \omega^2/gh$, Eqs. (1) and (2) are rearranged, respectively, to

$$S_{(\tau/\rho)(\tau/\rho)}(\omega, h) = \frac{1}{2} \nu_f \omega^3 S_{\zeta\zeta}(\omega); \quad \text{laminar}, \quad (3)$$

$$S_{(\tau/\rho)(\tau/\rho)}(\omega, h) = \frac{1}{8} (cz_0)^2 \omega^4 S_{\zeta\zeta}(\omega); \quad \text{rough}. \quad (4)$$

Thus the shear stress spectra in shallow water are given in terms of the deep water wave spectrum, and it should be noted that the dependence on the water depth disappears. Overall this is a consequence of transforming the waves from deep to shallow water and using the bed shear stress for laminar flow (Eqs. (A3) and (A8)) and for very rough beds (Eqs. (A3) and (A13)).

2.2. Laminar flow

The zeroth spectral moment of the bottom shear stress spectrum for laminar flow is obtained from Eq. (3) as

$$m_{0\tau/\rho} = \int_0^\infty S_{(\tau/\rho)(\tau/\rho)}(\omega, h) d\omega = \frac{\nu_f}{2} m_3, \quad (5)$$

where m_3 is the third wave spectral moment in deep water, i.e. the n th spectral moment of the deep water wave spectrum is defined as

$$m_n = \int_0^\infty \omega^n S_{\zeta\zeta}(\omega) d\omega; \quad n = 0, 1, 2, 3, 4, \dots \quad (6)$$

Thus, from Eq. (5) the significant value of the bottom shear stress height is obtained as

$$H_{s\tau/\rho} = 4\sqrt{m_{0\tau/\rho}} = 2\sqrt{2\nu_f m_3}. \quad (7)$$

2.3. Very rough beds

The zeroth spectral moment of the bottom shear stress spectrum for very rough beds is obtained from Eq. (4) as

$$m_{0\tau/\rho} = \frac{1}{8} (cz_0)^2 m_4, \quad (8)$$

where m_4 is the fourth spectral moment of the wave spectrum in deep water defined in Eq. (6). The most common model wave spectra are proportional to ω^{-5} for large ω , and thus m_4 does not exist. However, m_4 can be expressed in terms of the spectral moments m_0 , m_1 and m_2 , and the

spectral bandwidth parameters ε and ν are given in terms of the spectral moments of the deep water wave spectrum as (see e.g. Tucker and Pitt, 2001)

$$\varepsilon^2 = 1 - \frac{m_2^2}{m_0 m_4}, \quad (9)$$

$$\nu^2 = \frac{m_0 m_2}{m_1^2} - 1. \quad (10)$$

For a narrow-band wave process $\nu = \varepsilon/2$ (Longuet-Higgins, 1975), which gives

$$m_4 = \frac{m_1^2 m_2^2}{m_0 (5m_1^2 - 4m_0 m_2)}. \quad (11)$$

Thus, from Eq. (8) the significant value of the bottom shear stress height is obtained as

$$H_{s\tau/\rho} = 4\sqrt{m_{0\tau/\rho}} = \sqrt{2}cz_0\sqrt{m_4}, \quad (12)$$

where m_4 is given in Eq. (11).

3. Examples of results for a Phillips wave spectrum and wind statistics in deep water

Two examples are included to illustrate the applicability of the results for practical purposes using data typical for field conditions: a water depth with $h = 3$ m consisting of very rough beds with bed roughness $z_0 = 0.0094$ m representative for cobble according to Soulsby (1997, Fig. 4), and mud beds with median grain diameter $d_{50} = 0.03$ mm representative of medium silt according to Soulsby (1997, Fig. 4).

First, the common features of the two examples will be described. Examples of results are given by choosing the Phillips deep water wave spectrum for which analytical expressions can be obtained (see e.g. Holthuijsen, 2007; Tucker and Pitt, 2001)

$$S(\omega) = \alpha \frac{g^2}{\omega^5}, \quad \omega \geq \omega_p = \frac{g}{U_{10}}, \quad (13)$$

where $\alpha = 0.0081$ is the Phillips constant, ω_p is the spectral peak frequency, and U_{10} is the mean wind speed at the 10 m elevation above the sea surface. By using the definition of the spectral moments in Eq. (6) it follows that the significant wave height in deep water is

$$H_s = 4\sqrt{m_0} = 2\sqrt{\alpha} \frac{g}{\omega_p^2}. \quad (14)$$

Then it follows from Eqs. (11) and (12) for very rough beds that

$$H_{s\tau/\rho} = 2\sqrt{\alpha}gc_0z_0; \quad \text{rough.} \quad (15)$$

Moreover, for laminar flow it follows from Eq. (7) that

$$H_{s\tau/\rho} = 2\sqrt{2\nu_f\alpha g U_{10}}; \quad \text{laminar.} \quad (16)$$

Furthermore, the Phillips spectrum transformed to shallow water becomes

$$S_{\zeta\zeta}(\omega, h) = \frac{\omega^2 h}{2g} S_{\zeta\zeta}(\omega) = \alpha \frac{gh}{2\omega^3}; \quad \omega \geq \omega_p = \frac{g}{U_{10}}, \quad (17)$$

which gives the following significant wave height in shallow water:

$$H_{sh} = 4\sqrt{m_{0h}} = \frac{2\sqrt{\alpha gh}}{\omega_p}; \quad \text{shallow water,} \quad (18)$$

where $m_{0h} = \int_0^\infty S_{\zeta\zeta}(\omega, h) d\omega$.

It is noted that for very rough beds (Eq. (15)) $H_{s\tau/\rho}$ is independent of U_{10} , while for laminar flow (Eq. (16)) $H_{s\tau/\rho}$ depends on U_{10} . Consequently, the results for laminar flow can be obtained from available wind statistics for an ocean area, e.g. from a long-term distribution of U_{10} .

Different parametric models for the cumulative distribution function (*cdf*) or the probability density function (*pdf*) of U_{10} are given in the literature, see e.g. a recent review in Bitner-Gregersen (2015). In the present example the *cdf* of U_{10} given by Johannessen et al. (2001) is used to demonstrate the application of the results. This *cdf* is based on wind measurements covering the years 1973–1999 from the northern North Sea. The database consists of composite measurements from the Brent, Troll, Statfjord and Gullfaks fields as well as the weather ship Stevenson. Model data from the Norwegian hindcast archive (WINCH, gridpoint 1415) have been filled in for periods where measured data were missing. Thus a 25-year-long continuous time series has been used (see Johannessen et al., 2001 for more details), upon which the *cdf* of the 1-h values of U_{10} is described by the two-parameter Weibull model

$$P(U_{10}) = 1 - \exp\left[-\left(\frac{U_{10}}{\theta}\right)^\beta\right]; \quad U_{10} \geq 0, \quad (19)$$

with the Weibull parameters:

$$\theta = 8.426, \quad \beta = 1.708. \quad (20)$$

Now the long-term statistics of $H_{s\tau/\rho}$ for laminar flow can be derived by using this *cdf* of U_{10} . Statistical quantities of interest are, e.g. the expected value of $H_{s\tau/\rho}$, $E[H_{s\tau/\rho}]$, and the variance of $H_{s\tau/\rho}$, $\text{Var}[H_{s\tau/\rho}]$, which for laminar flow will be proportional to $E[U_{10}^{1/2}]$ and $\text{Var}[U_{10}^{1/2}]$, respectively. This requires calculation of $E[U_{10}^n]$, which for a Weibull distributed quantity is given by (Bury, 1975)

$$E[U_{10}^n] = \theta^n \Gamma\left(1 + \frac{n}{\beta}\right), \quad (21)$$

where Γ is the gamma function, and n is a real number. Furthermore (Bury, 1975):

$$\text{Var}[U_{10}^n] = E[U_{10}^{2n}] - (E[U_{10}^n])^2. \quad (22)$$

Moreover, the results are further exemplified by the deep water wave conditions corresponding to the expected value of U_{10} , i.e. given by $E[U_{10}] = 7.5$ m s⁻¹ according to Eqs. (20) and (21). Based on this it follows that:

- spectral peak frequency $\omega_p = g/E[U_{10}] = 1.308$ rad s⁻¹, corresponding to the spectral peak period $T_p = 2\pi/\omega_p = 4.8$ s,
- significant wave height in deep water, $H_s = 2\sqrt{\alpha}g/\omega_p^2 = 1.03$ m,
- significant wave height in shallow water, $H_{sh} = 2\sqrt{\alpha gh}/\omega_p = 0.75$ m,
- k_p from the shallow water dispersion relationship corresponding to ω_p , $k_p = \omega_p/\sqrt{gh} = 0.241$ rad m⁻¹,

- peak near-bed orbital displacement amplitude, $A_p = H_{sh}/(2k_p h) = 0.52$ m.

3.1. Example 1: Very rough beds

Now it follows that

- $A_p/z_0 = 55 < 300$, i.e. being in the range of the data of both Myrhaug et al. (2001) and Dixen et al. (2008) (see the Appendix and MH10 for more details). Thus both $c = 9$ and $c = 18$ are used in this example for very rough beds.

Then it follows from Eq. (15) that

$$H_{\tau/\rho} = 2\sqrt{\alpha g z_0} \begin{cases} 9 \\ 18 \end{cases} = \begin{cases} 0.15 \text{ m}^2 \text{ s}^{-2} \\ 0.30 \text{ m}^2 \text{ s}^{-2} \end{cases} \quad (23)$$

The critical shear stress for movement of the bottom material is given by Soulsby (1997) as

$$\left(\frac{\tau}{\rho}\right)_c = 0.055(s-1)g d_{50}, \quad (24)$$

where $s = 2.65$ is the sediment density to fluid density ratio taken as for quartz sand and $d_{50} = 12z_0$. This example gives $(\tau/\rho)_c = 0.10 \text{ m}^2 \text{ s}^{-2}$, showing that the bottom material will be exposed to erosion for both values of c . However, in other cases it might be that the two values of c will give different results. In such cases the user has to make the best judgement based on the location and situation considered.

3.2. Example 2: Mud beds

The given flow conditions are:

- density of water, $\rho = 1027 \text{ kg m}^{-3}$,
- kinematic viscosity of water at temperature 10°C and salinity 35‰, $\nu_f = 1.36 \times 10^{-6} \text{ m}^2 \text{ s}^{-1}$.

Now it follows that:

- the wave Reynolds number, $Re = U_p A_p / \nu_f = \omega_p A_p^2 / \nu_f = 2.6 \times 10^5$, i.e. the flow is in the laminar flow regime $Re \lesssim 3 \times 10^5$ (Soulsby, 1997) and $U_p = \omega_p A_p$.

Then it follows from Eqs. (16), (20) and (21) that

$$E[H_{\tau/\rho}] = 2\sqrt{2\nu_f \alpha g} E[U_{10}^{1/2}] = 0.00243 \text{ m}^2 \text{ s}^{-2}, \quad (25)$$

and from Eqs. (16), (20), (21) and (22) that the standard deviation (equal to the square root of the variance) of $H_{\tau/\rho}$ is

$$\sigma[H_{\tau/\rho}] = 2\sqrt{2\nu_f \alpha g \sigma[U_{10}^{1/2}]} = 0.00079 \text{ m}^2 \text{ s}^{-2}. \quad (26)$$

Thus the interval corresponding to the mean value \pm one standard deviation is given by $(0.00164 \text{ m}^2 \text{ s}^{-2}, 0.00322 \text{ m}^2 \text{ s}^{-2})$.

By following the examples in Whitehouse et al. (2000) (i.e. example 4.2 for erosion and example 8.1 for deposition), the critical bottom shear stress for erosion is $\tau_e = 0.197 \text{ N m}^{-2}$ and for deposition it is $\tau_d = 0.08 \text{ N m}^{-2}$. Thus it follows that $\tau_e/\rho = 0.00019 \text{ m}^2 \text{ s}^{-2}$ and $\tau_d/\rho = 0.000078 \text{ m}^2 \text{ s}^{-2}$, showing that the bed is exposed to erosion for this flow condition.

In general, mud beds exhibit cohesive properties and the details of the flow can only be understood by including a number of complex transport mechanisms; see e.g. Whitehouse et al. (2000) and Winterwerp and van Kesteren (2004) for further details. The flow over muds is not necessarily laminar, but will depend on the wave Reynolds number Re , which can be large enough corresponding to turbulent flow over smooth (or mud) beds, i.e. $Re \gtrsim 3 \times 10^5$. Furthermore, the results in Fredsøe and Deigaard (1992, Fig. 2.13) can be used to distinguish between laminar and turbulent flow for different combinations of grain size and Reynolds number. Further details including formulas which can be used for practical purposes are given in Soulsby (1997, Ch. 4.5).

4. Comments

Finally some comments are given on the present method versus common practice in coastal engineering. For calculating bottom shear stress for random waves in shallow water common practice would be to start from available data on joint statistics of H_s and T_p within directional sectors at a nearby offshore location; then to transform these by using a wave simulation model to obtain joint statistics of H_s and T_p at the relevant location; then to use this information as input for calculating the bottom shear stress. Alternatively, this paper provides a simple analytical method giving first estimates of random wave-induced bottom shear stress for very rough beds and mud beds from observed deep water sea surface wind statistics with an example based on in situ data obtained from the Northern North Sea. The Phillips deep water wave frequency spectrum is used to relate wind to waves together with the narrow-band and shallow water assumptions. Thus an analytical estimate of the associated bottom shear stresses is obtained. The narrow-band assumption is justified since the waves with the frequencies close to the spectral peak frequency are the most energetic contributing to the bed shear stresses in shallow water. Such simple methods are useful to be able to quickly make estimates which can be used for comparison and verification of more complete computational methods, as well as in situations when time and access to computational resources are limited (under e.g. field conditions). Moreover, it might also serve as a first inexpensive estimate of the quantities of interest before eventually applying more work-intensive computational tools.

5. Summary and conclusions

A simple analytical method which can be used to give estimates of the random wave-induced bottom shear stress for very rough beds and mud beds in shallow water based on wind conditions in deep water is provided. Results are exemplified by using long-term wind statistics from the northern North Sea and by giving examples representing realistic field conditions. The example calculations demonstrate that the sea bottom material will be exposed to erosion both for very rough beds and mud beds. The results should represent a useful tool for assessment of, e.g. the stability of scour protections in coastal environments where the stone size is large compared to the near-bed wave activity, as well as assessment of erosion and deposition of mud. The method should also represent a useful representation of the bottom

shear stress often required in operational estuarine, coastal and ocean circulation models based on, for example, available global wind statistics.

Acknowledgement

This work was carried out as part of the project “Air-Sea Interaction and Transport Mechanisms in the Ocean” funded by the Norwegian Research Council (221988). This support is gratefully acknowledged.

Appendix. Spectrum of seabed shear stresses in shallow water

Here a brief summary of the theoretical background from MH10 is given.

Consider an oscillatory wave boundary layer flow where the motion is horizontally uniform in the direction along the seabed. By using complex notation the free stream velocity outside the wave boundary layer is

$$u(t) = Ue^{i\omega t}, \quad (\text{A1})$$

where U is the near-bed orbital velocity amplitude, t is the time, ω is the cyclic wave frequency, and $i = (-1)^{1/2}$ is the complex unity. The seabed shear stress is

$$\tau(t) = \tau_m e^{i(\omega t + \varphi)}, \quad (\text{A2})$$

where φ is the phase angle between $\tau(t)$ and $u(t)$, and τ_m is the maximum seabed shear stress given by

$$\frac{\tau_m}{\rho} = \frac{1}{2} f_w U^2, \quad (\text{A3})$$

where ρ is the fluid density and f_w is the wave friction factor.

Now $u(t)$ can be expressed in terms of the free surface elevation $\zeta(t)$ as:

$$u(t) = \frac{\omega \zeta(t)}{\sinh kh}; \quad \zeta(t) = \zeta_A e^{i\omega t}, \quad (\text{A4})$$

where ζ_A is the wave amplitude, h is the water depth, and k is the wave number determined from the dispersion relationship for linear waves as given in Section 2.1. From Eqs. (A1) and (A4) it follows that

$$U = \frac{\omega \zeta_A}{\sinh kh}. \quad (\text{A5})$$

The wave spectrum in finite water, $S_{\zeta\zeta}(\omega, h)$, can be obtained by multiplying the deep water wave spectrum, $S_{\zeta\zeta}(\omega)$, with a depth correction factor, $\Psi(\omega, h)$, as

$$S_{\zeta\zeta}(\omega, h) = \Psi(\omega, h) S_{\zeta\zeta}(\omega). \quad (\text{A6})$$

In shallow water ($kh \ll 1$) (Holthuijsen, 2007, Section 8.3.2)

$$\Psi(\omega, h) = \frac{\omega^2 h}{2g}. \quad (\text{A7})$$

First, using laminar flow as a reference case, the wave friction factor and the phase angle are given as, respectively,

$$f_w = 2Re^{-0.5}; \quad Re = \frac{UA}{\nu_f}, \quad (\text{A8})$$

$$\varphi = \frac{\pi}{4}. \quad (\text{A9})$$

Here Re is the Reynolds number associated with the wave motion, $A = U/\omega$, and ν_f is the kinematic viscosity of the fluid. By using Eqs. (A1), (A3), (A4), (A8) and (A9), Eq. (A2) takes the form

$$\frac{\tau(t)}{\rho} = \frac{\sqrt{\nu_f \omega}}{\sinh kh} \zeta_A e^{i(\omega t + (\pi/4))}. \quad (\text{A10})$$

Then the Response Amplitude Operator (RAO) = ratio between the amplitude of the seabed shear stress, $\tau(t)/\rho$, and the amplitude of the free surface elevation, $\zeta(t)$, in shallow water is obtained as (i.e. corresponding to the magnitude of the transfer function)

$$RAO = \frac{(\nu_f \omega)^{1/2} \omega}{kh}. \quad (\text{A11})$$

Thus the seabed shear stress spectrum for laminar flow is given as

$$S_{(\tau/\rho)(\tau/\rho)}(\omega, h) = \frac{\nu_f \omega^3}{(kh)^2} \frac{\omega^2 h}{2g} S_{\zeta\zeta}(\omega). \quad (\text{A12})$$

For rough turbulent flow the transfer function between the free surface elevation and the seabed shear stress at beds with very large roughness can be found analytically. In this roughness regime the wave friction factor is given as

$$f_w = c \left(\frac{A}{z_0} \right)^{-1}, \quad (\text{A13})$$

where c is a constant. This variation of f_w was found by Sleath (1984) and Dixen et al. (2008) based on theoretical considerations; Myrhaug et al. (2001) and Dixen et al. (2008) found experimental evidence of this behaviour based on laboratory tests. The data used by Myrhaug et al. (2001) were in the range $1 \lesssim A/z_0 \lesssim 300$ with a bed roughness of nominal 1.0 cm diameter granite chippings. The Dixen et al. (2008) data were in the range $20 \lesssim A/z_0 \lesssim 90$ with a bed roughness using two kinds of stones as well as ping-pong balls. Myrhaug et al. (2001) found that $c = 18$. Dixen et al. (2008) proposed the friction factor $f_w = 4.86(A/z_0)^{-0.8}$ obtained as best fit to data in the range $6 < A/z_0 < 300$ (based on their own data plus other data; see Fig. 14 in their paper). However, by considering the scatter of the data in the range $6 < A/z_0 < 90$, the difference between using this friction factor or Eq. (A13) with $c = 9$ is not significant. Thus a friction factor proportional to $(A/z_0)^{-1}$ is used here to serve the purpose of demonstrating how this can be used to determine the seabed shear stress spectrum for very rough beds. The two different values of c (i.e. 9 and 18) suggest that c might depend strongly on the geometry of the large roughness elements. The phase angle, φ , is not known for the Myrhaug et al. (2001) data; φ was found to be in the range $19\text{--}23^\circ$ for the Dixen et al. (2008) data. Further details are given in MH10.

By combining Eqs. (A1), (A3), (A4), $A = U/\omega$ and (A13), Eq. (A2) takes the form of

$$\frac{\tau(t)}{\rho} = \frac{c z_0 \omega^2}{2 \sinh kh} \zeta_A e^{i(\omega t + \varphi)}, \quad (\text{A14})$$

and the RAO between the free surface elevation and the seabed shear stress in shallow water is obtained as

$$RAO = \frac{cz_0\omega^2}{2kh}. \quad (\text{A15})$$

Thus the seabed shear stress spectrum for rough turbulent flow over a bed with very large roughness is given as

$$S_{(\tau/\rho)(\tau/\rho)}(\omega, h) = \frac{c^2 z_0^2 \omega^4}{4(kh)^2} \frac{\omega^2 h}{2g} S_{\zeta\zeta}(\omega). \quad (\text{A16})$$

It should be noted that only the waves with wavelengths longer than approximately two times the water depth will give wave activity at the seabed. Thus, by using the deep water dispersion relationship $\omega^2 = gk$, this means that the waves at the seabed have frequencies below $(\pi g h^{-1})^{1/2}$.

References

- Bitner-Gregersen, E.M., 2015. Joint met-ocean description for design and operations of marine structures. *Appl. Ocean Res.* 51, 279–292, <http://dx.doi.org/10.1016/j.apor.2015.01.007>.
- Bury, K.V., 1975. *Statistical Models in Applied Science*. John Wiley & Sons, New York, 625 pp.
- Dixen, F., Hatipoglu, F., Sumer, B.M., Fredsøe, J., 2008. Wave boundary layer over a stone-covered bed. *Coastal Eng.* 55 (1), 1–20, <http://dx.doi.org/10.1016/j.coastaleng.2007.06.005>.
- Fredsøe, J., Deigaard, R., 1992. *Mechanics of Coastal Sediment Transport*. World Scientific, Singapore, 369 pp.
- Holthuijsen, L.H., 2007. *Waves in Oceanic and Coastal Waters*. Cambridge Univ. Press, Cambridge, UK, 387 pp.
- Johannessen, K., Meling, T.S., Haver, S., 2001. Joint distribution for wind and waves in the Northern North Sea. In: *Proceedings of the 11th International Offshore and Polar Engineering Conference*, Stavanger, Norway, vol. III, 1928.
- Longuet-Higgins, M.S., 1975. On the joint distribution of the periods and amplitudes of sea waves. *J. Geophys. Res.* 80, 2688–2694.
- Myrhaug, D., Holmedal, L.E., 2010. Seabed shear stress spectrum for very rough beds. *J. Offshore Mech. Arct. Eng.* 132 (3), 5 pp., <http://dx.doi.org/10.1115/1.4000501>.
- Myrhaug, D., Holmedal, L.E., Simons, R.R., MacIver, R.D., 2001. Bottom friction in random waves plus current flow. *Coastal Eng.* 43 (2), 75–92, [http://dx.doi.org/10.1016/S0378-3839\(01\)00007-2](http://dx.doi.org/10.1016/S0378-3839(01)00007-2).
- Nielsen, P., 1992. *Coastal Bottom Boundary Layers and Sediment Transport*. World Scientific, Singapore, 324 pp.
- Sleath, J.F.A., 1984. *Sea Bed Mechanics*. John Wiley & Sons, New York, 335 pp.
- Soulsby, R.L., 1997. *Dynamics of Marine Sands*. Thomas Telford, London, UK, 249 pp.
- Tucker, M.J., Pitt, E.G., 2001. *Waves in Ocean Engineering*. Elsevier, Amsterdam, 521 pp.
- Whitehouse, R., Soulsby, R.L., Roberts, W., Mitchener, H., 2000. *Dynamics of Estuarine Muds*. Thomas Telford, London, UK, 210 pp.
- Winterwerp, J.C., van Kesteren, W.G.M., 2004. *Introduction to the Physics of Cohesive Sediments in the Marine Environment*. Elsevier, Amsterdam, The Netherlands, 466 pp.



ORIGINAL RESEARCH ARTICLE

Possible means of overcoming sedimentation by motile sea-picoplankton cells

Oleh Pundyak*

Botanical Garden of Ukrainian National Forestry University, Lviv, Ukraine

Received 17 May 2016; accepted 16 September 2016

Available online 5 October 2016

KEYWORDS

Picoplankton;
Sedimentation;
Gravikinesis;
Friction anisotropy;
Antipredator behavior

Summary A model for overcoming the gravity by sea-picoplankton cells is proposed here. It is based on different means of escaping from potential predators used by cells of co-existing picoplankton species. These different means cause friction anisotropy of motile cells with strong antipredator behavior (AB). According to equations of stochastic movement used in this model for picoplankton cells with strong AB, collocated with high concentration of cells with weak or absent AB, the sedimentation can be considerably overcome.

© 2016 Institute of Oceanology of the Polish Academy of Sciences. Production and hosting by Elsevier Sp. z o.o. This is an open access article under the CC BY-NC-ND license (<http://creativecommons.org/licenses/by-nc-nd/4.0/>).

1. Introduction

Plankton microorganisms in wide range of sizes are extremely numerous in saline waters of seas and oceans. They are the key agents of global biogeochemical cycles (Strom, 2008) and their ecology is partly driven by their motility patterns, which

dictate their distributions and encounters with biotic and abiotic targets (Visser and Kiorboe, 2006). Many planktonic organisms are known to undergo diel vertical migrations (DVMs) up to tens of meters per day in the field (Smayda, 2010). DVM may allow individuals to avoid predation, for example by moving through haloclines (Bollens et al., 2012; Harvey and Menden-Deuer, 2012) and, in the case of phytoplankton, to balance daytime near-surface light exposure with nighttime nutrient uptake at depth (Cullen, 1985). Marine planktonic cells can undergo DVM in two ways: by gravitaxis or by gravikinesis (Eggersdorfer and Häder, 1991; Schuech and Menden-Deuer, 2014). The process of microorganisms' gravidependent spatial orientation is called gravitaxis (known historically as geotaxis). The motile microorganism's spatial orientating to move upwards and downwards is called negative and positive gravitaxis respectively (Roberts, 2006). Gravitaxis has two different aspects: biological and physical. The biological aspect of gravitaxis is

* Correspondence to: Botanical Garden of Ukrainian National Forestry University, 103 Gen. Chuprynka st., 79057 Lviv, Ukraine.

E-mail address: olepundyak@gmail.com.

Peer review under the responsibility of Institute of Oceanology of the Polish Academy of Sciences.



Production and hosting by Elsevier

expressed by the existence of certain cell receptors accepting gravistimulus and, through signaling chains, causing the change in the direction the cell moves (Hemmersbach and Häder, 1999). The physical aspect of gravitaxis is visible in the occurrence of hydrodynamic (Hagen et al., 2014; Roberts and Deacon, 2002) or density gradient (Kessler, 1985) torque which changes the orientation of the cell. The speed of some microorganisms depends on their orientation within the gravity field (excluding buoyancy of the whole cells). This phenomenon is called gravikinesis. So far, physiological mechanisms of gravikinesis have been well examined and described by Hemmersbach and Häder (1999) for example. Its physical aspect however has not yet been investigated and it might be expressed by an anisotropic interaction of the microorganisms with the water medium.

Many planktonic species are non-spherical, extended along their single axis and typically wider at the rear than at the front. Such an asymmetrical shape causes the above-mentioned torque orienting their fronts upward (Schuech and Menden-Deuer, 2014). Thus, it is natural to conclude that if these organisms need cell receptors for realizing DVM (Schuech and Menden-Deuer, 2014), then, for the simple overcoming of sedimentation, these organisms need only physical mechanisms, which are quite enough to direct the averaged locomotion force upwards. A considerable part of the biological diversity of motile picoplankton organisms (whose dimension varies from 0.2×10^{-6} to 2×10^{-6} m) consists of flagellar bacteria. The bacterial cell motor can switch the direction of its action. For example, this has been shown for the marine bacterium *Vibrio alginolyticus* (Xie et al., 2015). Therefore, cell asymmetry cannot play the part in their physical gravitaxis. Thus, a question can be raised: whether these organisms can overcome sedimentation without any special cellular mechanism for gravity perception, as it has been shown for asymmetric microplankton (Hemmersbach and Häder, 1999)? We have tried to answer this question positively taking into account antipredator behavior (AB) – the ability of picoplankton organisms to detect and escape their predators by outrunning them. ABs of different species vary considerably (Pernthaler, 2005). Analogical behavior has also been revealed for microplankton (Harvey and Menden-Deuer, 2012). As it has been shown, in presence of active predator the sexual and predatory activities of prey cells were inhibited (Harvey and Menden-Deuer, 2012). Thus, to simplify we excluded from our model predatory and sexual behaviors of the microorganisms facilitating the encounters between the cells. Although there are numerous picoplanktonic species in natural sea waters, for simplicity's sake we considered a collocation of only two species: those with strong and absent AB. The cells with strong AB always try to escape the others as potential predators. We have also taken into consideration the influence of thermal fluctuations on the movement of these tiny plankton microorganisms. Thus, the movement of a microorganism can be described by Langevin's equation, which considers random fluctuation force. Therefore its coordinate, velocity and acceleration depend on time randomly, too. However, when averaged, these quantities depend on time unambiguously. Such movement is called stochastic (Sklar, 1993). Let us show the possible result when an averaged fluctuation force, which acts on the cells with strong AB, is orientated upwards. By causing physical gravikinesis, described above, the averaged

fluctuation force can theoretically influence picoplankton to overcome sedimentation entirely.

2. Model description

Let us consider the movement of a microscopic particle in a viscous medium under the influence of gravity. The particle undergoes locomotion force F directed along the axis of symmetry of the particle (X'). Movement orientation of the particle randomly changes sharply. It also changes so as to prevent from encounter with a particle that has been detected further on the way. Such movement can be described as:

$$m\ddot{x} + h_x(\alpha)\dot{x} - (m - m_m)g - F_x(t) = A_x(t), \quad (1)$$

$$m\ddot{y} + h_y(\alpha)\dot{y} - F_y(t) = A_y(t), \quad (2)$$

$$m\ddot{z} + h_z(\alpha)\dot{z} - F_z(t) = A_z(t), \quad (3)$$

$$\mu\ddot{\alpha} + \gamma\dot{\alpha} - \Phi_\alpha(t) = H_\alpha(t), \quad (4)$$

where x , y , z are coordinates of the mass centrum of the particle; α is the vector of orientation of spherical angles: $\vec{\alpha} = (\alpha_x, \alpha_y, \alpha_z)$; g is gravity centrifugation; m and m_m are the particle mass and the mass of the medium of the same volume correspondingly; μ is the mass moment of the particle; $h_x(\alpha)$, $h_y(\alpha)$, $h_z(\alpha)$ are friction coefficients of the particle; γ is the moment of friction coefficient; $F_x(t)$, $F_y(t)$, $F_z(t)$ are projections of the locomotion force F on the coordinate axes; $\Phi_\alpha(t)$ is the moment of the force, which periodically changes the orientation of the particle sharply; $A_x(t)$, $A_y(t)$, $A_z(t)$ are projections of fluctuation force on coordinate axes; $H_\alpha(t)$ is the vector of the moment of fluctuation force.

For the sake of simplicity we can also describe the translational movement of the particle in an orthogonal coordinate system bounded with the axis (X'), along which the locomotion force always acts, as:

$$m\ddot{x}' + h_{x'}\dot{x}' - (m - m_m)g_{x'} - F = A_{x'}(t), \quad (5)$$

$$m\ddot{y}' + h_{y'}\dot{y}' - (m - m_m)g_{y'} = A_{y'}(t), \quad (6)$$

$$m\ddot{z}' + h_{z'}\dot{z}' - (m - m_m)g_{z'} = A_{z'}(t), \quad (7)$$

where x' , y' , z' are the new coordinates of the particle; $g_{x'}$, $g_{y'}$, $g_{z'}$ are the projections of gravity acceleration on axes X' , Y' , Z' correspondingly; $h_{x'}$, $h_{y'}$, $h_{z'}$ are the friction coefficients of the particle, which moves along the new axes.

Considering the stochastic character of Eqs. (1)–(7) and the fact that relaxation time of water is shorter than the time needed for a considerable change in the spatial position of a microscopic particle, we can neglect sharp changes in x' , $|x'|$, y' , y' , z' , z' during such changing of α , $\dot{\alpha}$, $\Phi(t)$ (Sklar, 1993). We can also neglect changes of the locomotion force considering that $|F| = \text{const}$ (prokaryotic cells switch their cell motors periodically). As it has been shown for *V. alginolyticus* the

frequency of cell motor switching is no higher than 100 Hz (Xie et al., 2015). Thus, for the sake of simplicity in the scale of 10^{-7} m and 10^{-9} s $\dot{x}'(t)$, $\dot{y}'(t)$, $\dot{z}'(t)$ in Eqs. (5)–(7) can be considered as:

$$\begin{aligned}\dot{x}'(t) &= \Delta\dot{x}'(t) + \bar{x}'(t), \dot{y}'(t) = \Delta\dot{y}'(t) + \bar{y}'(t), \dot{z}'(t) \\ &= \Delta\dot{z}'(t) + \bar{z}'(t); \end{aligned} \quad (8)$$

$$\begin{aligned}h_{x'}\bar{x}' &= F + (m-m_m)g_{x'}, h_{y'}\bar{y}' = (m-m_m)g_{y'}, h_{z'}\bar{z}' \\ &= (m-m_m)g_{z'}; \end{aligned} \quad (9)$$

$$|\Delta\dot{x}'(t)| = \frac{D_{x'}}{d_{x'}}, |\dot{y}'(t)| = |\dot{z}'(t)| = \frac{D_{y',z'}}{d_{y',z'}}, \quad (10)$$

where \bar{x}' , \bar{y}' , \bar{z}' are the averaged velocities of the particles identically orientated with respect to coordinate axes X , Y , Z and to the action of cell motors; $d_{x'}$ and $d_{y',z'}$ are the dimensions of the particles along the axes X' and Y' or Z' correspondingly; $D_{x'}$ and $D_{y',z'}$ are coefficients of diffusion along the axis X' and Y' or Z' correspondingly.

Having considered Eqs. (8) and (9), let us transform Eqs. (5)–(7) in:

$$\begin{aligned}m\ddot{x}' + h_{x'}\Delta\dot{x}' &= A_{x'}(t), \quad m\ddot{y}' + h_{y'}\Delta\dot{y}' \\ &= A_{y'}(t), \quad m\ddot{z}' + h_{z'}\Delta\dot{z}' = A_{z'}(t). \end{aligned} \quad (11)$$

Eq. (11) permit us to consider the particle in a state of equilibrium only under the condition:

$$|\bar{x}'| < \frac{D_{x'}}{d_{x'}}, \quad |\bar{y}'| < \frac{D_{y,z'}}{d_{y,z'}}, \quad |\bar{z}'| < \frac{D_{y,z'}}{d_{y,z'}}, \quad (12)$$

when $\dot{x}'(t)$, $\dot{y}'(t)$, $\dot{z}'(t)$ according to Eqs. (8) and (10) can change their sign independently from cell motor switching.

2.1. Time reversal transformation. Appearance of diffusional force

Let us obtain the sum of Eq. (11) for x' in points $t = \tau$ and $t = -\tau$; $\tau \neq 0$, where τ is the time during which the particle does not switch its cell motor and translocates a certain distance which is not equal to zero. Then let us average this sum with respect to the ensemble of a multitude of identical systems as we have already done (Pundyak, 2014). Then, if the system is in a state of equilibrium, according to the laws of equipartition and the symmetry of movement under time reversal transformation, we obtain:

$$\Lambda \equiv \bar{A}_{x'} = 0.5(h_1 - h_2)\Delta\bar{x}', \quad (13)$$

where Λ is the averaged fluctuation force (let us call Λ diffusional force); $\Delta\bar{x}'$ is the averaged diffusional velocity of such translocation; h_1 and h_2 are the averaged friction coefficients for a particle which moves in the same direction as the cell motor action and in the direction opposite to the cell motor action correspondingly. If the particle moves in a pure viscous medium with a speed not much higher than the speed of its Brownian motion (with low Reynolds number), then its h_1 always equals h_2 and so $\Lambda = 0$ (Happel and Brenner,

1983). But what happens in the case of particles with strong AB collocated with particles of the same dimension but without AB? Let us posit that while moving in the same direction as the cell motor action, the particles with strong AB do not encounter any other particles (as a consequence of active escaping them). While moving in the direction opposite to the cell motor action (as a random fluctuation process), the particles can encounter only the particles without AB. In the latter case the rate of impulse losses of the particle is bigger than in the former case. Therefore, for such a model a situation may happen when $h_1 \neq h_2$ and so $\Lambda \neq 0$.

2.2. Evaluation of friction anisotropy

Let the averaged friction coefficient of a particle with strong AB, which moves in the direction of its cell motor action (h_1) in consequence of escaping the other particles, be equal to the friction coefficient of a particle in a pure viscous medium h_0 . Let us find the averaged friction coefficient of a particle with strong AB, which moves in the direction opposite to the cell motor action (h_2). When the concentration of the particles without AB is relatively small (free volume is much bigger than common volume of these particles) and the both types of the particles are elastic, in the case of equipartition of directions and velocities of their movement, h_2 is evaluated as:

$$h_1 \approx h_0; h_2 \approx h_0 + \frac{2}{\pi} \cdot d \cdot \sqrt[3]{C} \cdot \sqrt[3]{m \cdot k}; \quad h_0 = \psi \cdot \eta \cdot d, \quad (14)$$

where η is viscosity of the medium; ψ is shape coefficient (for spherical particles according to Stock's formula $\psi = 3\pi$); d is the averaged dimension of the particles; C is the concentration of the particles without AB; k is the stiffness coefficient of the whole cells. The cell wall of picoplankton is able to deform by thermal fluctuation of several angstroms approximately. So, according to the law of equipartition, k is near 10^{-1} N m $^{-1}$. The viscosity of seawater within the range of salinity $S = 15-25$ g kg $^{-1}$ and temperature $t = 20-30^\circ$ C is of order 10^{-3} Pa s (Sharqawy et al., 2010). According to formula (14), friction anisotropy ξ may be described as:

$$\xi \equiv \frac{h_2 - h_1}{h_2 + h_1} \approx \frac{10^3 \cdot d^{3/2} \cdot \sqrt{C}}{1 + 10^3 \cdot d^{3/2} \cdot \sqrt{C}}. \quad (15)$$

The total concentration of picoplankton can reach 10^{12} cells m $^{-3}$ (Denaro et al., 2013). So, the latter limit of concentrations can be applied in formula (15). Thus, we can construct a table, which shows the dependence of the friction anisotropy ξ of the picoplanktonic particles with strong AB on concentrations of the particles without AB (Table 1). As

Table 1 The dependence of friction anisotropy ξ of the picoplanktonic particles with strong AB on the concentration (C) of the particles without AB.

Concentration C [cells m $^{-3}$]	ξ for the particles of 10^{-6} [m] diameter	ξ for the particles of 10^{-7} [m] diameter
$\sim 10^{12}$	$\sim 10^{-2}$	$\sim 10^{-3.5}$
$\sim 10^9$	$\sim 10^{-3}$	$\sim 10^{-4.5}$
$\sim 10^3$	$\sim 10^{-5}$	$\sim 10^{-6.5}$

the viscosity of seawater tends to decrease when the temperature increases (Sharqawy et al., 2010), then according to formulas (14) and (15) ξ is an increasing function of temperature.

2.3. Evaluation of diffusional force

Let us find $\overline{\Delta \vec{x}'}(t)$ in formula (13) by averaging the diffusional velocities of the particle during its direct translocation throughout the distance that is equal to the particle dimension (with respect to the ensemble of all identical systems, which contain only the particles moving since $t = 0$ till $t = \tau$). This $\overline{\Delta \vec{x}'}(t)$ is the result of averaging of $\Delta \vec{x}'(\Delta x', \Delta y', \Delta z', t)$ in all points of coordinate space $\Delta x', \Delta y', \Delta z'$ accessible to the particle for the time t . Coordinates $\Delta x'(t), \Delta y'(t), \Delta z'(t)$ of the particle can be determined as:

$$\begin{aligned} \Delta x'(t) &= \Delta x'(0) + \int_0^t \Delta \dot{x}'(t) dt; & y'(t) \\ &= \Delta y'(0) + \int_0^t \Delta \dot{y}'(t) dt; & z'(t) \\ &= \Delta z'(0) + \int_0^t \Delta \dot{z}'(t) dt, \end{aligned} \quad (16)$$

$\overline{\Delta \vec{x}'}(\Delta x', \Delta y', \Delta z', t) = 0$ in all points of the coordinate space excluding the points of averaged trajectory of the particle. Thus, if the particle volume V_{par} is near the whole volume $V_{acces}(t)$ accessible to the particle during time interval t , then analogically to Pundyak (2014) we obtain:

$$\overline{\Delta \vec{x}'}(t) = \frac{D_x}{d_x} \chi; \quad \chi(t) \approx \frac{V_{par}}{V_{acces}(t)}. \quad (17)$$

According to formulas (13) and (17):

$$\Lambda = \chi(t) \frac{D_x}{2d_x} (h_1 - h_2) = \chi(t) \frac{k_b T}{d_x} \xi. \quad (18)$$

If the locomotion or buoyant force is so high that according to Eq. (9) $|\overline{\vec{x}'}| \geq D_x/h_x$, then the condition (12) is invalid. Thus, in this case the system is not in equilibrium, therefore formula (18) is invalid and $\Lambda = 0$. Under the condition $|\overline{\vec{x}'}| < D_x/h_x$, the volume accessible to the particle moving in unbounded fluid, depends on t according to the law of diffusion, $V_{acces}(0) = 0$. Thus, having considered formula (17), we can calculate $\chi(t)$ in formula (18):

$$\begin{aligned} \chi(t) &\approx \frac{d_x d_{y,z}^2}{(B_{x'} t^{0.5} + d_{x'})(B_{y',z'} t^{0.5} + d_{y',z'})^2}; \\ B_{x'} &\equiv \sqrt{D_{x'}}; \quad B_{y',z'} \equiv \sqrt{D_{y',z'}}. \end{aligned} \quad (19)$$

When the particle exists for a long time ($t \rightarrow \infty$) in unbounded fluid, then according to formulas (18) and (19) $\Lambda = 0$. Although there is no report about AB of *V. alginolyticus*, let us consider our model particles with strong AB as having parameters of *V. alginolyticus*, which is well-studied (Xie et al., 2015). As it has been shown (Xie et al., 2015), averaged cell velocity of *V. alginolyticus* is about $5.5 \times 10^{-5} \text{ m s}^{-1}$. Its dimension is about $2 \times 10^{-6} \text{ m}$ and its mass is about 10^{-15} kg . According to (9) $F \sim k_b T/d$. So, in our model we can consider the situation when $|F| = k_b T/d$. Then

$$|F| + |G| \geq \frac{k_b T}{d}; \quad |F| - |G| < \frac{k_b T}{d}; \quad G \equiv (m - m_m) g_{x'}, \quad (20)$$

where G is buoyant force. According to Eq. (9) and condition (20) if the particle moves downwards, then $|\overline{\vec{x}'}| \geq D_x/h_x$, and $\Lambda = 0$, but if the particle moves upwards, then $|\overline{\vec{x}'}| < D_x/h_x$, and $\Lambda \neq 0$. Let us posit that after the moving downwards, the particle starts to move upwards at $t = 0$. Thus, time t of such an upward movement can be considered as the time of the diffusional force acting in formulas (18) and (19). According to formulas (18) and (19) the diffusional force has considerable influence on the particles movement only if the time of their upward movement is short. The diffusional force acts only during upward movement of the particle (during downward movement $|\overline{\vec{x}'}| > D_x/h_x$ and it equals zero) and always is directed upwards. In other words, although the orientation of a living microorganism within the depth of sea changes unceasingly, the averaged diffusional force is directed upwards constantly. To evaluate the influence of the diffusional force on the balancing of the particles let us average it with the respect to time and to spherical angle α_x :

$$\begin{aligned} \overline{\Lambda}(\tau) &= \overline{\chi}(\tau) \frac{k_b T}{d_x} \overline{\Omega}(\alpha_m) \xi; \quad \overline{\chi}(\tau) \\ &= \frac{1}{\tau} \int_0^\tau \chi dt; \quad \overline{\Omega}(\alpha_m) \equiv \frac{1}{(\alpha_m)} \int_0^{\alpha_m} P \\ &\quad \times (\alpha) \cos(\alpha) \sin(\alpha) d\alpha, \end{aligned} \quad (21)$$

where τ is the time of upward movement of the particle; α_m is the minimal value of spherical angle α_x (mentioned under Eq. (4) in Section 2) at which inequality (12) is valid; $P(\alpha)$ is possibility of the particle to move in the direction determined by the angle α_x . Let us consider the case of equal distribution of movement directions. According to condition (20) $\alpha_m = \pi/2$. Therefore according to formula (21) $\overline{\Omega}(\alpha_m) = 1/\pi$. The time scale of ballistic movement of *V. alginolyticus* is within 10^{-1} s (Xie et al., 2015). Therefore according to formulas (19) and (21) at the room temperature the quantity $\overline{\chi}(\tau)$ is near 1 and depends on temperature weakly. Cells of *V. alginolyticus* are of $2 \times 10^{-6} \text{ m}$ diameter (Xie et al., 2015). If the concentration of the particles without AB equals $10^{12} \text{ cells m}^{-3}$, which was observed in natural sea blooms (Denaro et al., 2013), according to Table 1 and formula (21) $\overline{\Lambda} \approx 10^{-17} \text{ N}$. Considering that *V. alginolyticus* can be denser than water by approximately several percent, the buoyant force for its cells is near 10^{-16} N . Thus, for motile picoplanktonic cells with strong AB collocated with the cells of similar dimensions without AB there may occur upward directed diffusional force, which is considerable when compared with buoyant force. As it has been mentioned above just after the Table 1 (Section 2.2) and clarified in this paragraph, according to formula (21) the diffusional force is an increasing function of temperature.

3. Discussion

Latter calculations support our hypothesis that physical gravikinesis can occur in bacterial plankton. However our model is also suitable for eukaryotic motile plankton of the same dimensions. Let us evaluate the possible role of the diffusional force for marine protists in wide range of sizes by

Table 2 Comparison the diffusional force with buoyant force for marine motile protists cells of different dimensions.

Organisms	Dimension (d), [m]	Buoyant force (B), [N]	\bar{A}_{\max} , [N]	\bar{A}_{\max}/B
Microplankton	$\geq 10^{-5}$	$\geq 10^{-13}$	$< 10^{-16}$	$< 10^{-3}$
	$\geq 2 \times 10^{-6}$	$\geq 8 \times 10^{-16}$	$< 10^{-15}$	< 1
Picoplankton	$\leq 2 \times 10^{-6}$	$\leq 8 \times 10^{-16}$	$> 10^{-15}$	> 1
	$\sim 10^{-7}$	$\sim 10^{-19}$	$\sim 10^{-14}$	$\sim 10^5$

calculating theoretically its maximal value according to formula (21), when $\bar{\chi} \rightarrow 1$; $\xi \rightarrow 1$:

$$\bar{A}_{\max} = \frac{k_b T}{\pi \cdot d_x}. \quad (22)$$

According to formula (22) and considering that plankton microorganisms are denser by no less than 1% compared to water, we can construct the following Table 2 for sea motile microorganisms classed by size.

According to the Table 2 only for picoplanktonic organisms the diffusional force may have a considerable value in comparison with buoyant force. Also, according to the Table 1, this can be applied to the organisms of 10^{-7} m dimensions, even if collocated with not very high (10^9 – 10^8 cells m^{-3}) concentrations of cells without AB. Thus, we can say, that picoplanktonic organisms with AB can overcome sedimentation without any special physiological mechanisms at high, but only natural, concentrations of collocated cells without AB. Our model shows clearly the gravity-overcoming possibility of picoplanktonic organisms with the strategy of outrunning predators. In other words, we are dealing with physical gravikinesis. Thus, we can conclude that, though poorly studied in the world of motile picoplankton, the strategy of outrunning predators can also serve as an adaptation to overcome sedimentation. This finding may stimulate further research in this field.

4. Conclusions

1. While in a state of equilibrium, sedimentation of motile particles with strong AB, collocated with particles without AB, decreases as a result of friction anisotropy.
2. The sedimentation may be overcome if the particles' dimensions are about 10^{-7} m and the concentration of the particles without AB is equal to or bigger than 10^8 cells m^{-3} .
3. Outrunning as an antipredator strategy of motile picoplankton sea organisms can cause the gravikinesis of a physical nature.

Acknowledgement

I would like to express my gratitude to Dr. Catherine Brown Tkacz for correcting my English in this article.

References

- Bollens, S., Quenette, J., Rollwagen-Bollens, G., 2012. Predator-enhanced diel vertical migration in a planktonic dinoflagellate. *Mar. Ecol.-Prog. Ser.* 447 (2), 49–54.
- Cullen, J., 1985. Diel vertical migration by dinoflagellates: roles of carbohydrate metabolism and behavioral flexibility. *Contr. Mar. Sci.* 27 (Suppl.), 135–152.
- Denaro, G., Valenti, D., Spagnolo, B., Basilone, G., Mazzola, S., Zgozi, S., Aronica, S., Bonanno, A., 2013. Dynamics of two picophytoplankton groups in Mediterranean sea: analysis of the deep chlorophyll maximum by a stochastic advection-reaction-diffusion model. *PLoS Biol.* 8 (6), e66765.
- Eggersdorfer, B., Häder, D.-P., 1991. Phototaxis, gravitaxis and vertical migrations in the marine dinoflagellate *Prorocentrum micans*. *FEMS Microbiol. Lett.* 85 (4), 319–326.
- Hagen, B., Kümmel, F., Wittkowski, R., Takagi, D., Löwen, H., Bechinger, C., 2014. Gravitaxis of asymmetric self-propelled colloidal particles. *Nat. Comm.* 5 (9), 1–7.
- Happel, J., Brenner, H., 1983. *Low Reynolds Number Hydrodynamics*. Martinus Nijhoff Publishers, Boston, Lancaster, 543 pp.
- Harvey, E.L., Menden-Deuer, S., 2012. Predator-induced fleeing behaviors in phytoplankton: a new mechanism for harmful algal bloom formation? *PLoS Biol.* 7 (9), e46438.
- Hemmersbach, R., Häder, D.-P., 1999. Gravitaxial responses of certain ciliates and flagellates. *FASEB J.* 13 (Suppl.), 69–75.
- Kessler, J.O., 1985. Hydrodynamic focusing of motile algal cells. *Nature* 313 (1), 218–220.
- Pernthaler, J., 2005. Predation on prokaryotes in the water column and its ecological implications. *Nat. Rev. Microbiol.* 3 (7), 537–546.
- Pundyak, O.I., 2014. Uncertainty of spatial distribution of inhomogeneous particles in limited volume. *Uzhhorod Univ. Sci. Herald Ser. Phys.* 35 (4), 225–228.
- Roberts, A.M., 2006. Mechanisms of gravitaxis in chlamydomonas. *Biol. Bull.* 210 (2), 278–280.
- Roberts, A.M., Deacon, F.M., 2002. Gravitaxis in motile microorganisms: the role of fore-aft body asymmetry. *J. Fluid Mech.* 452 (1), 405–423.
- Schuech, R., Menden-Deuer, S., 2014. Going ballistic in the plankton: anisotropic swimming behavior of marine protists. *Limnol. Oceanogr.* 4 (1), 1–16.
- Sharqawy, M.H., Lienhard, J.H., Zubair, S.M., 2010. The thermophysical properties of seawater: a review of existing correlations and data. *Desalin. Water Treat.* 16 (4), 354–380.
- Sklar, L., 1993. *Physics and Chance*. Cambridge University Press, 230 pp.
- Smayda, T.J., 2010. Adaptations and selection of harmful and other dinoflagellate species in upwelling systems. *Motility and migratory behavior. Prog. Oceanogr.* 85 (1–2), 71–91.
- Strom, S.L., 2008. Microbial ecology of ocean biogeochemistry: a community perspective. *Science* 320 (5879), 1043–1045.
- Visser, A., Kiorboe, T., 2006. Plankton motility patterns and encounter rates. *Oecologia* 148 (3), 538–546.
- Xie, L., Altindal, T., Wu, X.-L., 2015. An element of determinism in a stochastic flagellar motor switch. *PLoS Biol.* 11 (1), e0141654.



Available online at www.sciencedirect.com

ScienceDirect

journal homepage: www.journals.elsevier.com/oceanologia/



ORIGINAL RESEARCH ARTICLE

On the buoyant sub-surface salinity maxima in the Gulf of Riga

Taavi Liblik^{a,*}, Maris Skudra^{a,b}, Urmas Lips^a

^a Marine Systems Institute, Tallinn University of Technology, Tallinn, Estonia

^b Latvian Institute of Aquatic Ecology, Riga, Latvia

Received 1 August 2016; accepted 7 October 2016

Available online 23 October 2016

KEYWORDS

Salinity;
Thermocline;
Gulf of Riga;
Water exchange;
Intrusion

Summary Thermohaline structure in the Gulf of Riga (GoR) was investigated by a multi-platform measurement campaign in summer 2015. Stratification of the water column was mainly controlled by the temperature while salinity had only a minor contribution. Buoyant salinity maxima with variable strength were observed in the intermediate layer of the Gulf of Riga. The salinity maxima were likely formed by a simultaneous upwelling–downwelling event at the two opposite sides of the Irbe strait. The inflowing salty water did not reach the deeper (> 35 m) parts of the gulf and, therefore, the near-bottom layer of the gulf remained isolated throughout the summer. Thus, the lateral water exchange regime in the near bottom layer of the Gulf of Riga is more complicated than it was thought previously. We suggest that the occurrence of this type of water exchange resulting in a buoyant inflow and lack of lateral transport into the near-bottom layers might contribute to the rapid seasonal oxygen decline in the Gulf of Riga.

© 2016 Institute of Oceanology of the Polish Academy of Sciences. Production and hosting by Elsevier Sp. z o.o. This is an open access article under the CC BY-NC-ND license (<http://creativecommons.org/licenses/by-nc-nd/4.0/>).

1. Introduction

The water exchange regime of semi-enclosed basins largely determines their physical and ecological nature. The classical estuarine circulation scheme in the estuaries with positive freshwater flux includes an outflow in the upper layer and inflow in the deep layer (Geyer and MacCready, 2014). The exact water exchange regime and faith of the inflowing denser water depends on the size and shape of the estuary as well as its mouth area (Valle-Levinson, 2010). Nevertheless, typically the inflowing water is in contact with the bottom of

* Corresponding author at: Marine Systems Institute, Tallinn University of Technology, Akadeemia Rd. 15A, 12618 Tallinn, Estonia.

E-mail address: taavi.liblik@msi.ttu.ee (T. Liblik).

Peer review under the responsibility of Institute of Oceanology of the Polish Academy of Sciences.



Production and hosting by Elsevier

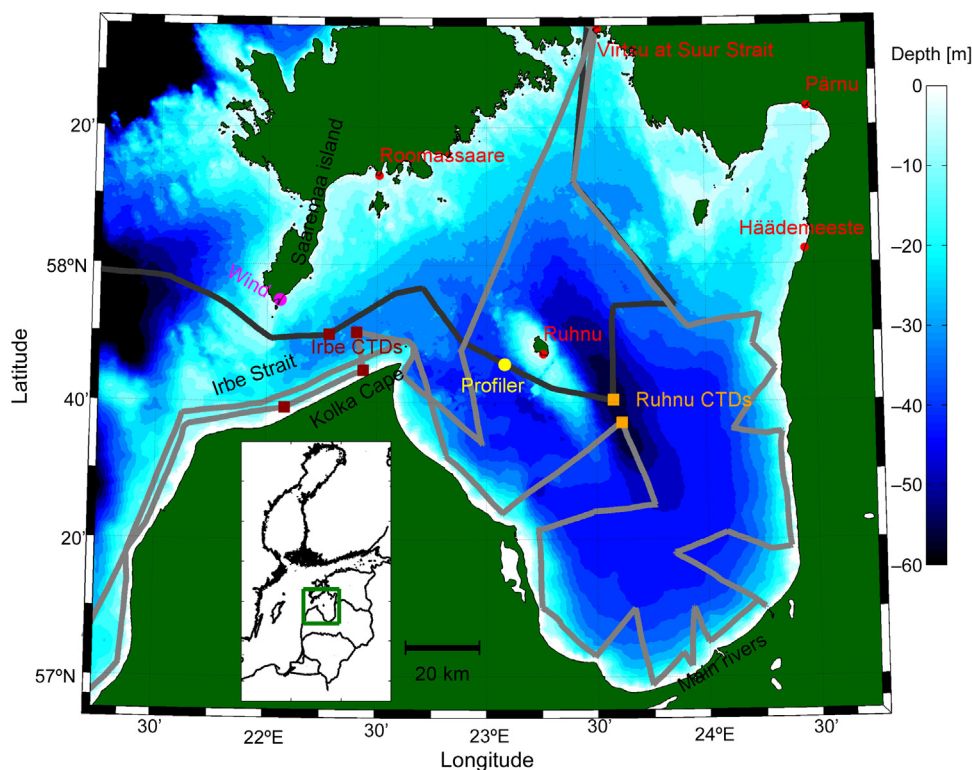


Figure 1 Map and topography of the Gulf of Riga. Color scale shows depth [m] of the study area. Lines show tracks of the RV Salme thermosalinograph surveys in July (darker gray) and August (brighter gray) 2015. Yellow circle represents the location of the moored profiler (buoy station), and red circles show locations where the coastal sea surface temperature time-series were acquired. Locations of Conductivity-Temperature-Depth (CTD) measurements at the Irbe Strait and Ruhnu Deep are shown as dark red and orange squares, respectively. The location of wind measurements at the Sõrve Cape station is shown as a magenta circle. The green box in the inlay map shows the location of the study area (Gulf of Riga) in the Baltic Sea.

the estuary. Exceptions might appear for the estuaries, which are separated from the adjacent sea basin by a sill. If the deeper layers of the estuary are filled with the saline water originating from the sporadic inflows, then the quasi-continuous water exchange over the sill involves inflowing water, which is too light to penetrate to the deepest layers of an estuary. Such regime can be found for several fjords (e.g. Belzile et al., 2016) and the Baltic Sea (Feistel et al., 2004). In the present study, we show that such water exchange regime can seasonally occur in a relatively large but shallow brackish estuary, the Gulf of Riga (GoR) as well.

The Gulf of Riga is a sub-basin of the eastern Baltic Sea. The gulf covers the area of 17 900 km², and its mean depth is 26 m. The deepest (> 50 m) area is in the central part of the gulf (Fig. 1). The gulf is connected to the Baltic Sea via two straits: the Irbe Strait in the west with the sill depth of 25 m, width of 28 km and cross-section of 0.4 km² and the Suur Strait in the north with the sill depth of 5 m, width of 6 km and cross-section of 0.04 km².

The water and salt budgets of the gulf are formed by the two sources: the saltier water from the open Baltic Sea (Baltic Proper) and the freshwater from the rivers and due to precipitation (e.g. Raudsepp, 2001; Skudra and Lips, 2016). The water from the open Baltic flows to the deep layer of the GoR (Laanearu et al., 2000) while the riverine water occupies the upper layer. Thus there is a vertical

salinity gradient present in the GoR (Skudra and Lips, 2016). The average river run-off to the gulf has been estimated approximately as 1000 m³ s⁻¹ (Berzinsh, 1995) while the average net precipitation to the gulf is about 80 m³ s⁻¹ (Omstedt and Axell, 2003). The 86% of the river run-off is discharged into the southern part of the gulf (Fig. 1, “Main rivers”) from the Daugava, Lielupe and Gauja rivers (Berzinsh, 1995). This river discharge, in combination with the water exchange through the two straits in the northern part of the gulf, forms the latitudinal salinity gradient (e.g. Stipa et al., 1999). Due to the strong inter-annual variability and seasonality of the river run-off, salinity in the gulf varies remarkably at the same time-scales (e.g. Raudsepp, 2001; Skudra and Lips, 2016; Stipa et al., 1999). Due to the shallowness of the Irbe and Suur Strait, water from beneath the permanent halocline of the Baltic Sea (e.g. Reissmann et al., 2009) cannot penetrate into the GoR. There are strong salinity fronts at both straits, which change their position influenced by the wind forcing and sea level differences between the basins (Astok et al., 1999; Lilover et al., 1998).

The heat budget of the gulf (like the whole Baltic) is driven by the fluxes through the sea surface. The gulf is stratified during summers when the temperature exceeds 18°C in the upper mixed layer (Skudra and Lips, 2016). In autumn–winter, the water column is mixed down to the bottom due to the thermal convection. Further, temperature falls

below the temperature of maximum density (Raudsepp, 2001; Stipa et al., 1999), and the gulf is at least partly covered by ice (Seinä and Palosuo, 1996) during winters.

The available modeling studies have shown that the heat exchange with the atmosphere and the heat content of the water column can be estimated relatively well in the Baltic (e.g. Westerlund and Tuomi, 2016). However, to simulate correct salinity distributions (both, vertical and lateral) and estimate salt fluxes between the basins and between different layers using numerical models is much more complicated (Lips et al., 2016b; Omstedt et al., 2014). This difficulty might show that the internal processes responsible for transport and mixing are described not precisely enough in such stratified, but relatively shallow basins. In the present study, we analyze the observed salinity distributions and vertical structures and relate them to the forcing.

Oxygen consumption under conditions of developed vertical stratification in summer could result in poor oxygen conditions in the near-bottom layer of deep central areas of the gulf (Aigars et al., 2015; Eglite et al., 2014). It has been argued based on the analysis of seasonal dynamics of environmental parameters and biomarkers for instance that the clam *Macoma balthica* could be stressed in late summer due to lower oxygen levels in August in the near-bottom layer of the Gulf of Riga (Barda et al., 2013). Furthermore, hypoxia at the water-sediment interface alters the phosphorus flux between the water column and sediments as well as nitrogen removal due to denitrification (Yurkovskis, 2004). Due to the sediment release of phosphorus in hypoxic conditions, the main pathway of phosphorus removal from the gulf is its relatively slow export to the Baltic Proper (Müller-Karulis and Aigars, 2011). Thus, reoccurrence of such poor oxygen conditions and benthic nutrient release could counteract decreases in the external nutrient load to the gulf similarly to the deeper Baltic basins including the Gulf of Finland (Pitkänen et al., 2001).

The main aim of the present study is to present the high-resolution view on the stratification development in the Gulf of Riga. Available investigations include the data only from episodic ship surveys (Stipa et al., 1999) or are concentrated on the long-term changes in the gulf (Raudsepp, 2001; Skudra and Lips, 2016). Studies in other basins of the Baltic have shown that implementing a new type of in situ platforms, such as moored vertical profilers (Lips et al., 2016a), Argo floats (Purokoski et al., 2013; Westerlund and Tuomi, 2016) or underwater gliders (Alenius et al., 2014; Karstensen et al., 2014), can improve the understanding of thermohaline processes. High-resolution continuous temperature–salinity measurements have not been conducted so far in the Gulf of Riga. To fill this gap, an autonomous profiler was deployed in the northwestern part of the gulf from May to September 2015.

2. Material and methods

2.1. Data

The dataset analyzed in the present study was collected from May to September 2015. Altogether 202 temperature and salinity profiles were collected by an autonomous vertical profiler equipped with OS316plus CTD (Conductivity,

Temperature, Depth) probe (Idronaut S.r.l.). The profiler has been successfully applied in the Gulf of Finland for several years now (Lips et al., 2016a). The profiler was set to collect measurements in a depth range from 2 to 37 m twice a day. Initial vertical resolution of measurements was 0.1 m, but after the preliminary data processing, the profiles were stored for analysis purposes with a vertical resolution of 0.5 m. The CTD probe was calibrated by manufacturer right before the deployment, and the data quality was checked against shipborne CTD profiles several times during the study.

The shipborne CTD and dissolved oxygen data (OS320plus CTD, Idronaut S.r.l.) together with the thermosalinograph (SBE45 MicroTSG, Sea-Bird Electronics; included in the flow-through system) data were used to study the spatial thermohaline fields in the area (Section 3.2). The salinity data was checked against the water sample analyses using a salinometer 8410A Portasal (Guildline). The oxygen sensor was calibrated before each survey and was checked against water sample analyses using an OX 4000 L DO meter (WWR International, LLC).

The long-term CTD dataset 1993–2012 compiled by Skudra and Lips (2016), collected under Estonian and Latvian national monitoring programs, was extended to 2015. This dataset together with HELCOM data (<http://ocean.ices.dk/helcom>, 25 February 2016) was used to evaluate the occurrence of the sub-surface salinity maxima in the past (Section 3.3).

Coastal temperature measurements at Ruhnu, Häädemeeste, and Roomassaare, provided by the Estonian Environmental Agency, were included in data analysis. Likewise, the level 3 SST (sea surface temperature) product over European Seas by Copernicus Marine Environment Monitoring Service (<http://marine.copernicus.eu/>) was used as background information. Wind measurements at the Sörve station were obtained from the Estonian Environmental Agency. The wind speed and direction, measured at 10 m height, were available every third hour as a 10 min average.

2.2. Calculations

The upper mixed layer (UML) depth was defined as the minimum depth where the criterion $\rho_z \geq \rho_3 + 0.15 \text{ kg m}^{-3}$ was satisfied (ρ_z is density at depth z , and ρ_3 is density at 3-m depth).

Relative contributions of temperature (ST_T) and salinity (ST_S) to the vertical stability of the water column were estimated as:

$$ST_T = \alpha \frac{dT}{dZ} \rho, \quad (1)$$

$$ST_S = \beta \frac{dS}{dZ} \rho, \quad (2)$$

where α is the thermal expansion coefficient, β is the saline contraction coefficient, ρ is the water density; dT/dZ and dS/dZ are the temperature and salinity gradients over the vertical distance dZ . Temperature and salinity profiles were both smoothed by 2.5 m window before the stability and intrusion index calculations. Stability (ST) of the water column was acquired by summation of ST_T and ST_S . Total

(contribution to) stability of the water column was calculated as vertically integrated ST_T , ST_S and ST . Likewise, the total contribution to the stability of the UML was calculated as vertically integrated ST_T , ST_S , and ST within the depth range of the UML.

In order to estimate the intensity of interleaving the intrusion index as the sum of negative salinity gradients [$\text{g kg}^{-1} \text{m}^{-1}$] was calculated same as by Lips et al. (2016a):

$$I = \sum_{z=h_1}^{z=h_2} \begin{cases} 0, & \text{if } \frac{dS}{dz} \geq 0 \\ \text{abs}\left(\frac{dS}{dz}\right), & \text{if } \frac{dS}{dz} < 0 \end{cases}, \quad (3)$$

where I is the intrusion index, h_1 and h_2 are the borders of the depth interval where the index was calculated. It means if salinity increases downwards throughout a profile, the index is zero. Contrary, if there is a strong sub-surface salinity maximum, the index has a higher value.

The apparent oxygen utilization (AOU) was used to show the difference between measured dissolved oxygen content and saturation level:

$$\text{AOU} = \text{DO}_{100} - \text{DO}_M, \quad (4)$$

where DO_{100} is oxygen concentration at saturation level (Weiss, 1970), and DO_M is the measured oxygen concentration.

Salinity values are given as Absolute Salinity [g kg^{-1}], density as potential density anomaly to a reference pressure of 0 dbar [σ_0 ; kg m^{-3}] and the unit of oxygen values is mg L^{-1} in the present paper. Density values in Section 3.3 are presented as arithmetic averages at 0–5 m and 32–38 m depth ranges in the Baltic Proper and in the Gulf of Riga, respectively.

3. Results

3.1. Temperature, salinity, density and stratification time-series at mooring station

3.1.1. General description

Water column structure was determined by the seasonal thermocline at the beginning of the study period (Fig. 2). Temperature decreased almost linearly from the base of the upper layer (9.3–10.0°C) at 15–20 m depth to the near-bottom layer (4.3–5.5°C). Vertical distribution of salinity was relatively even and ranged between 5.9 and 6.0 g kg^{-1} . Temporal development of the vertical thermohaline structure was characterized by a seasonal increase in temperature due to the atmospheric heat flux and a slight decrease in salinity in the upper layer in June. By the end of June, temperature (salinity) gradient from the upper layer to the near bottom (old winter water) layer was from 15.6 to 5.8°C and from 5.8 g kg^{-1} to 6.0 g kg^{-1} , respectively.

Advection of fresher water was observed at the buoy location in the upper 25 m in the first week of July. Salinity values below 5.4 g kg^{-1} were registered. At the same time, water temperature increased in the upper layer, which, however, cannot be related to the advection. First, the temperature maxima and salinity minima did not match exactly in time. Secondly, a simultaneous temperature increase and decrease after that were registered at all

coastal stations around the gulf, which implies that the atmospheric heat flux was responsible for this temperature change.

Further developments in July included a general increase in the upper layer temperature and intermittent appearances of fresher and saltier patches in the sub-surface layer at the depth range from 14 to 24 m. Less saline water in the upper layer and thick sub-surface intrusion of saltier water after that were observed at the end of July. Upper layer temperature reached its seasonal maximum of 20.4°C in mid-August. Upper layer salinity varied around 5.5 g kg^{-1} in the first half of August and was close to 5.7 g kg^{-1} in the second half of the month.

Vertical structure in September was characterized by heat loss to the atmosphere and by advection of fresher water to the buoy location. A temperature and salinity decrease in the upper layer, as well as thickening of the mixed layer, were observed during that period. Thus, it was the advection of fresher water that dominated over the vertical transport of salt in the upper layer salt flux. Interestingly, temperatures below 4.5°C were occasionally registered at the deepest measured horizon of 37 m even in September.

3.1.2. Stratification

Time series of the water column stability are presented in Fig. 3a. The higher (red) values mark the location of the pycnocline while the dark blue color indicates that water is vertically homogeneous. The seasonal thermocline was the main contributor to the stability of the water column (Fig. 3b). There were only a few occasions when the temperature gradients had an opposite effect and caused weakening of the vertical stratification.

Negative stability values due to the vertical salinity gradient occurred in July and August, and they were especially strong in the second half of July (Fig. 3c). Those layers were located in the thermocline and were compensated by the vertical temperature gradient. It has to be noted that the layer with inverse salinity gradient was always surrounded by the layers above and below it where the salinity was increasing with the depth (Fig. 3c). The explanation for such salinity derived stability distribution was the existence of sub-surface buoyant saltier water intrusion. Starting from the sea surface, the following gradients/layers were associated with the salinity maxima and could be distinguished: (1) layer with positive salinity gradient from the ambient water in the thermocline to the core of maxima layer (red color); (2) values close to zero that show the location of the core (white color); (3) layer with negative salinity gradient between the core and ambient deep layer water (blue color); (4) values close to zero that show the point (range) where salt intrusion water merged with the ambient water (white color); (5) positive salinity gradient in deep water (red color).

The integrated stability over the water column (Fig. 3d) showed that the thermal buoyancy dominated while salinity had a minor importance in the strength of stratification at the buoy location. The minor role of salinity can be at least partly related to the fact that the highest salinity (intrusion) was located in the intermediate layer and not in the bottom layer. The salty water near the bottom would have increased the stability over the water column.

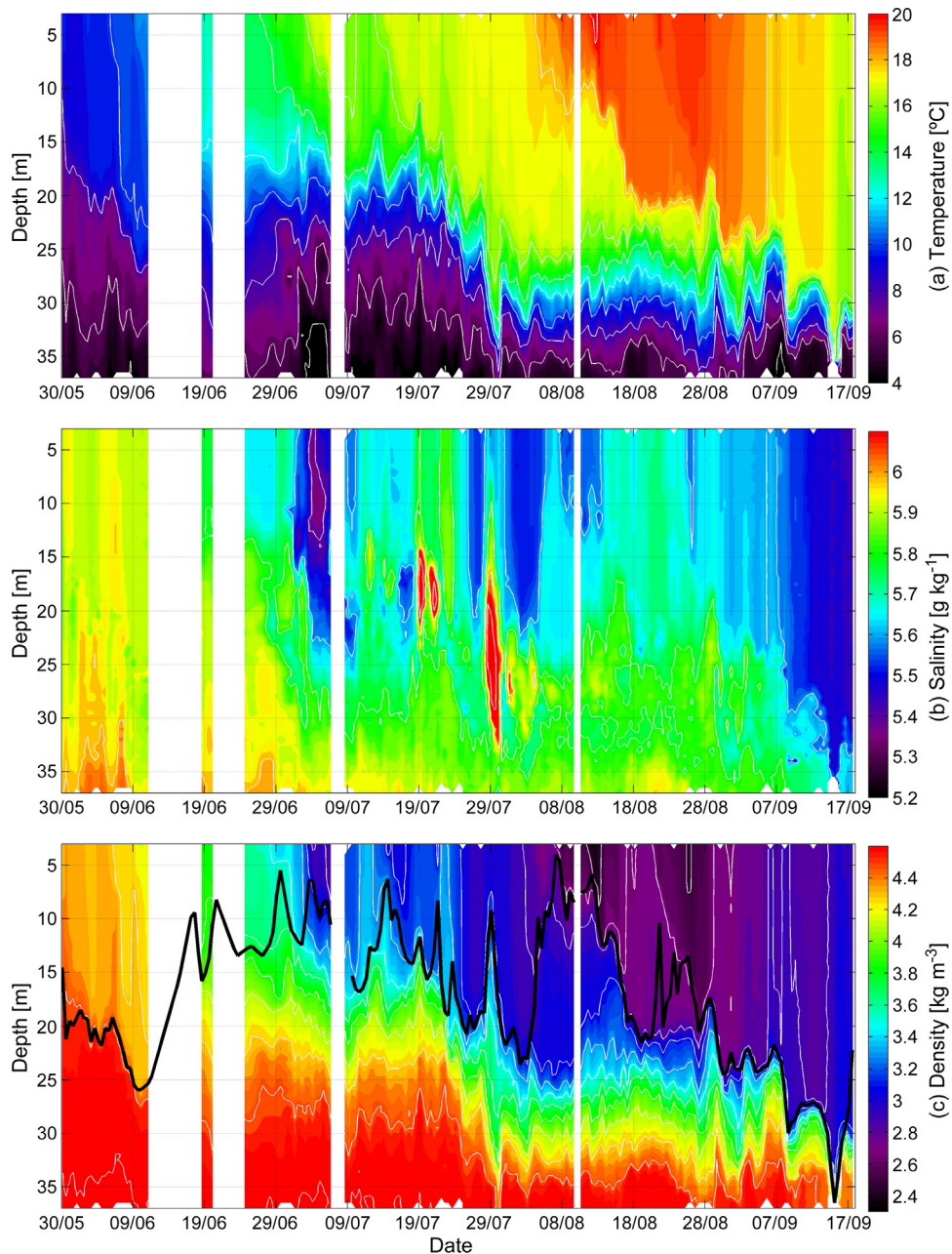


Figure 2 Time series of temperature [$^{\circ}\text{C}$], salinity [g kg^{-1}] and density anomaly [kg m^{-3}] at the buoy station from 30 May 2015 to 18 September 2015. Black line in the bottom panel is the upper mixed layer (UML) depth. The location of the mooring is shown as yellow circle in Fig. 1.

The UML depth ranged from a few meters to 35 m during the study period (Fig. 2c). The UML was mostly stabilized by the temperature while salinity had occasionally (at the beginning of July) an opposite effect (Fig. 3e). Salinity and temperature had a similar contribution to the stability at the beginning of August.

Time-series of intrusion index (Fig. 3f) show relatively low values (<0.05) until the beginning of July. It is noteworthy that intrusion index values differed from zero, most probably, due to the observed sub-surface freshwater patches (Fig. 2b). Occasional peaks of intrusion index up to 0.1 were observed until the beginning of September. The

highest values exceeded 0.2 and occurred in the second half of July.

3.1.3. Salinity fluctuations

The period with highest intrusion peaks is below described in more detail. It is noteworthy that immediately before the appearance of saltwater patches a clear signature of fresher water was registered at the 15–20 m depth (Fig. 4, 19 Jul 12:00). The core of this fresher layer had the salinity of $5.55\text{--}5.60 \text{ g kg}^{-1}$, and it lied in between the upper layer with the salinity of $5.75\text{--}5.80 \text{ g kg}^{-1}$ and deep layer with the salinity of 5.95 g kg^{-1} .

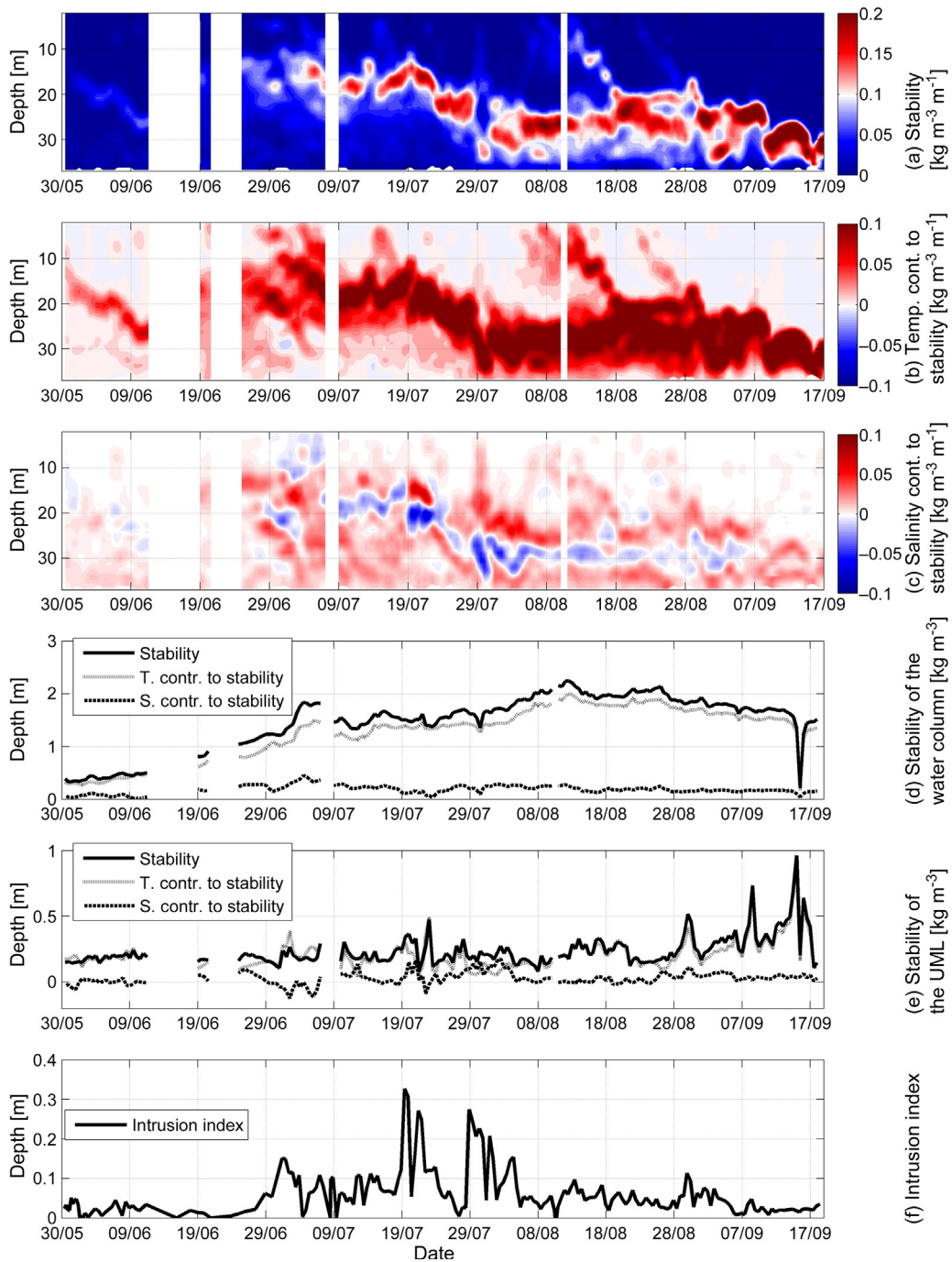


Figure 3 Temporal development of the following vertical stratification parameters at the buoy station from 30 May to 18 September 2015: stability (a; [$\text{kg m}^{-3} \text{m}^{-1}$]) and contribution of temperature (b) and salinity (c) to stability; integrated stability parameters [kg m^{-3}] for the whole water column (d) and for the upper layer (e); intrusion index (f).

Next, the saltier water (5.80 g kg^{-1}) appeared in the upper layer and rapidly (within our profiling interval of 12 h) the fresher water in the sub-surface layer was replaced by the salinity maximum (Fig. 4, 20 Jul 00:00). The saltier sub-surface layer was located in the depth range of 11–25 m and its core with the salinity of 6.45 g kg^{-1} was located at 17 m depth. The temperature of the core was 14.55°C while 3.5 m above the core it was 13.75°C . Thus, the salinity gradient above the core neutralized the negative buoyancy

due to the vertical temperature distribution. It was opposite below the core: strong thermocline stabilized the water column despite the negative salinity gradient. The sub-surface salinity maximum disappeared on 22 July. Fresher sub-surface water was observed from 23 July to 28 July while salinity in the upper layer decreased from 5.80 to 5.55 g kg^{-1} . The saltier water reappeared in the sub-surface layer on 29 July (Fig. 4 29 July 12:00). The core of the sub-surface layer was located at 22 m depth and had salinity and

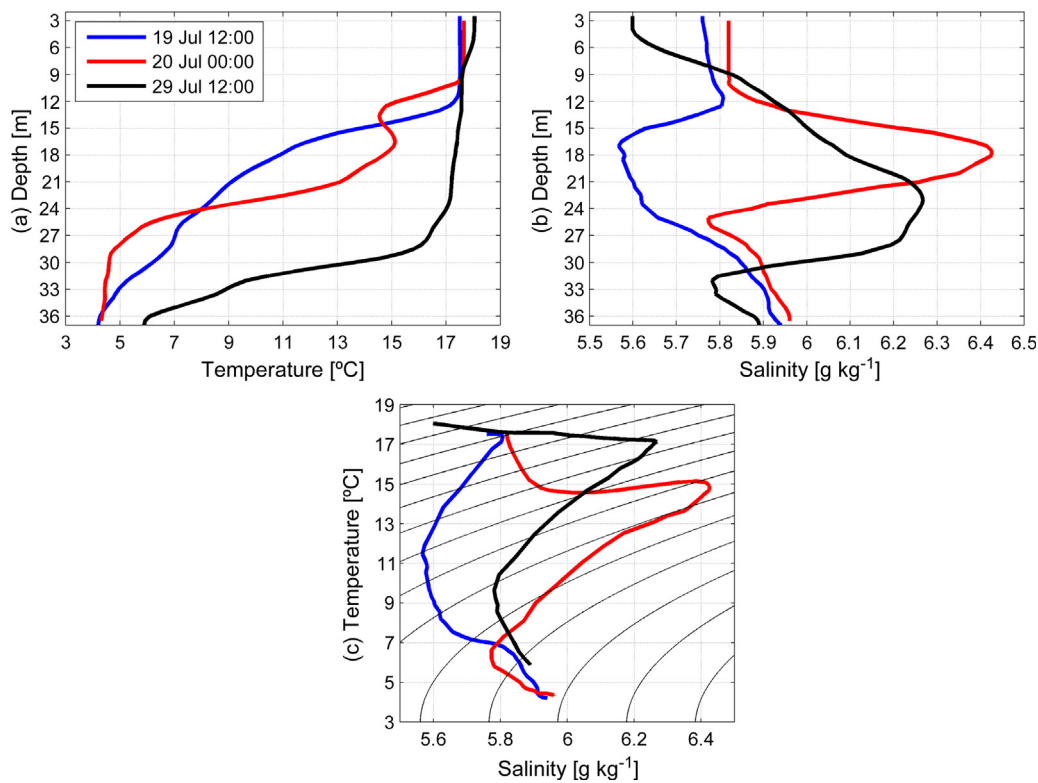


Figure 4 Selected profiles of temperature [$^{\circ}\text{C}$; a) and salinity [g kg^{-1} ; b) and respective temperature–salinity diagram with density anomaly [kg m^{-3} ; c) as contour lines in profiling station (the location is shown as a yellow circle in Fig. 1).

temperature of 6.30 g kg^{-1} and 17.15°C , respectively. The core was only slightly (0.15°C) warmer than the layer above. That temperature change had a minor contribution to the vertical stratification as salinity increased from 5.70 g kg^{-1} to 6.30 g kg^{-1} in the same depth range. The sub-surface salinity maximum, though much weaker, was observable until the end of August.

3.2. Origin of the salt intrusion

The observed saltier water could potentially penetrate to the GoR from the Baltic Proper via either the Irbe Strait or Suur Strait. The core of the observed salt maxima layer had the salinity of 6.45 , 6.30 g kg^{-1} and temperature of 14.55°C , 16.40°C on 20 July and 29 July, respectively. We can expect that if the source water has been modified, then it occurred because of mixing of it with the GoR ambient waters. The temperature–salinity curves (TS-curves) of the sub-surface salinity maxima cores indicate that this saltier water was slightly warmer than the surrounding GoR waters. Thus, if the observed core has been a subject of mixing, the source water of the salt maxima layers must have been saltier and slightly warmer than the observed core at the buoy station. Unfortunately, there were no continuous measurements available in the straits. Thus, we were not able to capture the entering process of the saltier waters directly. However, we collected some shipborne CTD profiles in the Irbe Strait area (Fig. 5). The other data source was made available by the thermosalinograph that autonomously recorded temperature and salinity of the water pumped from 2 m depth during the

surveys on board RV SALME. The two surveys that were included in the analysis were conducted on 14–15 July and 7–9 August.

The first survey was conducted through the central part of the Irbe Strait on 14–15 July while the vessel visited more the southern part during the second survey; though, one station in the central part was sampled as well. During the second survey, the area was visited twice: the first passage on 7–8 August and the second passage on 9 August.

During the both surveys, a strong salinity front was found in the upper layer in the Irbe Strait area. The front was captured near the longitude of 22°E by the survey on 14–15 July (Fig. 5). Salinity values below 6.20 g kg^{-1} were observed toward east from the longitude of 22°E . The front was located further in the east on 7–9 August. However, due to different tracks of the two surveys (the latter was conducted along the southern coast) we cannot confirm, whether it was a spatial feature or temporal displacement of the front.

The most remarkable feature in the upper layer temperature dynamics was the colder water observed in the strait on 14–15 July survey. The temperature of the upper layer was around or exceeding 17°C in the Baltic Proper and the gulf, but below 13°C inside of this cold feature (Fig. 5). Since the Irbe Strait is a topographic barrier between the open Baltic and the gulf, upwellings in both basins can potentially bring cold water to the upper layer in the Irbe area. Strong SW winds ($>10 \text{ m s}^{-1}$) occurred during the period from 5 to 10 July, i.e. favorable forcing for an upwelling in the GoR along the coast of the Saaremaa Island. Weaker winds from NW, i.e. from the favorable direction for the upwelling along

the Latvian coast in the Baltic Proper, prevailed from 11 to 15 July (Fig. 6). The satellite-derived sea surface temperature, as well as temperature measurements at the coastal stations and by the onboard thermosalinograph, indicated that the upwelling occurred in the NW part of the GoR in mid-July (Fig. 7). Since salinity in the whole water column was higher in the Baltic Proper than in the core of the upwelled cold water in the Irbe Strait (6.15 g kg^{-1}), this upwelled water cannot be a pure Baltic Proper water. On the other hand, the upwelled water was saltier than the GoR water. Thus, the upwelled water might be a mixture of waters from the both basins.

The only available profile in the Irbe Strait on 14–15 July was acquired eastward from the core of the upwelling (Fig. 5a). The profile revealed three layers: upper layer (15.00°C and 5.90 g kg^{-1}), deep layer (4.70°C and 5.95 g kg^{-1}) and salt maxima layer (12.15°C and 6.35 g kg^{-1}) between the former two (Fig. 8). The temperature profile, as

well as the satellite-derived sea surface temperature, showed that the station was in the upwelling zone but not in its coldest core area. Relatively low salinity of the upper layer (upwelled water) and deep layer at the station indicated that those waters originated from the gulf. The salt maxima layer at the station and coldest water in the upper layer observed by the thermosalinograph were similar. Though, the salt maxima water was slightly colder and saltier than in the upwelled water at the CTD station. Thus, the observed salt maxima layer water was likely mixed with warmer and fresher surface water before upwelled to the surface as registered by the thermosalinograph (Fig. 8).

The structure of the salt maximum was similar to the one observed at the buoy station, which suggests that the salt impulse entered the gulf likely via the Irbe Strait. The salt maxima at the thermocline were much saltier than the water below and above and the water in those layers was slightly

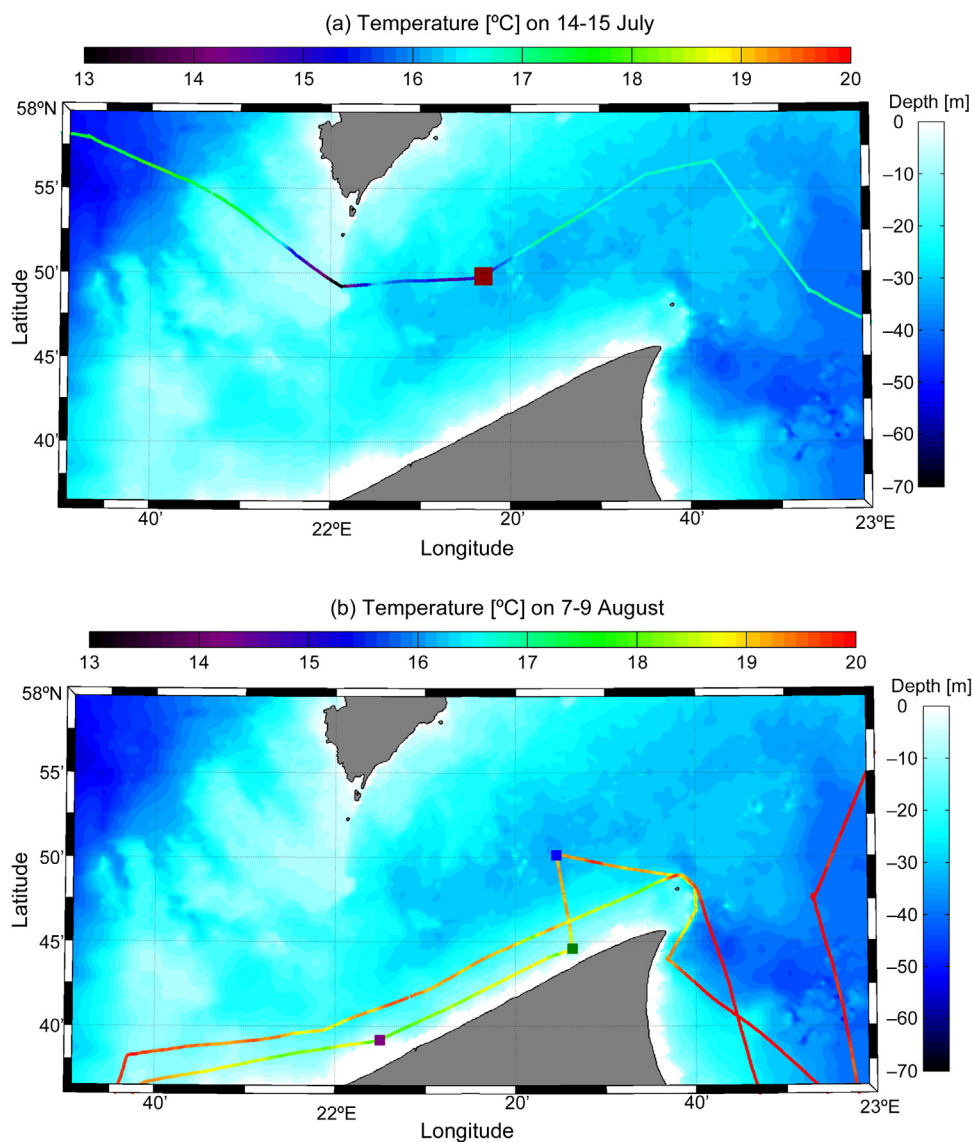


Figure 5 Temperature [$^\circ\text{C}$; a, b) and salinity [g kg^{-1} ; c, d) at 2 m depth acquired by the thermosalinograph on board RV SALME on 14–15 July (a, c) and 7–9 August (b, d). On vertical color bar sea depths [m] are shown.

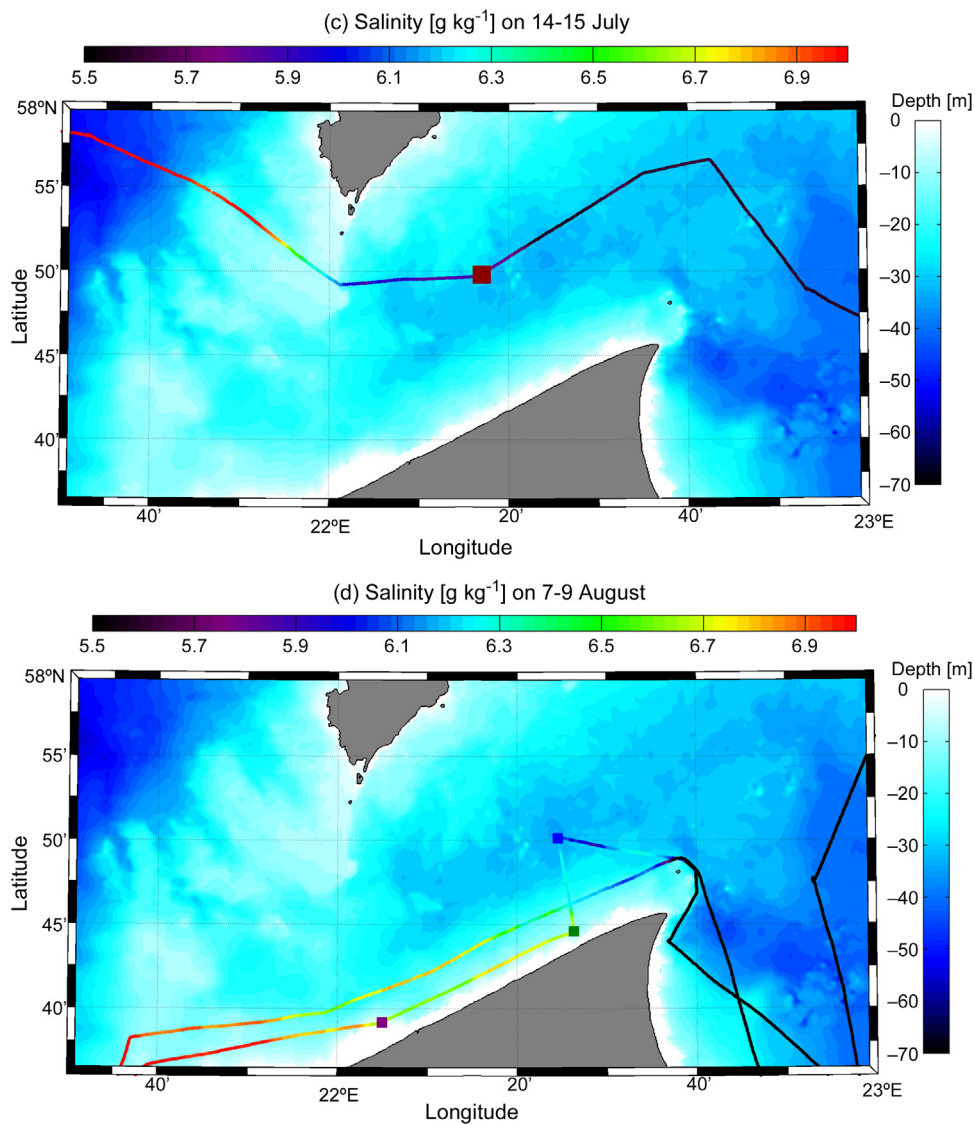


Figure 5 (Continued).

warmer than in the thermocline above. The latter indicates that the salt maxima water originates from the warmer layer above.

The similar structure of salt intrusion was found in the central part of the Irbe Strait on 9 August (Fig. 8). At the same time, high saline $>6.7 \text{ g kg}^{-1}$ and warm water was observed in the upper layer in the southern part of the strait (Figs. 5 and 8). TS-curves suggest that the salt maxima layer observed in the central part of the strait was a mixture of this high saline warm water and thermocline water of the GoR. The possible mechanism that can penetrate the warm and high saline water deeper is downwelling along the southern coast of the Irbe Strait. Indeed, SW wind that generates upwelling along the shore of the Saaremaa Island also causes downwelling along the southern coast of the strait. Moreover, the SW wind likely creates a coastal boundary current along the eastern coast of the Baltic Proper. It can be seen that at the station marked in green in Fig. 8, this warm, salty water has pushed over the fresher water. Thus, it likely caused some vertical mixing there as well.

In an upwelling cell along a boundary, the upwelled water is typically compensated by an onshore flow in the deeper layer. In the present case, upwelling occurred in the strait, which is relatively narrow and shallow. Thus, simultaneously with the upwelling, a downwelling occurred along the opposite coast, and the downwelled waters (originated from the Baltic Proper) rather fast reached the seabed. We suggest that the upwelled water was (at least partly) compensated by this warm and saltier downwelling water in the Irbe Strait. This hypothesis is supported by the TS-curves: one source water for the salt maxima layer observed in the central strait on 9 August (blue curve in Fig. 8) had almost the same TS-characteristics as the warm and saltier water in the southern part of the Irbe Strait (magenta and green curves in Fig. 8). Moreover, the same suggestion can be made on the basis of AOU vs. S curves (Fig. 8). This saltier and warm water was formed in the Irbe Strait and later spread to the gulf as upwelling–downwelling system relaxed.

Measurements at the coastal stations and buoy station reveal the temporal development of the upper layer

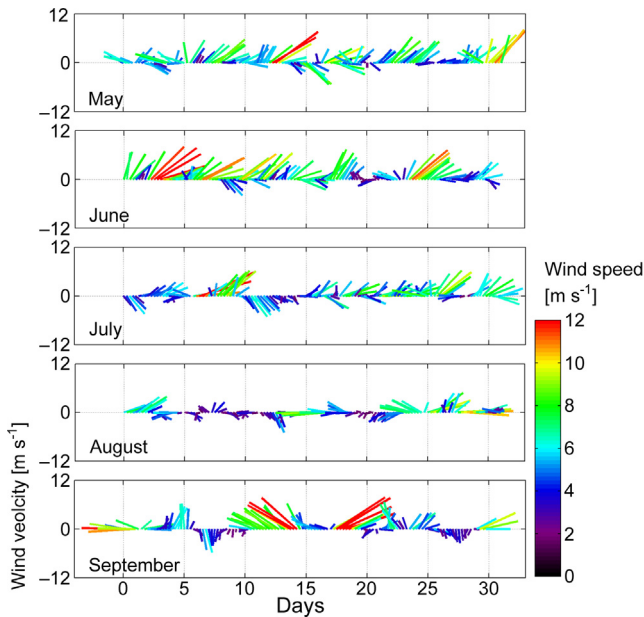


Figure 6 Wind vectors at the Sörve meteorological station in 2015. The location of the station is shown in Fig. 1 as a magenta circle.

temperature in different parts of the gulf. There were several synoptic events of cooling (at the beginning of August) and warming (at the beginning of July) that simultaneously occurred at all stations (Fig. 9). Those were atmospheric heat flux events. The seasonal temperature increase at Ruhnu and, especially, at the buoy lagged the other two stations until the end of June. This delay was related to the slower warming of the open gulf waters

comparing to the shallow coastal waters. The same tendency was in September, but this time, the slower cooling in the open sea resulted in a higher temperature at the buoy station than at the coastal stations. One can note that the lowest temperatures mostly occurred at Roomassaare in mid-July during a period of two weeks. Upwelling along the north-western coast of the gulf prevailed during this period. The Roomassaare station is not the best location to catch the upwelling in the Irbe Strait but as satellite derived sea surface temperature showed (Fig. 7), at least in some cases, upwelling events occurred in the Irbe Strait and at Roomassaare at the same time. Moreover, the period of upwelling coincided with the period of strongest salt maxima observed at the buoy station (intrusion index in Fig. 3f). This coincidence supports the suggestion that the salt pulses entered the gulf during the simultaneous upwelling in the northwestern gulf (along the shore of the Saaremaa Island) and downwelling along the southern coast of the Irbe Strait.

3.3. Earlier observations

In the previous subchapter, we suggested that the sub-surface saltwater maxima originated from the upper layer of the Baltic Proper and likely entered the gulf via the Irbe Strait. The pre-condition for the sub-surface buoyant salt maxima establishment is a specific density range of the saltwater. The inflowing salty water (or a product of its mixing with the ambient Gulf of Riga water) should be lighter than the deep layer water and denser than the upper layer water in the gulf. The upper layer density (presented as potential density anomaly σ_0) in the Baltic Proper in January–April is in a range of 5.5–6.0 kg m^{-3} (Fig. 10). Water cools down to the temperature of maximum density (2.6–2.7°C) every winter in the Gulf of Riga. Salinity over 6.9 g kg^{-1} (at the temperature of

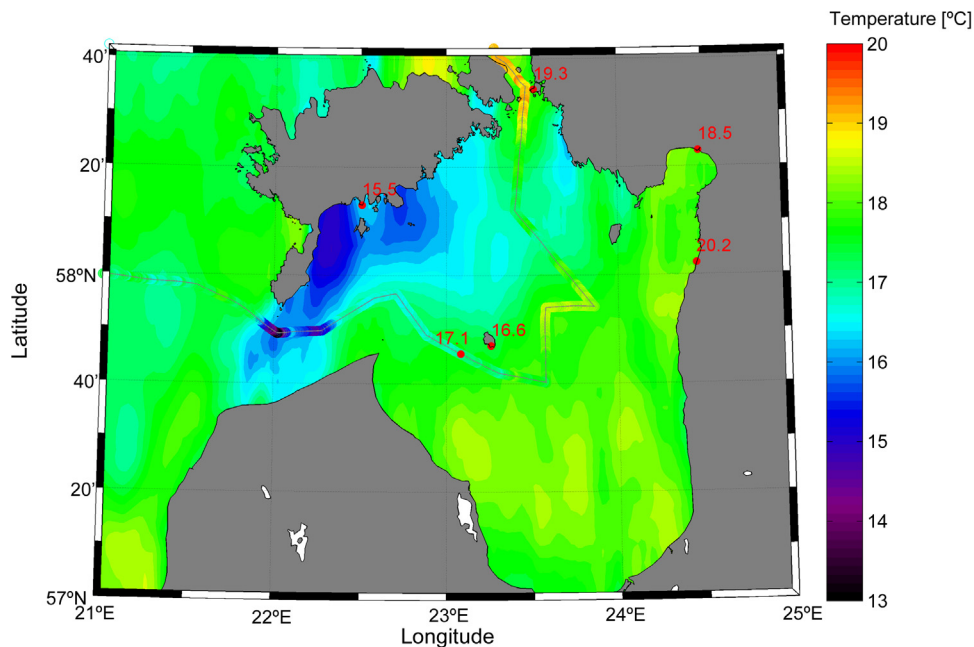


Figure 7 Satellite-derived sea surface temperature; upper layer temperature registered along the RV SALME track by thermo-salinograph, at the buoy station and selected coastal stations on 15 July 2015.

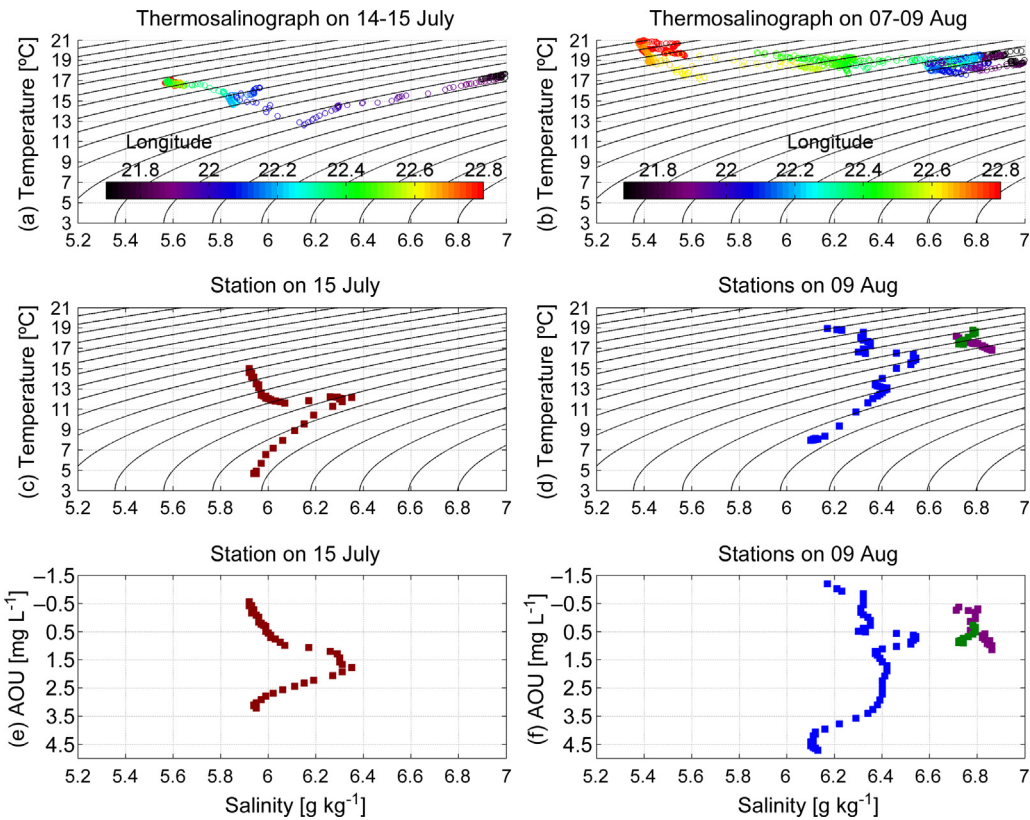


Figure 8 Temperature–salinity (TS) and apparent oxygen utilization (AOU) vs. salinity curves on 14–15 July and 7–9 August. TS-curves along the vessel track acquired by the Salmebox (a, b) and at selected Conductivity-Temperature-Depth (CTD) stations during the two analyzed surveys. Thermosalinograph tracks and locations of CTD stations are shown in Fig. 5 (station dots on the map have same colors as TS dots here). Color bars in the uppermost panel show the longitude.

2.6–2.7°C) would be necessary to reach the density of 5.5 kg m^{-3} . Salinity in the deepest layers of the gulf does not typically exceed 6.5 g kg^{-1} (Raudsepp, 2001). As shown in Fig. 10a, average density anomaly at the 32–38 m depth in

the Gulf of Riga is mostly below 5 kg m^{-3} . Thus, if the Baltic Proper water enters the Gulf of Riga in January–April, it must dive to the near-bottom layer of the gulf and sub-surface maxima as such cannot exist during winters.

As soon as the surface water in the Baltic Proper gets lighter due to the seasonal warming in June, the formation of sub-surface salinity maxima is feasible. In autumn, convection and wind stirring mix the denser deeper layer water and lighter upper layer water thoroughly. As a result, the deep layer temperature increases while salinity and density decrease. Therefore, sub-surface salinity maxima formation in October–November is not feasible anymore, and the dense Baltic Proper water flows to the near-bottom layer of the gulf. The upper layer water in the Baltic Proper tends to be lighter than water in the Gulf of Riga at 32–38 m depth during the timeframe from mid-July to the beginning of September (Fig. 10a). Thus, if the Baltic Proper water flows into the gulf during that time, it likely does not reach the bottom layers of the gulf and rather forms buoyant salt maxima. The temporal variability of the intrusion index, calculated based on the available full-resolution (0.5 m) CTD casts from the years 1993–2014, confirms latter and shows that the saltwater intrusions have been observed from mid-July to mid-September (Fig. 10b).

Comparison of the upper layer density in the Baltic Proper and the Gulf of Riga shows that latter water is always lighter. Even during the autumn-winter cooling period, when the

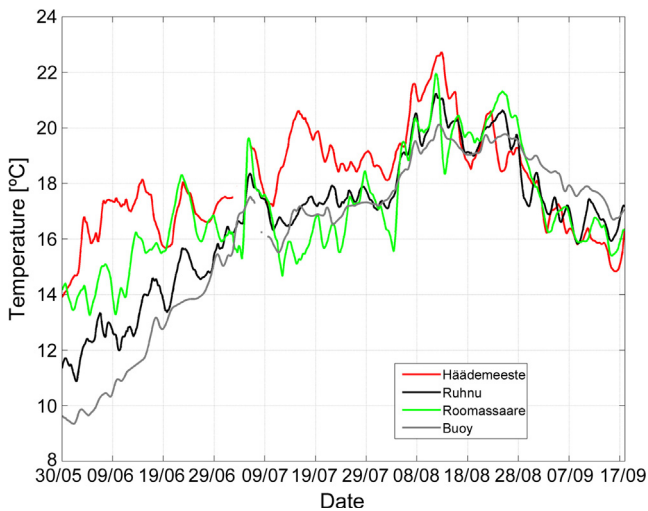


Figure 9 Upper layer water temperature at various locations in the Gulf of Riga. Coastal stations are shown as bright red circles and buoy location as a yellow circle in Fig. 1.

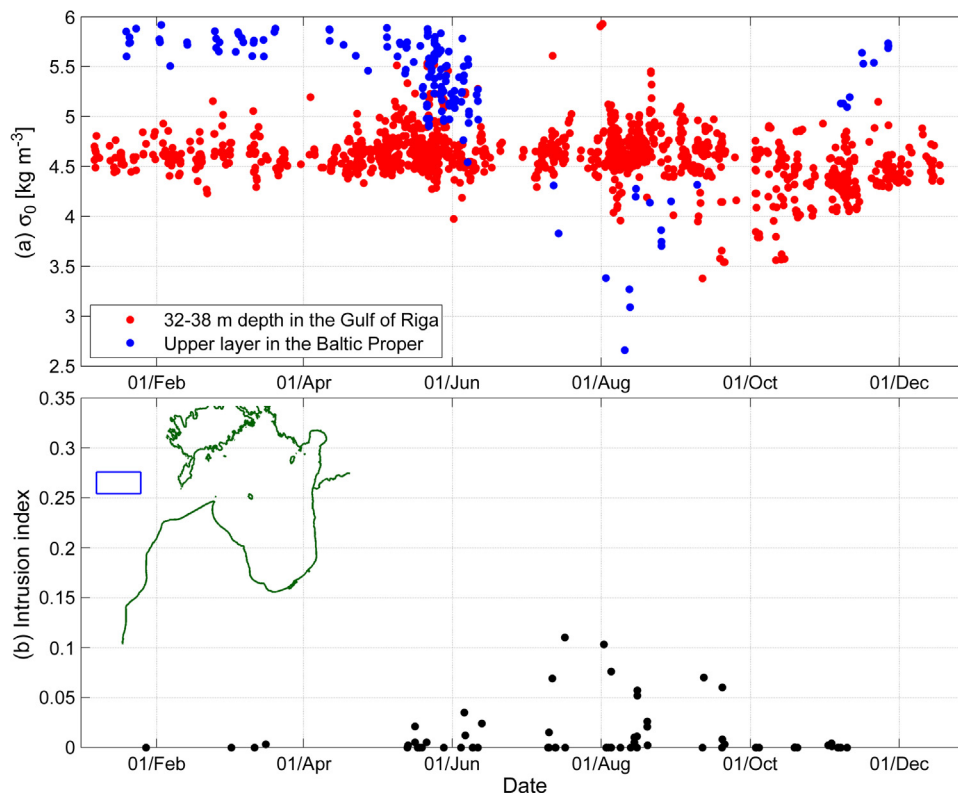


Figure 10 (a) Annual cycle of average potential density anomalies (σ_0 ; [kg m^{-3}]) in the 0–5 m layer of the Baltic Proper (1979–2014) and at the 32–38 m depth in the Gulf of Riga. (b) Intrusion index in the Gulf of Riga at ≥ 35 m deep stations (1993–2015); only high-resolution profiles were included. The blue box indicates the location of the analyzed profiles from the Baltic Proper. In the Gulf of Riga, all available deep enough measurements were included.

temperature in the Gulf of Riga drops faster than in the Baltic Proper, latter has still heavier upper layer water. This density difference shows that the water coming from the Baltic Proper cannot lie above the Gulf of Riga water.

In conclusion, we suggest that two types of Baltic Proper inflow regimes exist in the gulf. The near-bottom layer salt wedge regime is the only inflow pattern from October to May/June. In summer, from June/July to September, the regime leading to the formation of the buoyant salt intrusion (or saltier water patches) if the inflowing water originates from the upper layer or the regime resulting in the near-bottom salt wedge if the inflowing water originates from the layer beneath the seasonal thermocline can occur.

4. Discussion

The year 2015 was special for the Baltic Sea in two senses. First, strong barotropic Major Baltic Inflow (Matthäus et al., 2008) occurred in December 2014 (Mohrholz et al., 2015). Secondly, the winter 2014/2015 was exceptionally mild in the Baltic Sea area, and the Gulf of Riga was almost ice-free in winter (Uotila et al., 2015). However, we do not expect that these two events had a major impact on the thermohaline state of the gulf in summer 2015. It takes years to see the impact of a Major Inflow in the upper layer of the Baltic Proper (Reissmann et al., 2009), which is a salty water source

for the Gulf of Riga. Despite an exceptionally warm winter, the gulf was ventilated down to the bottom layer in the deepest part of the gulf in the Ruhnu Deep (Fig. 11). The mild winter might have an impact on the river discharge (Apsite et al., 2013) and, thereby, to the salinity of the gulf though (Raudsepp, 2001).

High-resolution profiling showed that stratification of the water column during the study period was mainly controlled by the temperature while salinity had only a minor impact. Likewise, the stability of the upper mixed layer was mostly controlled by the temperature. Nevertheless, the vertical stratification in spring is mostly created by the freshwater fluxes, at least in the southern part of the Gulf as suggested by Stipa et al. (1999). It is worth to perform high-resolution profiling in spring, to observe the development of stratification.

Distinctive sub-surface salt maxima were observed in the thermocline in July and August 2015. Due to the lack of data, spatial view on the salt maxima is quite limited. Anyhow, all three available CTD profiles (not shown here) from July to August registered in the Ruhnu Deep revealed the occurrence of salt maxima there. Thus, the maxima can reach the central or southern part of the gulf. It can be expected that the patches of sub-surface salt maxima only occasionally reached or passed the profiling station. In other words, the rapid disappearance of maxima layer observed at the buoy station was not a result of vertical mixing.

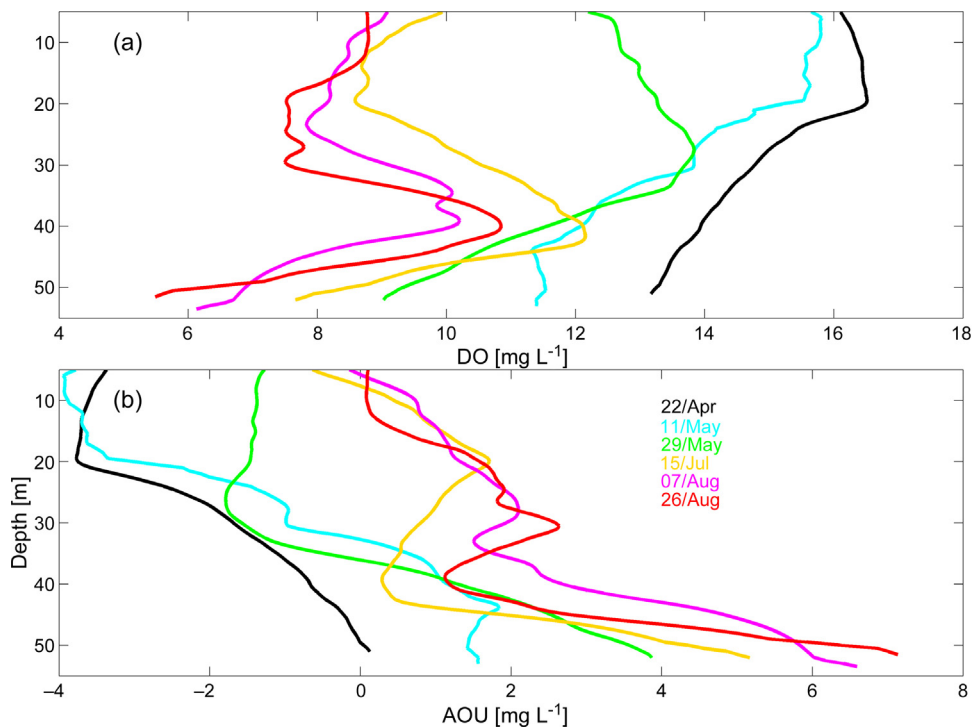


Figure 11 Dissolved oxygen content (a) and apparent oxygen utilization (AOU, b) profiles in the Ruhnu Deep stations in 2015. The location of stations is shown as orange circles in Fig. 1.

Likely, the salt maxima are intrusions of waters of different origin, e.g. as has been observed in the halocline of the Bornholm Basin in the vertical temperature distribution (e.g. Mohrholz et al., 2006). The only evidence of similar salt maxima in the GoR has been reported and measured earlier at two stations in the eastern part of the Irbe Strait by Stipa et al. (1999) on 29 August–1 September 1993. This observational evidence supports our suggestion that the patches of salt maxima enter the gulf via the Irbe Strait.

Episodic current measurements have revealed that the flow regime in the Irbe Strait is two-layered with an inflow in the deeper layer near the southern coast and an outflow along the northern coast (Lilover et al., 1998; Talpsepp, 2005). SW winds evoke upwelling in the Gulf of Riga side of the Irbe Strait along the Saaremaa Island and downwelling along the southern coast of the Irbe Strait. The upwelled Gulf of Riga water is replaced by the waters from the deeper layers of the Irbe Strait, which can be partly the salty and warm downwelling waters. The downwelling water mixes with the ambient Gulf of Riga sub-surface water and the outcome is the sub-surface salt maxima layer. The similar suggestion was drawn by Stipa et al. (1999) as well: downwelling depresses the seasonal pycnocline on the Baltic Proper side of the strait and creates a baroclinic pressure gradient along the strait, which might drive the Baltic Sea surface water, instead of the water below the seasonal pycnocline, into the Gulf of Riga. Stipa et al. (1999) suggested that downwelling occurred in the Baltic Proper along the Latvian coast in 1993 when they registered the salinity maxima in the area. The CTD-stations located closely to each other are to be sampled to check if only the baroclinic pressure gradient is needed (Stipa et al., 1999) for the

maxima layer generation, or also the cross-strait downwelling as we suggested in the present study plays a significant role here.

The salt maxima-favorable coupled upwelling–downwelling situation is evoked by SW winds. Comparison of wind conditions in July–August 2015 with the climatic averages (in July–August 1966–2015) shows that summer 2015 was not a very special year. The favorable SW winds (sector 180–270° was taken into account) occurred 39% of the time in July–August while the climatic occurrence of the wind from the same direction in July–August has been 41%. Likewise, the occurrence of strong SW winds (if only the winds with the speed of $>5 \text{ m s}^{-1}$ or $>10 \text{ m s}^{-1}$) in 2015 was close to climatic average.

The sub-surface salt maxima formation via the Suur Strait cannot be excluded. However Väinameri Archipelago is very shallow (mean depth 5 m) and large area between the open Baltic and GoR. Distance from 20 m isobath in the Baltic Proper through Väinameri to 20 m isobath in the GoR is ca 100 km. Thus, only very strong and long-lasting northerly wind impulse (Otsmann et al., 2001) could cause transport of saltier water via Väinameri Archipelago to the deeper parts of the Gulf of Riga. Temperature–salinity profiles during/after a northerly wind impulse are needed to check the possibility of this pathway.

The existence of fresher sub-surface waters found at the buoy station has also been predicted by numerical modeling (Lips et al., 2016c) in the western part of the gulf as a result of convergence between the low-salinity riverine waters transported from the southern part and waters from the Baltic Proper. The low salinity waters from the southern part of the Gulf of Riga can be transported as far as the buoy

station in the present study and even further to the north due to the prevailing whole-basin anticyclonic gyre with enhanced intensity of currents in the western part of the gulf during the summer period (Lips et al., 2016b).

Buoyant intrusions of inflowing waters are well-known features in the Western Baltic Sea. It is the water that has flown through the Danish Straits to the Baltic and which is not dense (light) enough to reach the bottom layers (to stay in the surface layer) of the Baltic. Buoyant temperature maxima form at the depths of the halocline in the Western Baltic if the baroclinic inflows occur during summer (e.g. Feistel et al., 2004). Note that in the Western Baltic case, the halocline (vertical salinity distribution) stabilizes the water column at the depth range of the temperature maxima while, in the Gulf of Riga case, it is the thermocline (temperature), which compensates the effect of the salinity decrease with the depth. Since the maxima formation is sensible to wind forcing, one might expect that the salt and water balance in the gulf will be impacted by the suggested wind regime changes in the future (Christensen et al., 2015).

Such buoyant inflow regime could be found in many semi-enclosed basins where a sill restricts the water exchange with the open sea with higher salinity/density. Currently, such regime is well known only in fjords (e.g. Belzile et al., 2016). In summer when the seasonal thermocline is present, certain forcing conditions could cause deepening of the upper mixed layer and the inflowing water originating from the surface (or thermocline) layer forms a buoyant salinity maximum in a basin.

The comparison of historical density data in the Gulf of Riga and Baltic Proper showed that the salt water maxima formation is feasible from June to September. Otherwise (in October–May), the Baltic Proper water dives to the near-bottom layer of the gulf and such intrusions do not appear. The seasonality in the water exchange regime was confirmed by an analysis of intrusion index: higher values have occurred from May to September. Thus, likely the maxima layer is a common feature of the gulf in summer and has not been noticed earlier (except at two stations by Stipa et al., 1999 in the Irbe Strait) due to very sparse data, which have been available.

The salinity measurements together with current measurements and high-resolution modeling are needed to estimate the role of sub-surface salinity maxima in the salt balance of the gulf. We checked the outputs of the existing operational models HIROMB-EST (Lagemaa, 2012), which uses the HIROMB-SMHI (Funkquist, 2001) model outcome at the open sea boundary, and the HBM (Berg and Poulsen, 2012). Both models did not capture the salt maxima formation and constantly underestimated salinity, by 0.6 g kg^{-1} on average, at least at the profiling location. It is worth to identify if the incapability of reproducing salt intrusions in the models might lead to a salinity underestimation in the whole gulf.

The AOU vs. salinity curves (Fig. 8) suggested that source water for the salt intrusion had almost saturated oxygen content. This result is not a surprise as the water was originating from the upper layer of the Baltic Proper. The Gulf of Riga has a high production (Seppälä and Balode, 1999) and high oxygen consumption (HELCOM, 2009) due to decomposition of organic material in the near-bottom layer. Lateral advection might be an important source of oxygen for the deep layers in the gulf, especially in summer, when strong

stratification impedes vertical mixing. However, if the inflowing saltier water does not reach the deeper bottom layers, the bottom remains isolated from this lateral advection of oxygen. Thus, the oxygen conditions in the near-bottom layer of the gulf strongly depend on the water exchange regime in the Irbe Strait. In summer 2015, the regime resulting in buoyant sub-surface saltwater intrusions prevailed, and the near-bottom layer of the gulf did not receive additional oxygen through the lateral advection. This suggestion can be confirmed by the six dissolved oxygen content and AOU profiles (Fig. 11) acquired from the Ruhnu Deep (Fig. 1) from April to August 2015.

Very high dissolved oxygen values were registered on 22 April. The oversaturation in the upper layer due to the spring bloom was up to 125% or 3.8 mg L^{-1} (shown as AOU negative values in Fig. 11b). Water was saturated in the deep layer indicating that winter convection reached the bottom. Oversaturation remained high in the upper layer, but already $1.4\text{--}1.9 \text{ mg L}^{-1}$ of oxygen was consumed in the deeper layer by 11 May. A continuous oxygen decline occurred from May to August in the deep layers and by the measurements on 26 August, the oxygen level was 5.5 mg L^{-1} at the temperature and salinity of 3.9°C and 6.0 g kg^{-1} , respectively. The estimated oxygen consumption (based on the AOU) from spring to the end of August had been 7.1 mg L^{-1} in the near-bottom layer. According to the HELCOM (2009), the oxygen decrease might lead to hypoxia in the Gulf of Riga but not every year.

5. Conclusions

- Occasionally very strong salinity maxima were observed in the sub-surface layer.
- The sub-surface salt maxima are intrusions of saline and warm water from the Baltic Proper.
- The potential mechanism of the maxima formation likely is a simultaneous upwelling and downwelling event in the Gulf of Riga side and open sea side of the strait, respectively.
- Due to the buoyant nature of the inflowing water, the near-bottom layer of the Gulf of Riga remains isolated from the lateral flows during summers.
- Latter favors the hypoxia formation in the Gulf of Riga.

Acknowledgments

This work was supported by institutional research funding IUT19-6 of the Estonian Ministry of Education and Research. We are thankful to N. Rünk for maintaining the thermosalinograph system. Likewise we thank Villu Kikas and Fred Buschmann for help in profiling system maintenance. We are thankful to Estonian Environmental Agency for providing coastal water temperature data and wind data time-series. We would like to thank participants of Estonian and Latvian national monitoring cruises in 2015 and the crew of RV Salme.

HELCOM data (<http://ocean.ices.dk/helcom>, 25 February 2016) and the level 3 SST (sea surface temperature) product over European Seas by Copernicus Marine Environment Monitoring Service (<http://marine.copernicus.eu/>) were used in the paper.

References

- Aigars, J., Poikane, R., Dalsgaard, T., Eglite, E., Jansons, M., 2015. Biogeochemistry of N, P and SI in the Gulf of Riga surface sediments: implications of seasonally changing factors. *Cont. Shelf Res.* 105, 112–120, <http://dx.doi.org/10.1016/j.csr.2015.06.008>.
- Alenius, P., Tikka, K., Barrera, C., 2014. Gliders for studies of multi-scale variability in the Baltic Sea. In: 6th IEEE/OES Baltic Int. Symp. (BALTIC) – Measuring and Modeling of Multi-Scale Interactions in the Marine Environment, Tallinn, Estonia, 26–29 May 2014, IEEE, 1–6, <http://dx.doi.org/10.1109/BALTIC.2014.6887867>.
- Apsite, E., Rudlapa, I., Latkovska, I., Elferts, D., 2013. Changes in Latvian river discharge regime at the turn of the century. *Hydrol. Res.* 44 (3), 554–569, <http://dx.doi.org/10.2166/nh.2012.007>.
- Astok, V., Otsmann, M., Suursaar, Ü., 1999. Water exchange as the main physical process in semi-enclosed marine systems: the Gulf of Riga case. *Hydrobiologia* 393, 11–18, <http://dx.doi.org/10.1023/A:1003517110726>.
- Barda, I., Purina, I., Rimsa, E., Balode, M., 2013. Seasonal dynamics of biomarkers in infaunal clam *Macoma balthica* from the Gulf of Riga (Baltic Sea). *J. Mar. Syst.* 129, <http://dx.doi.org/10.1016/j.jmarsys.2013.05.006>.
- Belzile, M., Galbraith, P.S., Bourgault, D., 2016. Water renewals in the Saguenay Fjord. *J. Geophys. Res. Oceans* 121 (1), 638–657, <http://dx.doi.org/10.1002/2015JC011085>.
- Berg, P., Poulsen, J.W., 2012. Implementation details for HBM. DMI Tech. Rep. No. 12-11. DMI, Copenhagen, 147 pp.
- Berzins, V., 1995. *Hydrology*. In: Ojaveer, O. (Ed.), *Ecosystem of the Gulf of Riga between 1920 and 1990*. Estonian Acad. Publ., Tallinn, 7–32.
- Christensen, O.-E., Kjellström, E., Zorita, E., 2015. Projected change – atmosphere. In: The BACC II Author Team (Eds.), *Second Assessment of Climate Change for the Baltic Sea Basin, Regional Climate Studies*. SpringerOpen, Geesthacht, 217–233, http://dx.doi.org/10.1007/978-3-319-16006-1_11.
- Eglite, E., Lavrinovic, A., Muller-Karulis, B., Aigars, J., Poikane, R., 2014. Nutrient turnover at the hypoxic boundary: flux measurements and model representation for the bottom water environment of the Gulf of Riga, Baltic Sea. *Oceanologia* 56 (4), 711–735, <http://dx.doi.org/10.5697/oc.56-4.711>.
- Feistel, R., Nausch, G., Heene, T., Piechura, J., Hagen, E., Sea, B., 2004. Evidence for a warm water inflow into the Baltic Proper in summer 2003. *Oceanologia* 46 (4), 581–598.
- Funkquist, L., 2001. HIROMB, an operational eddy-resolving model for the Baltic Sea. *Bull. Maritime Inst.* 28 (2), 7–16.
- Geyer, W.R., MacCready, P., 2014. The estuarine circulation. *Annu. Rev. Fluid Mech.* 46, 175–197, <http://dx.doi.org/10.1146/annurev-fluid-010313-141302>.
- HELCOM (Helsinki Commission), 2009. Eutrophication in the Baltic Sea: an integrated thematic assessment of the effects of nutrient enrichment in the Baltic Sea region. In: *Baltic Sea Environ. Proc.*, 115B, Helsinki Commission. 148 pp.
- Karstensen, J., Liblik, T., Fischer, J., Bumke, K., Krahnemann, G., 2014. Summer upwelling at the Boknis Eck time-series station (1982 to 2012) – a combined glider and wind data analysis. *Biogeosciences* 11 (13), 3603–3617, <http://dx.doi.org/10.5194/bg-11-3603-2014>.
- Laanejaru, J., Lips, U., Lundberg, P., 2000. On the application of hydraulic theory to the deep-water flow through the Irbe Strait. *J. Mar. Syst.* 25, 323–332.
- Lagemaa, P., 2012. Operational forecasting in Estonian marine waters. Tallinn Univ Tech., TUT Press, Tallinn, 130 pp.
- Lilover, M.J., Lips, U., Laanejaru, J., Liljebladh, B., 1998. Flow regime in the Irbe strait. *Aquat. Sci.* 60, 253–265.
- Lips, U., Kikas, V., Liblik, T., Lips, I., 2016a. Multi-sensor in situ observations to resolve the sub-mesoscale in the stratified Gulf of Finland, Baltic Sea. *Ocean Sci.* 12 (3), 715–732, <http://dx.doi.org/10.5194/os-12-715-2016>.
- Lips, U., Zhurbas, V., Skudra, M., Väli, G., 2016b. A numerical study of circulation in the Gulf of Riga, Baltic Sea. Part I: Whole-basin gyres and mean currents. *Cont. Shelf Res.* 112, 1–13, <http://dx.doi.org/10.1016/j.csr.2015.11.008>.
- Lips, U., Zhurbas, V., Skudra, M., Väli, G., 2016c. A numerical study of circulation in the Gulf of Riga. Baltic Sea. Part II: Mesoscale features and freshwater transport pathways. *Cont. Shelf Res.* 115, 44–52, <http://dx.doi.org/10.1016/j.csr.2015.12.018>.
- Matthäus, W., Nehring, D., Feistel, R., Nausch, G., Mohrholz, V., Lass, H.U., 2008. The inflow of highly saline water into the Baltic Sea. In: Feistel, R., Nausch, G., Wasmund, N. (Eds.), *State and Evolution of the Baltic Sea, 1952–2005*. Wiley, Hoboken, 265–309.
- Mohrholz, V., Dutz, G., Kraus, G., 2006. The impact of exceptional warm summer inflow events on the environmental conditions in the Bornholm Basin. *J. Mar. Syst.* 60 (3–4), 285–301, <http://dx.doi.org/10.1016/j.jmarsys.2005.10.002>.
- Mohrholz, V., Naumann, M., Nausch, G., Krüger, S., Gräwe, U., 2015. Fresh oxygen for the Baltic Sea—an exceptional saline inflow after a decade of stagnation. *J. Mar. Syst.* 148, 152–166, <http://dx.doi.org/10.1016/j.jmarsys.2015.03.005>.
- Müller-Karulis, B., Aigars, J., 2011. Modeling the long-term dynamics of nutrients and phytoplankton in the Gulf of Riga. *J. Mar. Syst.* 87 (3–4), 161–176, <http://dx.doi.org/10.1016/j.jmarsys.2011.03.006>.
- Omstedt, A., Axell, A., 2003. Modeling the variations of salinity and temperature in the large gulfs of the Baltic Sea. *Cont. Shelf Res.* 23 (3–4), 265–294, [http://dx.doi.org/10.1016/S0278-4343\(02\)00207-8](http://dx.doi.org/10.1016/S0278-4343(02)00207-8).
- Omstedt, A., Elken, J., Lehmann, A., Leppäranta, M., Meier, H.E.M., Myrberg, K., Rutgersson, A., 2014. Progress in physical oceanography of the Baltic Sea during the 2003–2014 period. *Prog. Oceanogr.* 128, 139–171, <http://dx.doi.org/10.1016/j.pocean.2014.08.010>.
- Otsmann, M., Suursaar, Ü., Kullas, T., 2001. The oscillatory nature of the flows in the system of straits and small semienclosed basins of the Baltic Sea. *Cont. Shelf Res.* 21 (15), 1577–1603, [http://dx.doi.org/10.1016/S0278-4343\(01\)00002-4](http://dx.doi.org/10.1016/S0278-4343(01)00002-4).
- Pitkänen, H., Lehtoranta, J., Räike, A., 2001. Internal nutrient fluxes counteract decreases in external load: the case of the estuarine eastern Gulf of Finland, Baltic Sea. *Ambio* 30 (4–5), 195–201.
- Purokoski, T., Eemeli, A., Nummelin, A., 2013. First long-term deployment of Argo float in Baltic Sea Argo's Inaugural operation in shallow, low-salinity water. *Sea Technol.* 54 (10), 41–44.
- Raudsepp, U., 2001. Interannual and seasonal temperature and salinity variations in the Gulf of Riga and corresponding saline water inflow from the Baltic Proper. *Hydrol. Res.* 32 (2), 135–160.
- Reissmann, J.H., Burchard, H., Feistel, R., Hagen, E., Lass, H.-U., Mohrholz, V., Nausch, G., Umlauf, L., Wiczorek, G., 2009. Vertical mixing in the Baltic Sea and consequences for eutrophication—a review. *Prog. Oceanogr.* 82 (1), 47–80, <http://dx.doi.org/10.1016/j.pocean.2007.10.004>.
- Seinä, A., Palosuo, E., 1996. The classification of the maximum annual extent of ice cover in the Baltic Sea 1720–1995. In: *MERI: Report Series of the Finnish Institute of Marine Research*, vol. 27. 79–91.
- Seppälä, J., Balode, M., 1999. Spatial distribution of phytoplankton in the Gulf of Riga during spring and summer stages. *J. Mar. Syst.* 23 (1), 51–68, [http://dx.doi.org/10.1016/S0924-7963\(99\)00050-0](http://dx.doi.org/10.1016/S0924-7963(99)00050-0).
- Skudra, M., Lips, U., 2016. Characteristics and inter-annual changes in temperature, salinity and density distribution in the Gulf of Riga. *Oceanologia* 59 (1), 37–48, <http://dx.doi.org/10.1016/j.oceano.2016.07.001>.
- Stipa, T., Tamminen, T., Seppälä, J., 1999. On the creation and maintenance of stratification in the Gulf of Riga. *J. Mar. Syst.* 23 (1–3), 27–49, [http://dx.doi.org/10.1016/S0924-7963\(99\)00049-4](http://dx.doi.org/10.1016/S0924-7963(99)00049-4).

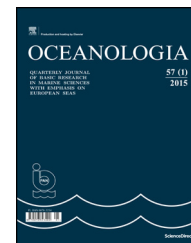
- Talpsepp, L., 2005. Coherent current oscillations and water exchange in the straits of the Gulf of Riga. *Oceanologia* 47 (2), 115–127.
- Uotila, P., Vihma, T., Haapala, J., 2015. Atmospheric and oceanic conditions and the extremely low Bothnian Bay sea ice extent in 2014/2015. *Geophys. Res. Lett.* 42 (18), 7740–7749, <http://dx.doi.org/10.1002/2015GL064901>.
- Valle-Levinson, A., 2010. *Contemporary issues in Estuarine Physics*. Cambridge Univ. Press, Cambridge, 326 pp.
- Weiss, R.F., 1970. The solubility of nitrogen, oxygen and argon in water and seawater. *Deep-Sea Res.* 17 (4), 721–735.
- Westerlund, A., Tuomi, L., 2016. Vertical temperature dynamics in the Northern Baltic Sea based on 3D modelling and data from shallow-water Argo floats. *J. Mar. Syst.* 158, 34–44, <http://dx.doi.org/10.1016/j.jmarsys.2016.01.006>.
- Yurkovskis, A., 2004. Long-term land-based and internal forcing of the nutrient state of the Gulf of Riga (Baltic Sea). *J. Mar. Syst.* 50 (3–4), 181–197, <http://dx.doi.org/10.1016/j.jmarsys.2004.01.004>.



Available online at www.sciencedirect.com

ScienceDirect

journal homepage: www.journals.elsevier.com/oceanologia/



ORIGINAL RESEARCH ARTICLE

Morphometric variations in white seabream *Diplodus sargus* (Linneus, 1758) populations along the Tunisian coast

Myriam Kaouèche*, Lilia Bahri-Sfar, Ibtissem Hammami, Oum Kalthoum Ben Hassine

Département de Biologie, Unité de Recherche Biologie Intégrative et Ecologie Fonctionnelle et Evolutive des milieux Aquatiques, UR11ES08, Faculté des Sciences de Tunis, Université Tunis El Manar, Tunisia

Received 10 March 2016; accepted 24 October 2016
Available online 5 November 2016

KEYWORDS

Morphometric variation;
Diplodus sargus;
Siculo-Tunisian Strait;
Ecological features

Summary Morphometric characters of the white seabream *Diplodus sargus* (Linnaeus 1758) were compared among samples collected from six marine and lagoon sites along the Tunisian coast to elucidate the impact of the geographical barrier of the Siculo-Tunisian Strait and/or the lagoon environment in the morphological variation among the Tunisian white seabream population. Two morphometric descriptors (twenty-five Truss elements and six traditional measurements) were used to study the pattern of this morphological variation. Univariate analysis of variance revealed significant differences ($P < 0.001$) for both traditional and Truss variables. Multivariate analysis using the two morphometric descriptors detected a clear variation in the body shape between *D. sargus* populations along the Tunisian coast. All these analyses showed the distinctness of the sample from El Biban lagoon compared to the remaining ones. This discrimination was due to the head and the peduncle of the studied fish. Varying degrees of differences were also observed between northern and southern samples, and between the lagoon and the marine samples. The morphological variations of the head explain also the discrimination between the different lagoons samples. Observed morphological heterogeneity seems to be related to the impact of ecological factors.

© 2016 Institute of Oceanology of the Polish Academy of Sciences. Production and hosting by Elsevier Sp. z o.o. This is an open access article under the CC BY-NC-ND license (<http://creativecommons.org/licenses/by-nc-nd/4.0/>).

* Corresponding author.

E-mail addresses: myrka26@gmail.com (M. Kaouèche), lilia.bahri@gmail.com (L. Bahri-Sfar), hammamibtissem@gmail.com (I. Hammami), kalthoum.benhassine@gmail.com (O.K.B. Hassine).

Peer review under the responsibility of Institute of Oceanology of the Polish Academy of Sciences.



Production and hosting by Elsevier

<http://dx.doi.org/10.1016/j.oceano.2016.10.003>

0078-3234/© 2016 Institute of Oceanology of the Polish Academy of Sciences. Production and hosting by Elsevier Sp. z o.o. This is an open access article under the CC BY-NC-ND license (<http://creativecommons.org/licenses/by-nc-nd/4.0/>).

1. Introduction

Morphological studies have long been useful to delimit marine fish stocks and describe their spatial distribution (Ihssen et al., 1981; Palma and Andrade, 2002). Such knowledge is important to elaborate management strategies for a better exploitation of fish resources (Bailey, 1997). Morphological variations between fish populations may be induced by several environmental factors. Several works have demonstrated morphological divergence on different regions of the fish body in several marine fish species (Hammami et al., 2013; Mejri et al., 2012; Turan, 2004; Wainwright et al., 2004). Such discrepancy could be explained by intrinsic specificities of each kind of the aquatic environment offering different ecological niches (Hammami et al., 2013).

In fact, such variations may be considered as adaptive responses to environmental variation in order to maintain relative fitness (Thompson, 1991).

Morphometric studies are based on a set of measurements which are continuous data, revealing the size and shape variation (Turan, 1999). The development of image analysis systems has facilitated progress and diversification of morphometric methods (Cadrin and Friedland, 1999). Truss network (Strauss and Bookstein, 1982) has been described as an

approach which enables covering the entire fish body in a uniform network and increases the possibility of extracting shape differences among populations (Turan and Basusta, 2001). Numerous works have used Truss approach in order to detect variation among fish populations (Cabral et al., 2003; Erdogan et al., 2009; Hammami et al., 2011, 2013; Palma and Andrade, 2002; Silva, 2003; Turan, 2004; Turan et al., 2004, 2005, 2006).

Sparid fishes are widespread in the Mediterranean Sea. Most of them are overexploited. The white seabream *Diplodus sargus* (Linnaeus, 1758) is one of the most important commercial seabream species in the Mediterranean Sea (Fischer et al., 1987). It lives in coastal rocky reef areas and coastal lagoons. Despite its great ecological and economic importance, and its large geographic distribution (Fischer et al., 1987), a few works have been carried out on Atlantic and Mediterranean white seabream populations focusing on their morphological variations (Palma and Andrade, 2002). Studied populations from the northern Mediterranean shores and the Atlantic ones showed some morphological dissimilarity between them. However, investigations are scarce along the southern Mediterranean shores, which are of a major importance as these shores extend over the two parts of the Siculo-Tunisian Strait.

Table 1 Sample locations of specimens of *Diplodus sargus* and main environmental features of sites. MSL \pm SE: mean standard length \pm standard error.

Geographic location	North of the Siculo-Tunisien Strait			South of the Siculo-Tunisien Strait		
	Bizertalagoon	Bizerta	Ghar El Melhlagoon	Mahdia	Gabes Gulf	El Bibanlagoon
Sites code	BIZL	BIZM	GEML	MAHM	GABM	BIBL
Environment type	Lagoon	Marine	Lagoon	Marine	Marine	Lagoon
Sample size	28	37	26	28	30	25
MSL [cm] \pm SE	13.3 \pm 0.7	13.8 \pm 0.9	14.9 \pm 1.2	14.5 \pm 1.3	11.3 \pm 0.2	14.8 \pm 0.6
Geographic coordinates	37°14'N 9°46'E	37°16'60" N 9°58'0" E	37°10'N 10°11'E	35°30' N 11°04' E	34°04'48" N 10°28'36" E	33°16' N 11°17' E
Vegetation	<i>Cymodocea nodosa</i> <i>Zostera noltii</i> <i>Zostera marina</i>	Posidonia Caulerpa <i>Jania rubens</i> (Molinier and Picard, 1954)	- <i>Ruppia cirrhosa</i> - <i>Cladophora</i> sp. (Moussa et al., 2005)	Phanerogams and Algae (Ben Hassine et al., 1999)	- <i>Cymodocea</i> - <i>Posidonia</i> - <i>Caulerpa</i> (Ben Othman, 1971)	- <i>Zostera noltii</i> - <i>Cymodocea nodosa</i> - <i>Caulerpa prolifera</i> - <i>Lithothamnium</i> sp. (Guelorget et al., 1982)
Tide	10–12 cm (Harzallah, 2003)	0.40 m (Blanco, 1992)	0.08–0.22 m (Moussa et al., 2005)	\approx 20 cm	2 m (Mensing, 1968)	\pm 0.5 m (max \approx 1 m) (Lemoalle and Vidy, 1984)
Currentology	Mediterranean Atlantic Water (Astraldi et al., 1999)	Mediterranean Atlantic Water (Astraldi et al., 1999)	Mediterranean Atlantic Water (Astraldi et al., 1999)	Levantine Intermediate water (Astraldi et al., 1999)	Levantine Intermediate water (Astraldi et al., 1999)	Levantine Intermediate water (Astraldi et al., 1999)
Temperature	13–32.5°C	21–22°C (low depths) 15–16°C (deep)	10.3–29.7°C (Ben Hassine, 1983)	15–25°C (Zakhama et al., 2005)	\approx 21.45°C (Drira; 2009)	13–30°C (Neifar, 2001)
Salinity	32–38.5‰	\approx 37‰	36–51‰ (Moussa et al., 2005)	\approx 37.1‰	38–39‰ (Hamza, 2003)	45–50‰ (Neifar, 2001)

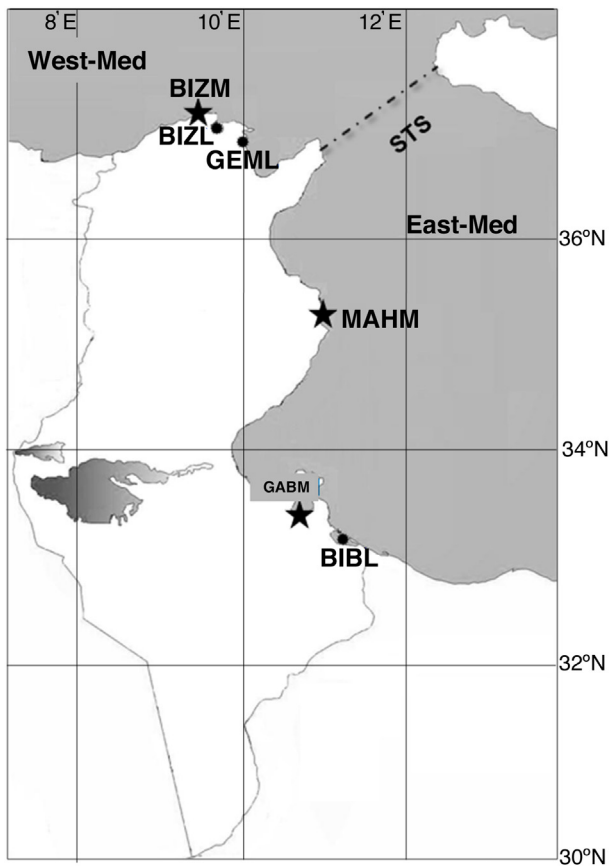


Figure 1 Location of sampling sites along the Tunisian coasts. ★: marine samples. ●: lagoon samples. BIZM: Bizerta, MAHM: Mahdia, GABM: Gabès Gulf, BIZL: Bizerta lagoon, GEML: Ghar El Melh lagoon and BIBL: El Biban lagoon. STS: Siculo-Tunisian Strait. West-Med: Western Mediterranean basin. East-Med: Eastern Mediterranean basin.

Indeed, Tunisian shores are a boundary area between eastern and western Mediterranean basins containing numerous lagoons. Such geographic position gives them a status of important ecological niche, which provides bio-diversity to Tunisian coasts resulting in a correlation with the morphology of fish populations. In this paper, the aim is to investigate the spatial morphological variation of *D. sargus* populations along the Tunisian coastline. Sampling was done among six localities characterised by different environmental features (Table 1, Fig. 1) using Truss network system (Strauss and Bookstein, 1982) and with some traditional measurements.

2. Material and methods

Samples were collected from six localities distributed along the Tunisian coast from June 2006 to January 2008. This sampling covered the north-eastern (Bizerta, Bizerta lagoon and Ghar El Melh lagoon) and the south-eastern (Mahdia, Gabès Gulf and El Biban lagoon) sectors. These localities differ by their environmental features such as temperature, salinity and currents (Fig. 1; Table 1).

Fishing gear used included trammel nets, long lines and weir. The sample sizes ranged from 25 to 37 individuals in each locality.

Morphological analysis has been significantly enhanced by image processing techniques, which have become a powerful tool that can complement other approaches to stock identification (Cadrin and Friedland, 1999). In order to describe the shape of fish, the Truss approach was used to create a network of fish body (Strauss and Bookstein, 1982). The left side of each fish, with the fins in the extended position, was photographed with a high quality digital camera mounted on a tripod. The landmark method is based on placing several homologous points called “landmarks” on the most important locations of the body shape image. Morphological landmarks were selected around the outline of the fish form (Turan, 1999). Landmark coordinates were performed on digital images using Visilog 6.480 software. The x and y coordinates of landmarks were chosen and recorded in agreement with the current literature (Loy et al., 2000; Palma and Andrade, 2002; Sara et al., 1999; Turan, 2004). To test the precision of landmarks placing, we have digitised one specimen from each sample twenty times and calculated the error variance for each variable. Eleven landmarks, which permitted the plotting of 25 measurements, were recorded (Fig. 2, Table 2). Six traditional measurements were added to our data set (Fig. 2; Table 2), which are:

- the eye diameter (\varnothing_{eye} : 13–14),
- the snout length ($leng_m$: 1–12),
- the operculum length ($leng_{op}$: 1–15),
- the distance between the operculum and the upper part of the head ($dist_{uh-op}$: 2–15),
- the distance between the operculum and the lower part of the head ($dist_{lh-op}$: 11–15),
- the length of the pectoral fin base ($leng_{pec-b}$: 16–17).

Size-dependent variation of morphometric characters was corrected using the allometric transformation given by Reist (1985): $M_{trans} = \log M - \beta (\log SL - \log SL_{mean})$, where M_{trans} is the transformed measurement, M is the original measurement, β is the within-group slope regressions of $\log M$ against $\log SL$, SL is the standard length of the fish and SL_{mean} is the overall mean of the standard length.

Truss and traditional measurements were analysed separately. ANOVA F -test was performed to examine the statistical significance of each measurement variation among the studied samples. In addition, the t -test was established to verify whether the averages of one variable are significantly different between two considered samples.

The discriminant function analysis (DFA) (Ramsay et al., 2009) was used to assess the pattern of morphological variation between samples and to reveal the degree of similarities or differences between the studied samples and the relative importance of each measurement for group separation. Wilks' λ (Everitt and Dunn, 1991) values were estimated to test the significance of observed discrimination for a combination of variables. The classification success rate (PCS) was evaluated based on the percentage of individuals correctly assigned into the original sample. All morphometric measurements and statistical analyses were performed using R 2.11.1 software.

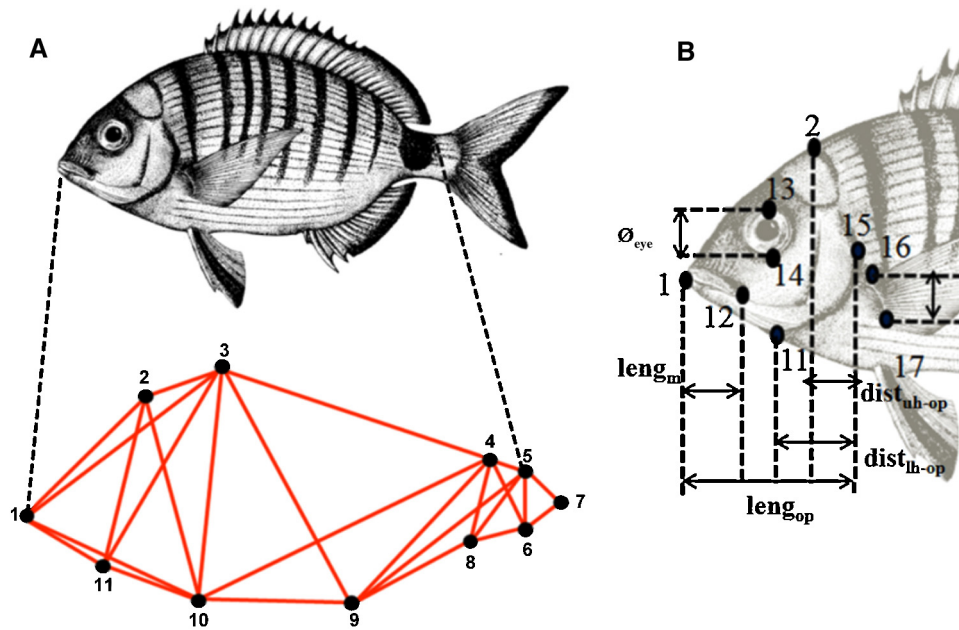


Figure 2 Location of landmarks (1–11) and additional points (12–17). Lines indicate the morphometric measures used for constructing Truss network on *Diplodus sargus*. Landmarks were illustrated as black dots. \varnothing_{eye} : 13–14: the eye diameter; $leng_m$: 1–12: the snout length; $leng_{op}$: 1–15: the operculum length; $dist_{uh-op}$: 2–15: the distance between the operculum and the upper part of the head; $dist_{lh-op}$: 11–15: the distance between the operculum and the lower part of the head; $leng_{pec-b}$: 16–17: the length of the pectoral fin base.

3. Results

3.1. Traditional measurements

The analysis of variance of the 6 traditional measurements revealed significant differences ($P < 0.001$) between samples at all variables (Table 2). The projection of all samples on DF1–DF2 plane showed the discrimination of the two lagoon samples, Bizerta lagoon in the north and El Biban lagoon in the south (Fig. 3). All other samples showed moderate overlapping (Fig. 3).

The significance of this morphological distinction was indicated by Wilk's criterion (Wilk's $\lambda = 0.1263$, $F = 14.491$, $P < 0.001$). The overall assignment of individuals into their original sample (PCS) was 65.5%. These values ranged from 50% for Ghar El Melh lagoon sample to 92% for El Biban one (Table 3). Such discrimination seemed to be defined by two measurements: the operculum length ($leng_{op}$) and the eye diameter (\varnothing_{eye}) (Table 2).

For a better understanding of the observed morphometric variation, we projected separately marine and lagoon samples. The plot obtained with DF1 and DF2 for the three lagoon samples (BIZL, GEML and BIBL) showed a significant discrimination (Wilk's $\lambda = 0.1138$, $F = 22.249$, $P < 0.001$) between northern (BIZL and GEML) and southern (BIBL) samples (Fig. 4a). The overall assignment of individuals into their original sample (PCS) was 90%. These values ranged from 89% for Ghar El Melh and Bizerta lagoons (GEML and BIZL) to 92% for El Biban lagoon sample (BIBL) (Table 4). Such distinction was again related to the operculum length ($leng_{op}$) and the eye diameter (\varnothing_{eye}) (Table 2). The t -test calculated between lagoon samples showed that El Biban lagoon has the lowest

average of the \varnothing_{eye} ($t_{GEML-BIBL} = 18.266$, $P < 0.01$ and $t_{BIZL-BIBL} = 23.171$, $P < 0.01$).

Across DF2, we observed a moderate discrimination between Ghar El Melh and Bizerta lagoon samples which is related to the variable $dist_{hl-op}$ (the distance between the operculum and the lower head part: 11–15).

The projection of the marine samples showed a partial overlapping between them with a slight discrimination (Wilk's $\lambda = 0.4193$, $F = 7.8903$, $P < 0.001$) of Bizerta sample (BIZM) highlighted by DF1 (Fig. 4b). The overall assignment of individuals into their original sample (PCS) was 73.36%. These values ranged from 67% to 79% (Table 5). Such distinction seems to be related to two traditional measurements, the snout length ($leng_s$: 1–12) and the distance between the operculum and the lower part of the head ($dist_{hl-op}$: 11–15).

3.2. Truss measurements

Twenty-five distances which define a network between the 11 homologous points were taken into consideration (Fig. 2). The variance analysis of these measurements revealed significant differences across mean values ($P < 0.001$) between samples for 23 variables (Table 2). The projection of all samples on DF1-DF2 plane showed a clear distinction between three groups (Fig. 5). The first one was formed by El Biban lagoon sample (BIBL) which showed a clear discrimination from all other samples (Wilk's $\lambda = 0.0069$, $F = 9.7553$, $P < 0.001$). The second group gathers the north-eastern samples (BIZM, BIZL and GEML) and the third one is made up of the south-eastern samples (Mahdia and Gabes gulf) across DF1 (Fig. 5). The overall assignment of

Table 2 Loadings from discriminant function of the 31 morphometric characters (25 Truss elements and 6 traditional measurements) for *Diplodus sargus*.

Samples	All samples			Lagoon samples			Marine samples		
	DF1	DF2	F	DF1	DF2	F	DF1	DF2	F
<i>Traditional measurements</i>									
	49.78%	21.43%		72.9%	27.1%		60.56%	39.44%	
leng _s : 1–12	−0.307	−0.325	10.776 ^{***}	−0.480	0.349	10.956 ^{***}	−0.620	0.040	8.933 ^{***}
leng _{op} : 1–15	−0.732	−0.189	29.193 ^{***}	−0.874	−0.183	67.493 ^{***}	−0.047	−0.019	0.048 ^{ns}
dist _{hu-op} : 2–15	0.423	0.066	13.701 ^{***}	0.547	0.015	12.183 ^{***}	−0.186	0.798	10.786 ^{***}
dist _{ht-op} : 11–15	−0.712	−0.664	33.477 ^{***}	−0.823	−0.535	69.415 ^{***}	−0.517	−0.546	11.149 ^{***}
Ø _{eye} : 13–14	−0.702	0.191	26.026 ^{***}	−0.854	0.139	58.33 ^{***}	0.263	0.505	5.078 ^{**}
dist _{base-pec} : 16–17	0.059	−0.375	4.390 ^{***}	0.003	−0.361	1.545 ^{***}	−0.442	0.279	5.346 ^{**}
	DF1	DF2	F	DF1	DF2	F	DF1	DF2	F
<i>Truss measurements</i>									
	29.22%	24.48%		54.47%	45.52%		55.49%	44.50%	
V1: 1–2	−0.559	0.318	28.827 ^{***}	−0.442	−0.483	21.682 ^{***}	0.686	0.070	36.479 ^{***}
V2: 2–3	0.651	−0.076	21.901 ^{***}	0.710	0.011	33.829 ^{***}	−0.572	−0.005	20.219 ^{***}
V3: 3–4	−0.526	0.360	18.880 ^{***}	−0.374	0.002	5.615 ^{***}	0.661	0.060	32.077 ^{***}
V4: 4–5	0.705	−0.366	41.543 ^{***}	0.641	−0.047	23.612 ^{***}	−0.792	−0.091	66.356 ^{***}
V5: 5–7	−0.368	0.195	14.588 ^{***}	−0.351	0.410	12.239 ^{***}	0.331	0.379	12.220 ^{***}
V6: 7–6	−0.820	0.297	77.389 ^{***}	−0.780	−0.146	54.082 ^{***}	0.892	0.041	132.95 ^{***}
V7: 6–8	0.695	−0.177	33.32 ^{***}	0.634	0.231	27.044 ^{***}	−0.755	−0.157	56.338 ^{***}
V8: 8–9	0.091	0.359	4.290 ^{**}	0.426	0.074	7.87 ^{***}	0.257	−0.053	3.149 [*]
V9: 9–10	−0.477	−0.398	17.51 ^{***}	−0.678	0.064	28.89 ^{***}	0.054	0.331	4.266 [*]
V10: 10–11	0.030	−0.299	15.496 ^{***}	−0.113	−0.428	6.860 ^{**}	−0.063	−0.321	4.055 [*]
V11: 11–1	−0.233	0.516	23.42 ^{***}	0.075	0.432	6.644 ^{**}	0.533	0.112	17.439 ^{***}
V12: 2–11	−0.696	0.344	46.199 ^{***}	−0.666	−0.179	29.660 ^{***}	0.775	0.002	58.438 ^{***}
V13: 11–3	−0.462	0.342	18.089 ^{***}	−0.284	−0.418	10.062 ^{***}	0.644	−0.076	29.634 ^{***}
V14: 3–10	−0.436	0.301	12.457 ^{***}	−0.303	−0.139	4.181 [*]	0.570	−0.116	20.934 ^{***}
V15: 10–4	−0.679	−0.181	26.905 ^{***}	−0.732	0.087	39.056 ^{***}	0.549	0.132	19.208 ^{***}
V16: 4–8	−0.521	0.022	12.027 ^{***}	−0.551	0.066	15.135 ^{***}	0.436	0.175	11.531 ^{***}
V17: 8–5	−0.257	−0.002	4.892 ^{***}	−0.338	0.326	8.766 ^{***}	0.436	0.175	1.410 ^{ns}
V18: 5–6	−0.787	0.225	57.018 ^{***}	−0.776	−0.104	51.016 ^{***}	0.119	0.148	80.174 ^{***}
V19: 6–4	−0.202	−0.064	3.321 ^{**}	−0.325	−0.194	5.499 ^{**}	0.794	0.251	1.865 ^{ns}
V20: 4–9	−0.257	0.516	13.341 ^{***}	0.143	0.266	3.001 ^{ns}	0.050	0.221	19.261 ^{***}
V21: 9–3	−0.461	0.296	15.553 ^{***}	−0.369	0.029	5.497 ^{**}	0.558	0.076	19.02 ^{***}
V22: 5–9	0.284	0.300	6.646 ^{***}	0.566	0.261	20.520 ^{***}	0.528	0.207	0.033 ^{***}
V23: 10–1	−0.183	0.310	4.777 ^{***}	0.067	−0.090	0.398 ^{ns}	−0.024	−0.014	10.812 ^{***}
V24: 2–10	−0.535	0.327	19.741 ^{***}	−0.462	−0.143	10.292 ^{***}	0.426	−0.166	26.364 ^{***}
V25: 1–3	−0.088	0.408	13.812 ^{***}	0.209	−0.603	18.121 ^{***}	0.621	−0.080	9.464 ^{***}

F: F-test's values, significance levels of F-test's P-values:

* $P < 0.05$.

** $P < 0.01$.

*** $P < 0.001$.

Bold text: variables related to discriminations. Ø_{eye}: 13–14: the eye diameter; leng_m: 1–12: the snout length; leng_{op}: 1–15: the operculum length; dist_{uh-op}: 2–15: the distance between the operculum and the upper part of the head; dist_{ht-op}: 11–15: the distance between the operculum and the lower part of the head; leng_{pec-b}: 16–17: the length of the pectoral fin base.

individuals into their original sample (PCS) was 86.33%. These values ranged from 82% for Bizerta marine sample to 93% for Gabes Gulf sample (Table 3). The discrimination between the north-eastern and the south-eastern samples seems to be mainly related to two Truss measurements, V6 and V18 (Table 2), defining the posterior body part (Fig. 2). The application of *t*-test between all samples showed that El Biban lagoon has the highest average of V6 compared to Bizerta and Ghar El Melh lagoon samples ($t_{\text{BIBL-BIZL}} = 97.790$, $P < 0.001$ and $t_{\text{BIBL-GEML}} = 30.725$, $P < 0.001$) whereas Bizerta

marine sample showed a lower average than Mahdia and Gabes Gulf samples ($t_{\text{MAHM-BIZM}} = 27.558$, $P < 0.001$ and $t_{\text{GABM-BIZM}} = 37.221$, $P < 0.001$).

For V18 variable, which is related to peduncle height, Bizerta marine specimens seemed to have the highest average compared to Mahdia marine sample ($t_{\text{BIZM-MAHM}} = 7.906$, $P < 0.01$). The *t*-test was also significant between El Biban and the two northern lagoons and showed that El Biban lagoon specimens have the highest average of V18 ($t_{\text{BIBL-BIZL}} = 44.514$, $P < 0.001$ and $t_{\text{BIBL-GEML}} = 9.178$, $P < 0.01$).

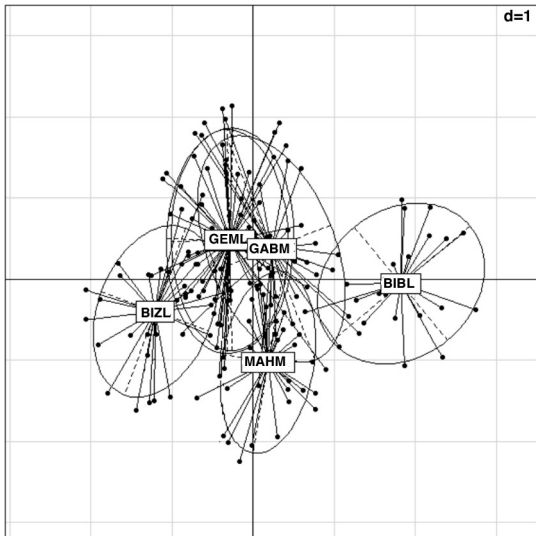


Figure 3 Plot of the first two discriminant functions of DFA scores with all samples using traditional measurements. BIZM: Bizerta, MAHM: Mahdia, GABM: Zarzis, BIZL: Bizerta lagoon, GEML: Ghar El Melh lagoon, BIBL: El Biban lagoon.

El Biban lagoon was discriminated from all other samples by DF2 and such distinction was mainly explained by the V11 variable which is related to the head length.

The plot obtained with DF1 and DF2 for lagoon samples showed a clear significant discrimination between them (Fig. 6a) (Wilk's $\lambda = 0.0174$, $F = 12.875$, $P < 0.001$). The overall assignment of individuals into their original sample (PCS) was 98.83% whereas values ranged from 97% to 100% (Table 4). Across DF1, the distinction of El Biban lagoon sample from Bizerta and Ghar El Melh lagoons seemed to be related again to V6 and V18 (peduncle region) (Table 2). The observed discrimination between Ghar El Melh and Bizerta lagoon samples, highlighted along DF2, seemed to be related to V25 variable which defines the head length (pre-dorsal

Table 3 Correct classification of all individuals into their original group using traditional and Truss measurements. BIZM: Bizerta, MAHM: Mahdia, ZARM: Zarzis, BIZL: Bizerta lagoon, GEML: Ghar El Melh lagoon and BIBL: El Biban lagoon.

Sample	BIBL	BIZL	BIZM	GEML	MAHM	GABM
<i>Traditional measurements</i>						
BIBL	92	0	0	0	0	8
BIZL	0	65	32	4	0	0
BIZM	0	6	58	13	10	13
GEML	0	0	4	50	46	0
MAHM	0	0	7	4	68	21
GABM	0	3	20	3	14	60
<i>Truss measurements</i>						
BIBL	92	0	0	0	8	0
BIZL	0	86	7	7	0	0
BIZM	0	8	82	10	0	0
GEML	0	0	15	80	4	0
MAHM	4	0	0	0	85	11
GABM	0	0	0	0	7	93

Bold text: Percentage of individuals correctly classified in their original group.

length) (Table 2). In fact, Ghar El Melh lagoon specimens showed the highest average of V25 ($t_{GEML-BIZL} = 21.734$, $P < 0.001$, $ddl = 55$).

The spatial projection of the marine samples on the factorial plane defined by the two first functions (DF1 and DF2) showed also a total discrimination (Wilk's $\lambda = 0.0271$, $F = 13.793^{***}$, $P < 0.001$) between northern and southern samples (Fig. 6b). The discrimination of Bizerta marine sample (BIZM) was highlighted by DF1. The overall assignment of individuals into their original sample (PCS) was 95.33%. These values ranged from 97% to 100%. This distinction seemed to be attributed to three Truss elements (V4, V6 and V18) which define the posterior body part (Table 2). Along the DF2, the two south-eastern samples, Mahdia and Gabes

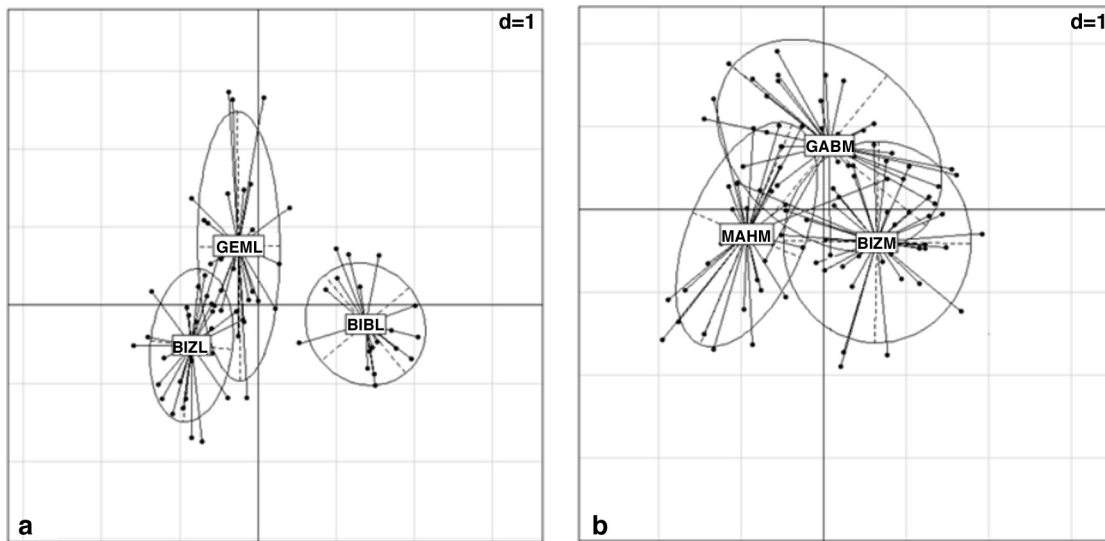


Figure 4 Plot of the first two discriminant functions of DFA scores with lagoon (a) and marine (b) samples using traditional measurements. BIZM: Bizerta, MAHM: Mahdia, GABM: Zarzis, BIZL: Bizerta lagoon, GEML: Ghar El Melh lagoon, BIBL: El Biban lagoon.

Table 4 Correct classification of lagoon individuals into their original group using traditional and Truss measurements. BIZM: Bizerta, MAHM: Mahdia, ZARM: Zarzis, BIZL: Bizerta lagoon, GEML: Ghar El Melh lagoon and BIBL: El Biban lagoon.

Sample	BIBL	BIZL	GEML
<i>Traditional measurements</i>			
BIBL	92	8	0
BIZL	0	89	11
GEML	0	11	89
<i>Truss measurements</i>			
BIBL	100	0	0
BIZL	0	97	3
GEML	0	0	100

Bold text: Percentage of individuals correctly classified in their original group.

Gulf, were discriminated (Fig. 6b). Such variation was explained by V5 which define the posterior part of the body (Table 2). Moreover, the application of the *t*-test showed that El Mahdia specimens have the highest averages of V5 ($t_{\text{MAHM-GABM}} = 11.809$, $P < 0.05$, $ddl = 59$).

4. Discussion

The morphometric analysis of six samples of *D. sargus* along Tunisian coasts revealed the discrimination of El Biban lagoon sample from all the remaining ones. This discrimination was highlighted with the two approaches. Different degrees of divergence were also detected between northern and southern samples, and between lagoon and marine samples. Several variables were implicated in this dissimilarity. These variables are mainly related to the head and the posterior part of the body.

Generally, fish exhibit greater morphological variability than other invertebrates and seem to be more sensitive to environmental fluctuations (Allendorf, 1988; Dunham et al., 1979; Thompson, 1991; Wimberger, 1992). Such variability

Table 5 Correct classification of marine individuals into their original group using traditional and Truss measurements. BIZM: Bizerta, MAHM: Mahdia, ZARM: Zarzis, BIZL: Bizerta lagoon, GEML: Ghar El Melh lagoon and BIBL: El Biban lagoon.

Sample	BIZM	MAHM	GABM
<i>Traditional measurements</i>			
BIZM	79	8	13
MAHM	4	75	21
GABM	20	13	67
<i>Truss measurements</i>			
BIZM	100	0	0
MAHM	0	89	11
GABM	0	3	97

Bold text: Percentage of individuals correctly classified in their original group.

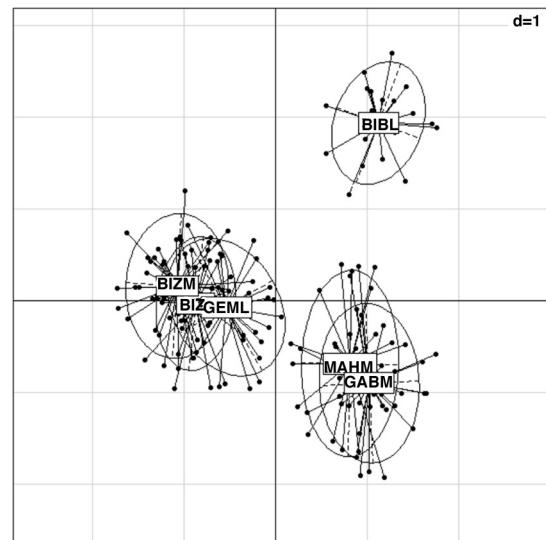


Figure 5 Plot of the first two discriminant functions of DFA scores with all samples using Truss measurements. BIZM: Bizerta, MAHM: Mahdia, GABM: Zarzis, BIZL: Bizerta lagoon, GEML: Ghar El Melh lagoon, BIBL: El Biban lagoon.

may be the result of different selective regimes generated by the type of habitat where the fish live (Slatkin, 1985; Swain and Foote, 1999) creating environmental discriminations. Indeed, sampling localities have different environmental features (Table 1) which may cause morphological adaptations. Several studies have demonstrated the relationships between morphological and functional traits of fish and ecological niches (Albouy et al., 2011; Farré et al., 2013; Price et al., 2011), e.g. body-shape adaptation to microhabitat utilisation.

Therefore, the divergence between El Biban sample and other samples seemed to be related to several measurements accounted for by the head (leng_{op} , \varnothing_{eye} and V11) and the posterior body part (V6 and V18). The same statement was raised by Palma and Andrade (2002). They showed a morphometric divergence between northern Mediterranean *D. sargus* samples and Atlantic ones related particularly to the head variables. These authors attributed the observed dissimilarity to environmental conditions and to ecological niches. They implied also the contribution of the natural geographical barriers, such as the Gibraltar Strait, to the emergence of differences between populations.

Indeed, morphometric variation results from differences in developmental rates and how the population responds to varying environmental conditions (Burns et al., 2009; Cachéra, 2013; Turan et al., 2004). Thus, the head morphological variation can be related to feeding behaviours (Delariva and Agostinho, 2001; Hyndes et al., 1997) or the exploitation of different ecological niches with different types of prey. El Biban lagoon specimens were characterised by a smaller head than the other populations. El Biban lagoon ecosystem presents some physicochemical particularities such as its high salinity (45–50‰; Neifar, 2001), its large size (30,000 ha) and its sandy bottom. These characteristics can offer a particular ecological niche to El Biban lagoon explaining such discrimination of specimens providing from it. The special hydrodynamic system in the south of Tunisia

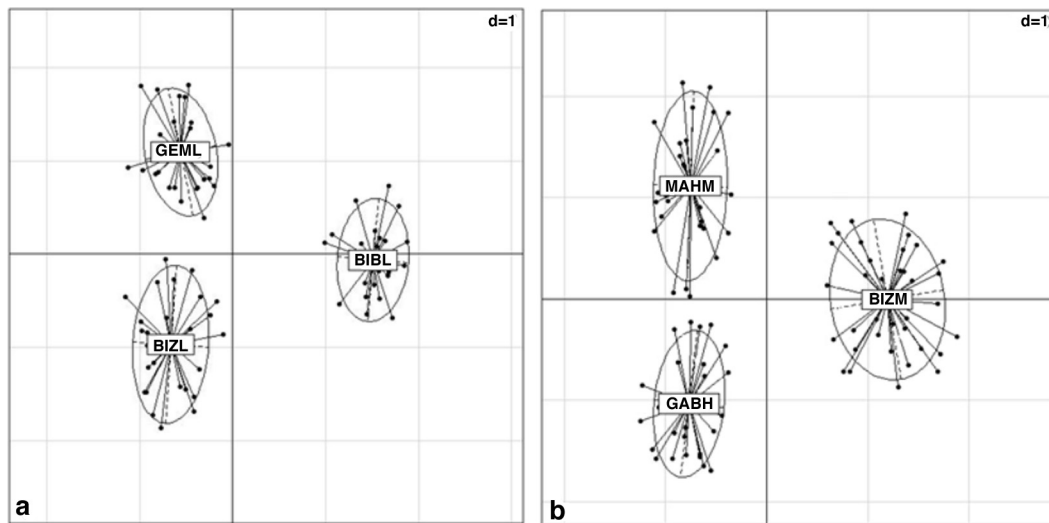


Figure 6 Plot of the first two discriminant functions of DFA scores with lagoon (a) and marine (b) samples using Truss measurements. BIZM: Bizerta, MAHM: Mahdia, GABM: Zarzis, BIZL: Bizerta lagoon, GEML: Ghar El Melh lagoon, BIBL: El Biban lagoon.

can also explain the observed variation especially at the posterior body part.

The morphological head variability explains also the discrimination between lagoons and was indicated by both approaches ($leng_{op}$, \emptyset_{eye} , $dist_{hl-op}$ and V25). This seemed to be related to intrinsic environmental characteristics of each lagoon ecosystem such as physico-chemical conditions, substrate nature and type and size of prey.

Moreover, coastal lagoon ecosystems are characterised by particular physical features (shallowness, relative isolation from the open, variable physical and ecological gradients) which create different types of habitat compared to those of the open sea (Pérez-Ruzafa et al., 2007). In addition, lagoons are richer nutritional areas that are often used as nursery areas, allowing fish larvae to develop and grow (Çoban et al., 2008). It is known that the environmental conditions influence morphometric characters (Swain and Foote, 1999) and during these early life stages, morphology is especially dependent on environmental conditions (Cheverud, 1988; Ryman et al., 1984).

Several studies showed an important variation of the head morphology. The discrimination between European samples of *Diplodus puntazzo* was also attributed to the head morphology (Palma and Andrade, 2002). Turan (2004) also associated the differentiation within Turkish *Trachurus mediterraneus* samples to head characters. Recently, the significant morphological divergence between lagoon and marine samples of Tunisian *Lithognathus mormyrus* populations was also attributed to the head morphology (Hammami et al., 2011, 2013).

The discrimination between the northern and the southern samples seemed to be particularly associated with the posterior body part especially to the peduncle region (V4, V6 and V18). This results mostly related to the swimming behaviour of the fish which varies according to species and to hydrodynamic constraints (e.g. water currents) (Costa and Cataudella, 2007). In fact, the southern marine area of Tunisia presents a complex hydrology with four different types of currents (Serbaji, 2000). The most important one

is the high tidal current which creates considerable sea level oscillations (Illou, 1999; Sammari et al., 2006). This region is also characterised by particular physico-chemical features, resembling closely features of the eastern Mediterranean waters rather than the western ones. Such characteristics can instigate morphological differences between populations. These results present environmental influences as a selective pressure on the morphology of body parts like the head or the peduncle.

However, morphological divergences among fish populations can be related to genetic differentiation or interaction between environmental and genetic components (Cabral et al., 2003; Favaloro and Mazzola, 2006). For several species, morphological divergences are associated with genetic differentiation (Bergek and Bjorklund, 2009; Lin et al., 2008). Sometimes, this kind of variation may not be directly caused by genetic factors (Ihsen et al., 1981; Turan, 1999). This seems to be the case with our data, as it cannot be explained by the genetic component because of the lack of genetic differentiation between samples of the northern and the southern sectors (Kaouèche et al., 2011). Moreover, morphological variation was observed between Atlantic and Mediterranean white seabream populations (Palma and Andrade, 2002) despite the high degree of homogeneity between samples of these areas (Bargelloni et al., 2005; Domingues et al., 2007; Gonzalez-Wanguemert et al., 2010). In the same context, homogeneity was also revealed for Tunisian *L. mormyrus* samples (Hammami et al., 2007) whereas authors demonstrated morphological heterogeneity between lagoons (Hammami et al., 2011, 2013).

Our work indicates the existence of different degrees of morphological differences between northern and southern *D. sargus* samples but also among the samples collected from different lagoons. Both approaches, Truss and traditional, converged and gave complementary results but it is clear that the Truss network provides more precise and relevant information. The phenotypic variability observed between samples suggests a strong implication of ecological conditions.

Acknowledgements

This work was supported by a scholarship from the Tunisian 'Ministère de l'Enseignement Supérieur et de la Recherche Scientifique et de la Technologie'. We are also grateful to two anonymous reviewers who helped to improve the quality of the manuscript, through their suggestions and constructive comments.

References

- Albouy, C., Guilhaumon, F., Villéger, S., Mouchet, M., Mercier, L., Culioli, J.M., Tomasini, J.A., Le Loc'h, F., Mouillot, D., 2011. Predicting trophic guild and diet overlap from functional traits: statistics, opportunities and limitations for marine ecology. *Mar. Ecol.-Prog. Ser.* 436, 17–28, <http://dx.doi.org/10.3354/meps09240>.
- Allendorf, F.W., 1988. Conservation biology of fishes. *Conserv. Biol.* 2, 145–148, <http://dx.doi.org/10.1111/j.1523-1739.1988.tb00165.x>.
- Astraldi, M., Balopoulos, S., Candela, J., Font, J., Gacic, M., Gasparini, G.P., Manca, B., Theocharis, A., Tintoré, J., 1999. The role of straits and channels in understanding the characteristics of Mediterranean circulation. *Prog. Oceanogr.* 44, 65–108, [http://dx.doi.org/10.1016/S0079-6611\(99\)00021-X](http://dx.doi.org/10.1016/S0079-6611(99)00021-X).
- Bailey, K.M., 1997. Structural dynamics and ecology of flatfish populations. *J. Sea. Res.* 37 (3–4), 269–280, [http://dx.doi.org/10.1016/S1385-1101\(97\)00018-X](http://dx.doi.org/10.1016/S1385-1101(97)00018-X).
- Bargelloni, L., Alarcon, J.A., Alvarez, M.C., Enzo, E., Magoulas, A., Palma, J., Patarnellot, T., 2005. The Atlantic–Mediterranean transition: discordant genetic patterns in two seabream species, *Diplodus puntazzo* (Cetti) and *Diplodus sargus* (L.). *Mol. Phylogenet. Evol.* 36 (3), 523–535, <http://dx.doi.org/10.1016/j.ympev.2005.04.017>.
- Ben Hassine, O.K., 1983. Les Copépodes parasites de poissons Mugilidae en Méditerranée occidentale (côtes françaises et tunisiennes). Morphologie, Bio-écologie, cycles évolutifs. (Thèse de Doctorat d'État). U.S.T.L., Montpellier, France, 452 pp.
- Ben Hassine, O.K., Benmansour, B., Neifer, L., Bahri, L., Haji, T., Chaouachi, B., Labaied, M., Majed, M., 1999. L'état de la biodiversité dans les sites à activité halieutique du littoral Est de la Tunisie. In: *L'homme et la mer*, vol. I. 277–333.
- Ben Othman, S., 1971. Observation hydrologiques: dragages et chalutages dans le Sud-Est tunisien. *Bull. Inst. Natn. Scien. Tech. Mer de Salammbô* 2 (2), 103–120.
- Bergeck, S., Bjorklund, M., 2009. Genetic and morphological divergence reveal local subdivision of perch (*Perca fluviatilis* L.). *Biol. J. Linn. Soc.* 96 (4), 746–758, <http://dx.doi.org/10.1111/j.1095-8312.2008.01149.x>.
- Blanco, B., 1992. Protection du littoral du Gouvernorat de Bizerte. Conseil de l'ordre des ingénieurs; Comité régional de Bizerte. 1–5.
- Burns, J.G., Dinardo, P., Rodd, F.H., 2009. The role of predation in variation in body shape in guppies *Poecilia reticulata*: a comparison of field and common garden phenotypes. *J. Fish. Biol.* 75 (6), 1144–1157, <http://dx.doi.org/10.1111/j.1095-8649.2009.02314.x>.
- Cabral, H.N., Marques, J.F., Rego, A.L., Catarino, A.I., Figueredo, J., Garcia, J., 2003. Genetic and morphological variation of *Synaptura lusitanica* Capello, 1868, along the Portuguese coast. *J. Sea Res.* 50 (2–3), 167–175, [http://dx.doi.org/10.1016/S1385-1101\(03\)00060-1](http://dx.doi.org/10.1016/S1385-1101(03)00060-1).
- Cachéra, M., 2013. Implications of morphological and functional traits for trophic relationships within fish communities and marine trophic network architecture. (Doctoral thesis). University of Sciences and Technology, Lille, France, 249 pp.
- Cadrin, S.X., Friedland, K.D., 1999. The utility of image processing techniques for morphometric analysis and stock identification. *Fish. Res.* 43 (1), 129–139, [http://dx.doi.org/10.1016/S0165-7836\(99\)00070-3](http://dx.doi.org/10.1016/S0165-7836(99)00070-3).
- Cheverud, J.M., 1988. A comparison of genetic and phenotypic correlations. *Evolution* 42 (5), 958–968, <http://dx.doi.org/10.2307/2408911>.
- Çoban, D., Saka, F., Firat, K., 2008. Morphometric comparison of cultured and lagoon caught gilthead seabream (*Sparus aurata* L. 1758). *Turk. J. Zool.* 32, 337–341.
- Costa, C., Cataudella, S., 2007. Relationship between shape and trophic ecology of selected species of Sparids of the Caprolace coastal lagoon (Central Tyrrhenian Sea). *Environ. Biol. Fish.* 78 (2), 115–123, <http://dx.doi.org/10.1007/s10641-006-9081-9>.
- Delariva, R.L., Agostinho, A.A., 2001. Relationship between morphology and diets of six neotropical loriciariids. *J. Fish. Biol.* 58 (3), 832–847, <http://dx.doi.org/10.1111/j.1095-8649.2001.tb00534.x>.
- Domingues, V.S., Santos, R.S., Brito, A., Alexandrou, M., Almada, V. C., 2007. Mitochondrial and nuclear markers reveal isolation by distance and effects of Pleistocene glaciations in the north-eastern Atlantic and Mediterranean populations of the white seabream (*Diplodus sargus*, L.). *J. Exp. Mar. Biol. Ecol.* 346, 102–113, <http://dx.doi.org/10.1016/j.jembe.2007.03.002>.
- Dunham, A.E., Smith, G.R., Taylor, J.N., 1979. Evidence for ecological character displacement in western American catostomic fishes. *Evolution* 33, 877–896.
- Erdogan, Z., Turan, C., Koç, H.T., 2009. Morphologic and Allozyme Analyses of European anchovy (*Engraulis encrasicolus* (L. 1758)) in the Black, Marmara and Aegean Seas. *Acta Adriat.* 50 (1), 77–90.
- Everitt, B.S., Dunn, G., 1991. *Applied Multivariate Data Analysis*. Edward Arnold, London, 219–220.
- Farré, M., Tuset, V.M., Maynou, F., Recasens, L., Lombarte, A., 2013. Geometric morphology as an alternative for measuring the diversity of fish assemblages. *Ecol. Indic.* 29, 159–166, <http://dx.doi.org/10.1016/j.ecolind.2012.12.005>.
- Favaloro, E., Mazzola, A., 2006. Meristic character counts and incidence of skeletal anomalies in the wild *Diplodus puntazzo* (Cetti, 1777) of an area of the south-eastern Mediterranean Sea. *Fish. Physiol. Biochem.* 32 (2), 159–166.
- Fischer, W., Bauchot, M.L., Schneider, M., 1987. *Fiches F.A.O. d'Identification Des Espèces Pour Les Besoins De La Pêche. Méditerranée Et Mer Noire*. Zone De Pêche 37. Vol. II. Vertébrés. FAO, Rome, 761–1530.
- Gonzalez-Wanguemert, M., Canovas, F., Perez-Ruzafa, A., Marcos, C., Alexandrino, P., 2010. Connectivity patterns inferred from the genetic structure of white seabream (*Diplodus sargus* L.). *J. Exp. Mar. Biol. Ecol.* 383, 23–31.
- Guelorget, O., Frisoni, G.F., Perhuisot, J.P., 1982. Contribution à l'étude biologique de la Bahiret el Biban, lagune du Sud-Est tunisien. Symposium SGF et ASF, "Transition eaux douces – eaux sales". *Mem. Soc. Geol. Fr. N.S.* 144, 173–186.
- Hammami, I., Bahri-Sfar, L., Kaouèche, M., Ben Hassine, O.K., 2007. Genetic characterisation of striped seabream (*Lithognathus mormyrus*) populations on both sides of a boundary area between eastern and western Mediterranean basins. *Cybiurn* 31 (2), 143–147.
- Hammami, I., Bahri-Sfar, L., Ben Hassine, O.K., 2011. Morphological variations of striped seabream, *Lithognathus mormyrus*, populations along the Tunisian coast. *J. Mar. Biol. Assoc. U. K.* 91 (6), 1261–1271.
- Hammami, I., Bahri-Sfar, L., Kaouèche, M., Grenouillet, G., Leks, S., Kara, M.H., Ben Hassine, O.K., 2013. Morphological characterization of striped seabream (*Lithognathus mormyrus*, Sparidae) in some Mediterranean lagoons. *Cybiurn* 37 (1–2), 27–139.
- Hamza, A., 2003. Le statut du phytoplancton dans le golfe de Gabès. (Doctoral thesis). University of Sfax, Tunisia, 298 pp.

- Harzallah, A., 2003. Transport de polluants dans la lagune de Bizerte simulé par un modèle de circulation de l'eau. *Bull. Inst. Natn. Scien. Tech. Mer de Salammbô* 30, 121–133.
- Hyndes, G.A., Platell, M.E., Potter, I.C., 1997. Relationships between diet and body size, mouth morphology, habitat and movement of six sillaginid species in coastal waters: implications for resource partitioning. *Mar. Biol.* 128 (4), 585–598.
- Ihssen, P.E., Booke, H.E., Casselman, J.M., Mcglade, J.M., Payne, N.R., Utter, F.M., 1981. Stock identification: materials and methods. *Can. J. Fish. Aquat. S.C.I.* 38 (12), 1838–1855, <http://dx.doi.org/10.1139/f81-230>.
- Illou, S., 1999. Impact Des Rejets Telluriques D'origines Domestiques Et Industrielles sur L'Environnement Côtier: Cas Du Littoral De La Ville De Sfax. (Doctoral thesis). University of Tunis II, 259 pp.
- Kaouèche, M., Bahri-Sfar, L., Gonzalez-Wanguemert, M., Perez-Ruzafa, A., Ben Hassine, O.K., 2011. Allozyme and mtDNA variation of white seabream *Diplodus sargus* populations in a transition area between western and eastern Mediterranean basins (Siculo-Tunisian Strait). *Afr. J. Mar. Sci.* 33 (1), 79–90, <http://dx.doi.org/10.2989/1814232X.2011.572342>.
- Lin, J., Quinn, T.P., Hilborn, R., Hauser, L., 2008. Fine-scale differentiation between sockeye salmon ecotypes and the effect of phenotype on straying. *Heredity* 101 (4), 341–350, <http://dx.doi.org/10.1038/hdy.2008.59>.
- Loy, A., Busilacchi, S., Costa, C., Ferlin, L., Cataudella, S., 2000. Comparing geometric morphometrics and outline fitting methods to monitor fish shape variability of *Diplodus puntazzo* (Teleostea: Sparidae). *Aquacult. Eng.* 21 (4), 104–110.
- Mejri, R., Lo Brutto, S., Hassine, N., Arculeo, M., Ben Hassine, O.K., 2012. Overlapping patterns of morphometric and genetic differentiation in the Mediterranean goby *Pomatoschistus tortonesei* Miller, 1968 (Perciformes, Gobiidae) in Tunisian lagoons. *Zoology* 115 (4), 239–244, <http://dx.doi.org/10.1016/j.zool.2012.02.002>.
- Molinier, R., Picard, J., 1954. Éléments de bionomie marine sur les côtes de Tunisie. *Bull. Stn. Oceanogr. Peche. Salammbô* 48, 3–47.
- Moussa, M., Baccar, L., Ben Khemis, R., 2005. La lagune de Ghar El Melh: Diagnostic écologique et perspectives d'aménagement hydraulique. *Rev. Sci. Eau.* 18 (2), 13–26.
- Neifar, L., 2001. Biodiversité Et Evolution Des Plathelminthes Parasites des Elasmobranches. (Doctoral thesis). University of Tunis II, Faculté Des Sciences De Tunis, 326 pp.
- Palma, J., Andrade, J.P., 2002. Morphological study of *Diplodus sargus*, *Diplodus puntazzo*, and *Lithognathus mormyrus* (Sparidae) in the Eastern Atlantic and Mediterranean Sea. *Fish. Res.* 57 (1), 1–8.
- Pérez-Ruzafa, A., Mompeán, M.C., Marcos, C., 2007. Hydrographic, geomorphologic and fish assemblage relationships in coastal lagoons. *Hydrobiologia* 577 (1), 107–125, <http://dx.doi.org/10.1007/s10750-006-0421-8>.
- Price, S.A., Holzman, R., Near, T.J., Wainwright, P.C., 2011. Coral reefs promote the evolution of morphological diversity and ecological novelty in labrid fishes. *Ecol. Lett.* 14 (5), 462–469, <http://dx.doi.org/10.1111/j.1461-0248.2011.01607.x>.
- Ramsay, J.O., Hooker, G., Graves, S., 2009. Functional Data Analysis with R and MATLAB. Springer, Dordrecht, 208 pp.
- Reist, J.D., 1985. An empirical evaluation of several univariate methods that adjust for size variation in morphometric data. *Can. J. Zool.* 63 (6), 1429–1439.
- Ryman, N., Lagercrantz, U., Andersson, L., Chakraborty, R., Rosenberg, R., 1984. Lack of correspondence between genetic and morphologic variability patterns in Atlantic herring (*Clupea harengus*). *Heredity* 5 (3), 687–704.
- Sammar, C., Koutitonsky, V.G., Moussa, M., 2006. Sea level variability and tidal resonance in the Gulf of Gabes, Tunisia. *Cont. Shelf Res.* 26, 338–350.
- Sara, M., Favaro, E., Mazzola, A., 1999. Comparative morphometrics of sharpnose seabream (*Diplodus puntazzo* Cetti, 1777) reared in different conditions. *Aquacult. Eng.* 19, 195–209.
- Serbaji, M.M., 2000. Utilisation d'un SIG Multi-Sources pour la compréhension et la gestion intégrée de l'écosystème côtier de la région de Sfax (Tunisie). (Doctoral thesis). University of Tunis II, 152 pp.
- Silva, A., 2003. Morphometric variation among sardine (*Sardina pilchardus*) populations from the northeastern Atlantic and the western Mediterranean. *ICES J. Mar. Sci.* 60 (6), 1352–1360.
- Slatkin, M., 1985. Gene flow in natural populations. *Ann. Rev. Ecol. Evol. Syst.* 16, 393–430.
- Strauss, R.E., Bookstein, F.L., 1982. The truss: body from reconstructions in morphometrics. *Syst. Zool.* 31 (2), 113–135.
- Swain, D., Foote, C.J., 1999. Stocks and chameleons: the use of phenotypic variation in stock identification. *Fish. Res.* 43, 113–128.
- Thompson, J.D., 1991. Phenotypic plasticity as a component of evolutionary chance. *Trends. Ecol. Evol.* 6 (8), 246–249, [http://dx.doi.org/10.1016/0169-5347\(91\)90070-E](http://dx.doi.org/10.1016/0169-5347(91)90070-E).
- Turan, C., 1999. A note on the examination of morphometric differentiation among fish populations: the truss system. *Turk. J. Zool.* 23, 259–263, doi:10.1.1.584.1003.
- Turan, C., 2004. Stock identification of Mediterranean horse mackerel (*Trachurus mediterraneus*) using morphometric and meristic characters. *ICES J. Mar. Sci.* 61 (5), 774–781, <http://dx.doi.org/10.1016/j.icesjms.2004.05.001>.
- Turan, C., Basusta, N., 2001. Comparison of morphometric characters of twaite shad (*Alosa fallax nilotica*, Geoffroy Saint-Hilaire, 1808) among three areas in Turkish seas. *B. Fr. Peche. Piscic.* 362/363, 1027–1035.
- Turan, C., Erguden, D., Turan, F., Gurlek, M., 2004. Genetic and morphologic structure of *Liza abu* (Heckel, 1843) populations from the rivers Orontes, Euphrates and Tigris. *Turk. J. Vet. Anim. Sci.* 28 (4), 729–734.
- Turan, C., Yalcin, Ş., Turan, F., Okur, E., Akyurt, İ., 2005. Morphometric comparisons of African catfish, *Clarias gariepinus*, populations in Turkey. *Folia. Zool.* 54 (1–2), 165–172.
- Turan, C., Oral, M., Öztürk, B., Duzgunes, E., 2006. Morphometric and meristic variation between stocks of Bluefish (*Pomatomus saltatrix*) in the Black, Marmara, Aegean and Northeastern Mediterranean Seas. *Fish. Res.* 79 (1), 139–147.
- Wainwright, P.C., Bellwood, D.R., Westneat, M.W., Grubich, J.R., Hoey, A.S., 2004. A functional morphospace for the skull of labrid fishes: patterns of diversity in a complex biomechanical system. *Biol. J. Linn. Soc.* 82, 1–25.
- Wimberger, P.H., 1992. Plasticity of fish body shape, the effects of diet, development, family and age in two species of *Geophagus* (Pisces: Cichlidae). *Biol. J. Linn. Soc.* 45 (3), 197–218.
- Zakhama, R., Sghaier, Y.R., Charfi, F., 2005. Biodiversité des amphipodes Gammaridae associés à l'herbier de *Posidonia oceanica* des côtes orientales de la Tunisie. *INOC – Mar. Coast. Protected. Areas* 274–277.



Available online at www.sciencedirect.com

ScienceDirect

journal homepage: www.journals.elsevier.com/oceanologia/



ORIGINAL RESEARCH ARTICLE

Current observations from a looking down vertical V-ADCP: interaction with winds and tide? The case of Giglio Island (Tyrrhenian Sea, Italy)

Laura Cutroneo^a, Gabriele Ferretti^a, Davide Scafidi^a,
Gian Domenico Ardizzone^b, Greta Vagge^a, Marco Capello^{a,*}

^a *DISTAV, University of Genoa, Genoa, Italy*

^b *“Sapienza”, University of Rome, Rome, Italy*

Received 22 July 2016; accepted 23 November 2016

Available online 14 December 2016

KEYWORDS

Currents;
Wind interactions;
Sea level;
Normalised Cross-
Correlation Function

Summary In the context of the environmental monitoring of the Concordia wreck removal project, measurements of currents, winds and sea level height were made along the eastern coast of the Giglio Island, Tyrrhenian Sea (Italy), during 2012–2013. The aim of the study was to investigate the effect of atmospheric forcing and periodic sea-level changes on the coastal currents. Normalised Cross-Correlation Function analysis allowed us to correlate these observations. A marked inter-seasonal variability was found in both current and local wind velocity observations but a significant level of correlation between the data was only found during strong wind events. Current and wind directions appeared to be uncorrelated and current measurements showed a predominant NW–SE direction, presumably linked to the shape and orientation of Giglio Island itself. During strong winds from the SSE, current flow was towards the NNW but it suddenly switched from the NNW to the SE at the end of wind events. The results show that, at Giglio Island, currents are principally dominated by the general cyclonic Tyrrhenian circulation, and, secondly, by strong wind events. The sea level had no effects on the current regime.

© 2016 Institute of Oceanology of the Polish Academy of Sciences. Production and hosting by Elsevier Sp. z o.o. This is an open access article under the CC BY-NC-ND license (<http://creativecommons.org/licenses/by-nc-nd/4.0/>).

* Corresponding author at: DISTAV, University of Genoa, 26 Corso Europa, I-16132 Genoa, Italy. Tel.: +39 01035338143; fax: +39 010352169. E-mail address: capello@dipteris.unige.it (M. Capello).

Peer review under the responsibility of Institute of Oceanology of the Polish Academy of Sciences.



Production and hosting by Elsevier

<http://dx.doi.org/10.1016/j.oceano.2016.11.001>

0078-3234/© 2016 Institute of Oceanology of the Polish Academy of Sciences. Production and hosting by Elsevier Sp. z o.o. This is an open access article under the CC BY-NC-ND license (<http://creativecommons.org/licenses/by-nc-nd/4.0/>).

1. Introduction

Sea and ocean circulation is generally characterised by the interactions of tidal currents, bathymetric constraints, wind forcing, and density gradients induced by river input and heat and mass (evaporation and rain) exchange. In this complex scenario, wind has been found to be the main forcing factor inducing currents, while tidal and baroclinic motions are of secondary importance (Bolaños et al., 2014). The barotropic component of the coastal circulation is mainly driven by local winds, but is also highly dependent on the topography of the marine basin, composed of sub-basin scale gyres that can be seasonally variable and recurrent (Molcard et al., 2002; Pierini and Simioli, 1998).

The periodic vertical motions produced by tides close to the coast induce (horizontal) currents with alternating floods and ebbs. In these water movements, tides can have local or regional and short-range or long-range influences (Naranjo et al., 2014). Close to the coast, sea level depends primarily on the periodic change of lunar and solar attraction (astronomic influences), but also on the local atmospheric pressure and wave and wind changes (atmospheric events) that induce non-periodic signals of varying strength (amplitude) and duration (low-frequency) which influence the daily periodic oscillations (Halverson, 2014; Tsimplis et al., 2011). Moreover, the magnitude of the sea level variation is site dependent. In fact, in areas characterised by very small tidal ranges, such as the Mediterranean Sea, the atmospheric effects may have greater amplitude than the normal tide and can partially or completely obscure the astronomic tide oscillations. These atmospheric effects vary, for example, with the direction, strength and duration of the wind and are also dependent on the morphology of the area and the depth of the body of water (Halverson, 2014).

In the context of the environmental monitoring of the Concordia wreck removal project, measurements of currents, winds and sea level were made during 2012–2013

along the eastern coast of the Giglio Island in the Tyrrhenian Sea (Italy) (Fig. 1). In order to study the general trend of the currents, and their daily and seasonal variations in relation to atmospheric forcing (winds) and periodic sea level changes (tides), a vertical Acoustic Doppler Current Profiler (V-ADCP) was deployed under a buoy from the 29th August 2012 to the 7th July 2013. The results of the cross-correlation analysis of the continuous data collected by the V-ADCP and the meteorological (wind velocity and direction) and sea level observations recorded at the permanent weather station of Giglio Porto are reported in this paper.

2. Study area

2.1. Geological and climatic characteristics of Giglio Island

Giglio Island (21.2 km²) lies in the northern part of the Tyrrhenian Sea in front of the Argentario headland, 14-km off the Tuscany coast (Fig. 1). The small town and the harbour of Giglio Porto are on the eastern side of the island (Fig. 1). The island is 90% composed of a monzogranitic pluton resulting from crystallisation of magma within the earth's crust and raised to the surface as a result of a tectonic extensional phase subsequent to the collision between the Adriatic and Corsica-Sardinia plates (Rossetti et al., 1999). The island's shape is roughly elliptical, 8.5 km long and 4.5 km wide, with its major axis oriented NNW-SSE. Its coasts are predominantly high and rocky with numerous small bays and inlets. The sea bottom off the Giglio Porto coast is characterised by a steep rocky slope that slopes quickly to a 100-m depth at a distance of about 350 m from the coast. Sea bottom, beneath 50-m depth, consists of more than 60% clay (Frezza and Carboni, 2009).

The island's climate is typically Mediterranean, with rare rainfall between May and October (almost completely absent

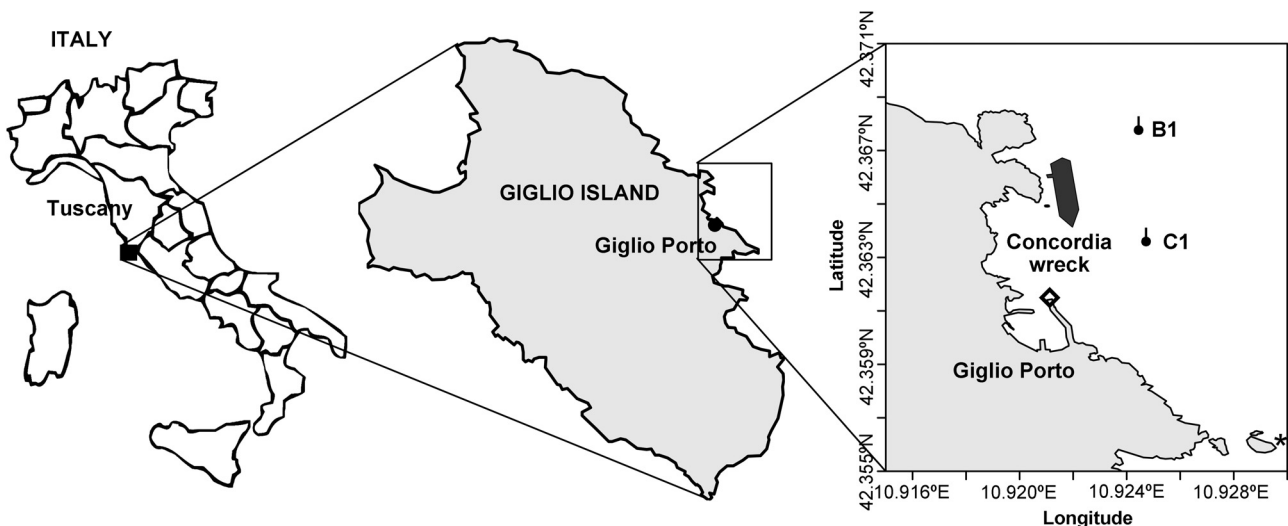


Figure 1 Location of the study area (Giglio Island, Italy). B1 and C1 are the buoys under which the V-ADCP was installed for the continuous monitoring of the currents; Concordia wreck black profile highlights the position of the vessel near the coast off Giglio Porto; the black rhombus shows the position of the weather station of the LaMMA Consortium (Environmental Modelling and Monitoring Laboratory for Sustainable Development) of the Tuscany Region; the black asterisk shows the collision point of the cruise vessel on the rocks.

in the summer months), and more frequent rainfall between November and April. The temperature is relatively mild in winter (minima $> 0^{\circ}\text{C}$) and high in summer (maxima $> 30^{\circ}\text{C}$). The weather conditions of the island are mostly influenced by wind action; in particular, the winds from the SE, S, SW and NE are linked with rains, while the winds from the NW, W and N are linked with dry weather. The N and NE winds typically blow during winter (December, January, and February) and can produce storms, while, in autumn and spring, strong SE and S–SW winds generate rough seas, principally on the southern and eastern coasts of the island. In summer, the dominant wind is from the S and of low velocity, generally associated with calm seas (<http://www.cmgez.info>).

2.2. The circulation and tides in the Tyrrhenian Sea

The study area is included in the general circulation of the Tyrrhenian Sea. This circulation is characterised by surface and intermediate layers represented by a well-defined flux of Atlantic Water (AW; the Tyrrhenian vein) entering the basin from the south along the eastern coast of Sicily and flowing counter-clockwise around the Tyrrhenian and northward along the Italian peninsula reaching the Channel of Corsica. Here, a part of the flow enters the Ligurian Sea, while another part moves in a cyclonic gyre off the Bonifacio Strait (Astraldi and Gasparini, 1994; Millot and Taupier-Letage, 2005; Vetrano et al., 2010). When the Tyrrhenian vein of the AW reaches the channel between Giglio Island and the Italian coast, currents are forced in an SE–NW direction, disturbed by gyres and counter-current induced by the interaction with the coastal morphology, friction with the shallow bottom, and the influence of the freshwater inputs from torrents and rivers. This situation was highlighted in satellite picture taken on the 13th November 2012 after heavy rains that hit the region (Fig. 2; source NASA).

The Tyrrhenian circulation suffers from some important seasonal changes, primarily in the northern part of the basin. Here, the water masses are mostly recirculated within the basin in summer, isolating the Tyrrhenian and Ligurian seas, with only a small part of the flow passing through the Corsica Channel; in winter and spring, the communication between the two basins is full (Astraldi and Gasparini, 1994; Pierini and Simioli, 1998; Schroeder et al., 2011).

In general, the maximum tidal range is relatively low in the Tyrrhenian Sea, equal 0.45 m (Ferrarin et al., 2013). Tidal



Figure 2 Evidence of the current coastal gyres produced by coast morphology and fresh water input from rivers. Satellite picture taken on the 13th November 2012 after heavy rains. Source: NASA.

oscillations (Table 1) are semidiurnal, with two highs and two lows during the day, which occur with different values during the year producing minor and major tides that are strongly correlated with the mean surface pressure variations; seasonal fluctuations have a progressive increase and sharp decrease, with the maximum signal in autumn (Mosetti and Purga, 1982; Polli, 1955). The mean sea level curve is dominated by a strong annual signal of 8 cm in amplitude (Cazenave et al., 2002).

Table 1 Mean tidal semi-diurnal and diurnal harmonic constituents (M2, S2, K1, and O1) expressed in amplitude (in cm) and phase (in degree, $^{\circ}$) at the tidal gauge of the Civitavecchia harbour during the period 1951–1952 (Polli, 1955). Solar annual component (Sa), solar semi-annual component (Ssa), solar monthly component (MSm), and lunar monthly component (Mm) at the tidal gauge of the Civitavecchia harbour during the period 1966–1968 (Mosetti and Purga, 1982).

Polli (1955)	M2 (the principle lunar semi-diurnal harmonic)	S2 (the principle solar semi-diurnal harmonic)	K1 (the principle luni-solar diurnal component)	O1 (the principle lunar diurnal component)
Period 1951–1952	10.9 cm, 258 $^{\circ}$	4.1 cm, 280 $^{\circ}$	2.8 cm, 202 $^{\circ}$	1.3 cm, 115 $^{\circ}$
Mosetti and Purga (1982)	Sa (solar annual component)	Ssa (solar semi-annual component)	MSm (solar monthly component)	Mm (lunar monthly component)
Period 1966–1968	5.6 cm, 216 $^{\circ}$	3.4 cm, 111 $^{\circ}$	0.8 cm, 276 $^{\circ}$	0.3 cm, 246 $^{\circ}$

3. Material and methods

The signal buoys delimiting the marine yard of the Concordia wreck removal project were located 300–500 m off Giglio Porto (Fig. 1) at the 80–100 m isobaths. The buoys (Resinex Trading Srl) were manufactured with an external shell in roto-moulded linear polyethylene and filled with elastomer polyurethane to guarantee buoyancy.

A Teledyne RDI 300-kHz downward-looking vertical four-beam V-ADCP was installed under buoy C1 on the 29th August 2012 and moved to buoy B1 on the 25th November 2012, at a fixed depth of 6 m to continuously monitor the currents. The 6-m depth was chosen because of the shape of the buoy, equipped with a pipe in its submerged part. The V-ADCP was powered by an internal battery pack and installed on the buoy cable with a stainless steel structure that avoided beam interaction with the cable itself. The instrument was equipped with an armoured submarine cable with a terminal above sea level from which data were downloaded.

The V-ADCP could measure current profiles (velocity and direction) and the intensity of the echo (backscatter) along a theoretical vertical line of about 120 m (RD, Instruments 2007) from the depth of installation (6 m) to the sea bottom. The size of V-ADCP bins was set at 4 m and the maximum number of bins at 16, to cover 70 m of the water column, and, hence, the first measurement bin was centred at a 10-m depth. The instrument measured the velocity [mm s^{-1}] and direction [$^{\circ}\text{N}$] of the current with a sampling of 6 min averaging 30 pings for each measurement (1 ping every 12 s).

The measurement period lasted from the 29th August 2012 till the 7th July 2013, but it was divided into sub-periods of non-equal duration depending on yard operations and weather conditions (Table 2). From the 29th August to the 25th November 2012, the instrument was fixed under buoy C1 (Fig. 1), but, due to the frequent removals and repositioning of the buoy for the manoeuvres of tugs and pontoons engaged in the yard operations, it was successively (from 25th November 2012) fixed under buoy B1 (Fig. 1) (Table 2) situated 800 m to the North.

The software used for the V-ADCP configuration and the data downloading was WinSC (RD Instruments, Inc.), while the software used for data processing was WinADCP (RD Instruments, Inc.).

Following the oceanographic convention, a current direction was defined as the direction towards which the currents were flowing. The monthly mean of the current velocity was

Table 2 Measurement periods of currents by V-ADCP and related position (under C1 or B1 buoy) (period time: dd/mm/yyyy).

	Period start	Period end
Buoy C1	29/08/2012	11/09/2012
	04/10/2012	30/10/2012
	23/11/2012	25/11/2012
Buoy B1	25/11/2012	11/12/2012
	31/12/2012	16/04/2013
	15/06/2013	27/06/2013
	30/06/2013	07/07/2013

calculated at different depths (10, 18, 30, 50, and 70 m) and released as histograms to show the velocity changes with depth during the study period. The data on the current velocity and direction were divided according to the astronomical seasons and plotted in rose diagrams to investigate the seasonal behaviour of the currents and highlight possible prevailing directions.

The meteorological parameters used in this study were measured at the weather station installed on the breakwater of the Giglio Porto harbour (Fig. 1) by the LaMMA (Environmental Modelling and Monitoring Laboratory for Sustainable Development) Consortium of the Region of Tuscany and the Italian Research Council. The weather station provided measurements of sea level [m], mean and maximum wind velocity [m s^{-1}] and prevailing wind and gust direction [$^{\circ}\text{N}$]. The wind direction was defined as the direction from which the winds were coming. The data were acquired considering a sampling of 10 min.

The weather data were used to support the marine weather bulletin of the Giglio Island activated immediately after the shipwreck. The weather station was composed of a shaft encoder floating hydrometer in a stilling and a 10-m height folding pole with wind velocity and direction sensors (Siap + Micros, S.r.l.) powered by a solar panel. The weather station was 0.5 and 1.2 km from buoys C1 and B1, respectively.

The complete temporal coverage of the data set is shown in Fig. 3.

As was done for the current data, the monthly wind means were also determined, and wind rose diagrams were drawn with the data of the hourly prevailing wind and wind gust.

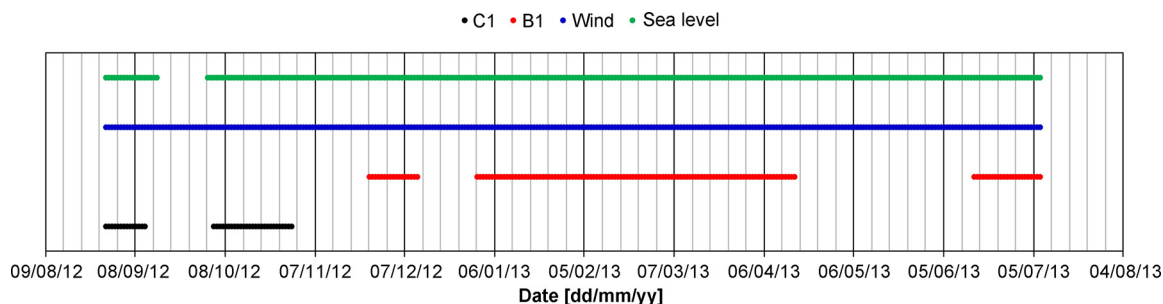


Figure 3 Temporal coverage of current data (under the buoys C1 and B1 in black and red, respectively), wind data (in blue), and sea level data (in green). (For interpretation of the references to color in this figure legend, the reader is referred to the web version of this article.)

Daily sea level means were extracted to highlight the trend of the sea level variations. Tidal harmonic analysis was performed on the hourly sea level data in the period 29th August 2012–7th July 2013, using the Harmgen free software (version 3.1.1, 2006), considering a package of 35 constituents including the four primary harmonic constituents of the semi-diurnal and diurnal frequencies (S2, M2, K1, and O1). Because tidal observations did not cover a full year period, we could not calculate or consider the annual and monthly harmonic components.

A core issue when dealing with time series is determining their pairwise similarity, i.e. the degree to which a given time series resembles another. Therefore, in order to evaluate the presence of possible correlations between the data measured by the V-ADCP (velocity and direction of current) and those provided by the weather station of the LaMMA Consortium (sea level, velocity and direction of wind), a procedure based on the use of the cross-correlation function (CCF) was applied. CCF is a standard method of estimating the degree to which two-time series are similar, and represents a useful measure of strength and direction of the correlation between two random variables (Wei, 2006). In this work, the Normalised Cross-Correlation Function (N-CCF) was considered: it is a popular and easily implemented metric that well follows the rapid changes and the amplitude of two compared signals, and makes it possible to evaluate both the degree of similarity between couples of compared datasets or images and the eventual time shift and delay between two-time series (Tsai et al., 2003; White and Peterson, 1994). N-CCF has found applications in a broad range of the earth sciences such as seismicity, meteorology, and hydrology (Campillo and Paul, 2003; Capello et al., 2016; Mc Millen, 1987; Thouvenot et al., 2016). N-CCF is defined as:

$$\text{N-CCF} = \frac{C_{12}(\tau)}{\sqrt{C_{11}(0)C_{22}(0)}}, \quad (1)$$

where

$$C_{12}(\tau) = \int_{-\infty}^{+\infty} a_1(t)a_2(t+\tau)dt, \quad (2)$$

where $a_1(t)$ and $a_2(t)$ are the two time series.

When dealing with digital data, the discrete (or digital) cross-correlation function is used and it is defined as:

$$C_{xy} = \sum_{m=-\infty}^{\infty} x(m)y(m+l), \quad (3)$$

where $x(m)$ and $y(m)$ are the two discrete-time signals.

The maximum value of the N-CCF (hereafter, the cross-correlation level or similarity level) measures the similarity between signals as a function of the lag of one relative to the other. The maximum correlation is when the maximum N-CCF value is equal to 1, whereas an N-CCF value equal to 0 indicates no correlation between signals.

Before the computation of the N-CCF, the time series data were processed applying the following procedure: (a) re-sampling to the common frequency of 0.0027778 Hz (the sampling frequency of the V-ADCP data) through an interpolation using a 4th degree polynomial (Scherbaum et al., 1999); (b) extraction of a continuous time window common to both the wind and current series [the period from 15:05 of the 31st December 2012 to 14:00 of the 16th April 2013 was

selected: in this time-period, the complete (without gaps) time series of observations recorded by both V-ADCP and weather station of Giglio Porto were available]; and (c) offset removal (e.g. removing from the time series the average value of all points).

The cross-correlation function was computed in order to assess the possible relationship between: (a) current velocity and direction measured at different depths (10 m and 18 m, 10 m and 30 m, 10 m and 50 m, 10 m and 70 m); (b) wind velocity and current velocity measured at different depths (10 m, 18 m, 30 m, 50 m, and 70 m); (c) prevailing direction of wind and direction of current measured at different depths (10 m, 18 m, 30 m, 50 m, and 70 m); and (d) sea level and current direction measured at 10-m depth.

4. Results

4.1. Current variability from moored measurements

The monthly mean current velocities (Fig. 4) show a progressive increase from August 2012 (81 mm s⁻¹ in the surface layer at buoy C1) to the autumnal and winter months (251 and 165 mm s⁻¹ of maxima measured in the surface layer at buoy B1 in November and December 2012, respectively), with a subsequent decrease in summer 2013 (84 mm s⁻¹ in the surface layer at buoy B1). A progressive decrease of current velocity was also visible analysing data from the surface layer (10-m depth) to the bottom layer (70-m depth) in the water column. Below the 50-m depth, the monthly mean current velocity attenuates and the maximum values decrease to values slightly higher than 100 mm s⁻¹ (maximum monthly mean value of 136 mm s⁻¹ was observed in November at buoy B1).

The maximum current velocity events (velocity > 500 mm s⁻¹ at the 10-m depth; Fig. 5) were recorded from the 27th November to the 3rd December 2012 (showing a maximum of 708 mm s⁻¹), on the 6th–7th and on the 18th March 2013 (showing a maximum of 816 mm s⁻¹).

With regard to the current direction, some differences were found among the values measured moving from the surface layer to the bottom in the four seasons. In fact, in the surface layer (10-m depth; Fig. 6a), currents were sharply oriented towards NNW and SSE, whereas moving to the bottom of the water column this effect tended to disappear and the current direction became more widespread (Fig. 6b). Analysing the data recorded at the different depths as a function of the seasons (Fig. 6a and b), it was possible to highlight a seasonal behaviour of current direction. In summer and spring, the prevailing current directions were SE with a smaller portion of NNW directions at the surface (Fig. 6a), while the SSE direction prevails with the greater depth (Fig. 6b). In autumn and winter, the currents are mainly oriented towards NNW in the whole water column, and at 50 and 70-m depths, there is a reversal of the direction with a slight prevalence of SSE near the bottom (Fig. 6b).

4.2. Variability in sea level

The sea level trend shown in Fig. 7 highlights the irregular behaviour shown by the sea level as a function of time. The

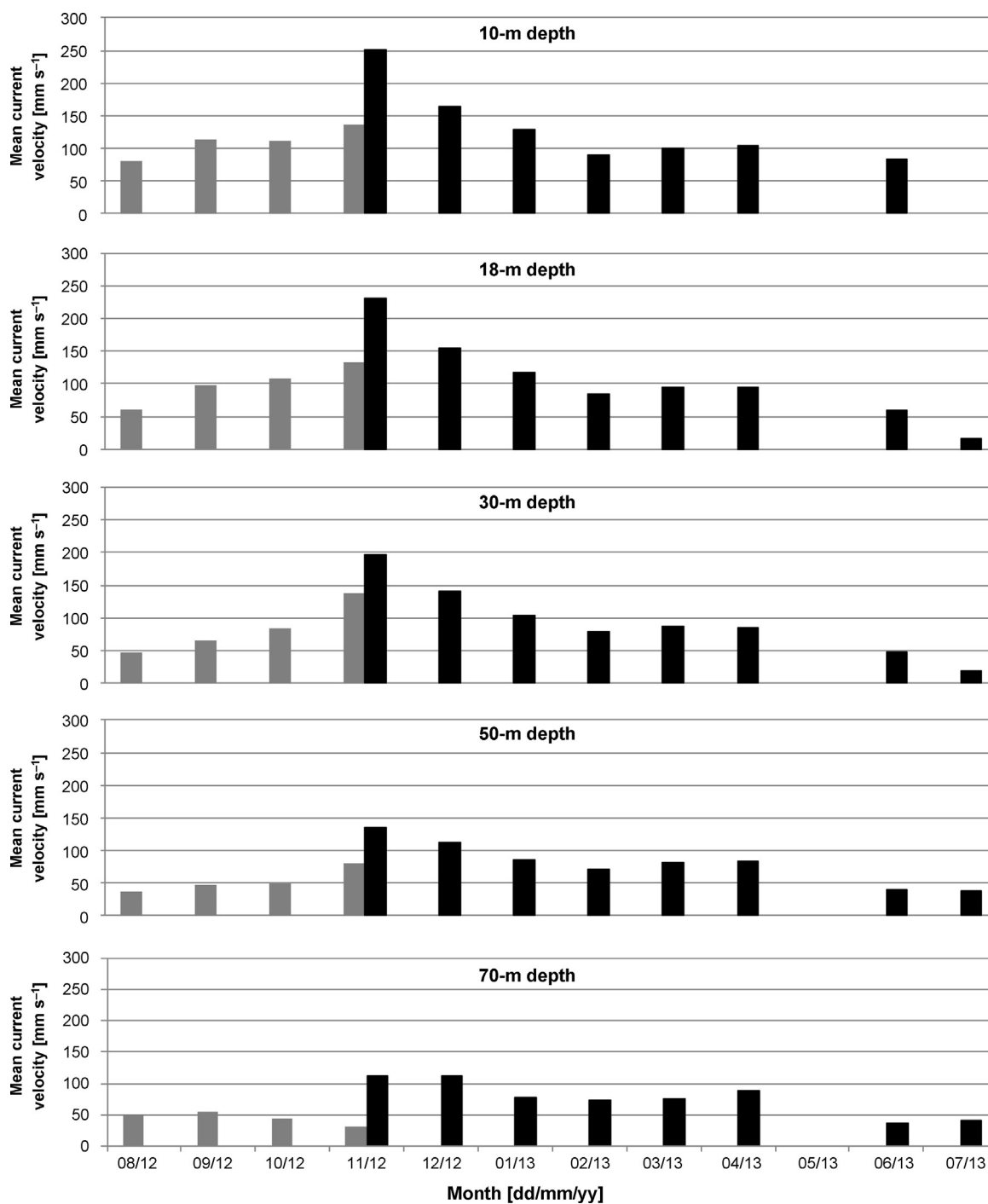


Figure 4 Monthly mean current intensities [mm s^{-1}] measured at 5 different depths in the water column (10, 18, 30, 50, and 70 m) at buoy C1 (grey) and B1 (black). Data of May 2013 are not available as well as data of July 2013 at 10-m depth.

sea level data, recorded at the weather station of Giglio Porto, ranged between -0.33 m and 0.49 m. Two minimum values (-0.31 and -0.33 m) were recorded on the 29th December 2012 and the 28th February 2013 in the presence of a strong N and light SW–SE wind, respectively, and a full moon (28th December 2012 and 26th February 2013). While two positive sea level peaks of 0.41 and 0.49 m (seiches), observed on the 27th and 31st October, respectively, were produced by persistent bad weather conditions, characterised by low atmospheric pressure, a strong SSE

wind, rough seas and heavy precipitation, in conjunction with a full moon (30th October). Maximum sea level variations were recorded in autumn and winter, while minimum variations were observed during late spring and summer.

The main tidal harmonic constituents are reported in Table 3: the main lunar semi-diurnal (M_2) prevails over the other constituents with an amplitude of 10.5 cm, four times stronger than the amplitude of the major diurnal constituent (K_1).

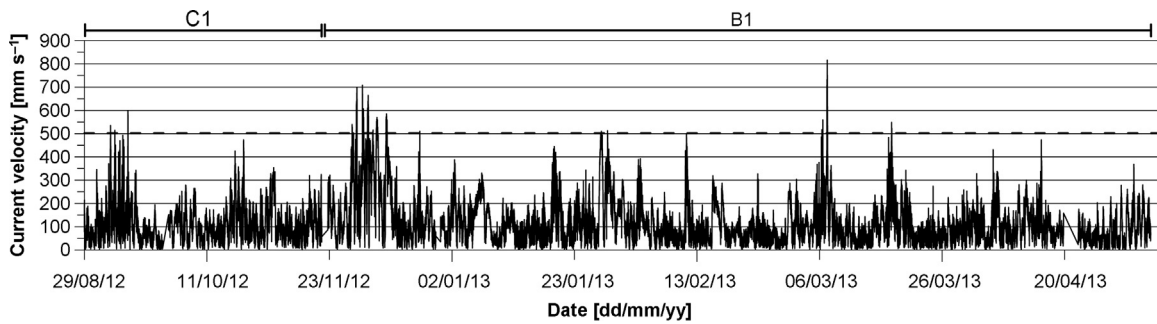


Figure 5 Current velocity distribution measured at 10-m depth during the entire measure period. The dotted line shows the current velocity of 500 mm s^{-1} .

4.3. Seasonal variability in winds

Wind velocity measured at the weather station of Giglio Porto ranged between 0 and 16.6 m s^{-1} and showed a monthly mean of 3.2 m s^{-1} in summer and of 4.9 m s^{-1} in winter (Fig. 8). Considering only the case of wind velocities higher than the mean value of the near gale velocities (15 m s^{-1}) according to the Beaufort Scale, only five events of significant wind were recorded in autumn and winter. The highest wind velocity was recorded on the 11th November 2012 during a robust anticyclonic front characterised by SE-oriented winds.

The rose diagrams (Fig. 9) reporting wind measurements show that winds originate mostly from two directions, SE and NNW; the strongest winds come from the SE. A SW wind direction is also visible mainly looking at the wind gusts diagram.

It is also possible to note some seasonal variation in the wind direction; in summer, winds come mainly from the NNW; in autumn, the predominant origin direction is the SE; in winter, the strongest winds come from the SE, whereas weaker winds come from the NW; in spring, the two prevailing directions (NNW and SE) are present, with a slight prevalence of the SE direction.

5. Data correlation results

Fig. 10 shows the results of the Normalised Cross-Correlation Function (N-CCF; Eq. (1)) obtained considering current velocities measured at different depths (Fig. 10a) and those resulting from correlating wind velocities and current velocities measured at different depths (Fig. 10b).

The time series of current velocities measured at different depths (Fig. 10a) exhibit a similarity level, which tends to decrease as the difference between measuring depth increases (y-axis of Fig. 10a); in fact, the cross-correlation level between the current velocity values measured at the 10-m depth and those measured at the 18-m depth is equal to 0.82, whereas for the data measured at the 10-m depth and at the 70-m depth the similarity decreases to 0.36.

It should be noted that the time shift (x-axis of Fig. 10a) in current velocity values measured at different depths changes too. Data measured at the 10-m depth and the 18-m depth are not phase-shifted, whereas the time shift between data measured at the 10-m depth and the 70-m depth is equal to about 1 h and 30 min (-1.5 h). Similar results are obtained by evaluating the similarity level between current directions measured at different depths (not showed in Fig. 10).

Between directions measured at the 10-m depth and those measured at the 18-m depth it is possible to observe 0.52 of similarity, while the similarity decreases to 0.16 when the data of the 10-m depth were compared to the data of the 70-m depth.

The correlation between the wind and current (time series) was extremely low (Fig. 10b). It was lower than 0.20 for the velocity data (Fig. 10b) and 0.10 for the direction data. This result shows that the wind does not seem to be related to the current velocity or rather the wind does not significantly influence the velocity and direction of the current.

In order to better investigate the correlation between the wind and current, a further analysis was performed estimating the N-CCF between wind velocity and current velocity measured at the 10-m depth for three events characterised by a wind velocity peak greater than 15 m s^{-1} (the mean velocity of the near gale wind; Figs. 11–13). In particular, three sub-windows with duration of approximately five days, around the 12th February 2013, the 7th March 2013, and the 18th March 2013, were analysed. Considering only these events, the correlation between the wind and current velocity significantly increased with respect to the previous analysis (performed considering the entire recording period), showing similarity levels greater than 0.50 (panel c in Figs. 11–13). The time shift between the wind and current velocities was very different in the three different cases. In fact, in the first case (Fig. 11), the time shift was equal to 4 h ca, in the second case (Fig. 12) it was 21 h, and in the third case it was 12 h ca (Fig. 13).

Other important experimental evidence concerns the relationship between the wind and current direction observed during these three events. In correspondence of maximum values of the wind and current velocity (highlighted in Figs. 11–13 by the dashes), a relationship between a SSE wind (e.g. “Scirocco” 135° – 180°) and a N current is visible. It must be noted that the events of strong wind extrapolated from the study period are all analogous, that is all come mainly from the SSE, and therefore, it is not possible to analyse other cases of strong winds with different directions. In Figs. 11–13 (panels b and e), it is possible to note an inversion of the current direction at the end of the wind action and the consequently variation in the current velocity: the current direction switches suddenly from the NW to the SE as if the system unbinds at the forcing end.

The last analysis has been performed computing the N-CCF between the sea level data and the current direction measured at the 10-m depth. These two signals appear uncorrelated (similarity level lower than 0.10).

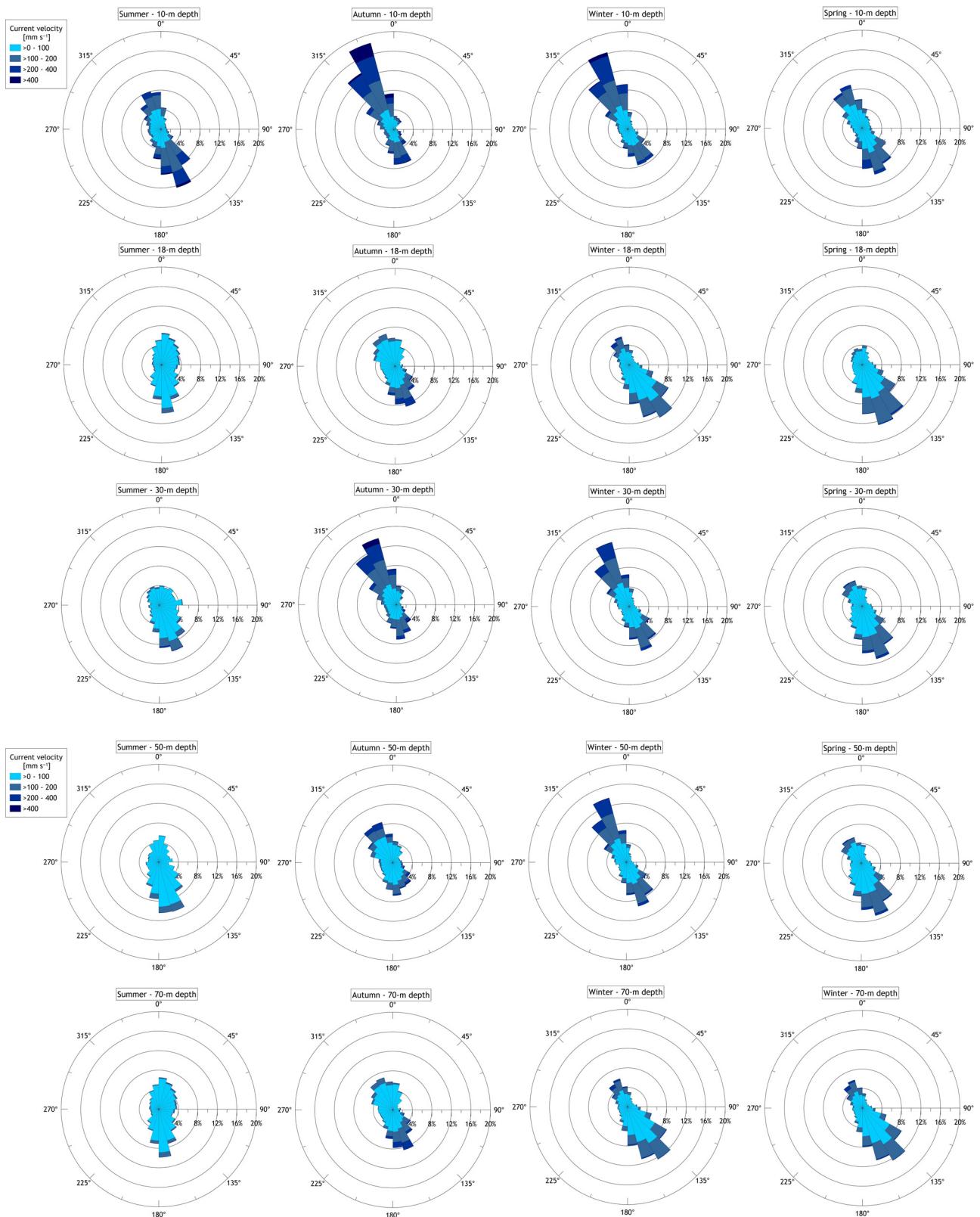
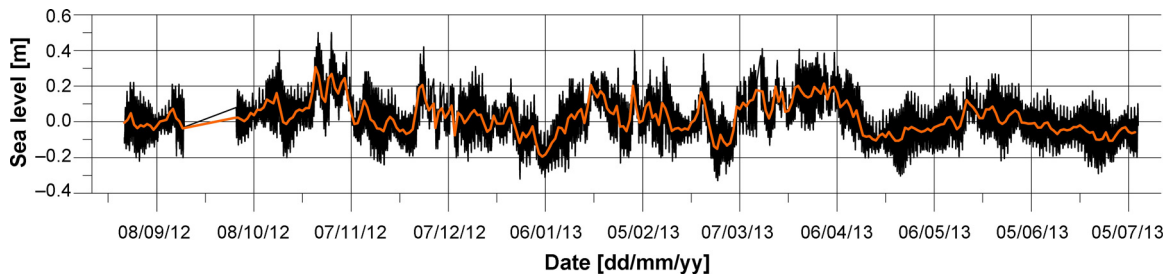
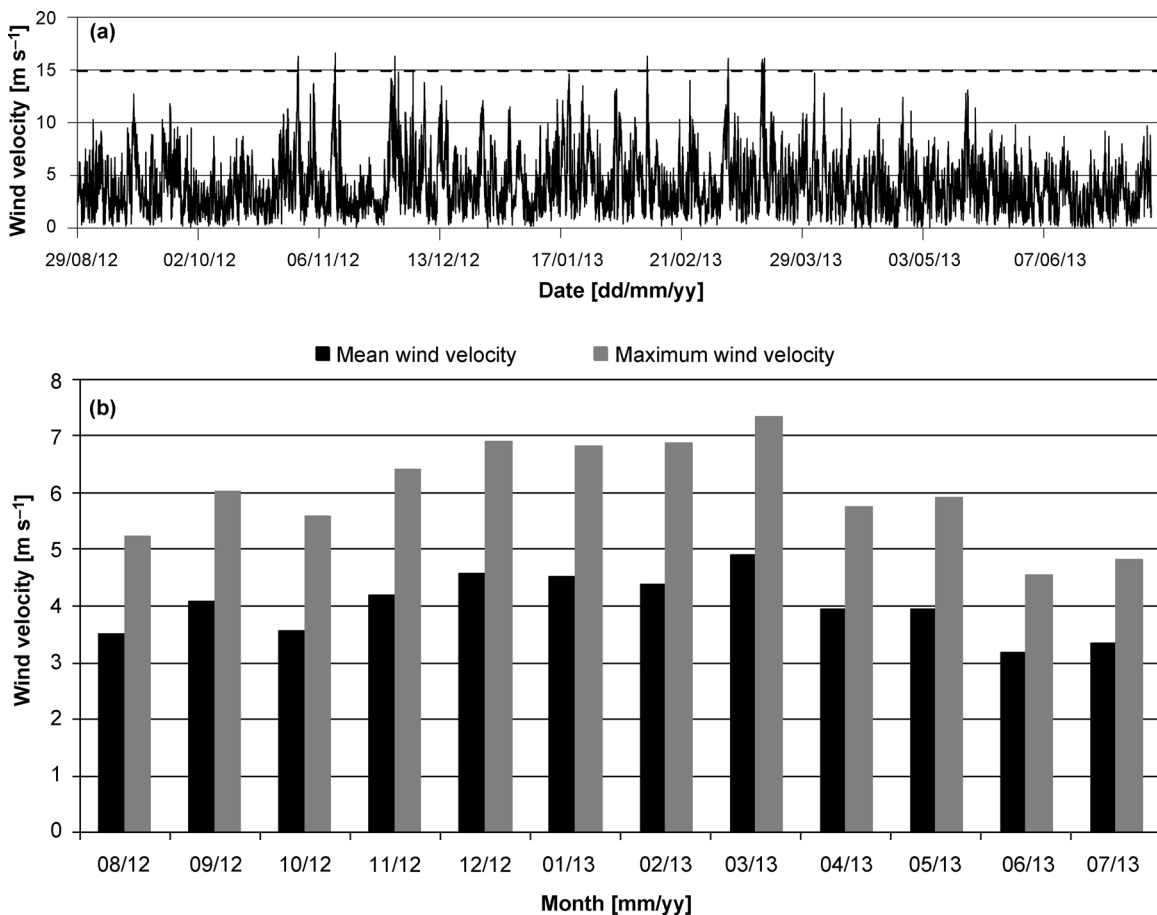


Figure 6 (a) Seasonal diagrams of current velocity and direction distribution measured at 10, 18 and 30-m depth from the 28th August 2012 to the 7th July 2013. Current direction, following oceanographic convention, is the direction to which the currents are going. (b) Seasonal diagrams of current velocity and direction distribution measured at 50 and 70-m depth from the 28th August 2012 to the 7th July 2013. Current direction, following oceanographic convention, is the direction to which the currents are going.

Table 3 Tidal semi-diurnal and diurnal harmonic constituents (M2, S2, K1, and O1) of Giglio Porto expressed in amplitude (in cm) and phase (in degree, °) and calculated between 29/08/2012 and 07/07/2013.

This study (Giglio Porto, Italy)	M2	S2	K1	O1
Period 29/08/2012–07/07/2013	10.5 cm, 258°	3.8 cm, 279°	2.6 cm, 199°	1.3 cm, 121°

**Figure 7** Hourly (in black) and daily mean (in orange) sea level [m] measurements recorded at the weather station of Giglio Porto between August 2012 and July 2013. (For interpretation of the references to color in this figure legend, the reader is referred to the web version of this article.)**Figure 8** Top panel: wind velocity measured at Giglio Porto between August 2012 and July 2013; the black dash line shows the mean value of the near gale wind (15 m s^{-1}). Bottom panel: monthly mean (black) and maximum (grey) values of wind velocity [m s^{-1}].

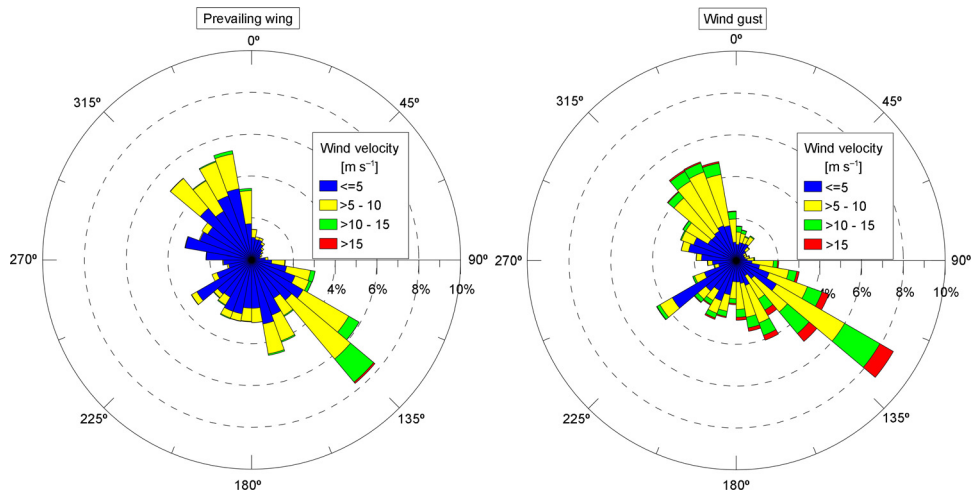


Figure 9 Rose diagrams showing the velocity and the direction of prevailing wind (left panel) and the maximum velocity and direction of gusts (right panel). The wind direction is here defined as the direction from which the wind is coming. Data are measured every 10 min at the weather station of Giglio Porto during the study period.

6. Discussion

The irregular trend of the sea level measured at the weather station of Giglio Porto highlighted the combined action of meteorological forcing (autumn-winter waves, atmospheric pressure and winds) and the astronomical tidal components (Earth-Moon-Sun gravitational relationship). Tidal amplitude was in accordance with the general range of the Tyrrhenian Sea (Alberola et al., 1995; Ferrarin et al., 2013). The main

tidal harmonic constituents found at Giglio Porto retraced the values found by both Polli (1955) at Civitavecchia harbour (Lazio, central Tyrrhenian Sea) and Androsov et al. (2002) at the Scylla station (northern Strait of Messina, Sicily, southern Tyrrhenian Sea) in both amplitude and phase, although our data set did not cover a full year. On the contrary, the Giglio Porto constituents were significantly different from those found in other seas (such as the Adriatic Sea; Janeković and Kuzmíc, 2005) or the Atlantic Ocean (Fanjul et al., 1997) due

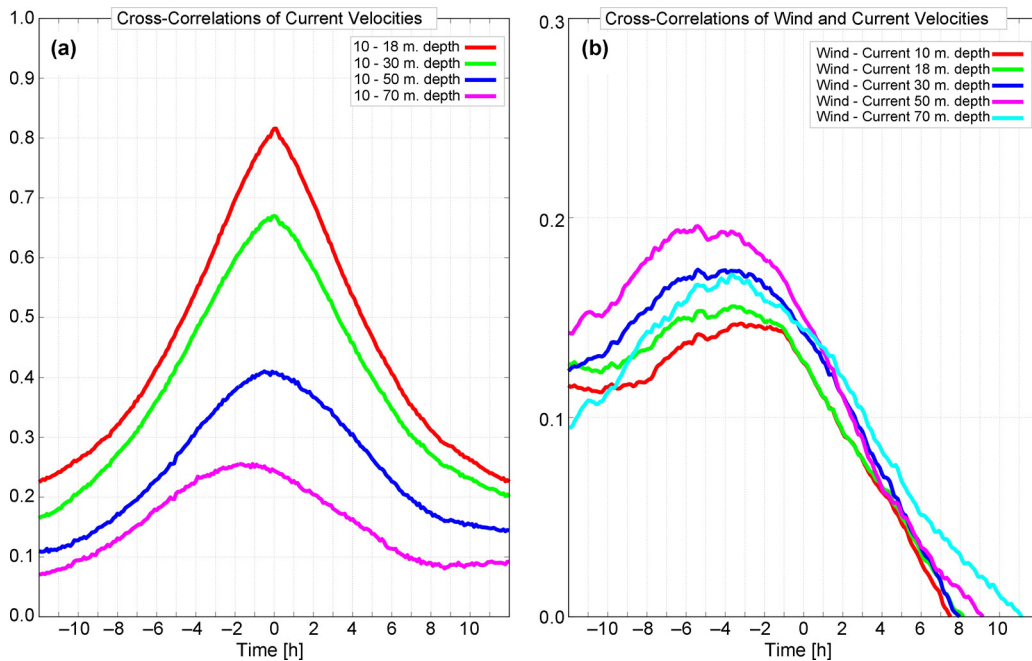


Figure 10 Normalised Cross-Correlations (N-CCF) obtained considering (a) current velocity measured at different depth [current measured at 10 and 18 m (red), 10 and 30 m (green), 10 and 50 m (blue), and 10 and 70 m (pink)], and (b) wind velocity and current velocity measured at different depth [10 m (red), 18 m (green), 30 m (blue), 50 m (pink), and 70 m (cyan)] in the whole period. Values are expressed in a 0–1 scale (y-axis), where 1 corresponds to the perfect correlation level, and 0 to the absence of correlation. The y scale of panel b is zoomed to 0.3 to better show the results. (For interpretation of the references to color in this figure legend, the reader is referred to the web version of this article.)

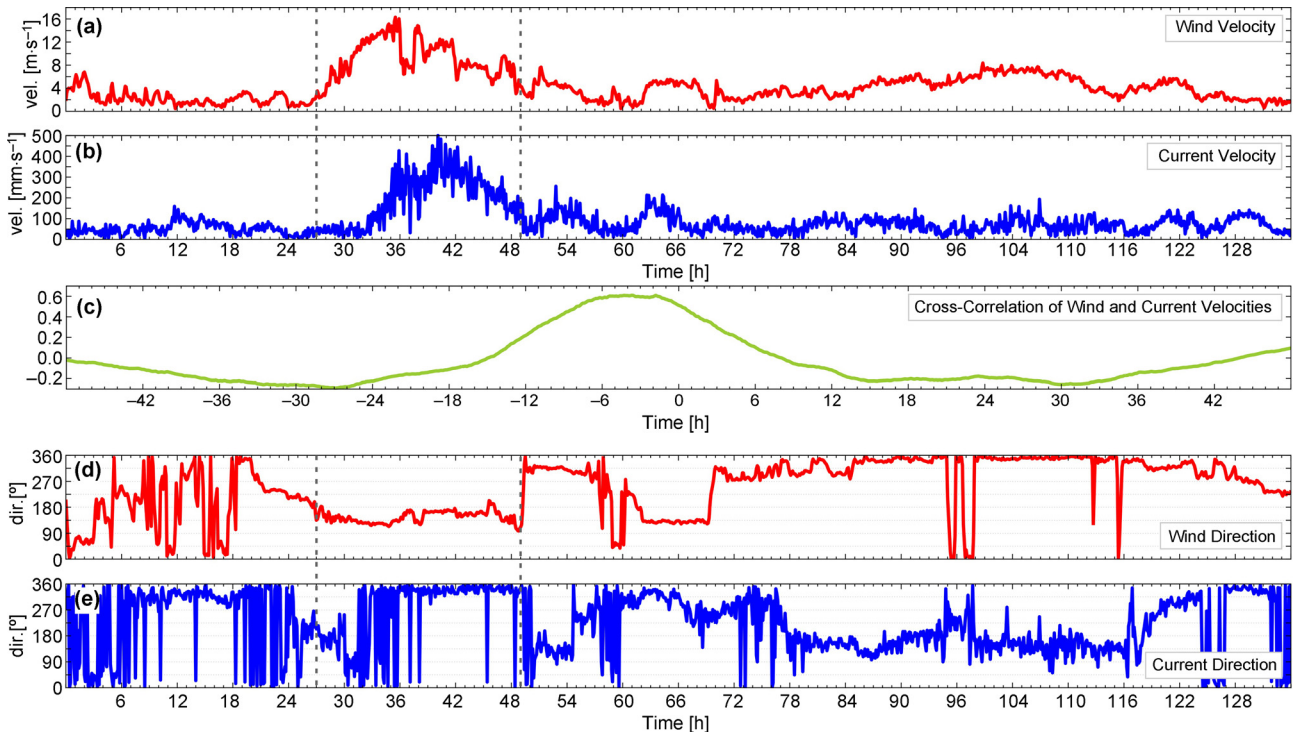


Figure 11 Analysis of the relation between wind and current during the period 9th–15th February 2013. (a) Wind velocity data, (b) current velocity data measured at 10 m depth, (c) Normalised Cross-Correlation Function (N-CCF) obtained considering wind and current velocity at 10-m depth, (d) wind direction data, and (e) current direction data at 10-m depth.

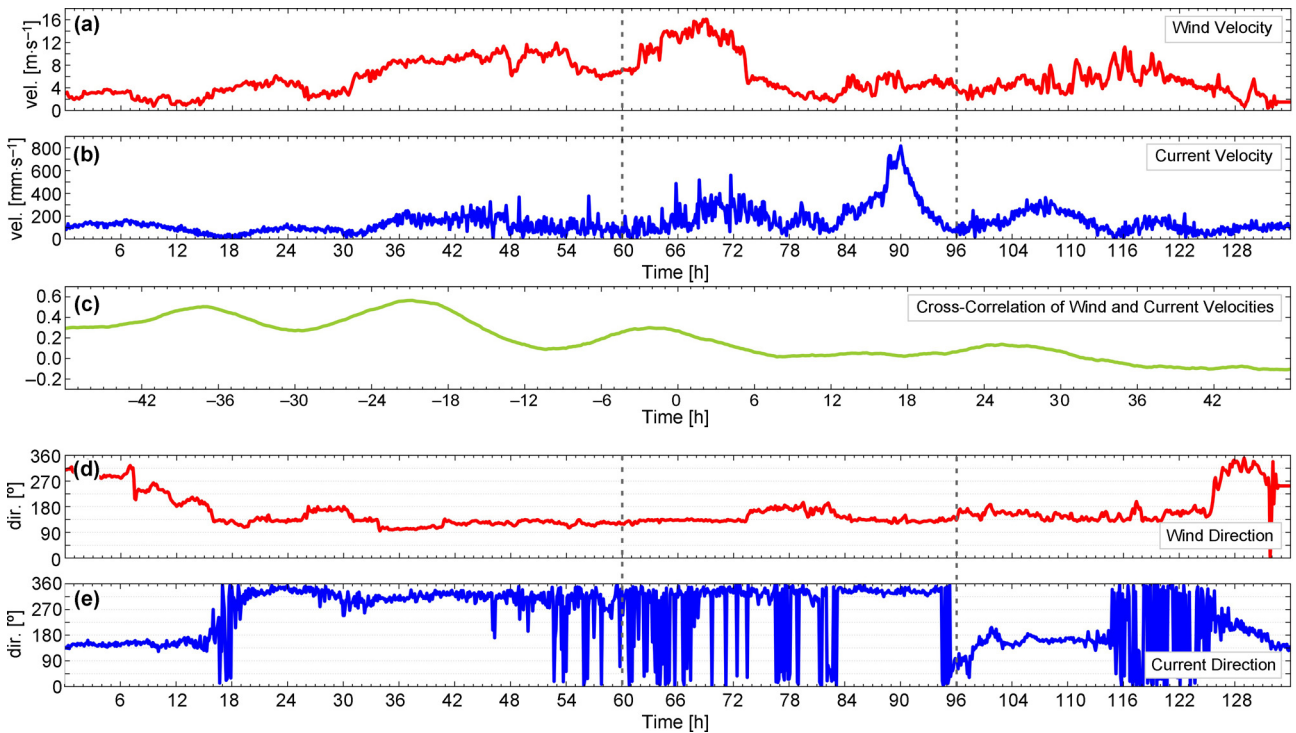


Figure 12 Analysis of the relation between wind and current during the period 3rd–9th March 2013. (a) Wind velocity data, (b) current velocity data measured at 10 m depth, (c) Normalised Cross-Correlation Function (N-CCF) obtained considering wind and current velocity at 10-m depth, (d) wind direction data, and (e) current direction data at 10-m depth.

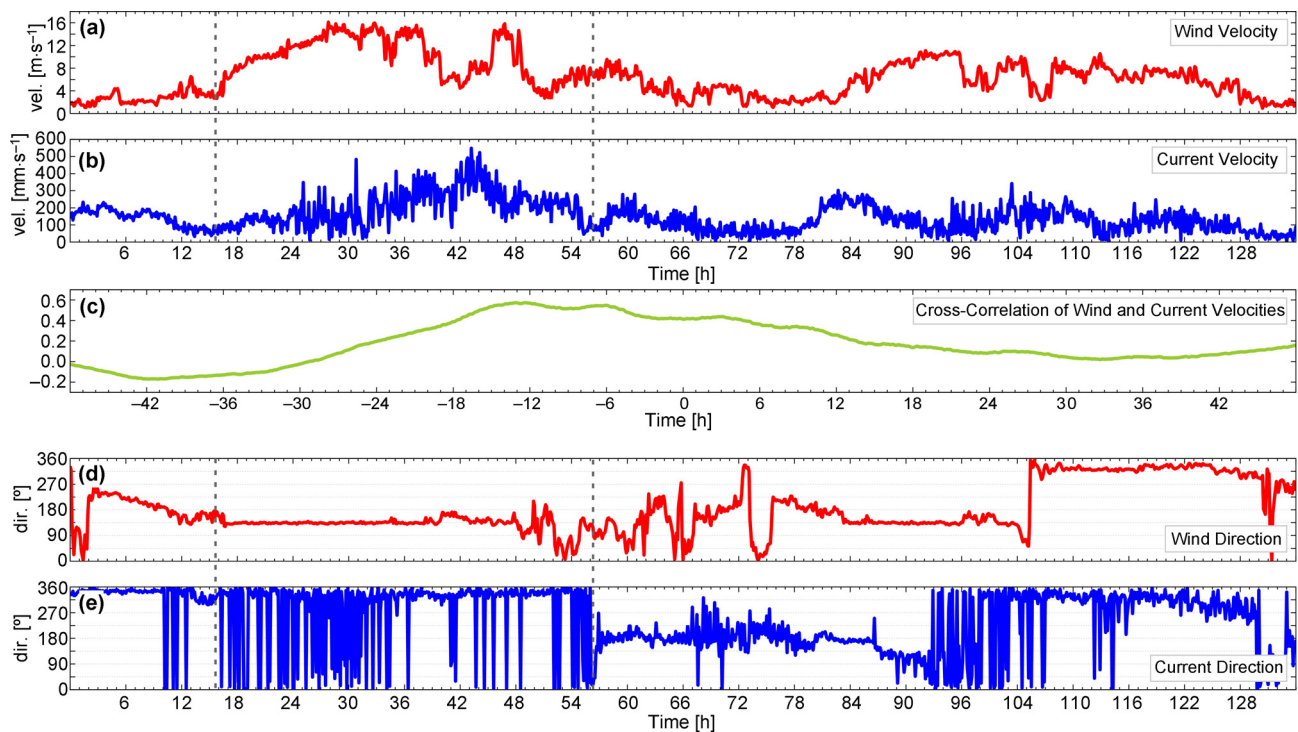


Figure 13 Analysis of the relation between wind and current during the period 16th–22nd March 2013. (a) Wind velocity data, (b) current velocity data measured at 10 m depth, (c) Normalised Cross-Correlation Function (N-CCF) obtained considering wind and current velocity at 10-m depth, (d) wind direction data, and (e) current direction data at 10-m depth.

to the different characteristics and dynamics that influence these water basins.

The results found in the area under study retrace the well known surface circulation characterised by the predominant movement of the water masses along a NW–SE direction (Schroeder et al., 2011), corresponding to the NNW–SSE orientation of the major axis of the Giglio Island and the channel between the island and the mainland (western coast of the Italian peninsula). This characteristic of the flow is evidence of the importance of the topography and morphology of the area (presence of islands, canyons, headlands, etc.) on the current regime (Gravili et al., 2001). The predominance of NW currents in winter and autumn is also induced by the corresponding overall cyclonic Tyrrhenian circulation (Iermano et al., 2016), whereas the frequent inversions of current direction in summer and spring may be related to episodes of Tyrrhenian current reversal (Gravili et al., 2001).

The inter-seasonal and daily variations in both velocity and direction of currents confirm the short period variability of the flow already found in the Tyrrhenian basin on a greater scale by Pierini and Simioli (1998), and subjected to study as a distinctive feature of oceanic basins.

The study of the interactions between external forcing processes and water mass circulation is typically carried out with numerical model simulations (Dumas et al., 2012; Lovato et al., 2010; Molcard et al., 2002; Pierini and Simioli, 1998) or the application, for example, of the Fourier or Wavelet transforms (Fontán et al., 2009; Lovato et al., 2010). The use of the NCCF in our case allowed us to highlight some of the main characteristics of the current structure and

behaviour in relation to external forcing. In fact, the decreasing similarity level in velocity and direction and the time shift in the currents with increasing depth can be evidence of both Ekman's theory (Bjerknes, 1964) and the time necessary for a boundary-forcing current to make a local barotropic adjustment (Gravili et al., 2001).

In general, as in the case of currents, the prevailing wind directions were shown to agree with the NNW–SSE orientation of the island's major axis and also the position of the weather station on the breakwater of Giglio Porto that is protected from winds from the western quadrants by the presence of the island. The direction (NNW–SSE) of the dominant wind is seasonally variable over the Giglio Island shelf, in accordance with the circulation (with opposite directions), as happens in the entire Tyrrhenian Sea (Pierini and Simioli, 1998). Nevertheless, on a long-time scale, the winds and currents do not seem to be correlated parameters in term of velocity and direction, as found in other cases on the continental shelf (e.g. south-eastern Australia; Wood et al., 2016). This condition is the opposite of what was found, for example by Lentz (2007) and Liu and Weisberg (2012), on the Middle Atlantic Bight and West Florida continental shelves, respectively, where the winds are seasonally consistent and generate steady seasonal responses in the circulation. Our results were also in contrast with what was found by Chen et al. (1996) over the Texas-Louisiana shelf, where the correlation between the along-shore currents and wind stress increases close to the coast. In addition to the wind behaviour, these differences can derive from the morphology of the shelf and the coasts and the effect of the prevailing large-scale circulation (Fontán et al., 2009; Liu and Weisberg,

2012; Wood et al., 2016), such as in our case the general Tyrrhenian circulation affects the current measured at the Giglio Porto buoy.

However, strong wind episodes (velocity $> 15 \text{ m s}^{-1}$) over a limited period of observation seem to be able to influence the current velocity pattern creating a cause-effect relationship that prevails in the action of the Tyrrhenian circulation. As already found by Li et al. (2014) in the Gulf of Maine (U.S.A.), the mean coastal current centred near the 100-m isobath can deviate fairly frequently due to effects of wind forcing and small-scale baroclinic structures. The effect of a strong wind on current velocity could be also be facilitated by the homogeneity of the water column; in fact, all the three cases studied took place in winter, when the water column was not yet stratified by the spring and summer warming of the atmosphere (Iermano et al., 2016).

Starting from the elaboration reported in Figs. 11–13, it was noted that without external forcing (e.g. strong wind), near the coast, the current direction reverses by 180° (e.g. counter-current) with respect to the Tyrrhenian flux, while on the occasion of a strong wind from the SE, also near the coast, the current direction alters to the North. This condition was also noted by Gravili et al. (2001) in the Gulf of Naples (south-eastern Tyrrhenian Sea), where a two-day interval of NW flow was followed by a rapid linear transition to an opposite flux.

The sea level and the current direction are not correlated, confirming the low influence of this phenomenon on the water masses in the Tyrrhenian basin, at least at the short distance from the coast that the buoy was located (Clarke and Battisti, 1981). Both the irregular sea level trend and the prevalence of the semi-diurnal M2 constant on the major diurnal constituents supports the argument that the tide does not have an evident and quantifiable (with the cross-correlation use) effect on the current. Therefore, the sea level is influenced by both the general Tyrrhenian circulation and the influence of the wind, phenomena of high intensity and long duration.

7. Conclusions

Thanks to the monitoring plan carried out during the removal operation of the Costa Concordia wreck at Giglio Island (Italy), in situ observations (August 2012–July 2013), including continuous current measurements and wind and sea level recordings, were used to study the variability of these phenomena near the island coasts in the Tyrrhenian basin.

The results showed a significant inter-seasonal variability in both local wind and current velocity, and also in their directions despite the fact that they are mainly forced to move in a NW–SE direction by the presence of the island. The currents are principally dominated by the general Tyrrhenian circulation, and only partially affected by the wind (only in strong wind cases), while the sea level has no effects on the current regime due to its low intensity.

The N-CCF is a metric commonly used to evaluate the degree of similarity between two signals, and is usually applied to seismic, hydrological and meteorological studies in the Earth sciences, but it seems to be a useful tool for oceanographic studies and analysis of the physical processes driving the local circulation and the relationship with forcing

factors. In fact, our contribution, with the N-CCF applied to the influence of the boundary forcing (wind and sea level) on the currents, provided evidence that can highlight and explain cause-effect relationships such as, for example, in the case of the high levels of correlation found between strong SE winds and currents or the absence of a correlation between currents and sea level.

Within this context, further analysis will be necessary to investigate the correlation level between currents and other directions of strong winds (e.g. NE and SW) measured at the Giglio Island to analyse the behaviour of the currents to these types of stress. Furthermore, the application of this method to other study cases in other locations with different oceanographic characteristics will allow us to confirm the usefulness of the N-CCF in oceanographic studies.

Acknowledgments

This research was undertaken using the weather data provided by the LaMMA Consortium of the Region of Tuscany and the Italian Research Council. In particular, the authors wish to thank Dr Carlo Brandini for his support in providing us with the wind and sea level data, and Prof. Paul K. Nixon for the English revision of the paper. Authors wish also to thank the anonymous Reviewers that have greatly improved the manuscript. This study was funded by Research Funding from Titan-Micoperi group. This paper was authorised for publication by Costa Crociere S.p.A.

References

- Alberola, C., Rousseau, S., Millot, C., Astraldi, M., Font, J., Garcia-Lafuente, J., Gasparini, G.P., Send, U., Vangriesheim, A., 1995. Tidal currents in the western Mediterranean Sea. *Oceanol. Acta* 18 (2), 273–284.
- Androsov, A.A., Kagan, B.A., Romanenkov, D.A., Voltzinger, N.E., 2002. Numerical modelling of barotropic tidal dynamics in the strait of Messina. *Adv. Water Resour.* 25 (4), 401–415, [http://dx.doi.org/10.1016/S0309-1708\(02\)00007-6](http://dx.doi.org/10.1016/S0309-1708(02)00007-6).
- Astraldi, M., Gasparini, G.P., 1994. The seasonal characteristics of the circulation in the Tyrrhenian Sea. In: La Viollette, P.E. (Ed.), *Seasonal Interannual Variability of the Western Mediterranean Sea*. Am. Geophys. Union, Washington, DC, 115–134, <http://dx.doi.org/10.1029/CE046p0115>.
- Bjerknes, J., 1964. Atlantic air–sea interaction. In: Landsberg, H.E., Van Mieghem, J. (Eds.), *Advances in Geophysics*. Academic Press, New York/London, 1–81.
- Bolaños, R., Tornfeldt Sørensen, J.V., Benetazzo, A., Carniel, S., Sclavo, M., 2014. Modelling ocean currents in the northern Adriatic Sea. *Cont. Shelf Res.* 87, 54–72, <http://dx.doi.org/10.1016/j.csr.2014.03.009>.
- Campillo, M., Paul, A., 2003. Long-range correlations in the diffusion seismic coda. *Science* 299 (5606), 547–549, <http://dx.doi.org/10.1126/science.1078551>.
- Capello, M., Cutroneo, L., Ferretti, G., Gallino, S., Canepa, G., 2016. Changes in the physical characteristics of the water column at the mouth of a torrent during an extreme rainfall event. *J. Hydrol.* 541 (Pt. A), 146–157, <http://dx.doi.org/10.1016/j.jhydrol.2015.12.009>.
- Cazenave, A., Bonnefond, P., Mercier, F., Dominh, K., Toumazou, V., 2002. Sea level variations in the Mediterranean Sea and Black Sea from satellite altimetry and tide gauges. *Global Planet. Change* 34 (1–2), 59–86, [http://dx.doi.org/10.1016/S0921-8181\(02\)00106-6](http://dx.doi.org/10.1016/S0921-8181(02)00106-6).

- Chen, C., Reid, R.O., Nowlin Jr., W.D., 1996. Near-inertial oscillations over the Texas–Louisiana shelf. *J. Geophys. Res.* 101 (C2), 3509–3524.
- Clarke, A.J., Battisti, D.S., 1981. The effect of continental shelves on tides. *Deep-Sea Res.* 28A (7), 665–682.
- Dumas, F., Le Gendre, R., Thomas, Y., Andréfouët, S., 2012. Tidal flushing and wind driven circulation of Ahe atoll lagoon (Tuamotu Archipelago, French Polynesia) from in situ observations and numerical modelling. *Mar. Pollut. Bull.* 65 (10–12), 425–440, <http://dx.doi.org/10.1016/j.marpolbul.2012.05.041>.
- Fanjul, E.A., Gomez, B.P., Sanchez-Arevalo, I.R., 1997. A description of the tides in the Eastern North Atlantic. *Prog. Oceanogr.* 40 (1–4), 217–244, [http://dx.doi.org/10.1016/S0079-6611\(98\)00003-2](http://dx.doi.org/10.1016/S0079-6611(98)00003-2).
- Ferrarin, C., Roland, A., Bajo, M., Umgieser, G., Cucco, A., Davolio, S., Buzzì, A., Malguzzi, P., Drofa, O., 2013. Tide-surge-wave modelling and forecasting in the Mediterranean Sea with focus on the Italian coast. *Ocean Model.* 61, 38–48, <http://dx.doi.org/10.1016/j.ocemod.2012.10.003>.
- Fontán, A., González, M., Wells, N., Collins, M., Mader, J., Ferrer, L., Esnaola, G., Uriarte, A., 2009. Tidal and wind-induced circulation within the Southeastern limit of the Bay of Biscay: Pasaia Bay. *Basque Coast. Cont. Shelf Res.* 29 (8), 998–1007, <http://dx.doi.org/10.1016/j.csr.2008.12.013>.
- Frezza, V., Carboni, M.G., 2009. Distribution of recent foraminiferal assemblages near the Ombrone River mouth (Northern Tyrrhenian Sea, Italy). *Rev. Micropléontol.* 52 (1), 43–66, <http://dx.doi.org/10.1016/j.revmic.2007.08.007>.
- Gravili, D., Napolitano, E., Pierini, S., 2001. Barotropic aspects of the dynamics of the Gulf of Naples (Tyrrhenian Sea). *Cont. Shelf Res.* 21 (5), 455–471, [http://dx.doi.org/10.1016/S0278-4343\(00\)00100-X](http://dx.doi.org/10.1016/S0278-4343(00)00100-X).
- Halverson, M.J., 2014. Atmospheric and tidal forcing of the exchange between Prince William Sound and the Gulf of Alaska. *Dyn. Atmos. Ocean.* 65, 86–106, <http://dx.doi.org/10.1016/j.dynatmoce.2013.12.001>.
- Iermano, I., Moore, A.M., Zambianchi, E., 2016. Impacts of 4-dimensional variational data assimilation in a coastal ocean model of southern Tyrrhenian Sea. *J. Mar. Syst.* 154 (Pt. B), 157–171, <http://dx.doi.org/10.1016/j.jmarsys.2015.09.006>.
- Janeković, I., Kuzmić, M., 2005. Numerical simulation of the Adriatic Sea principal tidal constituents. *Ann. Geophys.* 23, 3207–3218.
- Lentz, S.J., 2007. Seasonal variations in the circulation over the Middle Atlantic Bight continental shelf. *J. Phys. Oceanogr.* 38, 1486–1500, <http://dx.doi.org/10.1175/2007JPO3767.1>.
- Li, Y., He, R., McGillicuddy Jr., D.J., 2014. Seasonal and interannual variability in Gulf of Maine hydrodynamics: 2002–2011. *Deep-Sea Res.* 103 (Pt. II), 210–222, <http://dx.doi.org/10.1016/j.dsr.2013.03.001>.
- Liu, Y., Weisberg, R.H., 2012. Seasonal variability on the West Florida Shelf. *Prog. Oceanogr.* 104, 80–98, <http://dx.doi.org/10.1016/j.pocean.2012.06.001>.
- Lovato, T., Androsov, A., Romanenkov, D., Rubino, A., 2010. The tidal and wind induced hydrodynamics of the composite system Adriatic Sea/Lagoon of Venice. *Cont. Shelf Res.* 30 (6), 692–706, <http://dx.doi.org/10.1016/j.csr.2010.01.005>.
- Mc Millen, R.T., 1987. An eddy correlation technique with extended applicability to non-simple terrain. *Bound.-Lay Meteorol.* 43 (3), 231–245, <http://dx.doi.org/10.1007/BF00128405>.
- Millot, C., Taupier-Letage, I., 2005. Circulation in the Mediterranean Sea. *Handb. Environ. Chem.* 5 (Pt K), 29–66, <http://dx.doi.org/10.1007/b107143>.
- Molcard, A., Pinardi, N., Iskandarani, M., Haivogel, D.B., 2002. Wind driven general circulation of the Mediterranean Sea simulated with a Spectral Element Ocean Model. *Dyn. Atmos. Ocean.* 35 (2), 97–130, [http://dx.doi.org/10.1016/S0377-0265\(01\)00080-X](http://dx.doi.org/10.1016/S0377-0265(01)00080-X).
- Mosetti, F., Purga, N., 1982. First results on long- and midperiod tide distribution in Italian seas and their existence in the groundwater. *Il Nuovo Cimento* 5C (2), 143–158.
- Naranjo, C., Garcia-Lafuente, J., Sannino, G., Sanchez-Garrido, J. C., 2014. How much do tides affect the circulation of the Mediterranean Sea? From local processes in the Strait of Gibraltar to basin-scale effects. *Prog. Oceanogr.* 127, 108–116, <http://dx.doi.org/10.1016/j.pocean.2014.06.005>.
- Pierini, S., Simioli, A., 1998. A wind-driven circulation model of the Tyrrhenian Sea area. *J. Mar. Syst.* 18, 161–178.
- Polli, S., 1955. Variazioni delle costanti armoniche delle maree col livello del mare. *Ann. Geofis.* 8 (2), 202–207.
- Rossetti, F., Faccenna, C., Jolivet, L., Funicello, R., Tecce, F., Brunet, C., 1999. Syn- versus post-orogenic extension: the case of Giglio Island (Northern Tyrrhenian Sea, Italy). *Tectonophysics* 304 (1–2), 71–93, [http://dx.doi.org/10.1016/S0040-1951\(98\)00304-7](http://dx.doi.org/10.1016/S0040-1951(98)00304-7).
- Scherbaum, F., Johnson, J., Rietbrock, A., 1999. PITSA (Programmable Interactive Toolbox for Seismological Analysis). PITSA Users Manual, 222 pp.
- Schroeder, K., Haza, A.C., Griffa, A., Özgökmen, T.M., Poulain, P.M., Gerin, R., Peggion, G., Rixen, M., 2011. Relative dispersion in the Liguro-Provençal basin: from sub-mesoscale to mesoscale. *Deep-Sea Res. Pt. I* 58 (3), 209–228, <http://dx.doi.org/10.1016/j.dsr.2010.11.004>.
- Thouvenot, F., Jenatton, L., Scafidi, D., Turino, C., Potin, B., Ferretti, G., 2016. Encore ubaye: earthquake swarms, foreshocks, and aftershocks in the Southern French Alps. *Bull. Seismol. Soc. Am.* 106 (5), 2244–2257, <http://dx.doi.org/10.1785/0120150249>.
- Tsai, D.M., Lin, C.T., Chen, J.F., 2003. The evaluation of normalized cross correlations for defect detection. *Pattern Recogn. Lett.* 24 (15), 2525–2535, [http://dx.doi.org/10.1016/S0167-8655\(03\)00098-9](http://dx.doi.org/10.1016/S0167-8655(03)00098-9).
- Tsimplis, M., Spada, G., Marcos, M., Flemming, N., 2011. Multi-decadal sea level trends and land movements in the Mediterranean Sea with estimates of factors perturbing tide gauge data and cumulative uncertainties. *Global Planet. Change* 76 (1–2), 63–76, <http://dx.doi.org/10.1016/j.gloplacha.2010.12.002>.
- Vetrano, A., Napolitano, E., Iacono, R., Schroeder, K., Gasparini, G. P., 2010. Tyrrhenian Sea circulation and water mass fluxes in spring 2004: observations and model results. *J. Geophys. Res.* 115, C06023, <http://dx.doi.org/10.1029/2009JC005680>.
- Wei, W.W.S., 2006. Time Series Analysis, Univariate and Multivariate Methods, 2nd ed. Addison-Wesley, Boston, MA, 614 pp.
- White, R.J., Peterson, B.M., 1994. Comments on cross-correlation methodology in variability studies of active galactic nuclei. *Publ. Astron. Soc. Pac.* 106 (702), 879–889.
- Wood, J.E., Schaeffer, A., Roughan, M., Tate, P.M., 2016. Seasonal variability in the continental shelf waters off southeastern Australia: fact or fiction? *Cont. Shelf Res.* 112, 92–103, <http://dx.doi.org/10.1016/j.csr.2015.11.006>.



Available online at www.sciencedirect.com

ScienceDirect

journal homepage: www.journals.elsevier.com/oceanologia/



ORIGINAL RESEARCH ARTICLE

Spatio-temporal variability of the phytoplankton biomass in the Levantine basin between 2002 and 2015 using MODIS products

Roy El Hourany^a, Ali Fadel^a, Elissar Gemayel^b, Marie Abboud-Abi Saab^b, Ghaleb Faour^{a,*}

^a National Center for Remote Sensing, National Council for Scientific Research (CNRS), Beirut, Lebanon

^b National Center for Marine Sciences, National Council for Scientific Research (CNRS), Batroun, Lebanon

Received 13 May 2016; accepted 25 December 2016

Available online 6 January 2017

KEYWORDS

Mediterranean Sea;
Levantine basin;
Remote sensing;
MODIS;
Phytoplankton bloom;
Chlorophyll-*a*

Summary The Levantine basin in the Eastern Mediterranean Sea is subject to spatial and seasonal variations in primary production and physical-chemical properties both on a short and long-term basis. In this study, the monthly means of daily MODIS product images were averaged between 2002 and 2015, and used to characterize the phytoplankton blooms in different bioregions of the Levantine basin. The selected products were the sea surface temperature (SST), the chlorophyll-*a* concentration (Chl-*a*), the diffuse attenuation coefficient for downwelling irradiance at 490 nm (Kd₄₉₀) and the colored dissolved organic matter index (CDOM_{M_index}). Our results showed that phytoplankton blooms were spatially and temporally variable. They occurred in late autumn at the Nile Delta, in early spring and late summer at the eastern coastline, and in spring at the northeastern coastline. The northern coastline and the open water had a common bloom occurring in winter. The Nile Delta was found to be the most productive area of the Levantine basin showing high Chl-*a*. Kd₄₉₀ and Chl-*a* present a parallel co-variation indicating a dominance of Case 1 waters in the Levantine basin. The CDOM_{M_index} shows a phase shift with the Chl-*a* fluctuation. A strong inverse correlation was observed between both Chl-*a* and CDOM_{M_index} with SST, connoting an indirect relation represented by a depression of CDOM in summer by photobleaching, and a suppression of the chlorophyll-*a* concentration due to water

* Corresponding author at: National Center for Remote Sensing, National Council for Scientific Research (CNRS), P.O. Box 11-8281, Riad El Solh, 1107 2260 Beirut, Lebanon. Tel.: +961 3823423.

E-mail address: gfaour@cnrs.edu.lb (G. Faour).

Peer review under the responsibility of Institute of Oceanology of the Polish Academy of Sciences.



Production and hosting by Elsevier

<http://dx.doi.org/10.1016/j.oceano.2016.12.002>

0078-3234/© 2017 Institute of Oceanology of the Polish Academy of Sciences. Production and hosting by Elsevier Sp. z o.o. This is an open access article under the CC BY-NC-ND license (<http://creativecommons.org/licenses/by-nc-nd/4.0/>).

stratification, together with nutrient stress. An overestimation of the Chl-*a* values had been signaled by the use of the CDOM_index, suggesting a correction plan in a latter study.

© 2017 Institute of Oceanology of the Polish Academy of Sciences. Production and hosting by Elsevier Sp. z o.o. This is an open access article under the CC BY-NC-ND license (<http://creativecommons.org/licenses/by-nc-nd/4.0/>).

1. Introduction

The Mediterranean Sea is a semi-enclosed basin, covering approximately 0.8% of the world's ocean surface area. Although it has limited geographical dimensions, it is considered one of the most complex marine environments where little is known with regard to circulation dynamics, biogeochemistry and biological activity (Tanhua et al., 2013). The Mediterranean Sea presents a deficit in hydrological balance, as evaporation exceeds the supply of fresh water from streams and precipitation. This deficit is partially compensated by the inflow of Atlantic waters through the Strait of Gibraltar. This results in fresh, nutrient-poor surface flow into the basin with saltier, nutrient-rich deeper water outflow through the Strait of Gibraltar (Bethoux et al., 1992). Hydrological differences along the basin cause the presence of an increasing oligotrophic gradient from west to east.

The Eastern Mediterranean behaves in a similar manner, with surface inflow and deeper water outflow through the Straits of Sicily. This results in a west to east gradient of decreasing surface chlorophyll-*a* concentration (Chl-*a*) (Turley et al., 2000) that was observed from space (Antoine et al., 1995), with the Eastern Mediterranean Levantine waters exhibiting highly oligotrophic conditions. As a result, surface Chl-*a* in the Levantine basin normally don't exceed 0.4 mg m^{-3} (Abdel-Moati, 1990; Dowidar, 1984; Krom et al., 1991; Yacobi et al., 1995) except near the Nile Delta coast and other adjacent coasts where it can reach up to 80 mg m^{-3} (EIMP-CWMP, 2007).

The Levantine basin regroups the Egyptian northern coast where the Nile River discharges on its delta, the Sinai Peninsula's northern coast, the Israeli coast, the Lebanese coast, the Syrian coast, the southern Turkish coast and the coast of Cyprus. This region is nourished by small water streams, and the Nile River.

The knowledge of the space and time heterogeneity of phytoplankton growth in oligotrophic to ultra-oligotrophic conditions is essential to understand the marine ecosystem dynamics (Mann and Lazier, 2006). In the last decade, remote sensing of surface optical properties has provided synoptic views of the abundance and distribution of sea surface constituents, such as the concentration of Chl-*a* pigments (Su et al., 2015). Nowadays, many studies showed that time series of remotely sensed data can provide information on phytoplankton growth patterns, and related environmental conditions, to serve *in situ* assessments of ecosystem dynamics over wide space and time scales (Brando et al., 2012; Devlin et al., 2012; Kennedy et al., 2012; Schroeder et al., 2012).

The aim of the present work is to assess recurrent algal blooms in the Levantine basin, by using optical remote sensing data. To this end, a time series of data collected by the MODIS Terra and Aqua missions was selected to explore the large-scale, long-term features of the Chl-*a* fields in the

Levantine basin, between 2002 and 2015. In the following the MODIS-derived multi-annual database, used here to examine the variability of the Chl-*a* field at a monthly and climatological scale, will be introduced, together with a statistical application. Finally, the spatiotemporal patterns emerging from this analysis will be discussed, simultaneously with other MODIS remotely sensed parameters; sea surface temperature (SST), colored dissolved organic matter index (CDOM_index), and the diffuse attenuation coefficient for downwelling irradiance at 490 nm (Kd_490) and compared to previous studies results.

2. Material and methods

The MODIS Terra and aqua daily Level 2 products of SST, Chl-*a*, CDOM_index and Kd_490 computed with sensor standard algorithms from 2002 till 2015 were provided by the ocean-color.gsfc.nasa.gov portal.

The standard OC3 algorithm returns the near-surface Chl-*a* in mg m^{-3} at a spatial resolution of 1 km, calculated using an empirical relationship derived from *in situ* measurements of Chl-*a* and blue-to-green band ratios of water-leaving remote sensing reflectances (Rrs) developed by O'Reilly et al. (1998) and can be expressed as the following:

$$\log_{10}(\text{Chl-}a) = 0.2424 - 2.7423R + 1.8017R^2 + 0.0015R^3 - 0.1228R^4 \quad (1)$$

with

$$R = \log_{10} \left(\frac{\text{Max}(Rrs_{443}, Rrs_{488})}{Rrs_{547}} \right) \quad (2)$$

The empirical algorithm OC3M is an adapted form for MODIS, developed from SeaWiFS OC2 and OC4 algorithms.

Level 2 satellite-to-*in situ* match-up validation results are available for MODIS from the validation tool of the SeaWiFS Bio-Optical Archive and Storage System (SeaBASS), showing a global correlation coefficient above 0.75 with a RMSE = 0.3 mg m^{-3} . For this study, the same standard sensor algorithm was used for waters differing in the degree of eutrophication.

For the SST estimation, the satellite measurement is made by sensing the ocean radiation in two or more wavelengths within the infrared part of the electromagnetic spectrum which can then be empirically related to SST. In this case, the MODIS SST product provides sea surface temperature [°C] at a spatial resolution of 1 km.

The Kd_490 (in m^{-1} , 1-km spatial resolution) is calculated using an empirical relationship derived from *in situ* spectroradiometric data from oceanographic stations of Kd_490 and blue-to-green band ratios of remote sensing reflectances (Rrs) belonging to a wide variety of water types (Austin and Petzold, 1981).

The sensor default algorithm can be expressed as the following:

$$\text{KD2M} : \log_{10}(K_{\text{bio}}(490)) = -0.8813 - 2.035R + 2.5878R^2 - 3.4885R^3 - 1.5061R^4, \quad (3)$$

$$K_{d490} = K_{\text{bio}}(490) + 0.0166 \quad (4)$$

with

$$R = \log_{10} \left(\frac{R_{rs488}}{R_{rs547}} \right). \quad (5)$$

Examining the consistency of the empirical algorithm has been the object of many studies (Lee, 2005; Morel et al., 2007; O'Reilly et al., 2000; Werdell and Bailey, 2005; Yeh et al., 1997).

And last, Morel and Gentili (2009) stated that the CDOM absorption coefficient, noted α , tends to increase with increasing Chl-*a* in a non-linear manner, according to:

$$\alpha(400; \text{Chl-}a) = 0.065 \text{Chl-}a^{0.63}. \quad (6)$$

A quantitative way of analytically showing the relationship when the CDOM–[Chl] proportions change, consists of imposing deviations from the equation above, by introducing a factor larger or lesser than unity, noted as CDOM_index:

$$\alpha(400; \text{Chl-}a) = \text{CDOM}_{\text{index}} 0.065 \text{Chl-}a^{0.63}. \quad (7)$$

The α values for the other wavelengths of interest are:

$$\alpha(412; \text{Chl-}a) = \text{CDOM}_{\text{index}} 0.0524 \text{Chl-}a^{0.63}, \quad (8)$$

$$\alpha(440; \text{Chl-}a) = \text{CDOM}_{\text{index}} 0.0316 \text{Chl-}a^{0.63}, \quad (9)$$

$$\alpha(490; \text{Chl-}a) = \text{CDOM}_{\text{index}} 0.0129 \text{Chl-}a^{0.63}, \quad (10)$$

$$\alpha(555; \text{Chl-}a) = \text{CDOM}_{\text{index}} 0.004 \text{Chl-}a^{0.63}. \quad (11)$$

The colored dissolved organic matter index (Level 2, 1-km resolution) quantifies the deviation in the relationship between the absorption of CDOM and Chl-*a*, where 1 represents the mean for Case 1 waters, and values above or below 1 indicate excess or deficit in CDOM (Morel and Gentili, 2009). Its primary purpose is to correct chlorophyll retrievals as the index provides a direct estimate of a deviation index, described as the ratio between the actual CDOM content and the normal content, expected in Case 1 waters from the local chlorophyll concentration. Therefore, the index value above or below 1 can indicate an underestimation or overestimation of the estimated Chl-*a* using the standard sensor algorithm. The only validation work was performed by Morel and Gentili (2009) following the algorithm retrieval.

A selection of 4173 daily images was performed for each product while merging both MODIS Terra and Aqua daily images in order to select and retain the maximum of best quality pixels. The selection of these pixels was possible due to many quality Level 2 flags and masks suggested on SeaDas, complying with the masks used for the Level 3 binned products on the oceancolor.gsfc.nasa.gov portal. The binning process is based on the NASA SeaWiFS binning operator, giving the ability to aggregate the pixel data into arithmetic mean

while confining to each pixel its place in a Level 3 grid using a geographical information system. While calculating the arithmetic mean, the quality flags and masks allow excluding the pixels that are affected by clouds, sunglint, very high radiance, straylight contamination, low water leaving radiance, algorithm failure, atmospheric correction failure and suspected navigation quality. In the end, the output that emerges from this process is a time series of binned monthly images with a resolution of 1 km².

3. Information retrieval

Lavender et al. (2009) have conducted a research over the Egyptian continental shelf to assess the temporal shifts of the chlorophyll level in this region and detect the Nile's bloom between 1997 and 2006. In order to detect the surface Chl-*a* variability and its spatial changes across the Delta shelf, the area was divided geographically into two bio-geographical areas, the inner (0–50 m depth) and outer (50–200 m depth) shelf, based on knowledge of the biophysical regimes (effects alongshore currents and surface run-off on quality and productivity of coastal water off the delta coast).

Therefore, a similar division was applied in this study, on the Nile delta's shelf and on the Gulf of Iskenderun due to the presence of a large continental shelf, while also adding an open water zone (>200 m in depth) as a bio-geographical area. Along the eastern and northern coastlines, an additional bio-geographical area was also created: from 0 till 200 m in depth, regarding the narrowness of the continental shelf and the number of pixels covered by this area (Fig. 1).

In order to determine each subdivision's ocean color characteristics, a bathymetry image (ETOPO-1 bedrock) is used to limit each subdivision in a drawn bathymetry mask using ArcGIS 10. ETOPO1 is an arc-minute global relief model of Earth's surface that integrates land topography and ocean bathymetry. It was built from numerous global and regional data sets and provided by NOAA agency and acquired from ngdc.noaa.gov.

The calculated average of every subdivision for each of the parameters was done using ArcGIS 10 while extracting the value of the pixels averaged under each of the bathymetry mask, and followed by a statistic study performed on SPSS statistics 20. The latter consists on the retrieval of the maxima, minima, average, and standard deviation of the parameters time series for each subdivision. A Pearson correlation study was performed *via* pairing the time series of Chl-*a* and Kd₄₉₀, Chl-*a* and CDOM_index, Chl-*a* and SST and finally CDOM_index and SST for each subdivision.

4. Results

4.1. Statistical and climatology results

The biogeographic subdivisions were applied on the computed monthly images of SST (Fig. 2), Chl-*a* (Fig. 3), CDOM_index (Fig. 4) and Kd₄₉₀ (Fig. 5) in order to assess the variation of these features monthly between 2002 and 2015.

The recordings of the sea surface temperature between 2002 and 2015 follow an annual cycle with the lowest temperatures in February and March and the highest temperatures in July and August. In this time laps, the lowest monthly sea surface temperature average recorded was on February

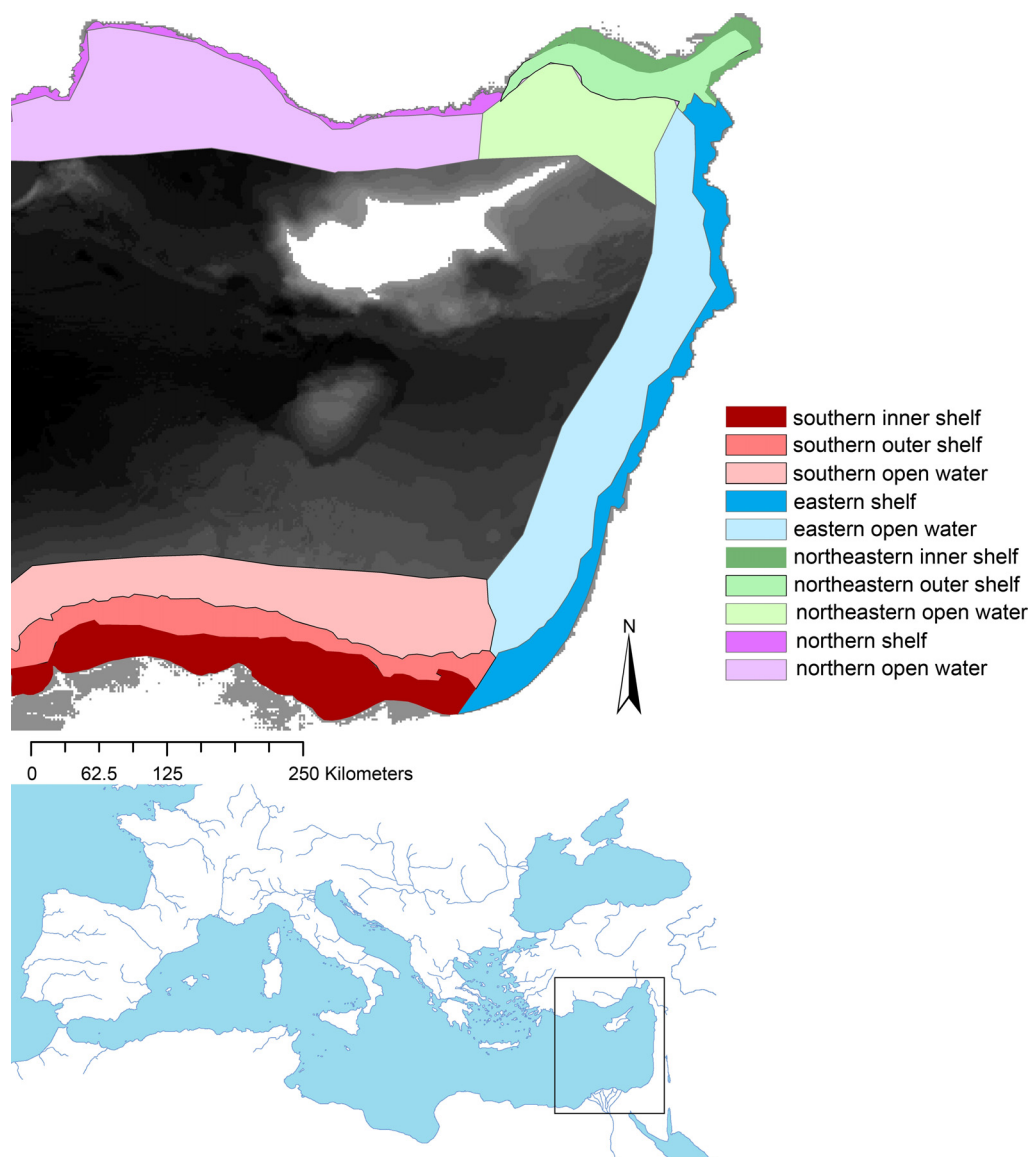


Figure 1 The Levantine basin subdivided into biogeographic regions using ETOPO-1 bathymetry map.

2004 with 16.51°C , and the highest monthly temperature average recorded was on August 2012 with 29.22°C .

The monthly averaged Chl-*a* (Fig. 6) shows a seasonal rhythmicity in open water, but it is altered while moving to the coast, characterized with higher Chl-*a* and turbid waters. These results show that the monthly climatology of Chl-*a* (Fig. 7) is different for each biogeographic subdivision. For instance, the southern coastal region is characterized by an increase of Chl-*a* in late autumn, reaching a maximum mean of 2.8 mg m^{-3} in December 2010, whereas in the eastern coastal region the Chl-*a* peak is observed in late winter, recording a peak of 1.28 mg m^{-3} in April 2006, and early autumn, reaching a maximum mean of 1.1 mg m^{-3} in September 2005. In the Gulf of Iskenderun and Mersin Bay, the Chl-*a* peak is observed in spring, reaching a maximum mean of 3.8 mg m^{-3} in April 2012, followed by a slight increase in late summer, and in the northern coastal region the Chl-*a* reach a maximum in winter, at 1.1 mg m^{-3} in February 2009. Finally, in the open water region, the Chl-*a* peak is observed in winter, reaching a maximum mean at 0.33 mg m^{-3} (Table 1).

The monthly average of the K_d_{490} ranges between 0.2 m^{-1} (22.5 m of euphotic depth) in December 2010 and 0.12 m^{-1} in June 2007 near the delta, 0.11 m^{-1} in April 2006 (41 m of euphotic depth) and 0.04 m^{-1} in May 2014 near the eastern coast, 0.27 m^{-1} (16.7 m of euphotic depth) in April 2012 and 0.08 m^{-1} in March 2014 at the Gulf of Iskenderun and Mersin Bay, 0.1 m^{-1} (45 m of euphotic depth) and 0.03 m^{-1} in July 2014 at the northern coast (Table 1).

The CDOM_index values are all above 1, fluctuating between 2 and 5.78. The index shows that the highest overall mean is recorded on the southern inner shelf with 4.25. Yet the correspondent variability within the series from 2002 till 2015 is the least, recording a standard deviation of 0.54. On the other hand, the lowest mean is recorded on the northern shelf, with an index of 3.17, and with the highest correspondent standard deviation of 0.86 within the time series. While observing the CDOM_index climatology images, a preeminent cluster of high CDOM_index is visible at the southern outer shelf and at the northeastern outer shelf and some regions witness a seasonal CDOM_index fluctuation (Table 1).

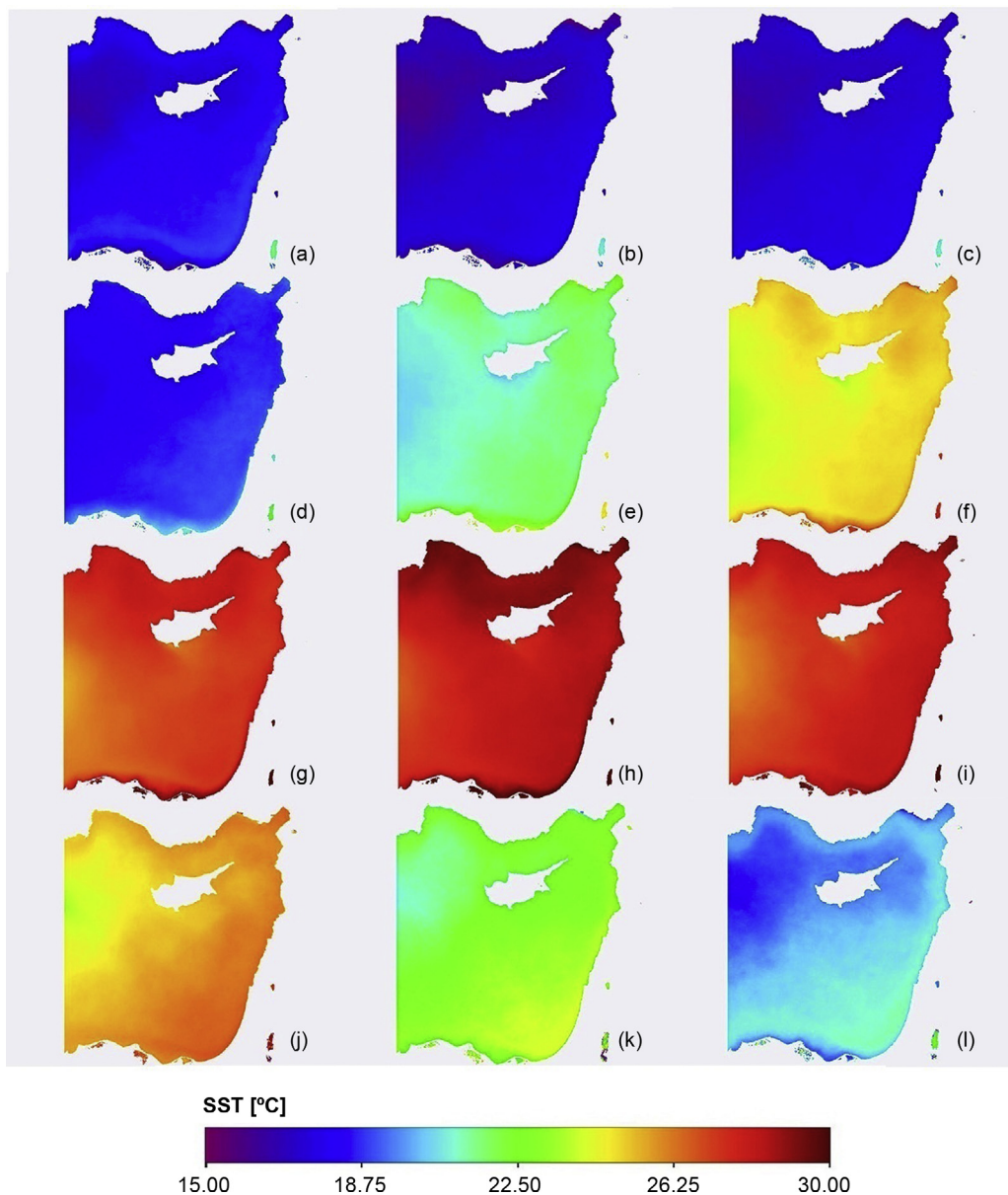


Figure 2 Monthly climatology sea surface temperature averaged using Level 2 SST data from MODIS Aqua and Terra, over the 14 studied years in the Levantine basin [(a) January, (b) February, (c) March, (d) April, (e) May, (f) June, (g) July, (h) August, (i) September, (j) October, (k) November, (l) December].

The climatology monthly average calculated for each parameter for the Levantine basin (Fig. 8) shows that the Chl-*a* and Kd₄₉₀ are covariant, drawing a similar behavior recording the highest values in February, and the lowest in July. Whereas the CDOM_{index} is ahead with a one-month phase shift, showing a maximum index value in March and the lowest value in September. The SST is inversely behaving where the highest SST recorded in August and the lowest in February.

4.2. Pearson correlation results

The correlation between the Chl-*a* and the attenuation coefficient Kd₄₉₀ monthly means was highly significant in

all biogeographic subdivisions (above 0.9, significant at the 0.01 level) (Fig. 9).

The Chl-*a* and the colored dissolved organic matter index monthly means were weakly correlated in the subdivisions (0; –50 m). However, the correlation strengthens while passing gradually to the open waters, representing a correlation factor shifting from 0.009 and 0.128 at the shelf to a significant 0.57 in the open waters. In addition, the correlative analysis between the two products data (Chl-*a*, CDOM_{index}) and the SST monthly means showed a high inverse correlation factor while moving far from the coast, noting the passage from 0.157 to a significant 0.759 between SST and Chl-*a*, and from 0.088 to a significant 0.7 between SST and CDOM_{index}, significant at the 0.01 level (Fig. 9).

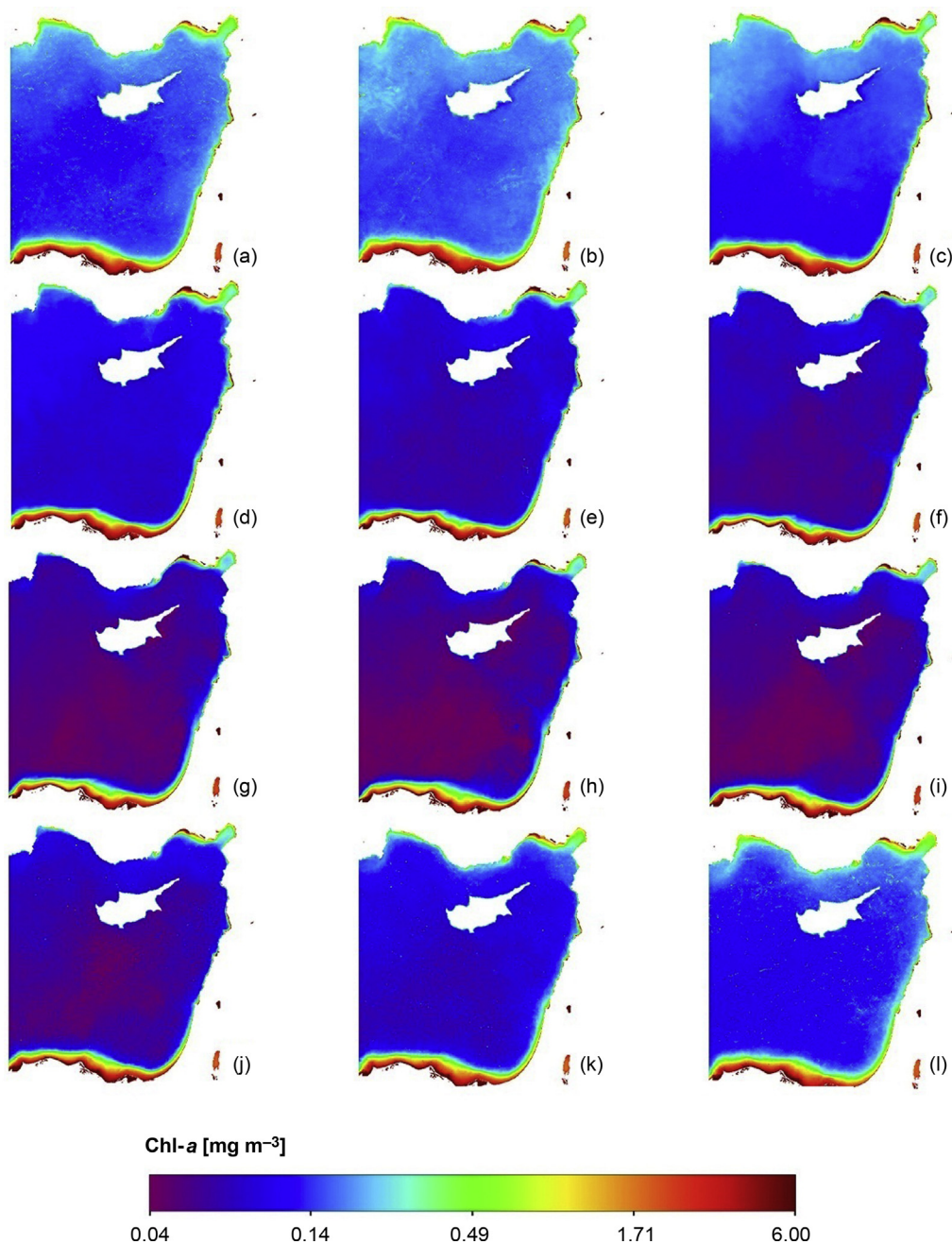


Figure 3 Monthly climatology chlorophyll-*a* concentration averaged using Level 2 Chl-*a* data from MODIS Aqua and Terra, over the 14 studied years in the Levantine basin [(a) January, (b) February, (c) March, (d) April, (e) May, (f) June, (g) July, (h) August, (i) September, (j) October, (k) November, (l) December].

5. Discussion

5.1. Algal bloom patterns

The increase of Chl-*a* is a result of the phytoplankton heavy multiplication inducing seasonal blooms. This occurs when the climatic and biochemical factors are propitious, such as the elevation of the SST, the increase of the sun irradiance budget and the availability of nutrients such as phosphates and nitrates (Krom et al., 2003).

The climatology images of Chl-*a* and the descriptive statistics show that the most productive regions of the Levantine basin are the Nile's Delta, the Gulf of Iskenderun and Mersin bay. This relatively high productivity is due to the higher nutrient inputs (rivers and pollution sources) and the presence of a larger continental shelf where the majority of the oceanic burial of organic carbon occurs (Hedges and Keil, 1995; Premuzic et al., 1982). The Chl-*a* climatology results showed a seasonal cycle at the Nile Shelf, the Chl-*a* starts to arise in autumn to reach a maximum in winter (February). This bloom is accounted to the Nile flood that occurs each early autumn

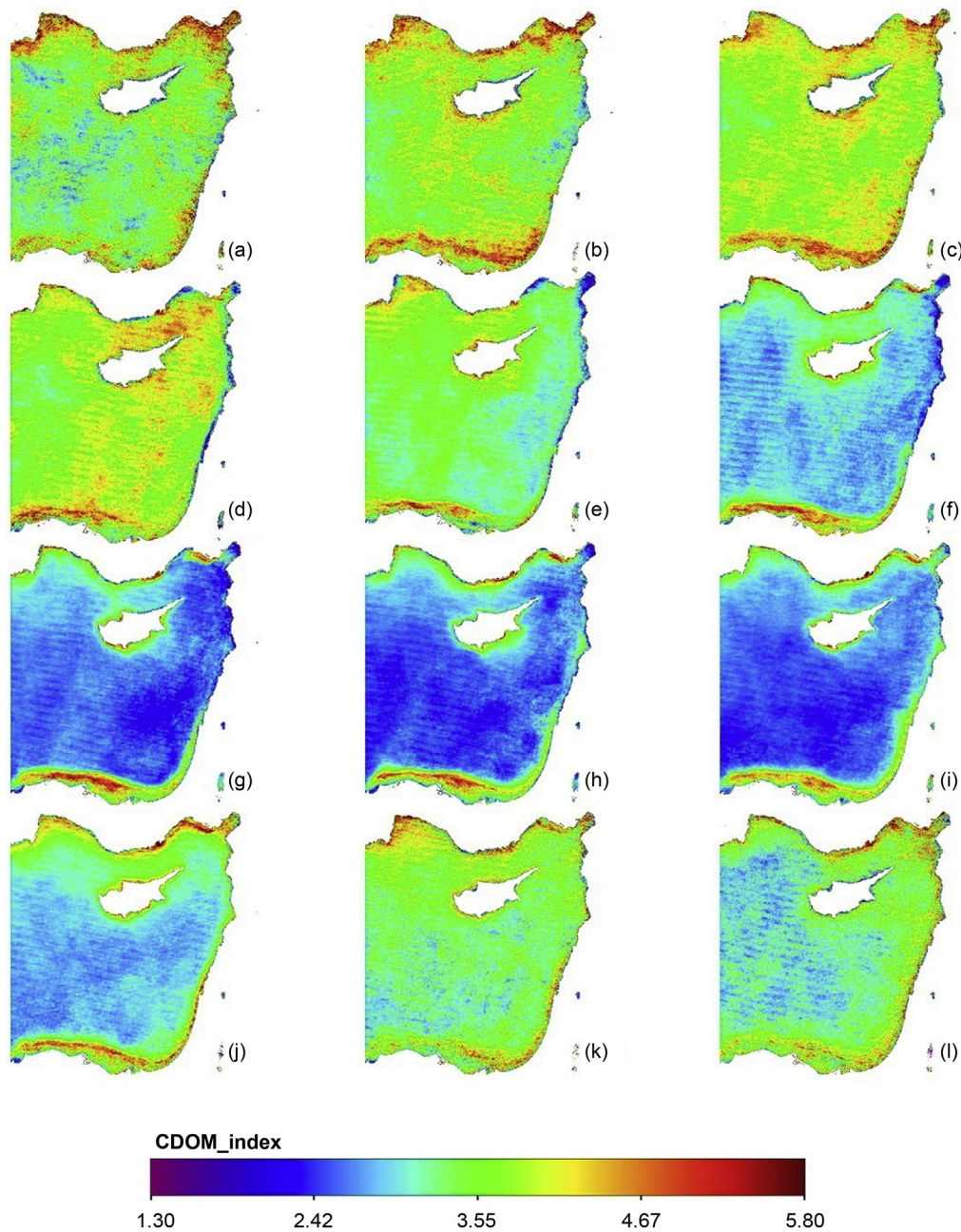


Figure 4 Monthly climatology colored dissolved organic matter index averaged using Level 2 CDOM_index data from MODIS Aqua and Terra, over the 14 studied years in the Levantine basin [(a) January, (b) February, (c) March, (d) April, (e) May, (f) June, (g) July, (h) August, (i) September, (j) October, (k) November, (l) December].

(Lavender et al., 2009). Adding to that, a maximum average of 2.75 mg m^{-3} is noted in February at the Nile delta, which is in agreement with the study of Dowidar (1984) estimating a Chl-*a* maximum of 2.8 mg m^{-3} observed in winter.

On the other hand, at the northeastern subdivisions where the Gulf of Iskenderun and Mersin bay are located, the Chl-*a* peaks exponentially indicating an early spring phytoplankton bloom, due to the propitious climatic factors in this season, and decrease gradually and slowly till winter. The slight increase of Chl-*a* in August suggests the presence of an autumnal bloom. This regime points at the richness of this coastal zone, where the nutrient load is not a limiting factor. The Gulf of Iskenderun and Mersin Bay are both situated in the

south of Turkey and are subjected to heavy anthropogenic activities (Karakaya and Evrendilek, 2011; Yilmaz et al., 1992). The increase in accumulating input of nutrients like nitrogen and phosphorus via Ceyhan (Gulf of Iskenderun) and Yenice (Mersin Bay) rivers and man-made run offs promotes phytoplankton and phytobenthos production (Yilmaz et al., 1992).

Meanwhile, the eastern and northern coastline is less productive, compared to both the southern and northeastern areas of the Levantine basin. This may be associated with the presence of a narrow shelf with no prominent upwelling phenomenon (Caddy, 1998) (Fig. 1).

In this study two conspicuous phytoplankton blooms were observed at the eastern coastline: a spring bloom in March–

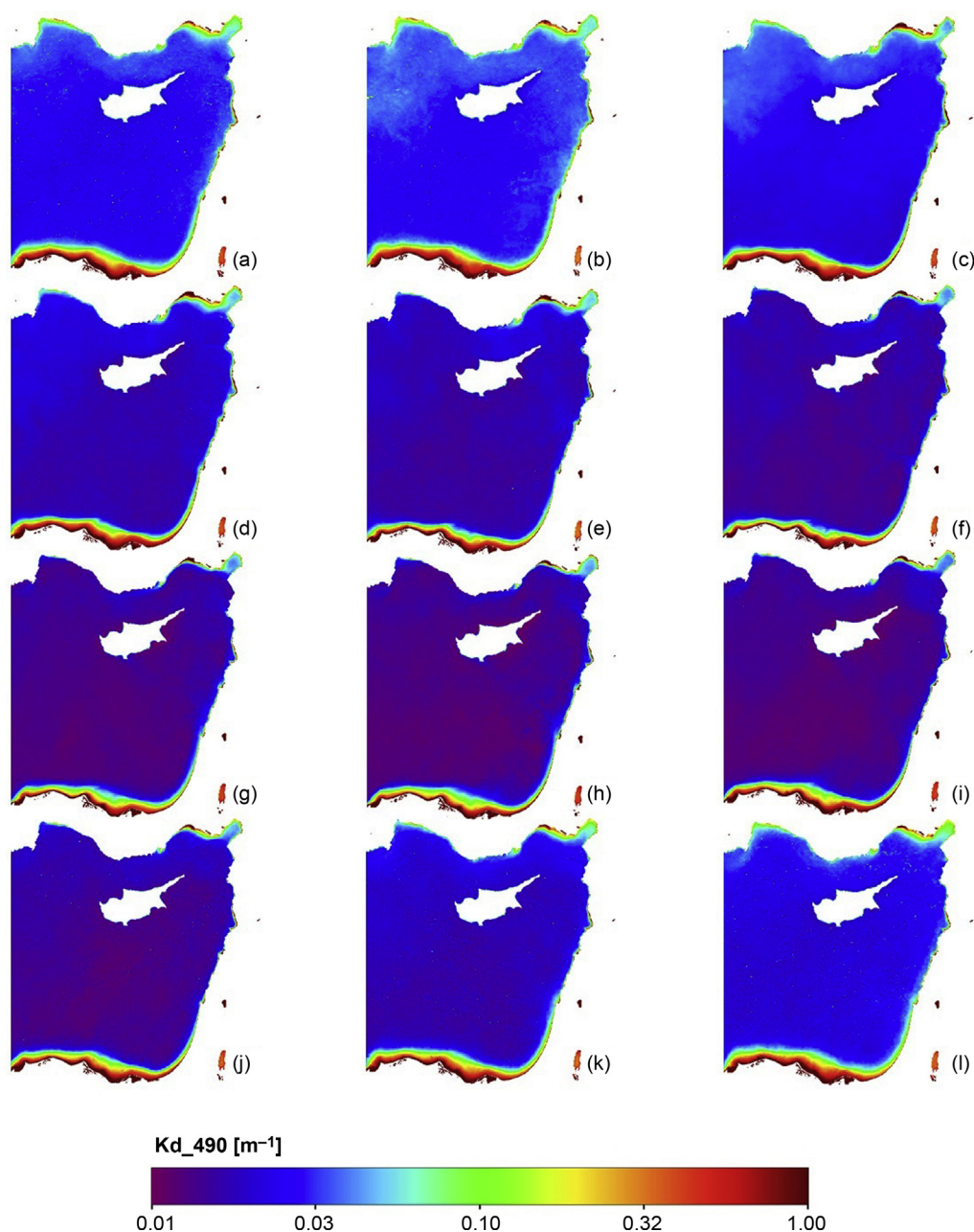


Figure 5 Monthly climatology diffuse attenuation coefficient for downwelling irradiance at 490 nm averaged using Level 2 Kd_{490} data from MODIS Aqua and Terra, over the 14 studied years in the Levantine basin [(a) January, (b) February, (c) March, (d) April, (e) May, (f) June, (g) July, (h) August, (i) September, (j) October, (k) November, (l) December].

April and autumnal bloom peaking by the end of August. The autumnal blooms are accounted to the regenerated nutrient stuck in the upper layer of the sea after the settlement of the summer thermocline. The average Chl-*a* concentrations near the same coastal region ranged between 0.29 and 1.29 mg m^{-3} which is consistent with the results of [Abboud-Abi Saab \(1992\)](#), [Abboud-Abi Saab et al. \(2008\)](#) and [Azov \(1986\)](#) at the eastern coast, where Chl-*a* ranged between 0.1 and 1 mg m^{-3} . Many sites along the coast show higher values of Chl-*a* and Kd_{490} within the climatology images. These sites correspond to major cities and their seaports (Tartous in Syria, Beirut, Jounieh and Sidon in Lebanon, Haifa, Netanya and Tel Aviv in Israel), water stream estuaries and agricultural crops near

the coast (such as Al Hamidiyah in Syria). The combination of these factors induces the fertilization of the coastal waters and leads to an increase of the phytoplankton biomass and the suspended particles abundance.

The northern coastline is less productive than any part of the Levantine basin, due to nutrient depletion in this area. This region is qualified of euphotic with low nutrient input; this is reflected on standing stocks of phytoplankton and hence on the Chl-*a* ([Yilmaz et al., 1992](#)).

In fact, the results of the chlorophyll-*a* imagery show a single winter phytoplankton bloom, peaking in February in the open water of the Levantine basin. This bloom seems to be induced by the increase of solar irradiance and the

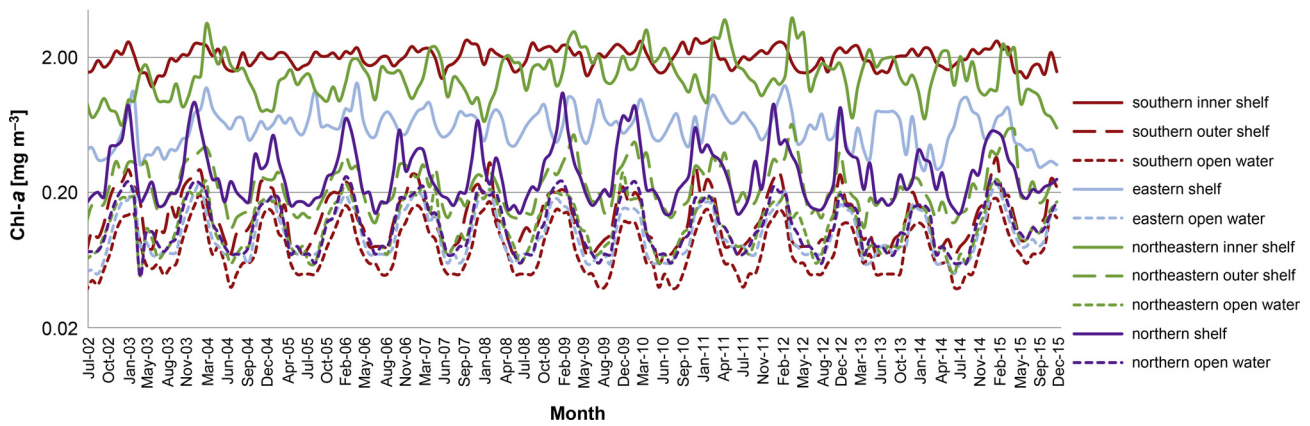


Figure 6 Monthly chlorophyll-a concentration averaged over the 14 studied years for each subdivided bioregion in the Levantine basin.

availability of nutrients (Krom et al., 2003). In this study, the short detected winter bloom in the open water is explained by the basin's trophic level, where the phytoplankton bloom is limited by the short nutrient availability after water mixing in winter (Krom et al., 1991, 1992). This bloom ceases shortly when the surface waters run out of nutrient. However, the spatio-temporal variability of blooms detected in our study on coastal regions is linked to the fertilization by nutrient input originating from estuaries, coastal runoffs, and anthropogenic activities, leading to an enhancement of the phytoplankton bloom.

5.2. Sea surface temperature and algal blooms

The correlation between the SST and Chl-a data shows a high inverse correlation factor of 0.76 while moving far from the coastal region. Fig. 8 draws an inverse Chl-a behavior compared to the SST. Such result can be related to several reasons such as photoacclimation, water stratification and the

optimum temperature of the blooming phytoplankton species (Xing et al., 2014). Moreover, when surface waters are cold in winter, deeper water rises to the surface bringing nutrients to sunlit areas and leading to a phytoplankton bloom.

Low correlation factors between SST and Chl-a recorded near the coastal area can be due to the land and anthropogenic interference. Such interference affects the annual blooming cycle via nutrient input originating from river runoff, as well as from urban and agricultural point sources, leading to an intensification of microbial activity coupled with the blooming of phytoplankton communities near affected areas.

5.3. Euphotic layer and algal blooms

The relationship between Chl-a and the attenuation coefficient seems to be strong, showing a significantly high correlation coefficient of 0.9 in all the subregions of the Levantine basin. And adding to that, the Kd₄₉₀ monthly

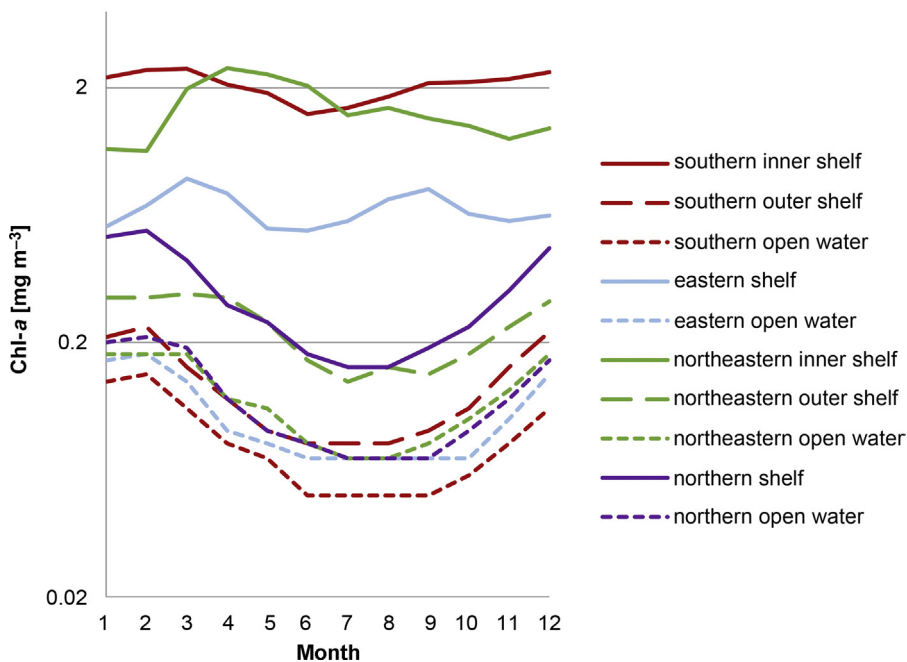


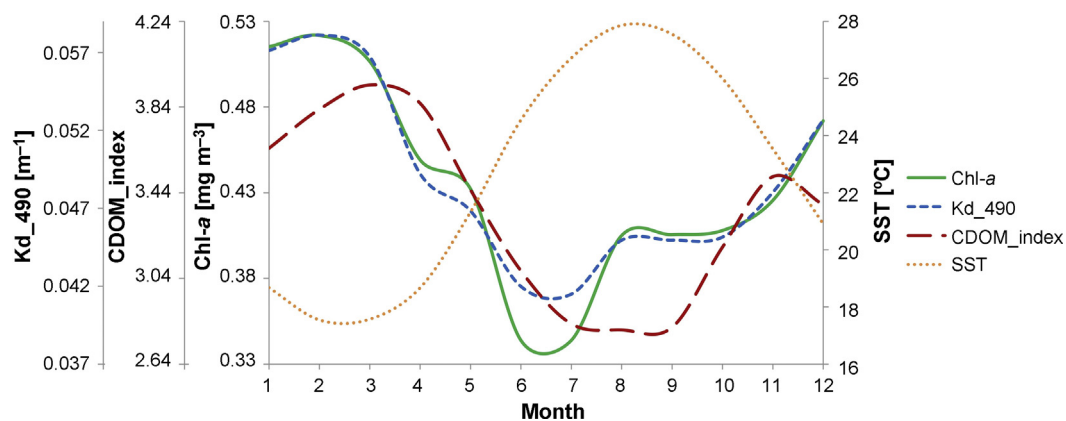
Figure 7 Monthly climatology chlorophyll-a concentration averaged over the 14 studied years for each subdivided bioregion in the Levantine basin.

Table 1 Descriptive statistics retrieved from the monthly images for the different biogeographic regions of the Levantine basin for the studied parameters.

Descriptive statistics			Minimum	Maximum	Mean	Std. deviation
Southern region	Inner shelf (<50 m)	Chl- <i>a</i> [mg m^{-3}]	1.40	2.75	2.06	0.31
		Kd ₄₉₀ [m^{-1}]	0.12	0.20	0.16	0.02
		CDOM_index	2.44	5.38	4.25	0.54
	Outer shelf (50 m; 200 m)	Chl- <i>a</i> [mg m^{-3}]	0.06	0.33	0.14	0.06
		Kd ₄₉₀ [m^{-1}]	0.02	0.05	0.03	0.01
		CDOM_index	2.68	5.77	3.68	0.68
	Open water (>200 m)	Chl- <i>a</i> [mg m^{-3}]	0.04	0.19	0.08	0.04
		Kd ₄₉₀ [m^{-1}]	0.02	0.04	0.03	0.004
		CDOM_index	2.18	4.82	3.22	0.69
Eastern region	Shelf (<200 m)	Chl- <i>a</i> [mg m^{-3}]	0.29	1.29	0.67	0.18
		Kd ₄₉₀ [m^{-1}]	0.04	0.11	0.07	0.012
		CDOM_index	1.60	4.71	3.39	0.59
	Open water (>200 m)	Chl- <i>a</i> [mg m^{-3}]	0.05	0.33	0.11	0.04
		Kd ₄₉₀ [m^{-1}]	0.02	0.05	0.03	0.005
		CDOM_index	2.22	4.96	3.29	0.66
Northeastern region	Inner shelf (<50 m)	Chl- <i>a</i> [mg m^{-3}]	0.67	3.5	1.65	0.63
		Kd ₄₉₀ [m^{-1}]	0.08	0.27	0.13	0.03
		CDOM_index	1.44	4.68	3.35	0.78
	Outer shelf (50 m; 200 m)	Chl- <i>a</i> [mg m^{-3}]	0.11	0.64	0.23	0.09
		Kd ₄₉₀ [m^{-1}]	0.03	0.07	0.04	0.01
		CDOM_index	2.33	5.78	3.72	0.71
	Open water (>200 m)	Chl- <i>a</i> [mg m^{-3}]	0.05	0.28	0.12	0.05
		Kd ₄₉₀ [m^{-1}]	0.02	0.05	0.03	0.006
		CDOM_index	2.23	5.05	3.52	0.74
Northern region	Shelf (<200 m)	Chl- <i>a</i> [mg m^{-3}]	0.14	1.09	0.31	0.18
		Kd ₄₉₀ [m^{-1}]	0.03	0.1	0.05	0.015
		CDOM_index	1.3	4.81	3.18	0.86
	Open water (>200 m)	Chl- <i>a</i> [mg m^{-3}]	0.06	0.26	0.12	0.06
		Kd ₄₉₀ [m^{-1}]	0.02	0.05	0.03	0.006
		CDOM_index	2.09	5.48	3.65	0.65

climatology in Fig. 8 shows the same pattern variability as the Chl-*a* in the Levantine basin, proving that the phytoplankton cycle is the first to affect the depth of the euphotic layer. In the same way, the majority of the Levantine's waters correspond to Case 1 waters.

Hotspots of turbid Case 2 waters are well indicated by the high Kd₄₉₀ and Chl-*a* values, noting the Nile Delta where the Nile enriches the zone with a high load of suspended materials. The Chl-*a* appears to be related to suspended particulate matter in high turbidity zones where the euphotic layer is

**Figure 8** Chl-*a*, Kd₄₉₀, CDOM_index and SST monthly climatology for the Levantine basin averaged over the 14 studied years.

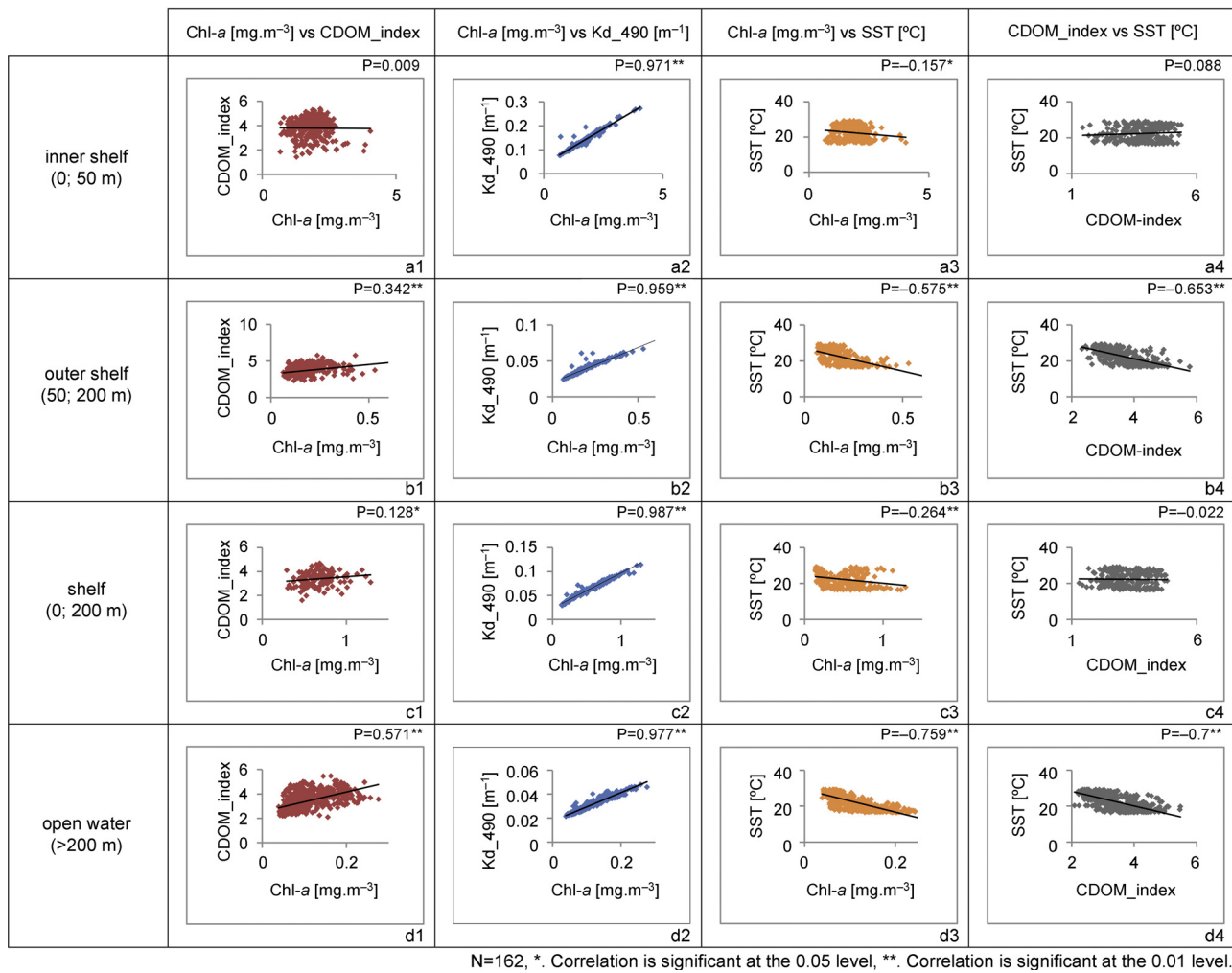


Figure 9 Scatter plots and correlation coefficients of each paired parameters in the different biogeographic regions of the Levantine basin.

shallow; algal blooms are induced by nonlimiting nutrients in very turbid water (Cloern, 1987; Harding et al., 1986; Lehman, 1992; Pennock, 1985).

5.4. Colored dissolved organic matter and algal blooms

The climatology monthly average of the Levantine basin (Fig. 8) shows a conspicuous CDOM_index peak in March, one month ahead of the Chl-*a* peak in February. The correlation coefficient between the CDOM_index and Chl-*a* in this study weakly strengthens while moving far from the coast. This can be observed also *via* the rhythmic variability gained by the averaged CDOM_index coinciding partially with the rhythmicity of Chl-*a* within the Case 1 waters. Theoretically, CDOM production is associated to the phytoplankton activity in Case 1 waters, yet many results suggested the decoupling of CDOM and phytoplankton both globally and regionally (Morel et al., 2010; Siegel et al., 2002; Xing et al., 2014). The elevation of CDOM_index to high index values can be due to the riverine runoff and point source loads in coastal regions. While in the open waters, the phytoplankton bloom activity is the principal contributor to the index variability.

The latter decrease of the CDOM_index between May and August can be mainly due to processes such as photobleaching at a high solar radiation intensity (Xing et al., 2014) and microbial activity (Coble, 2007). In fact, a high inverse correlation factor was observed in our study between the SST and CDOM_index while moving far from the coast (≈ 0.7). This can be related to a surface CDOM depression by photobleaching processes, referred as photodegradation or photo-oxidation (Morel and Gentili, 2009; Xing et al., 2014), leading to say that the CDOM variability seems to be also dependent on the SST. Therefore, with the intensification of water column stratification in summer, mixing of the surface layer becomes limited by the installed thermocline; the CDOM load caught within the unmixed surface layer is exposed to high solar radiation, resulting in a significant photochemical degradation, explained by the changes in fluorescent properties and absorbance losses (Zhang et al., 2015). And last in September where the phytoplankton blooming starts to manifest in most of the coastal areas, the CDOM_index arises.

The CDOM_index climatology images show abnormal variability of the index in the open sea domain and highlighted by high index values (>3) with the highest values of standard deviation. As the index represents the ratio between the CDOM content and the Chl-*a*, a high index

cluster was noted at the outer shelf of the Nile, the Gulf of Iskenderun, Mersin bay and near the northern coast. These regions can be classified as a transition from Case 2 to Case 1 waters where the Chl-*a* values are quite low, yet they are in direct influence of coastal CDOM advection by surface currents. As a result, the ratio between the advected CDOM and the Chl-*a* is increased in such areas. Moreover, the variability of the CDOM and the Chl-*a* are supposedly related in the open sea, and as a result, the index should be close to 1. Such high mean values of the index in the open water bioregion indicate an overestimation of low Chl-*a* by the standard sensor algorithm while applied for the Levantine basin, referred as the most oligotrophic domain in the Mediterranean Sea. Errors in Chl-*a* estimation can be accounted to the application of standard retrieval algorithms and standard atmospheric corrections (Kowalczyk et al., 2010), which are mainly developed and validated using a global *in situ* database, reducing the specificity of the algorithm.

6. Conclusion

In this work we assessed the algal blooms in the Levantine basin, by using various optical remote sensing data from 2002 to 2015. Most of the Levantine basin's waters can be classified as Case 1 waters where the Chl-*a* and Kd₄₉₀ are co-variant, showing a strong relation between phytoplankton blooms and the determination of the euphotic depth. The CDOM and Chl-*a* were directly and indirectly related, as their relationship is mainly affected by physical and biochemical factors. The SST variability is inversely correlated to both CDOM and Chl-*a* parameters, and the CDOM variability seemed to be more related to the SST variation. In addition, phytoplankton blooms were mainly winter blooms in the open water of the Levantine basin. Spatial and temporal variability of these blooms were observed near coastal regions due to variations in the physical, biochemical and anthropogenic factors.

The data derived from MODIS imagery is a consistent source to study the temporal behavior. The overestimation of Chl-*a* values highlighted by the CDOM_{index} should be corrected. The problems of the lack of a proper atmospheric correction model, the availability of *in situ* data, and the complexity of the optical properties of the Levantine basin waters will remain a limitation.

Acknowledgments

This work was performed under the support of the Lebanese National Center for Remote Sensing, Lebanese National Council for the Scientific Research.

The daily composites of SST, Chl-*a*, Kd₄₉₀ and CDOM_{index} were retrieved from the L2 product of the MODIS Aqua and Terra available at the ocean color website (<http://oceancolor.gsfc.nasa.gov/>), NASA Goddard Space Flight Center, Ocean Ecology Laboratory, Ocean Biology Processing Group (Moderate-resolution Imaging Spectroradiometer (MODIS) Aqua Ocean Color Data; 2014).

Reprocessing: NASA OB.DAAC, Greenbelt, MD, USA, http://dx.doi.org/10.5067/AQUA/MODIS_OC.2014.0,

http://dx.doi.org/10.5067/TERRA/MODIS_OC.2014.0 [accessed on 11.05.2016].

References

- Abboud-Abi Saab, M., 1992. Day-to-day variation in phytoplankton assemblages during spring blooming in a fixed station along the Lebanese coastline. *J. Plankton Res.* 14 (8), 1099–1115, <http://dx.doi.org/10.1093/plankt/14.8.1099>.
- Abboud-Abi Saab, M., Fakhri, M., Sadek, E., Matar, N., 2008. An estimate of the environmental status of Lebanese littoral waters using nutrients and chlorophyll-*a* as indicators. *Lebanese Sci. J.* 9 (1), 43–60.
- Abdel-Moati, M.A., 1990. Particulate organic matter in the subsurface chl-*a* maximum layer of the Southeastern Mediterranean. *Oceanol. Acta* 13 (3), 307–315.
- Antoine, D., Morel, A., André, J.M., 1995. Algal pigment distribution and primary production in the eastern Mediterranean as derived from coastal zone color scanner observations. *J. Geophys. Res.* 100 (C8), 16193–16209, <http://dx.doi.org/10.1029/95JC00466>.
- Austin, R.W., Petzold, T.J., 1981. The determination of the diffuse attenuation coefficient of sea water using the Coastal Zone Color Scanner. *Oceanography from Space*, vol. 13. Plenum Press, 239–256, http://dx.doi.org/10.1007/978-1-4613-3315-9_29.
- Azov, Y., 1986. Seasonal patterns of phytoplankton productivity and abundance in nearshore oligotrophic waters of the Levant Basin (Mediterranean). *J. Plankton Res.* 8 (1), 41–53, <http://dx.doi.org/10.1093/plankt/8.1.41>.
- Bethoux, J.P., Morin, P., Madec, C., Gentili, B., 1992. Phosphorus and nitrogen behaviour in the Mediterranean Sea. *Deep Sea Res.* 39 (9), 1641–1654, [http://dx.doi.org/10.1016/0198-0149\(92\)90053-V](http://dx.doi.org/10.1016/0198-0149(92)90053-V).
- Brando, V., Dekker, A., Park, Y., Schroeder, T., 2012. Adaptive semianalytical inversion of ocean colour radiometry in optically complex waters. *Appl. Optics* 51 (15), 2808–2833, <http://dx.doi.org/10.1364/AO.51.002808>.
- Caddy, J.F., 1998. Issues in Mediterranean Fisheries Management: Geographical Units and Effort Control: Studies and reviews No. 70. FAO, Rome, 56 pp.
- Cloern, J.E., 1987. Turbidity as a control on phytoplankton biomass and productivity in estuaries. *Cont. Shelf Res.* 7 (11–12), 1367–1381, [http://dx.doi.org/10.1016/0278-4343\(87\)90042-2](http://dx.doi.org/10.1016/0278-4343(87)90042-2).
- Coble, P.G., 2007. Marine optical biogeochemistry: the chemistry of ocean color. *Chem. Rev.* 107 (2), 402–418, <http://dx.doi.org/10.1021/cr050350+>.
- Devlin, M., Schroeder, T., McKinna, L., Brodie, J., Brando, V., Dekker, A., 2012. Monitoring and mapping of flood plumes in the Great Barrier Reef based on *in situ* and remote sensing observations. In: Chang, N. (Ed.), *Environmental Remote Sensing and Systems Analysis*, CRC Press, Boca Raton, 147–190, (Chapter 8).
- Dowidar, N.M., 1984. Phytoplankton biomass and primary productivity of the southeastern Mediterranean. *Deep Sea Res. Pt. II* 31 (6–8), 983–1000, [http://dx.doi.org/10.1016/0198-0149\(84\)90052-9](http://dx.doi.org/10.1016/0198-0149(84)90052-9).
- EIMP-CWMP, 2007. Annual report on status of the water quality of the Egyptian Mediterranean coastal waters during 2006. The Egyptian Environment Affair Agency, <http://www.eeaa.gov.eg/eimp/reports/ArrAnnualMed2006.pdf>.
- Harding, L.W., Meeson, B.W., Fisher, T.R., 1986. Phytoplankton production in two east coast estuaries: photosynthesis-light functions and patterns of carbon assimilation in Chesapeake and Delaware bays. *Estuar. Coast. Shelf Sci.* 23 (6), 773–806, [http://dx.doi.org/10.1016/0272-7714\(86\)90074-0](http://dx.doi.org/10.1016/0272-7714(86)90074-0).
- Hedges, J.I., Keil, R.G., 1995. Sedimentary organic preservation: an assessment and speculative synthesis. *Mar. Chem.* 49 (2–3), 81–115, [http://dx.doi.org/10.1016/0304-4203\(95\)00008-F](http://dx.doi.org/10.1016/0304-4203(95)00008-F).

- Karakaya, N., Evrendilek, F., 2011. Monitoring and validating spatio-temporal dynamics of biogeochemical properties in Mersin Bay (Turkey) using Landsat ETM+. *Environ. Monit. Assess.* 181 (1), 457–464, <http://dx.doi.org/10.1007/s10661-010-1841-5>.
- Kennedy, K., Schroeder, T., Shaw, M., Haynes, D., Lewis, S., Bentley, C., Paxman, C., Carter, S., Brando, V., Bartkow, M., Hearn, L., Mueller, J., 2012. Long term monitoring of photosystem II herbicides – correlation with remotely sensed freshwater extent to monitor changes in the quality of water entering the Great Barrier Reef, Australia. *Mar. Pollut. Bull.* 65 (4), 292–305.
- Kowalczyk, P., Darecki, M., Zablocka, M., Górecka, I., 2010. Validation of empirical and semi-analytical remote sensing algorithms for estimating absorption by Coloured Dissolved Organic Matter in the Baltic Sea from SeaWiFS and MODIS imagery. *Oceanologia* 52 (2), 171–196, <http://dx.doi.org/10.5697/oc.52-2.171>.
- Krom, M.D., Brenner, S., Kress, N., Neori, A., Gordon, L.I., 1992. Nutrient dynamics and new production in a warm-core eddy from the Eastern Mediterranean. *Deep Sea Res.* 39 (3), 467–480, [http://dx.doi.org/10.1016/0198-0149\(92\)90083-6](http://dx.doi.org/10.1016/0198-0149(92)90083-6).
- Krom, M.D., Groom, S., Zohary, T., 2003. *The Eastern Mediterranean*. In: Black, K.D., Shimmiel, G.B. (Eds.), *The Biogeochemistry of Marine Systems*. Blackwell Publ., Oxford, 91–122.
- Krom, M.D., Kress, N., Brenner, S., Gordon, L.I., 1991. Phosphorus limitation of primary productivity in the Eastern Mediterranean. *Limnol. Oceanogr.* 36 (3), 424–432, <http://dx.doi.org/10.4319/lo.1991.36.3.0424>.
- Lavender, S.J., Moufaddal, W.M., Pradhan, Y.D., 2009. Assessment of temporal shifts of chlorophyll levels in the Egyptian Mediterranean shelf and satellite detection of the Nile bloom. *Egyptian J. Aquat. Res.* 35 (2), 121–135.
- Lee, Z.-P., 2005. A model for the diffuse attenuation coefficient of downwelling irradiance. *J. Geophys. Res.* 110 (C2), <http://dx.doi.org/10.1029/2004jc002275>.
- Lehman, P.W., 1992. Environmental factors associated with long-term changes in chlorophyll concentration in the Sacramento-San Joaquin delta and Suisun bay, California. *Estuaries* 15 (3), 335–348, <http://dx.doi.org/10.2307/1352781>.
- Mann, K.H., Lazier, J.R.N., 2006. *Dynamics of Marine Ecosystems: Biological–Physical Interactions in the Oceans*, 3rd edn. Blackwell Publ., Malden, 496 pp.
- Morel, A., Claustre, H., Gentili, B., 2010. The most oligotrophic subtropical zones of the global ocean: similarities and differences in terms of chlorophyll and yellow substance. *Biogeosciences* 7 (10), 3139–3151, <http://dx.doi.org/10.5194/bg-7-3139-2010>.
- Morel, A., Gentili, B., 2009. A simple band ratio technique to quantify the colored dissolved and detrital organic material from ocean color remotely sensed data. *Remote Sens. Environ.* 113 (5), 998–1011, <http://dx.doi.org/10.1016/j.rse.2009.01.008>.
- Morel, A., Huot, Y., Gentili, B., Werdell, P.J., Hooker, S.B., Franz, B.A., 2007. Examining the consistency of products derived from various ocean color sensors in open ocean (Case 1) waters in the perspective of a multi-sensor approach. *Remote Sens. Environ.* 111 (1), 69–88, <http://dx.doi.org/10.1016/j.rse.2007.03.012>.
- O'Reilly, J.E., Maritorena, S., Mitchell, B.G., Siegel, D.A., Carder, K.L., Garver, S.A., Kahru, M., McClain, C.R., 1998. Ocean color chlorophyll algorithms for SeaWiFS. *J. Geophys. Res.* 103 (C11), 24937–24953, <http://dx.doi.org/10.1029/98JC02160>.
- O'Reilly, J.E., Maritorena, S., O'Brien, M.C., Siegel, D.A., Toole, D., Chavez, D., Smith, R.C., Mueller, J.L., Mitchell, B.G., Kahru, M., Chavez, F.P., 2000. SeaWiFS postlaunch calibration and validation analyses, part 3, S.B. Hooker & E.R. Firestone (eds.), NASA Tech. Memo 2000-206892 Vol. 11, NASA Goddard Space Flight Center, 49 pp.
- Pennock, J.R., 1985. Chlorophyll distribution in the Delaware estuary: regulation by light limitation. *Estuar. Coast. Shelf Sci.* 21 (5), 711–725, [http://dx.doi.org/10.1016/0272-7714\(85\)90068-X](http://dx.doi.org/10.1016/0272-7714(85)90068-X).
- Premuzic, E.T., Benkovitz, C.M., Gaffney, J.S., Walsh, J.J., 1982. The nature and distribution of organic matter in the surface sediments of world oceans and seas. *Org. Geochem.* 4 (2), 63–77, [http://dx.doi.org/10.1016/0146-6380\(82\)90009-2](http://dx.doi.org/10.1016/0146-6380(82)90009-2).
- Schroeder, T., Devlin, M., Brando, V.E., Dekker, A.G., Brodie, J., Clementson, L., McKinna, L., 2012. Inter-annual variability of wet season freshwater plume extent into the Great Barrier Reef lagoon based on satellite coastal ocean colour observations. *Mar. Pollut. Bull.* 65 (4–9), 210–223, <http://dx.doi.org/10.1016/j.marpolbul.2012.02.022>.
- Siegel, D.A., Maritorena, S., Nelson, N.B., Hansell, D.A., Lorenzi-Kayser, M., 2002. Global distribution and dynamics of colored dissolved and detrital organic materials. *J. Geophys. Res.* 107 (C12), 21.1–21.14, <http://dx.doi.org/10.1029/2001JC000965>.
- Su, J., Tian, T., Krasemann, H., Schartau, M., Wirtz, K., 2015. Response patterns of phytoplankton growth to variations in re-suspension in the German Bight revealed by daily MERIS data in 2003 and 2004. *Oceanologia* 57 (4), 328–341, <http://dx.doi.org/10.1016/j.oceano.2015.06.001>.
- Tanhua, T., Hainbucher, D., Schroeder, K., Cardin, V., Álvarez, M., Civitarese, G., 2013. The Mediterranean Sea system: a review and an introduction to the special issue. *Ocean Sci.* 9 (5), 789–803, <http://dx.doi.org/10.5194/os-9-789-2013>.
- Turley, C.M., Bianchi, M., Christaki, U., Conan, P., Harris, J.R.W., Psarra, S., Ruddy, G., Stutt, E.D., Tselepidis, A., Van Wambeke, F., 2000. Relationship between primary producers and bacteria in an oligotrophic sea – the Mediterranean and biogeochemical implications. *Mar. Ecol.-Prog. Ser.* 193, 11–18, <http://dx.doi.org/10.3354/meps193011>.
- Werdell, P.J., Bailey, S.W., 2005. An improved bio-optical data set for ocean color algorithm development and satellite data product validation. *Remote Sens. Environ.* 98 (1), 122–140, <http://dx.doi.org/10.1016/j.rse.2005.07.001>.
- Xing, X., Claustre, H., Wang, H., Poteau, A., D'Ortenzio, F., 2014. Seasonal dynamics in colored dissolved organic matter in the Mediterranean Sea: patterns and drivers. *Deep-Sea Res. Pt. I* 83, 93–101, <http://dx.doi.org/10.1016/j.dsr.2013.09.008>.
- Yacobi, Y.Z., Zohary, T., Kress, N., Hecht, A., Roberts, R.D., Waiser, M., Wood, A.M., Li, W.K.W., 1995. Chlorophyll distribution throughout the southeastern Mediterranean in relation to the physical structure of the water mass. *J. Marine Syst.* 6 (3), 179–190, [http://dx.doi.org/10.1016/0924-7963\(94\)00028-A](http://dx.doi.org/10.1016/0924-7963(94)00028-A).
- Yeh E.-N., Barnes R.A., Darzi M., Kumar L., Early E.A., Johnson B.C., Mueller J.L., Trees C.C., 1997. Case Studies for SeaWiFS Calibration and Validation, Part 4, S.B. Hooker & E.R. Firestone (eds.), NASA Tech. Memo. 104566, Vol. 41, NASA Goddard Space Flight Center, Greenbelt, Maryland, 35 pp.
- Yilmaz, A., Baştürk, Ö., Saydam, A.C., Ediger, D., Yılmaz, K., Hatipoğlu, E., 1992. Eutrophication in İskenderun Bay, Northeastern Mediterranean (Science for the Total Environment). In: Vollenweider, R.A., Marchetti, R., Viviani, R. (Eds.), *Marine Coastal Eutrophication*. Elsevier, Amsterdam, 705–717, <http://dx.doi.org/10.1016/B978-0-444-89990-3.50062-6>.
- Zhang, Y., Hu, C., Yu, T., 2015. Photodegradation of chromophoric dissolved organic matters in the water of Lake Dianchi, China. *Front. Environ. Sci. Eng.* 9 (4), 575–582, <http://dx.doi.org/10.1007/s11783-014-0664-y>.



Available online at www.sciencedirect.com

ScienceDirect

journal homepage: www.journals.elsevier.com/oceanologia/



ORIGINAL RESEARCH ARTICLE

Toward downscaling oceanic hydrodynamics – suitability of a high-resolution OGCM for describing regional ocean variability in the South China Sea

Meng Zhang^{*}, Hans von Storch

Institute for Coastal Research, Helmholtz Zentrum Geesthacht, Geesthacht, Germany

Received 22 June 2016; accepted 4 January 2017

Available online 18 January 2017

KEYWORDS

Ocean downscaling;
STORM;
The South China Sea

Summary We suggest to transfer the empirical downscaling methodology, which was developed mostly for atmospheric dynamics and impacts, to regional ocean problems. The major problem for doing so is the availability of decades-long and homogeneous and spatially detailed data sets. We have examined the performance of the STORM multidecadal simulation, which was run on a 0.1° grid and forced with 1950–2010 NCEP re-analyses, in the South China Sea and found the data suitable. For demonstration we build with this STORM-data downscaling model for the regional throughflow.

The STORM data is compared with AVISO satellite observations and the ocean re-analysis dataset C-GLORS. We find the seasonal patterns and the inter-annual variability of sea surface height anomaly in both the C-GLORS data and the STORM simulation consistent with the AVISO-satellite data. Also the strong westward intensification and the seasonal patterns of South China Sea circulation steered by the monsoon have been presented well. As an important indicator of vertical movement, the sea surface temperature distribution maps are also very close, especially for the narrow upwelling region in summer. We conclude that the output of the STORM simulation is realistically capturing both the large-scale as well as the small-scale dynamical features in the South China Sea.

© 2017 Institute of Oceanology of the Polish Academy of Sciences. Production and hosting by Elsevier Sp. z o.o. This is an open access article under the CC BY-NC-ND license (<http://creativecommons.org/licenses/by-nc-nd/4.0/>).

^{*} Corresponding author at: Helmholtz-Zentrum Geesthacht Centre for Materials and Coastal Research, Max-Planck-Str. 1, 21502 Geesthacht, Germany. Tel.: +49(0)4152 87-1851; fax: +49(0)4152 87-2832.

E-mail address: meng.zhang@hzg.de (M. Zhang).

Peer review under the responsibility of Institute of Oceanology of the Polish Academy of Sciences.



Production and hosting by Elsevier

<http://dx.doi.org/10.1016/j.oceano.2017.01.001>

0078-3234/© 2017 Institute of Oceanology of the Polish Academy of Sciences. Production and hosting by Elsevier Sp. z o.o. This is an open access article under the CC BY-NC-ND license (<http://creativecommons.org/licenses/by-nc-nd/4.0/>).

1. Introduction

As the largest semi-enclosed marginal sea located in the southeast Asian waters, the South China Sea (SCS) covers an area of about 3.5 million km² in total, with an average depth more than 2000 m and a maximum depth of about 5000 m. It is surrounded by China, Vietnam, Philippine Islands, Malaysia and other countries. Via the Luzon Strait, Taiwan Strait and the Strait of Malacca, it connects the Pacific Ocean, East China Sea and Indian Ocean (Fang et al., 2006a, b, 2012; Ho et al., 2000; Hu et al., 2000; Li et al., 2003).

Due to the influence of the East Asian monsoon system, the SCS circulation represents significant seasonal characteristics. Previous studies have been carried out to analyze the features of the SCS circulation. Dale (1956) determined the SCS surface circulation in winter and summer for the first time from the ship drift data, which clearly revealed the seasonal differences. Wyrtki (1961) pointed out that the monsoon is the main driver of the SCS circulation.

The advent of satellite remote sensing technology allowed the analysis of the details of the SCS circulation. Ho et al. (2000) has described the seasonal variability of sea surface height (SSH) based on the TOPEX/Poseidon altimeter data during 1992–1997. Fang et al. (2006b) used the gridded 11-year AVISO SSH data, which merged data from TOPEX/Poseidon, ERS and Jason, for characterizing the low frequency variability of the SCS surface circulation and to discuss its relationship with El Niño-Southern Oscillation. The conclusion of the annual variability responding to the change of monsoon was confirmed by their study.

Recently, several numerical simulations of the SCS circulation were done. Such simulations help extend our knowledge about past variations beyond the short time period of satellite observations and beyond the sparse sampling of in situ observation and ship observation. Wei et al. (2003) embedded a fine-grid ocean model of the China Sea into a global model so that open boundary conditions were no longer needed. Their modeled monthly SSH anomalies (SSHA) were similar to the TOPEX/Poseidon data, and the model could seasonably reproduce the SCS Southern Anticyclonic Gyre in summer and the SCS Southern Cyclonic Gyre in winter. Using this model, the seasonal features of the water intruding into the SCS through the Luzon Strait in different ocean layers were investigated. Wang et al. (2006) modeled the inter-annual variability of the SCS circulation and its relation to wind stress and El Niño through on an irregular grid. Such numerical simulations allowed the detailed study of processes and physical mechanisms of some mesoscale phenomena, for example, the topographical effect on the coastal upwelling in the north SCS (Wang et al., 2012, 2014).

In spite of those signs of progress, a systematic, detailed, homogeneous and comprehensive description of the SCS circulation on regional and local scales across several decades is hardly available. The “empirical downscaling” methodology may help to generate such descriptions, which will also allow for detection externally driven change as well as projecting possible future change on such regional scales. Most downscaling efforts were directed at atmospheric phenomena (Benestad et al., 2008; von Storch et al., 1993), but a few oceanic applications dealing with local sea level were presented in the 1990s (Cui et al., 1995; von Storch and Reichardt, 1997).

An alternative to empirical downscaling is dynamical downscaling using regional dynamical models (oceanographic examples are provided by Kauker and von Storch, 2000; Schrum et al., 2003); however, this approach is more challenging and cost-intensive than the empirical approach; also the empirical approach may deal with local phenomena, which are possibly less well resolved by dynamical models. Therefore, we explore the potential of the empirical downscaling of oceanic dynamics.

For doing so for the South China Sea (SCS), we need a consistent and homogeneous description of the regional space-time variability in that region. As a first preparational step, we examine the suitability of a multidecadal global simulation “STORM” with the MPI-OM, the high-resolution global ocean model of the Max Planck Institute of Meteorology (MPI; Li and von Storch, 2013; von Storch et al., 2012), which was forced by NCEP atmospheric re-analyses.

The high resolution of about 1/10° makes STORM capable to describe the small-scale features, while the temporal coverage over 60 years enables STORM to analyze the long-term variability of the SCS circulation. In addition, STORM provides the large-scale states. Therefore, STORM is a good choice for constructing the statistical relationship between large and small scales. Also all relevant second-moment statistics have been archived by accumulating two-variable-products at every time step (von Storch et al., 2012).

In this paper, we first assess the performance of STORM in describing the SCS circulation, by comparing with AVISO altimeter measurements and ocean re-analysis dataset C-GLORS. In Section 2, these three data sets are described in detail. Section 3 presents the comparisons, in terms of sea surface height anomalies (SSHA), surface current and sea surface temperature (SST). Eventually, for demonstration, an empirical downscaling model has been constructed (Section 4), which allows deriving the monthly seasonal near-surface regional throughflow in the South China Sea from the regional wind fields.

2. Dataset description

2.1. Satellite observations

The monthly SSALTO (SSALTO multimission ground segment)/Duacs (Data Unification and Altimeter Combination System) gridded SSHA (sea surface height anomaly) data set from Archiving, Validation and Interpretation of Satellite Data in Oceanography (AVISO) covers almost the entire global ocean with a resolution of 0.25° from 1993 to 2014. It has been built from several satellite products, including TOPEX-POSEIDON, ERS, JASON and ENVISAT (AVISO, 1996, 2009).

As a consequence of its high quality, the AVISO SSHA data has often been used as reference to validate global model output and characterize regional currents (Fang et al., 2006a,b). In this paper, we compare the AVISO SSHA data with SSHA from the STORM simulation and the ocean re-analysis C-GLORS.

2.2. The ocean re-analysis dataset C-GLORS

The ocean reanalysis dataset C-GLORS (version 4) has the same horizontal 0.25° grid resolution as AVISO. It has been

produced by the global ocean re-analysis system of CMCC (The Euro-Mediterranean Center for Climate Change), which has assimilated in situ observations of temperature, salinity (from moorings and ARGO floats) and sea surface height (from AVISO satellite data; [Storto and Masina, 2014](#); [Storto et al., 2016](#)).

The monthly dataset from 1982 to 2013 can be downloaded from their website <http://www.cmcc.it/c-glors/>.

2.3. The STORM/NCEP simulation

Three high-resolution global ocean-only simulation STORM from the German STORM consortium employed the state-of-the-art model MPI-OM and was forced by the NCEP-NCAR reanalysis data ([Li and von Storch, 2013](#); [Tim et al., 2015](#); [von Storch et al., 2012](#)). This simulation operates with a tri-polar grid – with a very fine grid spacing of about 0.1° and only 2.3 km at the finest grid, and 80 unevenly distributed levels in vertical. The simulation was run for 6 decades of years, 1950–2010. For fair comparison, STORM was interpolated on a horizontal 0.25° -grid.

Several aspects of the STORM simulation data have been examined, such as the oceanic Lorenz energy cycle for the World Ocean ([von Storch et al., 2012](#)), the sea surface temperature (SST) near Benguela current as well as the decadal variability and trends of the upwelling system there ([Tim et al., 2015](#)). The simulation was found to be mostly realistic, even if some biases prevailed.

3. Assessing the realism of the STORM data

The three data sets, STORM, C-GLORS and AVISO cover different variables, and descriptions for different time windows. The satellite AVISO contains only sea surface height for 1993–2014, while the re-analysis C-GLORS provide the full range of dynamical variables for 1982–2013 and STORM for 1950–2010.

We consider AVISO as the data set closest to reality; thus we examine first, how well the derived products C-GLORS and STORM compare with AVISO. The realism of C-GLORS in terms of SSHA, leads us to assessing the quality of STORM with respect to other variables by comparing it with C-GLORS. The first step demonstrates the suitability of using all C-GLORS variables; the second step suggests that STORM provides a realistic description across the 60 year time window 1950–2012.

3.1. SSHA in AVISO, C-GLORS and STORM

SSEA is often used to analyze the ocean dynamics and the upper layer circulation ([Cheng et al., 2016](#); [Fang et al., 2006b](#); [Li et al., 2003](#); [Wei et al., 2003](#)). This data is available from AVISO in 1993–2014. For the comparisons with C-GLORS and STORM, the joint period from 1993 to 2010 has been chosen.

The observed AVISO-SSEA is the actual state subject to the influences of dynamical, eustatic and steric effects, whereas the modeled SSHA from STORM and C-GLORS only describe the dynamical effects and not eustatic and steric effects. According to the fifth report of IPCC ([IPCC, 2013](#)), the growth of the global mean sea level since the 1970s is mostly caused

by the thermal expansion of global warming and glacier loss. For removing the difference influenced by eustatic and steric effect, we subtract the trend of AVISO. In case that the trend related to dynamical effect is removed as well, for fair comparison, SSHA from C-GLORS and STORM are also detrended.

The climatological seasonal mean states of detrended SSHAs of STORM and C-GLORS ([Fig. 1](#)) show good agreement with AVISO. In winter (DJF), basin-wide low SSHAs control the east part of the SCS, which presents the cyclonic currents in the upper layer in the whole SCS. Furthermore, in these three datasets, two low SSHA centers located in the north and south SCS respectively. In summer (JJA), the situation is just opposite. Anti-cyclonic currents dominate the SCS region in all the three datasets, however a maximum SSHA over 0.1 m appears near the Luzon Strait in AVISO and C-GLORS, which is a little lower in STORM.

The (temporal) standard deviation of the seasonal means represents interannual variability. The patterns of detrended SSHA standard deviation distributions ([Fig. 2](#)) for the four seasons of three datasets are similar. As December in 1992 is not available, there are only 17 months in winter (DJF), but 18 months in other three seasons. All of them show that, in winter and spring, the deviation near Luzon Strait is always higher than adjacent seas, and in summer and autumn, strong variability centers in the Vietnam's coast water. Compared with AVISO and C-GLORS, the STORM simulates stronger variability in Luzon Strait in summer and autumn, yet weaker variability in the Vietnam coast in spring. In summer, the area of the center with strong variability near Vietnam is closer to AVISO, compared with C-GLORS.

Empirical Orthogonal Functions (EOF) decompose the time series of SSHA fields, several orthogonal modes capture the main variability ([von Storch and Zwiers, 1999](#); [Wang et al., 2006](#)). We apply the EOF decomposition to the three detrended datasets, after removing the mean annual cycle (by subtracting a multi-year monthly average). The EOFs have been normalized so that the standard deviation of the time coefficients (principal component, PC) is 1 – so that the different intensity of the EOFs is given by the patterns.

The main feature of the first EOF pattern (EOF1; [Fig. 3](#)) describes an overall simultaneous in- or decrease in the SCS. The amplitude in the east is greater than it in other regions. The EOF1s of C-GLORS and STORM are generally consistent with AVISO. However, a small negative center with small area and weak intensity appears in C-GLORS and three similar centers occur in STORM. Seen from the figures, also the EOF time series for three datasets vary similarly. The time series in C-GLORS and STORM closely correlate with AVISO, with the correlation coefficients of 0.94 and 0.91, respectively. In 1997, SSHAs in all three datasets dropped suddenly and then rebounded quickly in 1998. With respect to the represented percentage of the variance, 25.1% in STORM is closer to 27.0% in AVISO, than 36.6% in C-GLORS.

The second EOF (EOF2) patterns in three datasets all show a strong anti-cyclonic gyre located off the Vietnam coast and extending northeastward to reach Philippine Islands, covering most part of the north SCS. The remaining areas are associated with negative value. The coverage of intensity over 0.05 m in STORM is larger than that in AVISO, while the positive values in C-GLORS are all under 0.05 m. The

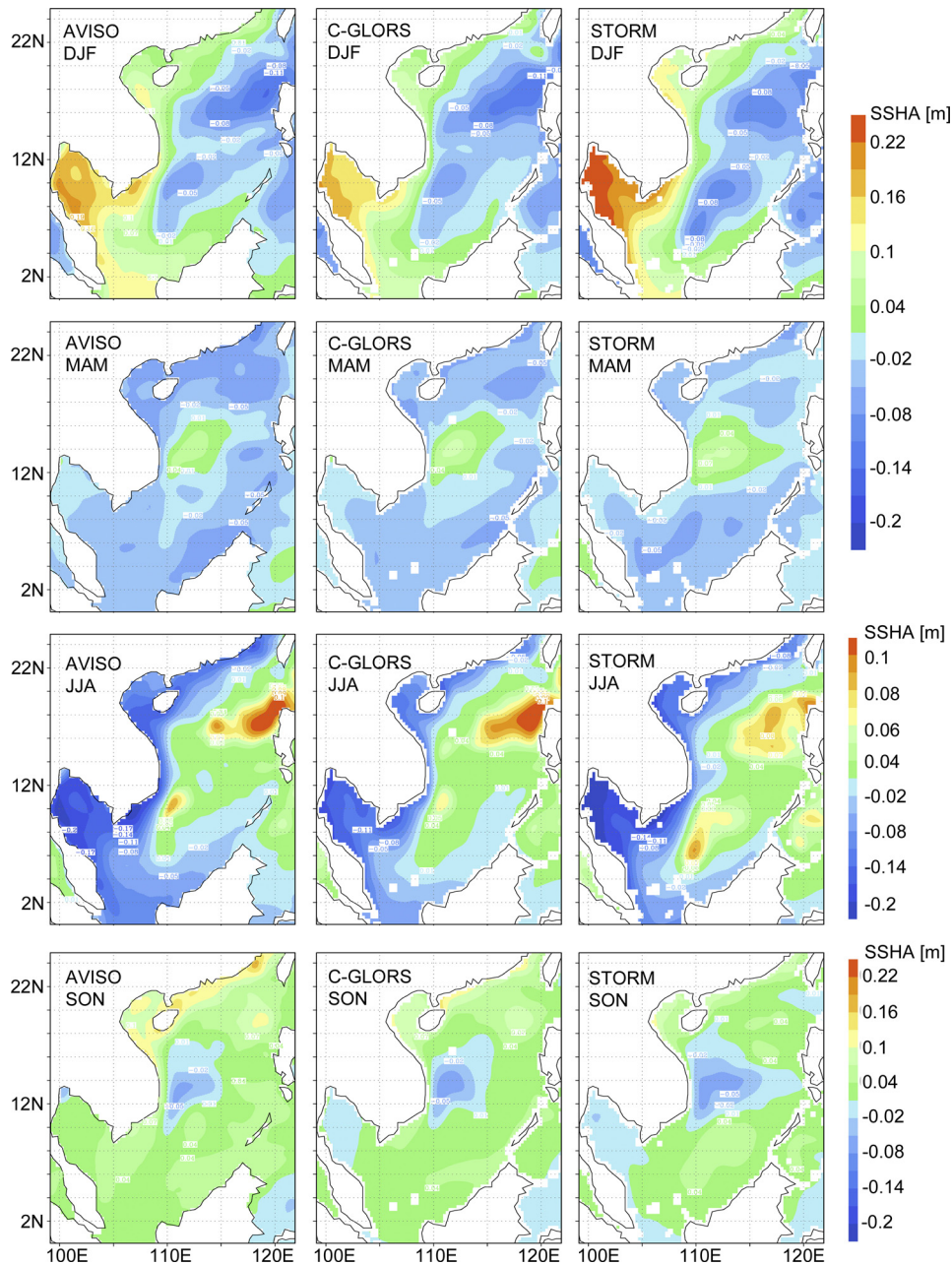


Figure 1 1993–2010 seasonal means of detrended sea surface height anomalies (SSHA) [m] according to AVISO, C-GLORS and STORM. From top to bottom: DJF, MAM, JJA and SON.

percentages of variance described by both STORM and C-GLORS are greater than AVISO. Their EOF2 coefficient time series of C-GLORS and STORM show correlations with AVISO 0.80 and 0.77, respectively.

Our analysis demonstrates that C-GLORS and STORM have the ability to capture the main variability features of the SCS dynamics in terms of seasonal variance and interannual variability of SSHA. C-GLORS shows greater similarity, which is not surprising as it has assimilated AVISO satellite data. We think the similarity of SSHA in AVISO and C-GLORS points to the plausibility that also other parameters of C-GLORS may be considered mostly realistic. Therefore, we will continue assessing STORM, with C-GLORS as a reference, in the

following chapter. In the following, we assess the description of surface currents and SST in the joint period 1982–2010 shared by C-GLORS and STORM.

3.2. Surface current fields in C-GLORS and STORM

The first level for ocean horizontal current fields in STORM is at 6 m depth, so we choose this level as surface to perform comparison and get the C-GLORS currents at 6 m depth through vertical interpolation.

The seasonal mean surface current fields of STORM and C-GLORS (Fig. 4) show similar variability.

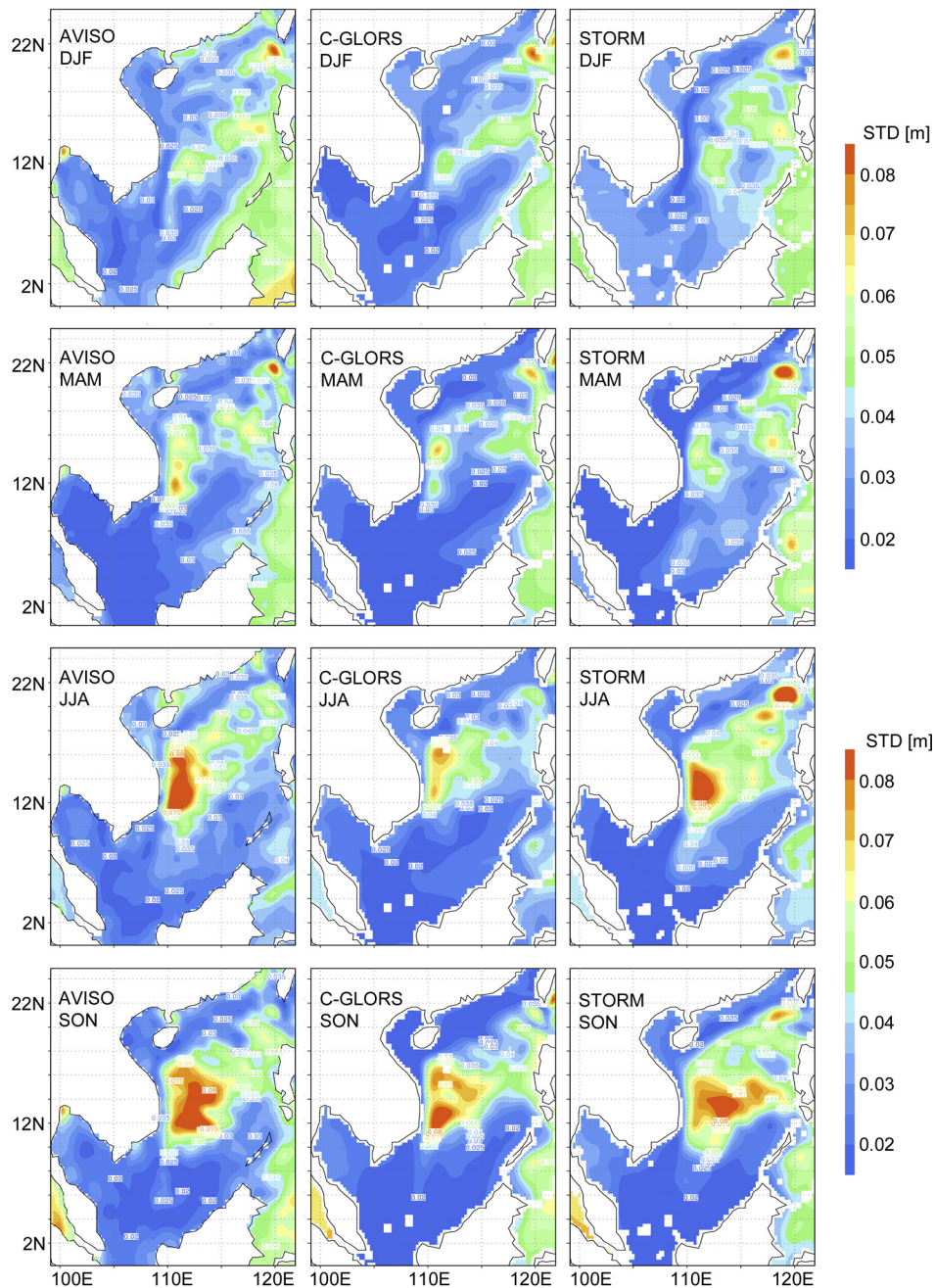


Figure 2 1993–2010 standard deviations (STD) [m] of seasonal detrended SSHA according to AVISO, C-GLORS and STORM. From top to bottom: DJF, MAM, JJA and SON.

In winter, strong counterclockwise currents dominate the southern SCS. The Kuroshio intrudes through the Luzon Strait from east to west and then divides into two branches, with the smaller one moving northward into the Taiwan Strait, the bigger one moving westward and then turning southward as a strong western boundary current along the coast. High-speed currents take place in the Luzon Strait, along the western boundary of the SCS (especially along the east coast of Malay Peninsula), and in the large cyclonic eddy of the southern SCS.

In summer, the strong currents along western boundary turn northward, which is consistent with the SCS monsoon, and clockwise currents occupy the southern SCS. At the same time, a strong flow offshore the Vietnam meanders to the

central SCS and another flows northward along the southeast coast of China. In spring and autumn, two cyclonic eddies locate in the northern and southern SCS respectively. The seasonal patterns presented in STORM and C-GLORS are alike. But, the speeds in STORM are generally higher than those in C-GLORS, which may be due to the higher spatial resolution of STORM which may allow the simulation of more small-scale phenomena.

The EOFs of sea surface current (after subtracting the annual cycle) from the two data sets show similar inter-annual variability and explain the similar variance (11.9% in C-GLORS and 9.2% in STORM). The main features of the EOF1 patterns from both two data are the strong alongshore

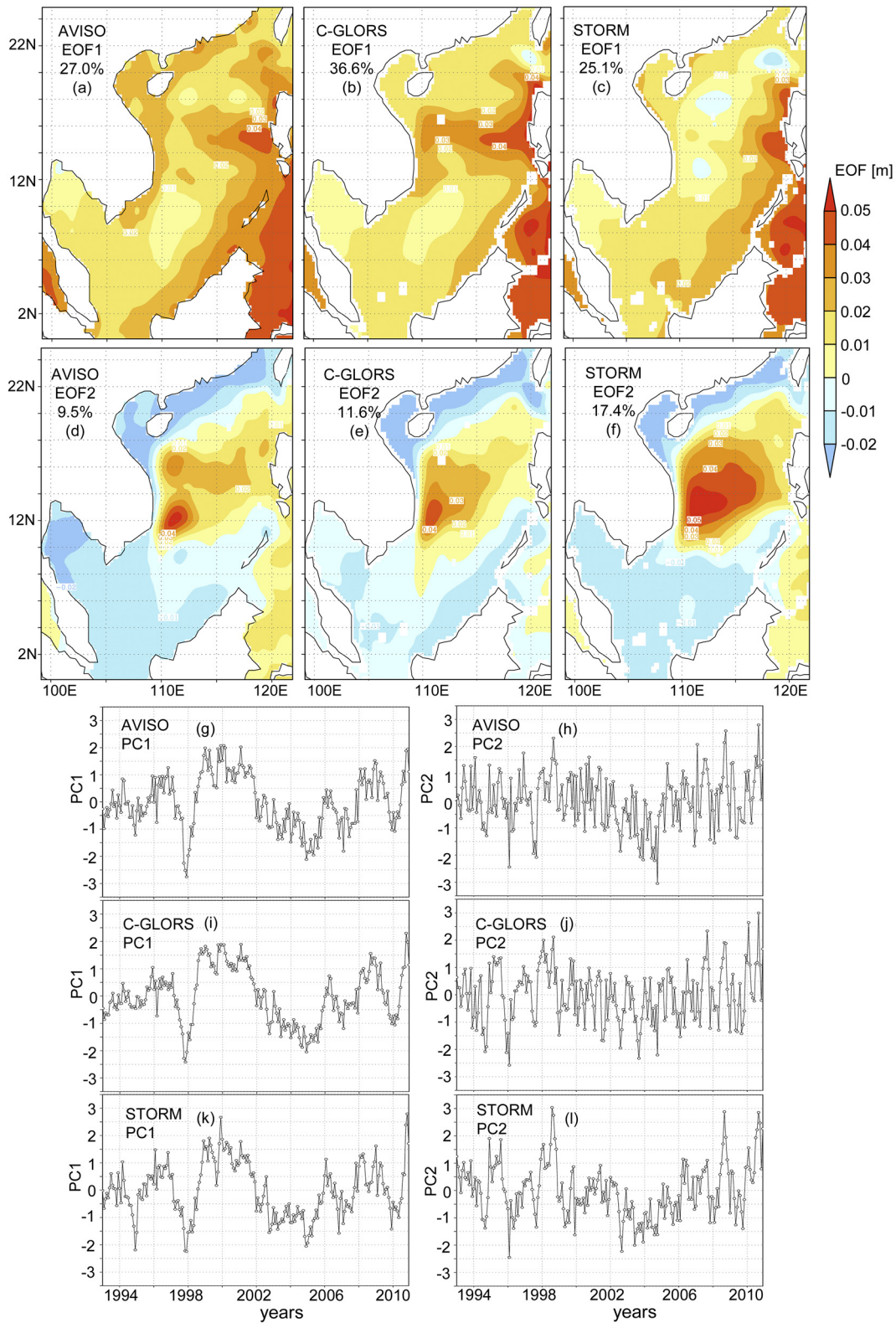


Figure 3 (a–f) The first two EOFs [m] of 1993–2010 monthly detrended SSHA (removing mean annual cycle) according to AVISO, C-GLORS and STORM. From top to bottom: EOF1 and EOF2. (g–l) The time coefficients for the first two EOFs of AVISO (top), C-GLORS (middle) and STORM (bottom), after detrending and subtraction of the mean annual cycle. From left to right: EOF1 and EOF2.

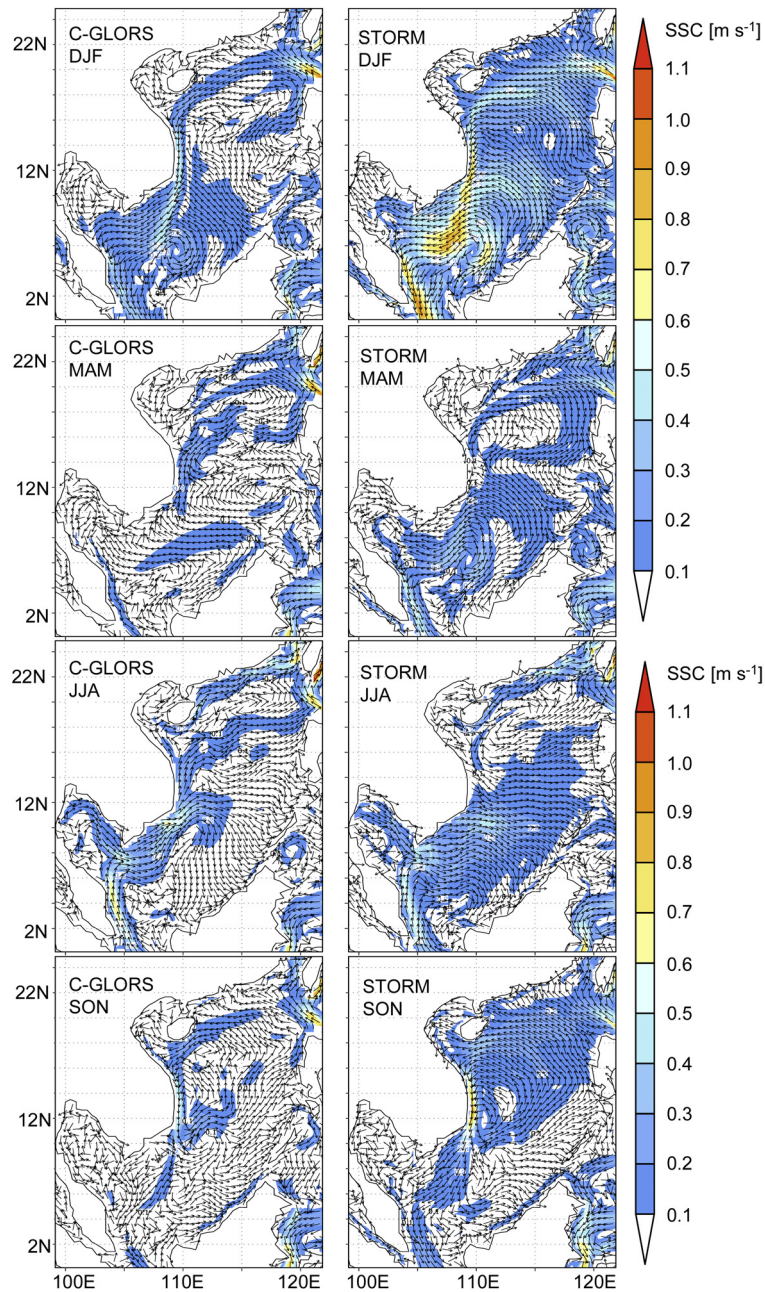


Figure 4 1982–2010 seasonal mean of sea surface currents (SSC; at 6 m depth) [m s^{-1}] according to C-GLORS and STORM. From top to bottom: DJF, MAM, JJA and SON.

southward currents and a gyre located in the middle SCS. The currents intrude into the SCS from the Pacific through the Luzon Strait and flow into the Pacific through the passage at the south of Philippines. The current speeds in STORM are a little higher than in C-GLORS for the region with slow (less than 0.02 m s^{-1}) currents.

3.3. SST in C-GLORS and STORM datasets

The distribution of SST can be deeply influenced by the ocean currents and its variance can be regarded as an important indicator of current variability, including vertical currents. In this section, SST is considered for evaluating the ability of the STORM dataset to reproduce the SCS dynamics.

The distributions of SST in the SCS (Fig. 5) show obvious seasonal differences. In winter, spring and autumn, most isotherms show northeast-southwest direction. The closer the area is to the Equator, the hotter the sea surface is. The SST in the SCS in summer is almost uniform but, with marked small upwelling regions in the southeast of China and near Vietnam. Previous studies (Fang et al., 2012; Wang et al., 2012, 2014; Xie et al., 2003) have demonstrated the presence of regional upwelling, which brings much colder water from deeper layer to the surface. STORM generates higher temperatures in summer in most regions, and it presents a stronger upwelling with larger temperature gradient than C-GLORS. The area with coldest seawater and largest gradient off the Southeast Vietnam coast is very close to the

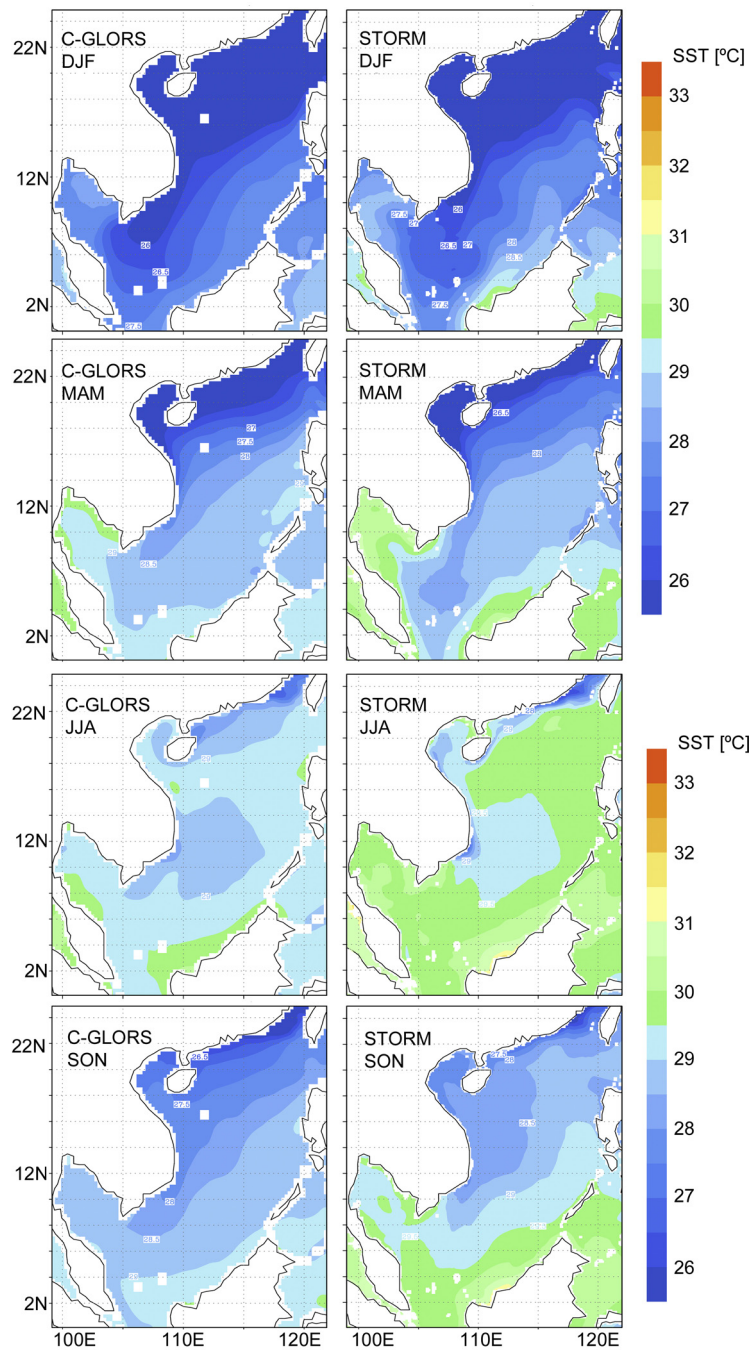


Figure 5 1982–2010 seasonal means of sea surface temperature (SST) [°C] according to C-GLORS and STORM. From top to bottom: DJF, MAM, JJA and SON.

land, then, with the limitation of horizontal resolution, C-GLORS may not be able to resolve these very small-scale phenomena. So STORM has an advantage in this case. The study of [Tim et al. \(2015\)](#) has found similarly colder SST in STORM compared with coarser observations in the South Atlantic.

4. A case of regional ocean downscaling

According to the assessment above, the capability of STORM to describe the large-scale state and small-scale variability

has been verified. STORM is forced with atmospheric states given by NCEP, which is believed to be mostly homogenous since 1958 in describing “large-scale” (regional) variability. Thus, the STORM data set should be suitable for building empirical downscaling models for specifying regional and local phenomena and their statistics in the ocean.

For demonstrating this option, we have built one empirical downscaling model, as an example. As predictand we use the surface throughflow in the South China Sea and its neighboring seas ($0\text{--}25^\circ\text{N}$, $99^\circ\text{--}122^\circ\text{E}$), as given by the time series of the 1st EOF of deseasonalized monthly currents on the 0.25° grid ([Fig. 6](#)); as predictors the monthly wind speed

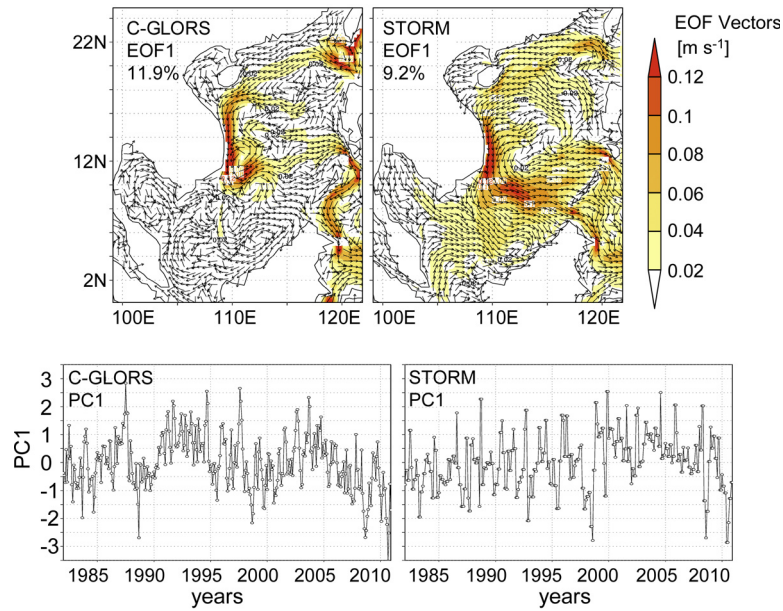


Figure 6 The first vector EOF [m s^{-1}] and the corresponding coefficient of 1982–2010 monthly sea surface currents (SSC; at 6 m depth) according to C-GLORS and STORM.

at 10 m height ($0\text{--}25^\circ\text{N}$, $99^\circ\text{--}122^\circ\text{E}$, including the land) as given by the 2.5° gridded NCEP re-analysis. The empirical model linking the predictors and the predictand is multiple linear regression (MLR).

As the instability of the quality of the NCEP1 before the year 1958, this experiment is performed during the period of 1958–2010. We choose the first 33 years (with 396 months) as the training period to construct the model and the last 20 years (with 240 months) as validation period.

There are several preparational steps to pre-process the data:

1. First, the annual cycle in both the predictors and the predictands are removed for both two periods.
2. Second, for the training period 1958–1990, after detrending the data, we get the first principal component PC1_C of the detrended and de-seasonalized currents C, and the principal components PCs_W of the detrended and de-seasonalized winds W. The pattern EOF1_C (not shown) presents almost the same pattern as that one given in Fig. 6. Using these PCs, we build the MLR models.
3. Third, for the validation period, the currents (and winds) are projected on EOF1_C (EOFs_W) to generate the pre-

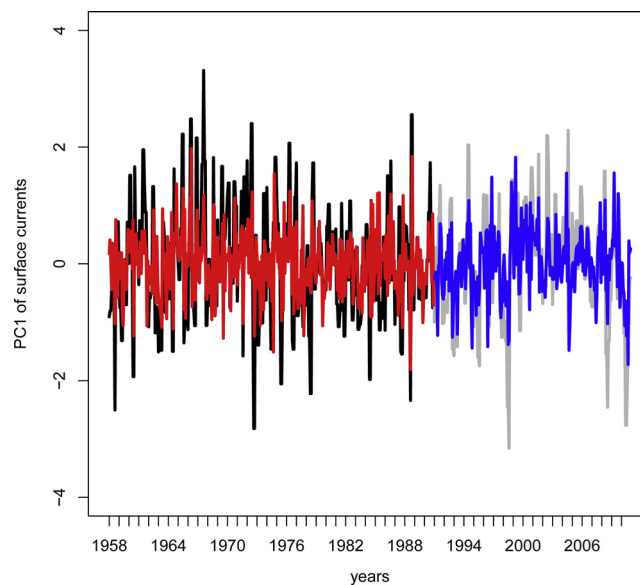


Figure 7 The original PC1 (the black line and the gray line) and the fitted PC1 (the red line and the blue line) of the surface currents for the training period and the validation period.

dictand PC1_C and the predictors PCs_W. The skill of the MLR model can be assessed by “predicting” PC1_C in the validation period by feeding the MLR model with the predictors PCs_W.

The number of PCs of predictors to be used for the construction of the downscaling model has an effect on the model skill. Too many PCs involved in the construction may result in the overfitted problem (Titus et al., 2013). After some tests, we find that the first 3 PCs of wind as predictors for the model construction performs well. The original PC1 and the fitted PC1 for both the training period and the validation period are shown in Fig. 7. The correlation coefficients between the predictand and the predicted PC1_C amounts to 0.55 in the training period 1958–1990, and 0.66 in the validation period (1991–2010).

The regressed predictand exhibits a similar, albeit smaller, variability to that one during the training period. We conclude that the multiple linear regression based on the principal component is good enough to build the statistical model to predict the non-seasonal variability of surface currents in the SCS.

5. Conclusions

Often, studies on the statistics of meso-scale SCS dynamics and scale-interactions suffer from insufficient observations in terms of spatial resolution and temporal coverage. One way of overcoming this limitation is to build empirical downscaling models for regional and local oceanic phenomena. A major problem for doing so is the availability of suitable data sets for constructing such empirical models.

One approach for solving this problem is to use multi-decadal simulations with high-resolution ocean models forced by atmospheric reanalyses. For instance, the German consortium STORM project has produced a global high-resolution ocean dataset STORM, integrated with atmospheric forcing for the time period 1950–2010 and a one-tenth degree horizontal resolution. This dataset is found to generate realistically the variability on large and small scales in the SCS and statistics of small-scale features of the SCS dynamics. Using this data set, we built a statistical models of the links between large and small scales in the SCS, i.e. an empirical downscaling model.

For determining the STORM data as suitable, we introduce the global gridded AVISO satellite observations and the ocean re-analysis dataset C-GLORS in this study to evaluate the ability of STORM to reproduce the SCS dynamical structure. As C-GLORS have much more parameters than AVISO, for the joint period and the shared variable SSHA, we first verified the quality of C-GLORS and STORM. After that, we regard C-GLORS as “observations” to carry out the assessment of other variables (surface currents and SST) generated by STORM.

Overall, STORM and C-GLORS show good agreement with AVISO in reconstructing the SCS dynamical characteristics. The seasonal variability of SSHA resolved from STORM is very close to AVISO with the maximum center in the same locations, even though C-GLORS having assimilated the AVISO altimeter data is closer. The distributions of maximum SSHA standard deviation for four seasons from the three datasets are alike, but C-GLORS and STORM differ from the observed

distribution, with respect to the intensity in winter and spring, the area of strong inter-annual variability in summer and autumn off the southeast Vietnam. The EOF decomposition of SSHA identifies similar patterns of interannual variability. A difference is that emergence of several small opposite centers far away from the coastline presented in EOF1 patterns of C-GLORS and STORM. The reason is not clear.

STORM hindcasts the same seasonal upper circulation and inter-annual variability as C-GLORS, however, it generates stronger current intensity, which may be caused by the increase in resolution. As for SST, even though STORM still overestimates the SST for most areas, the temperature distribution of STORM shows great similarity with C-GLORS, with colder temperature off the Vietnam coast (the strong upwelling area) in summer. The STORM description of the SCS circulation and some small-scale phenomena near coastline, for instance upwelling, is quite satisfactory.

A major albeit technical advantage of STORM is not only the availability of more dynamical variables, but also the longer time period, namely 1950, or 1958, until 2010.

Taking advantage of STORM, one statistical downscaling model has been built successfully to estimate the non-seasonal variability of the SCS surface currents for the past 60 years. The multiple linear regression based on the principal component shows skill.

While this downscaling model is merely an example demonstrating the potential, further downscaling models will be built in this spirit on the regional and local phenomena in the South China Sea, related to the formation of eddies, to coastal upwelling and other phenomena. These models may then also be used to derive scenarios of possible future change but also to change prior to 1950.

Acknowledgments

We thank the Helmholtz-Zentrum Geesthacht (HZG) for supporting the authors' research and the Chinese Scholarship Council (No. 201406330048) for funding the first author's studying abroad at the HZG. The authors are grateful to the Max Planck Institute of Meteorology (MPI) for providing the STORM simulations and to the Euro-Mediterranean Center for Climate Change (CMCC) for providing the C-GLORS data set, and we appreciate their suggestions.

References

- AVISO, 1996. AVISO User Handbook Merged Topex/Poseidon Products (GDR-Ms), AVI-NT-02-101-CN Edn. 3.0, Romonville St-Agne, France, 199 pp.
- AVISO, 2009. SSALTO/DUACS User Handbook: (M) SLA and (M) ADT Near-real Time and Delayed Time Products, Reference: CLS-DOS-NT-06-034, 29 pp.
- Benestad, R.E., Hanssen-Bauer, I., Chen, D., 2008. Empirical-statistical Downscaling. World Scientific Publishing Company Incorporated, Singapore, 228 pp.
- Cheng, X.H., Xie, S.P., Du, Y., Wang, J., Chen, X., Wang, J., 2016. Interannual-to-decadal variability and trends of sea level in the South China Sea. *Clim. Dyn.* 46 (9), 3113–3126, <http://dx.doi.org/10.1007/s00382-015-2756-1>.
- Cui, M.C., von Storch, H., Zorita, E., 1995. Coastal sea-level and the large-scale climate state – a downscaling exercise for the

- Japanese islands. *Tellus Ser. A* 47 (1), 132–144, <http://dx.doi.org/10.1034/j.1600-0870.1995.00008.x>.
- Dale, W.L., 1956. Wind and drift currents in the South China Sea. *Malays. J. Trop. Geogr.* 8, 1–31.
- Fang, G.H., Chen, H.Y., Wei, Z.X., Wang, Y.G., Wang, X.Y., Li, C.Y., 2006b. Trends and interannual variability of the South China Sea surface winds, surface height, and surface temperature in the recent decade. *J. Geophys. Res.* 111 (C11S16), 2156–2202, <http://dx.doi.org/10.1029/2005JC003276>.
- Fang, W.D., Guo, J.J., Shi, P., Mao, Q.W., 2006a. Low frequency variability of South China Sea surface circulation from 11 years of satellite altimeter data. *Geophys. Res. Lett.* C11S16, <http://dx.doi.org/10.1029/2006GL027431>.
- Fang, G.H., Wang, G., Fang, Y., Fang, W.D., 2012. A review on the South China Sea western boundary current. *Acta Oceanol. Sin.* 31 (5), 1–10, <http://dx.doi.org/10.1007/s13131-012-0231-y>.
- Ho, C.R., Zheng, Q.N., Soong, Y.S., Kuo, N.J., Hu, J.H., 2000. Seasonal variability of sea surface height in the South China Sea observed with TOPEX/Poseidon altimeter data. *J. Geophys. Res. Oceans* 105 (C6), 13981–13990, <http://dx.doi.org/10.1029/2000JC900001>.
- Hu, J., Kawamura, H., Hong, H., Qi, Y., 2000. A review on the currents in the South China Sea: seasonal circulation, South China Sea warm current and Kuroshio intrusion. *J. Oceanogr.* 56 (6), 607–624, <http://dx.doi.org/10.1023/A:1011117531252>.
- IPCC, 2013. Summary for Policymakers. In: *Climate Change 2013: The Physical Science Basis. Contribution of Working Group I to the Fifth Assessment Report of the Intergovernmental Panel on Climate Change*, Cambridge Univ. Press, Cambridge, United Kingdom/New York, USA, 10–11.
- Kauker, F., von Storch, H., 2000. Statistics of “synoptic circulation weather” in the North Sea as derived from a multiannual OGCM simulation. *J. Phys. Oceanogr.* 30 (12), 3039–3049, [http://dx.doi.org/10.1175/1520-0485\(2000\)030<3039:SOSCWI>2.0.CO;2](http://dx.doi.org/10.1175/1520-0485(2000)030<3039:SOSCWI>2.0.CO;2).
- Li, H.M., von Storch, J.S., 2013. On the fluctuating buoyancy fluxes simulated in a 1/10 degrees OGCM. *J. Phys. Oceanogr.* 43 (7), 1270–1287, <http://dx.doi.org/10.1175/JPO-D-12-080.1>.
- Li, L., Xu, J.D., Jing, C.S., Wu, R.S., Guo, X.G., 2003. Annual variation of sea surface height, dynamic topography and circulation in the South China Sea – a TOPEX/Poseidon satellite altimetry study. *Sci. China Ser. D* 46 (2), 127–138.
- Schrum, C., Siegmund, F., John, M., 2003. Decadal variations in the stratification and circulation patterns of the North Sea. Are the 1990 unusual? *ICES Mar. Sci. Sympos.* 121–131.
- Storto, A., Masina, S., 2014. Validation of the CMCC Global Ocean Eddy-Permitting Reanalysis (C-GLORS). *Centro Euro-Mediterraneo sui Cambiamenti Climatici*, Bologna, Italy, 11 pp.
- Storto, A., Masina, S., Navarra, A., 2016. Evaluation of the CMCC eddy-permitting global ocean physical reanalysis system (C-GLORS, 1982–2012) and its assimilation components. *Q. J. R. Meteorol. Soc.* 142 (695), 738–758, <http://dx.doi.org/10.1002/qj.2673>.
- Tim, N., Zorita, E., Hunicke, B., 2015. Decadal variability and trends of the Benguela upwelling system as simulated in a high-resolution ocean simulation. *Ocean Sci.* 11 (3), 483–502, <http://dx.doi.org/10.5194/os-11-483-2015>.
- Titus, M.L., Sheng, J., Greatbatch, R.J., Folkins, I., 2013. Improving statistical downscaling of general circulation models. *Atmos. Ocean* 51 (2), 213–225, <http://dx.doi.org/10.1080/07055900.2013.774259>.
- von Storch, H., Reichardt, H., 1997. A scenario of storm surge statistics for the German bight at the expected time of doubled atmospheric carbon dioxide concentration. *J. Clim.* 10 (10), 2653–2662, [http://dx.doi.org/10.1175/1520-0442\(1997\)010<2653:ASOSSS>2.0.CO;2](http://dx.doi.org/10.1175/1520-0442(1997)010<2653:ASOSSS>2.0.CO;2).
- von Storch, H., Zwiers, F.W., 1999. *Statistical Analysis in Climate Research*. Cambridge Univ. Press, 293–305.
- von Storch, H., Zorita, E., Cubasch, U., 1993. Downscaling of global climate-change estimates to regional scales – an application to Iberian rainfall in wintertime. *J. Clim.* 6 (6), 1161–1171, [http://dx.doi.org/10.1175/1520-0442\(1993\)006<1161:DOGCCCE>2.0.CO;2](http://dx.doi.org/10.1175/1520-0442(1993)006<1161:DOGCCCE>2.0.CO;2).
- von Storch, J.-S., Eden, C., Fast, I., Haak, H., Hernández-Deckers, D., Maier-Reimer, E., Marotzke, J., Stammer, D., 2012. An estimate of the Lorenz energy cycle for the world ocean based on the STORM/NCEP simulation. *J. Phys. Oceanogr.* 42 (12), 2185–2205, <http://dx.doi.org/10.1175/JPO-D-12-079.1>.
- Wang, Y., Fang, G., Wei, Z., Qiao, F., Chen, H., 2006. Interannual variation of the South China Sea circulation and its relation to El Niño, as seen from a variable grid global ocean model. *J. Geophys. Res.* 111, C11S14, <http://dx.doi.org/10.1029/2005JC003269>.
- Wang, D.X., Zhuang, W., Xie, S.P., Hu, J.Y., Shu, Y.Q., Wu, R.S., 2012. Coastal upwelling in summer 2000 in the northeastern South China Sea. *J. Geophys. Res. Oceans* 117, C04009, <http://dx.doi.org/10.1029/2011JC007465>.
- Wang, D.X., Shu, Y.Q., Xue, H.J., Hu, J.Y., Chen, J., Zhuang, W., Zu, T.T., Xu, J.D., 2014. Relative contributions of local wind and topography to the coastal upwelling intensity in the northern South China Sea. *J. Geophys. Res. Oceans* 119 (4), 2550–2567, <http://dx.doi.org/10.1002/2013JC009172>.
- Wei, Z.X., Fang, G.H., Choi, B.H., Fang, Y., He, Y.J., 2003. Sea surface height and transport stream function of the South China Sea from a variable-grid global ocean circulation model. *Sci. China Ser. D* 46 (2), 139–148, <http://dx.doi.org/10.3969/j.issn.1674-7313.2003.02.005>.
- Wyrtki, K., 1961. *Physical Oceanography of the Southeast Asian Waters, Scientific Results of Marine Investigations of the South China Sea and the Gulf of Thailand*, NAGA Rep. 2. Scripps Inst. Oceanogr., La Jolla, CA, 195 pp.
- Xie, S.P., Xie, Q., Wang, D.X., Liu, W.T., 2003. Summer upwelling in the South China Sea and its role in regional climate variations. *J. Geophys. Res. Oceans* 108, C83261, <http://dx.doi.org/10.1029/2003JC001867>.



SHORT COMMUNICATION

Microorganisms associated with charophytes under different salinity conditions

Marija Kataržytė*, Diana Vaičiūtė, Martynas Bučas, Greta Gyraitė, Jolita Petkuvienė

Marine Science and Technology Centre, Klaipeda University, Klaipėda, Lithuania

Received 17 August 2016; accepted 21 October 2016

Available online 4 November 2016

KEYWORDS

Net primary production of charophytes;
Abundance of bacteria and fungi;
Taxa composition of fungi;
Freshwater and brackish water;
Curonian Lagoon;
Baltic Sea

Summary Microorganisms associated with aquatic macrophytes can in various ways interact with a plant and influence its activity and *vice versa*. A low-salinity intrusion into freshwater environment can affect plant-microorganism interactions. In this study, effects of different salinity conditions on the abundance and community composition of associated microorganisms with charophytes in the Curonian Lagoon were assessed. From the results, we found that short term salinity changes affected the abundance of bacteria and fungi associated with charophytes, whereas no response was reflected in the taxa composition of fungi, showing that other factors could be of more importance. The increased fungi abundances and different fungi composition in August in comparison to June was probably related to senescence process of aquatic vegetation. 8 fungi taxa were isolated and identified in association with charophytes, while higher diversity was revealed by DGGE technique.

© 2016 Institute of Oceanology of the Polish Academy of Sciences. Production and hosting by Elsevier Sp. z o.o. This is an open access article under the CC BY-NC-ND license (<http://creativecommons.org/licenses/by-nc-nd/4.0/>).

* Corresponding author at: Marine Science and Technology Centre, Klaipeda University, H. Manto 84, LT-92294 Klaipėda, Lithuania. Tel.: +370 46398879.

E-mail address: marija.katarzyte@jmtc.ku.lt (M. Kataržytė).
Peer review under the responsibility of Institute of Oceanology of the Polish Academy of Sciences.



Production and hosting by Elsevier

Aquatic macrophytes, especially charophytes (*Characeae*), are considered as important biological quality element for fresh and brackish water bodies (Kufel and Kufel, 2002; Mathieson and Nienhuis, 1991 and references therein). In moderately shallow and eutrophic lagoons, charophytes are responsible for stabilization of clear-water states by causing inhibition of phytoplankton (Hilt, 2015). Dense beds of charophytes provide shelter, food and substrate for benthic invertebrates, fish and waterfowls (Dugdale et al., 2006;

Schmieder et al., 2006). Charophytes are also hosts for various microorganisms such as fungi and bacteria (Berg and Hagemann, 2009; Hempel et al., 2008). Microorganisms associated with aquatic vegetation form biofilm and are rich in antimicrobial compounds, which may protect macrophytes from hostile environment (Berg and Hagemann, 2009). On the other hand, colonies of epiphytic microorganisms, such as cyanobacteria (*Gleotrichia* sp.), might cause decrease of photosynthetic activity, nutrient uptake or very fast decay of macrophytes (Armstrong et al., 2001; Hudon et al., 2009). Although there are studies on the importance of microorganisms associated with macrophytes (Andrews and Harris, 2000; Egan et al., 2014, 2013), little is known about interactions between fungi (Godinho et al., 2013) and macrophytes.

Declining distribution and diversity of macrophytes, including charophytes, have been observed in many regions worldwide including the brackish Baltic Sea (e.g. Blindow, 2000; Pitkänen et al., 2013). Eutrophication and its consequences (increased pelagic productivity, water turbidity and reduced light availability) are assumed to be the most important threats to macrophytes (Blindow et al., 2003; Kovtun-Kante et al., 2014). It has been experimentally documented (Blindow and Schütte, 2007) that besides the negative effect of water turbidity the changes in salinity may increase stress for freshwater charophytes in transitional water bodies, such as the Curonian Lagoon. This stress could be enhanced by a human pressure, for instance, by dredging the canal connecting the lagoon and the Baltic Sea (Zemlys et al., 2013). The elevated salinity can affect both sexual reproduction and vegetative propagation (Blindow et al., 2003). Moreover, the changes in salinity may affect charophytes growth rates, incrustation of thalli, etc. (Pajusalu et al., 2015; Puche and Rodrigo, 2015; Rodrigo et al., 2015; Urbaniak, 2010 and references therein). Under such unfavorable and changing environmental conditions, stressed plants could be the ideal host for various microorganisms, such as bacteria and fungi, whose effect on a host can be contradictory, e.g., microorganisms can cause disease in their host (Egan et al., 2014, 2013). Eukaryotic fungi have less of an impact than bacteria in aquatic systems unless their habitat is relatively constant over time, either the nutrient source is difficult to degrade or fungi are in specific interactions with other organisms, such as mutualism, commensalism, parasitism and predation (Wurzbacher et al., 2010). Generally, fungi contribute to biofilm processes (Cantrell et al., 2006) and several of endophytic fungi are mutualistic (positively affect hosts while also obtain nutrition for growth and reproduction from tissues of hosts), thus both better resist abiotic stress *via* symbiosis (Rodriguez et al., 2009). However, there is a lack of understanding how freshwater macrophytes (including charophytes) and with them associated bacteria and fungi are affected by more frequent intrusions of saline waters.

Therefore, the aim of this study was to determine salinity effects on the microorganisms associated with charophytes from the Curonian Lagoon. We analyzed the net primary production of charophytes, abundance, and community composition of associated microorganisms from two sites that differ by frequency of brackish water intrusions, and performed *ex situ* experiment manipulating salinity. The composition of fungi associated with charophytes was evaluated using two techniques: nutrient media and PCR-DGGE analysis.

The Curonian Lagoon is situated in the southeastern part of the Baltic Sea (Fig. 1) and it is the largest lagoon (surface area 1584 km²) in Europe. The lagoon is shallow (mean depth 3.8 m) and hypereutrophic, almost entirely restricted from the Baltic Sea (Bresciani et al., 2012). The Klaipėda Strait provides the only and narrow connection (width of 0.4 km) to the Sea, while in the eastern part of the lagoon the Nemunas River (one of the largest rivers in the Baltic region) is entering the lagoon. Therefore, the Curonian Lagoon is always influenced by mixing masses of brackish and fresh-riverine waters. The inflow of brackish-waters depends on a wind speed and its direction, whereas the largest part of the lagoon consists of fresh water, which is mainly influenced by discharge of the Nemunas River. Intrusions of brackish waters usually occur in the northern part of the Curonian Lagoon, but sometimes they were recorded 40 km away from the Klaipėda Strait (Zemlys et al., 2013).

Two sampling sites (Fig. 1) with different salinity conditions were selected in order to compare microorganisms associated with charophytes. The first site (BW) was situated in the northern part near Kairiai, where annual mean salinity was 2.0–3.0 PSU and salinity > 0.5 PSU was observed 150–250 days per year (Zemlys et al., 2013). The second site (FW) was situated in the central part of the lagoon near Ventė, where annual mean salinity was 0.5–1.0 PSU and salinity > 0.5 PSU was observed 85–150 days per year.

During two sampling campaigns in June and August of 2014 *in situ* temperature, salinity and dissolved oxygen (DO) were measured using YSI 460 multiple probes. Samples of surface water were collected for analysis of dissolved inorganic phosphorus (DIP), nitrogen oxides (NO_x = NO₃ + NO₂), dissolved organic carbon (DOC), alkalinity and total phosphorus (TP). Aliquots for measurements of nutrients, DOC and TP were immediately filtered through Whatman GF/F into 10, 30 and 20 ml glass tubes respectively. For alkalinity analysis unfiltered water samples were used.

Nutrients were analyzed within 12 h by standard methods (Grasshoff et al., 2009) using continuous flow analyzer (San++, Skalar, sensitivity 0.3 μM). DOC was measured by the combustion catalytic oxidation method (at 680°C) with total organic carbon (TOC) analyzer Shimadzu. Water alkalinity was estimated by acid titration (Jenkins and Moore, 1977). TP was spectrophotometrically analyzed at 850 nm after acid persulphate oxidation (Grasshoff et al., 2009).

The *in situ* rates of net primary production (NPP) of charophytes were measured by the light–dark bottle technique (Blindow et al., 2006). Three replicates of 60 ml Winkler glass bottles were filled with water and immediately fixed with Winkler reagents for initial concentration of dissolved oxygen analysis. In the light and dark bottles (3 replicates each), weighted thalli of charophytes were added for incubation for 4 h in a climate chamber under the conditions close to *in situ* (incident photon flux density was 400 μE s⁻¹ m⁻², temperature 20–22°C). Synchronously, the NPP of pelagic primary producers was measured. However, it was negligible (up to 0.2% of total NPP), therefore total NPP was used in the analysis.

Five charophyte plants were collected for assessment of associated microorganisms.

Two *ex situ* experiments were performed with the most common charophytes (*Chara aspera* and *Chara contraria*) from the Curonian Lagoon: before (June) and after (August)

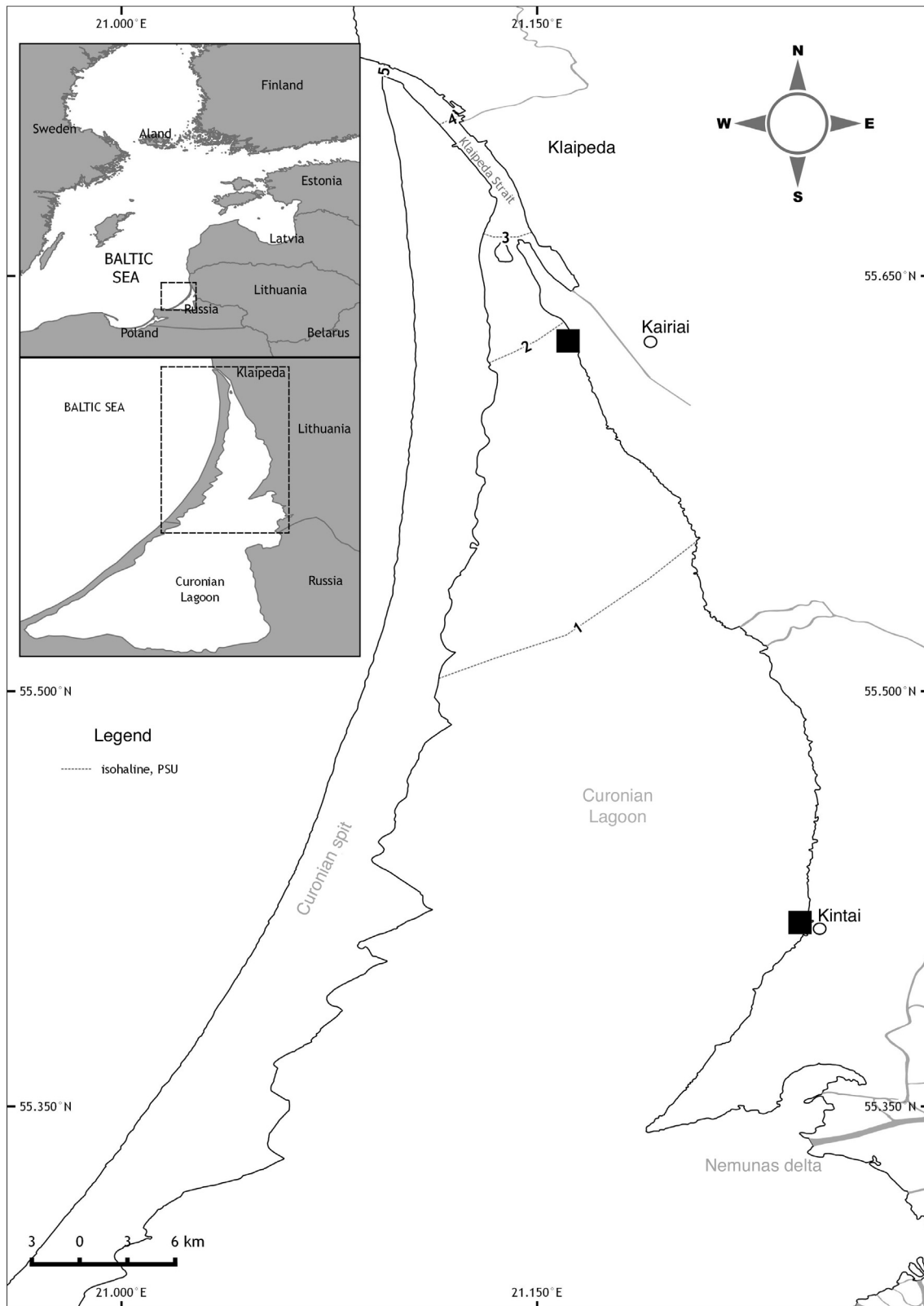


Figure 1 The study area and two sampling sites (indicated by squares), where different water masses dominate: brackish-water (BW) and freshwater (FW). The isohalines of near bottom salinity are taken from the modeled data (Umgiesser et al., 2004) during vegetation period in 2014.

the vegetation peak of charophytes. Each experiment lasted for 2 weeks. Nine intact sediment cores (i.d. 8 cm, height 30 cm) with dominant charophytes inside were collected by hand corer in 1.5 m depth (within 50–150 m from the shore) at each of two stations (Fig. 1). Intact cores were kept in a refrigerator and transferred to the laboratory within 4 h. The cores with charophytes were submerged (with the top open) in 3 incubation tanks with *in situ* water, maintaining its temperature close to natural near bottom conditions in the lagoon. These tanks were manipulated with 3 different treatments of salinity (0 PSU, 3 PSU and 6 PSU). Water was constantly stirred by rotating Teflon-coated magnet, which was fixed to the inner wall of each core for gentle water mixing avoiding sediment resuspension (Kientz et al., 2011). After two weeks, charophytes were taken from each core and pooled into sterile centrifuge tubes, kept in a refrigerator and carried into the lab within 4 h for further analysis of associated microorganisms. Simultaneously, the NPP of charophytes were measured before and after the incubation under different salinity conditions by the light–dark bottle technique as described above for *in situ* NPP measurements. Thalli of charophytes were weighted prior the incubation. Since the weight of charophytes may vary due to species and thalli specific content of calcium or magnesium carbonate (Kufel et al., 2016), each salinity treatment was performed in triplicates.

For associated microorganisms analyses, 5 plants from each experimental core were put into separate sterile centrifuge tubes, weighted, gently washed with sterile water to remove accidentally attached epiphytic microorganisms from the water column. For evaluation of endophytic microorganism presence in *in situ* samples, one set of charophytes were washed with a mixture of ethanol (50%) and sodium hypochlorite (1%) to remove all microorganisms from the surface (Kientz et al., 2011). Samples were homogenized,

serially diluted and plated onto Petri dishes with different agar media (3 replicates each). Potato dextrose agar was used for fungi cultivation and Luria broth agar for bacteria. A number of colonies were recalculated into values of colonies forming units (CFU) per gram of fresh charophytes weight. Purified fungal cultures were identified to species or generic taxonomic rank and collected for further molecular analysis. DNA was extracted from freeze-dried parts of charophytes with NucleoSpin kit for soil, according to the instructions of manufacture. The ITS2 region of fungal rDNA was amplified with primer pair ITS3GC and ITS4 (White et al., 1990) and DNA amplified, according to Duarte et al. (2008). Denaturing gradient gel electrophoresis analysis was performed using DGGEK – 2401 denaturing gradient gel electrophoresis system (C.B.S Scientific Company, INC). For fungal DNA, 10 µl samples from the PCR products were loaded on 8% [w/v] polyacrylamide gel in 1× Tris–acetate–EDTA (TAE) with denaturing gradient from 30 to 70%.

The statistical hypotheses about estimates were tested using several parametric and nonparametric statistical criteria depending on data properties (Table 1). All statistical tests were performed in R 3.2.0 (R Core Team, 2015) and using “nparcomp” package (Konietschke et al., 2015).

At freshwater (FW) site, water salinity was <1 PSU during the two sampling periods, whereas at brackish water (BW) site the salinity was almost 2 and 6 times higher in June and August, respectively (Table 2). The water temperature was around 16°C during both sampling campaigns at two sites. At both sites, the concentrations of DO, alkalinity, DIP, and TP were higher in June than in August, whereas the concentrations of DOC were in the opposite. The mean concentrations of water alkalinity and TP concentration were statistically significantly higher at FW site compared to BW site ($t = 5.5$, $df = 10$, $p < 0.001$; $t = 8.3$, $df = 10$, $p < 0.001$, respectively). The concentrations of NO_x during sampling were around

Table 1 Statistical methods used in this study to test the null hypothesis.

Statistical test	Statistical hypothesis
Welch's two sample <i>t</i> -test	The concentration of water alkalinity and total phosphorus (TP) do not statistically significantly differ between stations (FW and BW). The mean net primary production (NPP) of charophytes does not statistically significantly differ in June and August. <i>In situ</i> measured mean NPP (separately in each site) does not significantly differ from the mean NPP in the experiment set-up (corresponding treatments of salinity). The mean abundance of fungi from <i>in situ</i> samples does not significantly differ from the abundance of bacteria.
Analysis of variance (ANOVA)	The mean NPP of charophytes does not significantly differ between two sites and different salinities. The mean abundance of microorganisms (separately bacteria and fungi) does not significantly differ among the stressed conditions in June and August.
Tukey's honest significant difference (HSD) test	The mean abundance of microorganisms (separately bacteria and fungi) does not significantly differ among the contrasts of the two sites in June and August. The mean abundance of microorganisms (separately bacteria and fungi) does not significantly differ among the contrasts of the stressed conditions in June and August.
Nonparametric Tukey-type test	The mean NPP of charophytes (separately in each site) does not significantly differ among the salinity treatments.
Spearman rank correlation (r_s)	There is no relationship between the abundance of bacteria and fungi from <i>in situ</i> , the experiment set-up and different seasons.

Table 2 The main water column physical and chemical characteristics at two study sites (freshwater – FW and brackish water – BW) in the Curonian Lagoon in June and August, 2014.

Site	Month	Salinity [PSU]	Temperature [°C]	DO [mg l ⁻¹]	Alkalinity [mg l ⁻¹]	DOC [mmol l ⁻¹]	NO _x [μmol l ⁻¹]	DIP [μmol l ⁻¹]	TP [μmol l ⁻¹]
FW	June	0.19	16.3	10.1	2.3 ± 0.7	0.8 ± 0.1	28.3 ± 5.5	0.2 ± 0.02	2.5 ± 0.2
BW	June	1.96	16.3	12.5	1.6 ± 0.1	0.8 ± 0.2	1.8 ± 0.7	0.2 ± 0.01	1.3 ± 0.1
FW	August	0.17	16	8.8	2.6 ± 0.04	0.5 ± 0.05	1.7 ± 0.2	0.3 ± 0.01	3.0 ± 0.2
BW	August	6.44	16	7.9	2.0 ± 0.1	0.3 ± 0.05	2.6 ± 0.3	0.4 ± 0.1	1.6 ± 0.1

2–3 μmol l⁻¹, except in June at FW site, where its concentration reached 28.3 ± 5.5 μmol l⁻¹. The concentrations of DIP ranged from 0.2 to 0.4 μmol l⁻¹ at both sites.

The mean net primary production (NPP) of charophytes in June and August were 1.4 ± 0.9 and 2.1 ± 0.6 mg C L⁻¹ g ww⁻¹ h⁻¹, respectively, which did not significantly differ ($t = -1.57$, $df = 7.79$, $p > 0.05$). However, there was a significant interaction ($F = 7.84$, $df = 1$, $p < 0.05$) between the site and the salinity, therefore NPP was averaged over different salinities and sites for the further analysis (Fig. 2). *In situ* measured means of NPP in FW and BW sites did not significantly differ (respectively, $t = 0.38$, $df = 2$, $p > 0.05$ and $t = 1.13$, $df = 2$, $p > 0.05$) from the means of corresponding treatments of salinity (3 PSU and 0 PSU) in the experiment set-up. Significantly (nonparametric Tukey-type test $p < 0.05$) lower NPP of charophytes at BW site was measured after incubation in the salinity treatments of 0 PSU and 6 PSU than in the treatment 3 PSU, whereas at FW site it was significantly ($p < 0.01$) lower after incubation in the treatments of 3 PSU and 6 PSU. These reduced NPP show a potential stress of charophytes due to the changed salinity conditions in respect to those that commonly occur at BW and FW sites.

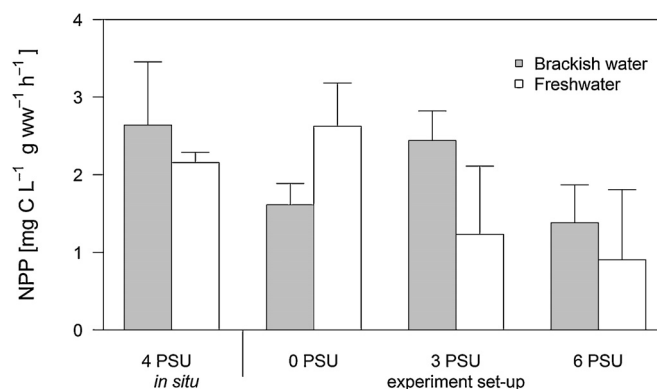
In order to test if these stressed conditions also affected bacteria and fungi associated with charophytes, the experiment set-up salinity treatments at sites were classified in the two groups according to the differences in NPP of charophytes: (1) natural conditions – 3 PSU at BW site and 0 PSU at FW site, and (2) stressed conditions – 0 PSU and 6 PSU at BW site, 3 PSU and 6 PSU at FW site.

From *in situ* samples, charophytes were colonized by bacteria in relatively high abundances from 2.2×10^4 CFU g⁻¹ fw to 8.0×10^4 CFU g⁻¹ fw (Fig. 3a). In June, the mean abundance of bacteria did not significantly differ (Tukey's HSD $p > 0.05$) between the two sites, while in August it was significantly higher only at BW site ($p < 0.05$).

The mean abundance of fungi from *in situ* samples was significantly ($t = 5.25$, $df = 15.97$, $p < 0.01$) lower than the abundance of bacteria and varied from 0.02×10^4 to 1.2×10^4 CFU g⁻¹ fw (Fig. 3b). In June, the mean abundance of fungi did not significantly differ (Tukey's HSD $p > 0.05$), while in August the fungal abundance at FW site increased almost 17-fold than in June (Tukey's HSD $p < 0.05$).

Similar patterns of bacterial and fungal abundances were observed in the experimental set-up, respectively. From *in situ* data in June, there was low correlation ($r_s = 0.29$, $N = 9$, $p > 0.05$) between bacteria and fungi abundance, whereas negative moderate correlation ($r_s = -0.61$, $N = 7$, $p > 0.05$) was determined in August. In the experiment set-up, there were negative low correlations in June ($r_s = -0.34$, $N = 18$, $p > 0.05$) and August ($r_s = -0.23$, $N = 18$, $p > 0.05$). All correlations were not statistically significant.

We also tested the effect of stressed conditions by water salinity to the mean abundance of bacteria and fungi associated with charophytes (Fig. 3c and d) from *in situ* and experiment set-up. From *in situ* samples, the mean abundance of bacteria was significantly (Tukey's HSD $p < 0.01$) higher under the stressed conditions in August than in the other contrasts, whereas in the experiment set-up it was significantly higher from the stressed conditions in June. From *in situ* samples, the mean abundance of fungi was

**Figure 2** The mean (±standard deviation) net primary production of charophytes in the Curonian Lagoon (*in situ*) and the experiment set-up with different salinities (0, 3 and 6 PSU) at two sites (freshwater and brackish water), 2014. The *in situ* salinity values are averaged field measurements (given in Table 2).

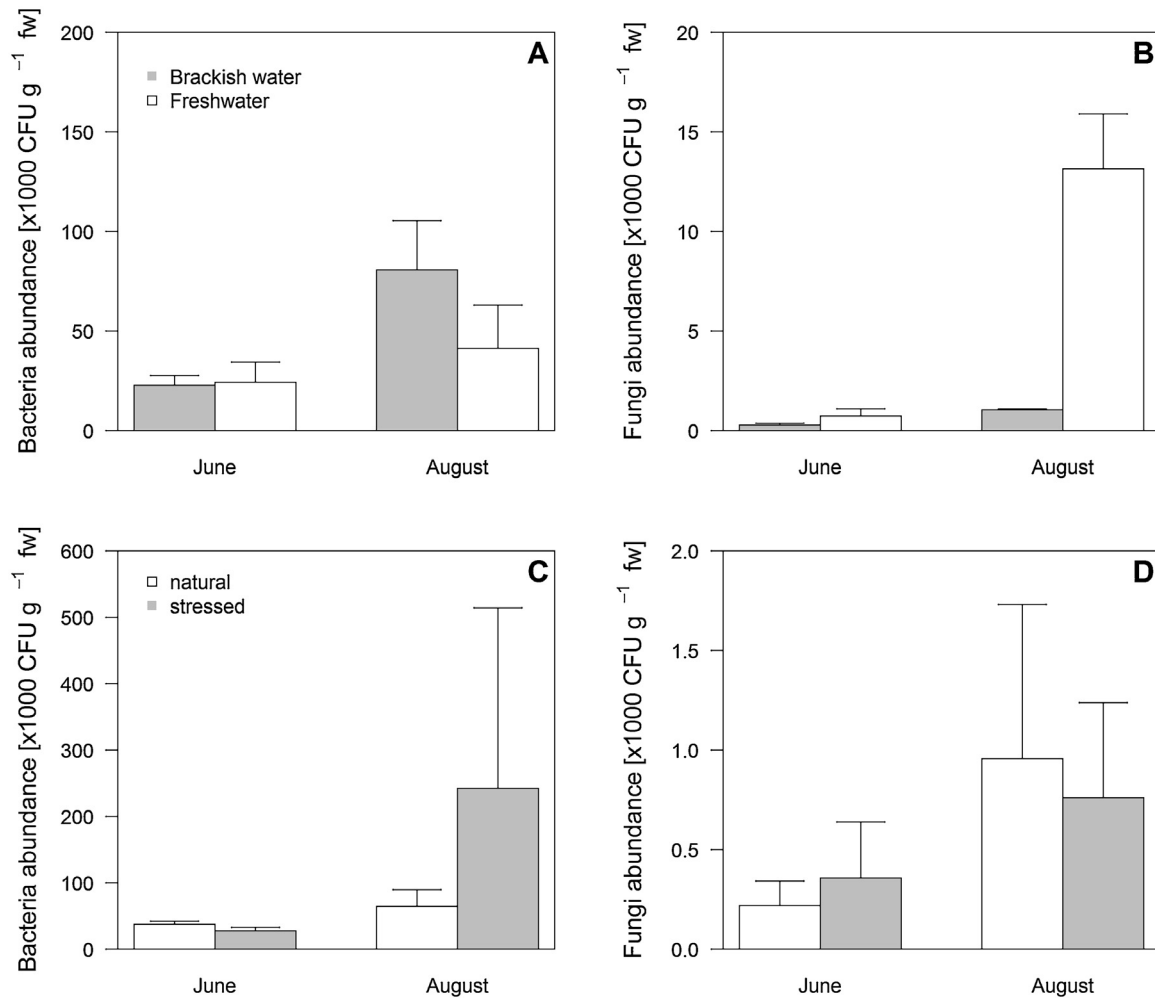


Figure 3 The mean (\pm standard deviation) abundance of bacteria and fungi associated with charophytes from two study sites (brackish water and freshwater) in the Curonian Lagoon (A and B) and in the experimental set-up under natural and stressed conditions (C and D), in June and August, 2014.

significantly (Tukey's HSD $p < 0.01$) higher under the natural conditions in August than in the other contrasts, whereas in the experiment set-up it was significantly higher from the natural conditions in June. There was no significant ($F = 2.20$, $df = 1$, $p > 0.05$) effect of the stress conditions.

In total, 8 taxa of fungi isolated on nutrient agar were identified to the genus level, whereas several not identified taxa were pooled into mycelia sterile group due to the lack of sporulation or other important features (Table 3). The number of fungi associated with charophytes *in situ* increased from 3 in July to 8 in August. During these periods, the similar pattern was observed from the experimental set-up.

Eighteen fungi operational taxonomical units (OTU) were found throughout the study, where 4 of them occurred frequently (Table 3); bands were considered common if they were found on $\geq 50\%$ of the dates. Although, the mean number of fungal OTU at BW site was higher compared with FW site, it did not significantly differ ($t = 1.5$, $df = 6.0$, $p > 0.05$).

The most common isolated taxa was *Cladosporium* sp., which was found at various salinity conditions in both months. *Alternaria* sp., *Rhizopus* sp., *Rhodotorula* sp. and *Fusarium* sp. were found only in samples from August (Table 3).

To the best of our knowledge, there are only a few studies about abundance of microorganisms associated with charophytes, and only one of them considers fungi (Berg and Hagemann, 2009; Hempel et al., 2008). Our results showed that the mean abundance of bacteria associated with charophytes was significantly higher than the one of fungi. The determined abundance of bacteria in the Curonian Lagoon was similar to the results obtained by Berg and Hagemann (2009), where *Chara hispida* plants from a lake habitat were colonized by bacteria in 0.3×10^5 – 4×10^5 CFU g^{-1} fw abundance. However, the mean abundance of fungi was 1×10^2 CFU g^{-1} fw, which was two times lower than in our study. Bacteria dominate over fungi on living and healthy plant due to different colonization and nutrition strategy: most bacteria are more efficient than fungi in the use of simple polysaccharides and peptides (Romani et al., 2012 and references therein) and are interacting as epiphytes (Egan et al., 2013), while fungi usually live as endophytes (Porrás-Alfaro and Bayman, 2011; Rodríguez et al., 2009) and only to some degree act as epiphytes in the phyllosphere of a plant.

In our study, the *in situ* abundance of bacteria and fungi increased at both sites during August (Fig. 3a). This pattern can be explained to some extent by findings in the studies of

Table 3 Presence (+) of fungi associated with charophytes after isolation on nutrient agar in June and August from two sites (freshwater and brackish water) and at different salinity treatments: from 0 to 6.44 PSU (* – *in situ* measurements). The number of fungal taxa assessed by cultivation on nutrient media and taxonomic units by denaturing gradient gel electrophoresis (DGGE). DGGE analysis data from August are missing due to the failed analysis.

Fungal taxa (abbreviation)	June				August													
	Brackish water				Freshwater				Brackish water				Freshwater					
	0	1.96*	3	6	0	0.19*	3	6	0	3	6	6.44*	0	0.17*	3	6		
<i>Alternaria</i> sp.											+	+		+				
<i>Aspergillus</i> sp.		+				+		+						+	+	+	+	
<i>Cladosporium</i> sp. (CLA)		+		+	+	+		+			+	+			+			
<i>Mucor</i> sp.		+							+	+	+	+			+	+		
<i>Penicillium</i> sp.		+				+		+						+	+	+	+	
<i>Rhizopus</i> sp.												+				+	+	
<i>Rhodotorula</i> sp.												+			+			
<i>Fusarium</i> sp.												+		+	+		+	
<i>Mycelia sterile</i>	+			+	+		+	+	+	+	+	+	+	+	+	+	+	
Yeasts				+	+				+		+			+				
Total fungal taxa	1	4		3	3	1	4	1	3	3	2	4	8	5	8		5	5
Fungal operational taxonomic units (DGGE)	4	8		10	11	5	6	8	1									

bacterias (Hempel et al., 2008; Romani et al., 2012), where older shoots usually enhance the growth of bacteria due to increased leak of organic compounds and inorganic nutrients. In the Curonian Lagoon, almost 12 fold difference in fungi abundance between FW and BW sites in August (Fig. 3b) indicates earlier senescence of charophytes at FW site. This could be explained by the different hydrological conditions at those two sites: a higher amount of organic material and more turbid waters from river inflow at FW site than at BW site (Kreves et al., 2007). Shallow freshwater aquatic ecosystems having abundant and diverse amount of organic matter (from both autochthonous and allochthonous origins) are a suitable habitat for microbial communities (Wetzel and Søndergaard, 1998; Wurzbacher et al., 2010). Abundant saprophytic fungi spores or hyphae from the water column and sediment can attach to a plant with lower photosynthetic activity and develop as epiphytes, meanwhile most of the endophyte fungi begin to act as saprobes and rapidly colonize decaying material (Porrás-Alfaro and Bayman, 2011; Zuccaro et al., 2008). Bacteria are also abundant in such environment (Wetzel and Søndergaard, 1998). However, in our study, the observed significantly lower abundance of bacteria at FW site compared with BW in August could be affected by fungal activities. It is known that microorganisms sharing the common host and substrate can interact in a synergistic or antagonistic manner (Mille-Lindblom et al., 2006; Zuccaro et al., 2008). Fungi are more efficient than bacteria in the use of complex polysaccharides and peptides and can inhibit the growth of bacteria by producing antibiotic substances at the same time (Romani et al., 2012 and references therein).

Our results from the *in situ* and the experimental set-up clearly showed the optimal salinities for the net primary production (NPP) of charophytes (see Fig. 2). The *in situ* rates of NPP from FW and BW sites were closest to NPP from the treatments that corresponded salinity appropriate for the sites (0 and 3 PSU, respectively). The similar pattern was

found in the southern Sweden (Blindow et al., 2003), where the highest rate of photosynthesis of *C. aspera* collected from freshwater lake was at 0 PSU, whereas plants collected from brackish water of the Baltic Sea (ca. 8 PSU) had their optima at 5–10 PSU. On the other hand, the significant decrease of NPP in our experiment was determined in the treatments that did not correspond *in situ* salinities, and therefore indicated stress of charophytes due to changes in salinity. According to Blindow et al. (2003), plants do not gradually adapt to increasing salinities and probable salinity shock can be feasible and affect physiological processes such as germination and photosynthesis.

Based on the data from our experimental set-up, we found that bacteria are partly affected by short term salinity changes (3 PSU at FW and 6 PSU at BW sites), which resulted in the increase of bacteria abundance. This can be due to increased leak of organic compounds and inorganic nutrients (Hempel et al., 2008; Romani et al., 2012) from stressed plants. Meanwhile, higher organic and lower phenolic content in a host plant seems to explain (Hempel et al., 2008) that the higher mean abundance of bacteria are observed at BW site than at FW site in August. Fungi abundance in the experimental set-up was significantly suppressed by short term changes in salinity only at FW site in August where the highest fungal activity was observed in *in situ* conditions. This could be caused by direct inhibition effect of saline water on fungi activity in the decomposition processes (Connolly et al., 2014) or indirect effect as salinity can trigger plant responsive mechanism against environmental stress (Holzinger and Pichrtová, 2016). Plant starts to produce secondary metabolites that protect the cell against environmental stress and possess antifungal properties (Ghazala et al., 2004; Juan et al., 2014), which can suppress epiphytic fungi.

In this study, the fungal diversity indicated by culturing method was lower in comparison with DGGE method. Microscopic or culture based methods usually underestimate the

diversity of fungi in comparison with molecular methods (Duarte et al., 2012) due to a small size of identified organisms, the absence of distinguishing phenotypic characters and that most of the microorganisms cannot be cultured (Duarte et al., 2012). On the other hand, molecular methods can show a presence of not active (dead) microorganisms (Duarte et al., 2012). The combination of traditional (fungal strain cultivation on agar media) and molecular techniques is the best option for identification of fungal community associated with macrophytes.

From our isolated fungi, *Alternaria* sp. and *Cladosporium* sp. are considered as one of the most common fungi taxa of the aquatic algae (Loque et al., 2009; Zuccaro et al., 2003). Both taxa appear to lack host specificity, having been isolated as fungal endophytes from numerous locations and hosts (Flewelling et al., 2015 and references therein). Fungi taxa observed from the samples in August (*Fusarium*, *Penicillium*, *Aspergillus*, *Cladosporium*, *Mucor* and *Rhizopus*) are dominating genera of terrigenous micromycetes, which propagules are abundant in the water column and bottom sediments (Voronin, 2014). Most of the fungi belonging to those genera are saprophytes and their spores or hyphae from the water column and sediment can attach to a plant and take part in decomposition processes (Wurzbacher et al., 2010). In August, their presence in association with charophytes and increased abundance could indicate senescence processes of charophytes.

There were a similar number of culturable fungi taxa at both study sites. Slightly higher diversity at BW site was observed in June based on DGGE analysis. It is known that diversity of fungi usually decreases with increasing salt concentration (Kis-Papo et al., 2001). Although, fungi can exhibit broad salt tolerance, higher fungal diversity is observed in brackish than in marine or freshwater environment (El-Sharouny et al., 2009; Mohamed and Martiny, 2011; Ristanović and Miller, 1969). Osmotic pressure by salinity can affect the production of conidia and growth of filamentous fungi (Mert and Ekmekçi, 1987). Nevertheless, other abiotic factors can influence fungal diversity, such as temperature, substrate (nutrient availability), pH, hydrostatic pressure and oxygen (Bärlocher and Boddy, 2016).

Thus, it is evident that more understanding is needed in ecological interactions between microorganisms and their hosts under dynamic environmental conditions (such as estuaries) in order to predict ecosystem changes according to ecological scenarios (e.g. climate change). The discovered diversity of fungi, especially of endophytic origin, could be an interesting study object for applied scientists to assess capabilities for production of bioactive compounds (Schulz et al., 2002). It is known that *Alternaria* sp. possess antimicrobial and anticancer activity, *Cladosporium* sp. – antimicrobial and insecticidal activity (Flewelling et al., 2015; Schulz et al., 2008), *Penicillium* and *Aspergillus* – antialgal, antimicrobial, anticancer, antioxidant, and insecticidal bioactivity (Flewelling et al., 2015).

In this study, we have shown that with charophytes associated bacteria dominate over fungi. In the end of the vegetation period, considerably lower fungi abundance at the site frequently affected by brackish water than at the freshwater site indicates that charophyte beds are in better status in the brackish water environment, whereas at the freshwater site saprophytic fungi are most likely to take part

in senescence process of vegetation. The short salinity changes partly influenced the abundance of associated bacteria and fungi; therefore, other environmental factors than salinity could be important, including the reaction of hosts (e.g., production of secondary metabolites). The revealed diversity of fungal taxa associated with charophytes may serve for future applied research on the importance of these fungi for biologically active metabolites.

Acknowledgement

Financial support was provided by Research Council of Lithuania (Contract Nr. VAT-MIP-040/2014).

References

- Andrews, J.H., Harris, R.F., 2000. The ecology and biogeography of microorganisms on plant surfaces. *Annu. Rev. Phytopathol.* 38 (1), 145–180, <http://dx.doi.org/10.1146/annurev.phyto.38.1.145>.
- Armstrong, E., Yan, L., Boyd, K.G., Wright, P.C., Burgess, J.G., 2001. The symbiotic role of marine microbes on living surfaces. *Hydrobiologia* 461 (1–3), 37–40, <http://dx.doi.org/10.1023/A:1012756913566>.
- Bärlocher, F., Boddy, L., 2016. Aquatic fungal ecology – how does it differ from terrestrial? *Fungal Ecol.* 19, 5–13, <http://dx.doi.org/10.1016/j.funeco.2015.09.001>.
- Berg, G., Hagemann, M., 2009. Microorganisms associated with *Chara hispida* L. show a high antagonistic potential towards bacteria. *IOBC/wprs Bull.* 43. Jt. COST Action 873, 271–275.
- Blindow, I., 2000. Distribution of Charophytes along the Swedish coast in relation to salinity and eutrophication. *Int. Rev. Hydrobiol.* 85 (5–6), 707–717, [http://dx.doi.org/10.1002/1522-2632\(200011\)85:5/6<707::AID-IROH707>3.0.CO;2-w](http://dx.doi.org/10.1002/1522-2632(200011)85:5/6<707::AID-IROH707>3.0.CO;2-w).
- Blindow, I., Dietrich, J., Möllmann, N., Schubert, H., 2003. Growth, photosynthesis and fertility of *Chara aspera* under different light and salinity conditions. *Aquat. Bot.* 76 (3), 213–234, [http://dx.doi.org/10.1016/S0304-3770\(03\)00053-6](http://dx.doi.org/10.1016/S0304-3770(03)00053-6).
- Blindow, I., Hargeby, A., Meyercordt, J., Schubert, H., 2006. Primary production in two shallow lakes with contrasting plant form dominance: a paradox of enrichment? *Limnol. Oceanogr.* 51 (6), 2711–2721, <http://dx.doi.org/10.4319/lo.2006.51.6.2711>.
- Blindow, I., Schütte, M., 2007. Elongation and mat formation of *Chara aspera* under different light and salinity conditions. In: Gulati, R.D., Lammens, E., Pauw, N.D., Donk, E.V. (Eds.), *Shallow Lakes in a Changing World, Developments in Hydrobiology*. Springer, Netherlands, 69–76.
- Bresciani, M., Giardino, C., Stroppiana, D., Pilkaitytė, R., Zilius, M., Bartoli, M., Razinkovas, A., 2012. Retrospective analysis of spatial and temporal variability of chlorophyll-*a* in the Curonian Lagoon. *J. Coast. Conserv.* 16 (4), 511–519, <http://dx.doi.org/10.1007/s11852-012-0192-5>.
- Cantrell, S.A., Casillas-Martinez, L., Molina, M., 2006. Characterization of fungi from hypersaline environments of solar salterns using morphological and molecular techniques. *Mycol. Res.* 110 (8), 962–970, <http://dx.doi.org/10.1016/j.mycres.2006.06.005>.
- Connolly, C.T., Sobczak, W.V., Findlay, S.E., 2014. Salinity effects on Phragmites decomposition dynamics among the Hudson River's freshwater tidal wetlands. *Wetlands* 34 (3), 575–582, <http://dx.doi.org/10.1007/s13157-014-0526-1>.
- Duarte, S., Cássio, F., Pascoal, C., 2012. Denaturing Gradient Gel Electrophoresis (DGGE) in microbial ecology—insights from freshwaters. In: Magdeldin, S. (Ed.), *Gel Electrophoresis – Principles and Basics*. InTech, Croatia, 173–195, <http://www.intechopen.com/books/gel-electrophoresis-principles-and-basics>.
- Duarte, S., Pascoal, C., Alves, A., Correia, A., Cássio, F., 2008. Copper and zinc mixtures induce shifts in microbial communities

- and reduce leaf litter decomposition in streams. *Freshw. Biol.* 53 (1), 91–101, <http://dx.doi.org/10.1111/j.1365-2427.2007.01869.x>.
- Dugdale, T.M., Hicks, B.J., De Winton, M., Taumoepeau, A., 2006. Fish enclosures versus intensive fishing to restore charophytes in a shallow New Zealand lake. *Aquat. Conserv.* 16 (6), 193–202, <http://dx.doi.org/10.1002/aqc.711>.
- Egan, S., Fernandes, N.D., Kumar, V., Gardiner, M., Thomas, T., 2014. Bacterial pathogens, virulence mechanism and host defence in marine macroalgae. *Environ. Microbiol.* 16 (4), 925–938, <http://dx.doi.org/10.1111/1462-2920.12288>.
- Egan, S., Harder, T., Burke, C., Steinberg, P., Kjelleberg, S., Thomas, T., 2013. The seaweed holobiont: understanding seaweed–bacteria interactions. *FEMS Microbiol. Rev.* 37 (3), 462–476, <http://dx.doi.org/10.1111/1574-6976.12011>.
- El-Sharouny, H.M., Gherbawy, Y.A.M.H., Abdel-Aziz, F.A., 2009. Fungal diversity in brackish and saline lakes in Egypt. *Nova Hedwigia* 89 (3–4), 437–450, <http://dx.doi.org/10.1127/0029-5035/2009/0089-0437>.
- Flewelling, A.J., Currie, J., Gray, C.A., Johnson, J.A., 2015. Endophytes from marine macroalgae: promising sources of novel natural products. *Curr. Sci.* 109 (1), 88–111.
- Ghazala, B., Naila, B., Shameel, M., Shahzad, S., Leghari, S.M., 2004. Phycochemistry and bioactivity of two stonewort algae (Charophyta) of Sindh. *Pak. J. Bot.* 36 (4), 733–743.
- Godinho, V.M., Furbino, L.E., Santiago, I.F., Pellizzari, F.M., Yokoya, N.S., Pupo, D., Alves, T.M., Junior, P.A.S., Romanha, A.J., Zani, C. L., Cantrell, C.L., Rosa, C.A., Rosa, L.H., 2013. Diversity and bioprospecting of fungal communities associated with endemic and cold-adapted macroalgae in Antarctica. *ISME J.* 7 (7), 1434–1451, <http://dx.doi.org/10.1038/ismej.2013.77>.
- Grasshoff, K., Kremling, K., Ehrhardt, M., 2009. *Methods of Seawater Analysis*. John Wiley & Sons, Weinheim, 632 pp.
- Hempel, M., Blume, M., Blindow, I., Gross, E.M., 2008. Epiphytic bacterial community composition on two common submerged macrophytes in brackish water and freshwater. *BMC Microbiol.* 8, 58, <http://dx.doi.org/10.1186/1471-2180-8-58>.
- Hilt, S., 2015. Regime shifts between macrophytes and phytoplankton – concepts beyond shallow lakes, unravelling stabilizing mechanisms and practical consequences. *Limnetica* 34 (2), 467–480.
- Holzinger, A., Pichrtová, M., 2016. Abiotic stress tolerance of charophyte green algae: new challenges for omics techniques. *Front. Plant Sci.* 7, 1–17, <http://dx.doi.org/10.3389/fpls.2016.00678>.
- Hudon, C., Cattaneo, A., Gagnon, P., 2009. Epiphytic cyanobacterium *Gloeotrichia pismus* as an indicator of nitrogen depletion. *Aquat. Microb. Ecol.* 57 (2), 191–202, <http://dx.doi.org/10.3354/ame01344>.
- Jenkins, S.R., Moore, R.C., 1977. A proposed modification to the classical method of calculating alkalinity in natural waters. *J. Am. Water Works Assoc.* 69 (1), 56–60.
- Juan, M., Casas, J.J., Elorrieta, M.A., Bonachela, S., Gallego, I., Fuentes-Rodríguez, F., Fenoy, E., 2014. Can submerged macrophytes be effective for controlling waterborne phytopathogens in irrigation ponds? An experimental approach using microcosms. *Hydrobiologia* 732 (1), 183–196, <http://dx.doi.org/10.1007/s10750-014-1875-8>.
- Kientz, B., Thabard, M., Cragg, S.M., Pope, J., Hellio, C., 2011. A new method for removing microflora from macroalgal surfaces: an important step for natural product discovery. *Bot. Mar.* 54 (5), 457–469, <http://dx.doi.org/10.1515/BOT.2011.053>.
- Kis-Papo, T., Grishkan, I., Oren, A., Wasser, S.P., Nevo, E., 2001. Spatiotemporal diversity of filamentous fungi in the hypersaline Dead Sea. *Mycol. Res.* 105 (06), 749–756, <http://dx.doi.org/10.1017/S0953756201004129>.
- Konietschke, F., Placzek, M., Schaarschmidt, F., Hothorn, L.A., nparcomp: an R software package for nonparametric multiple comparisons and simultaneous confidence intervals. *J. Stat. Softw.* 64 (9), <http://dx.doi.org/10.18637/jss.v064.i09>.
- Kovtun-Kante, A., Torn, K., Kotta, J., 2014. In situ production of charophyte communities under reduced light conditions in a brackish water ecosystem. *Est. J. Ecol.* 63 (1), 28–38, <http://dx.doi.org/10.3176/eco.2014.1.03>.
- Kreys, A., Koreiviene, J., Paskauskas, R., Sulijene, R., 2007. Phytoplankton production and community respiration in different zones of the Curonian lagoon during the midsummer vegetation period. *Transit. Water Bull.* 1 (1), 17–26.
- Kufel, L., Kufel, I., 2002. *Chara* beds acting as nutrient sinks in shallow lakes—a review. *Aquat. Bot.* 72 (3–4), 249–260, [http://dx.doi.org/10.1016/S0304-3770\(01\)00204-2](http://dx.doi.org/10.1016/S0304-3770(01)00204-2).
- Kufel, L., Strzatek, M., Biardzka, E., 2016. Site- and species-specific contribution of charophytes to calcium and phosphorus cycling in lakes. *Hydrobiologia* 767 (1), 185–195, <http://dx.doi.org/10.1007/s10750-015-2498-4>.
- Loque, C.P., Medeiros, A.O., Pellizzari, F.M., Oliveira, E.C., Rosa, C. A., Rosa, L.H., 2009. Fungal community associated with marine macroalgae from Antarctica. *Polar Biol.* 33 (5), 641–648, <http://dx.doi.org/10.1007/s00300-009-0740-0>.
- Mathieson, A.C., Nienhuis, P.H., 1991. *Intertidal and Littoral Ecosystems*. Elsevier, New York, 564 pp.
- Mert, H.H., Ekmekçi, S., 1987. The effect of salinity and osmotic pressure of the medium on the growth, sporulation and changes in the total organic acid content of *Aspergillus flavus* and *Penicillium chrysogenum*. *Mycopathologia* 100 (2), 85–89, <http://dx.doi.org/10.1007/BF00467099>.
- Mille-Lindblom, C., Fischer, H.J., Tranvik, L., 2006. Antagonism between bacteria and fungi: substrate competition and a possible tradeoff between fungal growth and tolerance towards bacteria. *Oikos* 113 (2), 233–242, <http://dx.doi.org/10.1111/j.2006.0030-1299.14337.x>.
- Mohamed, D.J., Martiny, J.B., 2011. Patterns of fungal diversity and composition along a salinity gradient. *ISME J.* 5 (3), 379–388, <http://dx.doi.org/10.1038/ismej.2010.137>.
- Pajusalu, L., Martin, G., Pöllumäe, A., Paalme, T., 2015. Direct effects of increased CO₂ concentrations in seawater on the net primary production of charophytes in a shallow, coastal, brackish-water ecosystem. *Boreal Environ. Res.* 20 (3), 413–422.
- Pitkänen, H., Peuraniemi, M., Westerborn, M., Kilpi, M., Numers, M. V., 2013. Long-term changes in distribution and frequency of aquatic vascular plants and charophytes in an estuary in the Baltic Sea. *Ann. Bot. Fenn.* 50 (SA), 1–54.
- Porras-Alfaro, A., Bayman, P., 2011. Hidden fungi, emergent properties: endophytes and microbiomes. *Ann. Rev. Phytopathol.* 49 (1), 291–315, <http://dx.doi.org/10.1146/annurev-phyto-080508-081831>.
- Puche, E., Rodrigo, M.A., 2015. Increased water salinity negatively affects charophytes from a spring created within the Albufera de València Natural Park. *Limnetica* 34 (2), 349–364.
- R Core Team, 2015. R: A Language and Environment for Statistical Computing. R Foundation for Statistical Computing, Vienna, Austria, <https://www.R-project.org/>.
- Ristanović, B., Miller, C.E., 1969. Salinity tolerances and ecological aspects of some fungi collected from fresh-water, estuarine and marine habitats. *Mycopathol. Mycol. Appl.* 37 (3), 273–280, <http://dx.doi.org/10.1007/BF02051361>.
- Rodrigo, M.A., Rojo, C., Segura, M., Alonso-Guillén, J.L., Martín, M., Vera, P., 2015. The role of charophytes in a Mediterranean pond created for restoration purposes. *Aquat. Bot.* 120, 101–111, <http://dx.doi.org/10.1016/j.aquabot.2014.05.004>.
- Rodríguez, R.J., White Jr., J.F., Arnold, A.E., Redman, R.S., 2009. Fungal endophytes: diversity and functional roles. *New Phytol.* 182 (2), 314–330, <http://dx.doi.org/10.1111/j.1469-8137.2009.02773.x>.
- Romani, A.M., Artigas, J., Ylla, I., 2012. Extracellular enzymes in aquatic biofilms: microbial interactions versus water quality effects in the use of organic matter. In: Lear, G., Lewis, G.

- (Eds.), *Microbial Biofilms: Current Research and Applications*. Caister Acad. Press, Wymondham, 153–174.
- Schmieder, K., Werner, S., Bauer, H.-G., 2006. Submersed macrophytes as a food source for wintering waterbirds at Lake Constance. *Aquat. Bot.* 84 (3), 245–250, <http://dx.doi.org/10.1016/j.aquabot.2005.09.006>.
- Schulz, B., Boyle, C., Draeger, S., Römmert, A.-K., Krohn, K., 2002. Endophytic fungi: a source of novel biologically active secondary metabolites. *Mycol. Res.* 106 (9), 996–1004, <http://dx.doi.org/10.1017/S0953756202006342>.
- Schulz, B., Draeger, S., dela Cruz, T.E., Rheinheimer, J., Siems, K., Loesgen, S., Bitzer, J., Schloerke, O., Zeeck, A., Kock, I., Hussain, H., Dai, J., Krohn, K., 2008. Screening strategies for obtaining novel, biologically active, fungal secondary metabolites from marine habitats. *Bot. Mar.* 51 (3), 219–234, <http://dx.doi.org/10.1515/BOT.2008.029>.
- Umgiesser, G., Canu, D.M., Cucco, A., Solidoro, C., 2004. A finite element model for the Venice Lagoon, Development, set up, calibration and validation. *J. Mar. Syst.* 51 (1–4), 123–145, <http://dx.doi.org/10.1016/j.jmarsys.2004.05.009>.
- Urbaniak, J., 2010. Estimation of carbonate and element content in charophytes – methods of determination. *Polish J. Environ. Stud.* 19 (2), 413–417.
- Voronin, L.V., 2014. Terrigenous micromycetes in freshwater ecosystems (review). *Inland Water Biol.* 7 (4), 352–356, <http://dx.doi.org/10.1134/S1995082914040191>.
- Wetzel, R.G., Søndergaard, M., 1998. Role of submerged macrophytes for the microbial community and dynamics of dissolved organic carbon in aquatic ecosystems. In: Jeppesen, E., Søndergaard, M., Christoffersen, K. (Eds.), *The Structuring Role of Submerged Macrophytes in Lakes*. Springer, New York, 133–148.
- White, T.J., Burns, T., Lee, S., Taylor, J.W., 1990. Amplification and direct sequencing of fungal ribosomal RNA genes for phylogenetics. In: Innis, M.A., Gelfand, D.H., Sninsky, J.J., White, T.J. (Eds.), *PCR Protocol: A Guide to Methods and Applications*. Academic Press, New York, 315–322.
- Wurzbacher, C.M., Bärlocher, F., Grossart, H., 2010. Fungi in lake ecosystems. *Aquat. Microb. Ecol.* 59 (2), 125–149, <http://dx.doi.org/10.3354/ame01385>.
- Zemlys, P., Ferrarin, C., Umgiesser, G., Gulbinskas, S., Bellafiore, D., 2013. Investigation of saline water intrusions into the Curonian Lagoon (Lithuania) and two-layer flow in the Klaipėda Strait using finite element hydrodynamic model. *Ocean Sci.* 9 (3), 573–584, <http://dx.doi.org/10.5194/os-9-573-2013>.
- Zuccaro, A., Schoch, C.L., Spatafora, J.W., Kohlmeyer, J., Draeger, S., Mitchell, J.I., 2008. Detection and identification of Fungi intimately associated with the brown seaweed *Fucus serratus*. *Appl. Environ. Microbiol.* 74 (4), 931–941, <http://dx.doi.org/10.1128/AEM.01158-07>.
- Zuccaro, A., Schulz, B., Mitchell, J.I., 2003. Molecular detection of ascomycetes associated with *Fucus serratus*. *Mycol. Res.* 107 (12), 1451–1466, <http://dx.doi.org/10.1017/S0953756203008657>.



Available online at www.sciencedirect.com

ScienceDirect

journal homepage: www.journals.elsevier.com/oceanologia/



SHORT COMMUNICATION

Oceanographic observations in the Nordic Sea and Fram Strait in 2016 under the IO PAN long-term monitoring program AREX

Waldemar Walczowski*, Agnieszka Beszczynska-Möller, Piotr Wieczorek, Malgorzata Merchel, Agata Grynczel

Institute of Oceanology, Polish Academy of Sciences, Sopot, Poland

Received 13 December 2016; accepted 25 December 2016

Available online 13 January 2017

KEYWORDS

Nordic Seas;
Physical oceanography;
Atlantic water

Summary Since 1987 annual summer cruises to the Nordic Seas and Fram Strait have been conducted by the IO PAN research vessel *Oceania* under the long-term monitoring program AREX. Here we present a short description of measurements and preliminary results obtained during the open ocean part of the AREX 2016 cruise. Spatial distributions of Atlantic water temperature and salinity in 2016 are similar to their long-term mean fields except for warmer recirculation of Atlantic water in the northern Fram Strait. The longest observation record from the section N along 76°30'N reveals a steady increase of Atlantic water salinity, while temperature trend depends strongly on parametrization used to define the Atlantic water layer. However spatially averaged temperature at different depths indicate an increase of Atlantic water temperature in the whole layer from the surface down to 1000 m.

© 2017 Institute of Oceanology of the Polish Academy of Sciences. Production and hosting by Elsevier Sp. z o.o. This is an open access article under the CC BY-NC-ND license (<http://creativecommons.org/licenses/by-nc-nd/4.0/>).

1. The IO PAN long-term monitoring program AREX

The northernmost polar region is most sensitive to global climate change and its effects are most exaggerated and have the biggest impact in the Arctic. Climate change is faster and more severe in the Arctic, which is warming at a rate of almost twice the global average (Cohen et al., 2014; Serreze et al., 2009). A steady temperature increase, observed both in the atmosphere and in the ocean, has a profound impact on the sea ice cover in the sub-Arctic seas

* Corresponding author at: Institute of Oceanology, Polish Academy of Sciences, 81-712 Sopot, Poland. Tel.: +48 58 73 11 904; fax: +48 58 551 21 30.

E-mail address: walczows@iopan.gda.pl (W. Walczowski).

Peer review under the responsibility of Institute of Oceanology of the Polish Academy of Sciences.



Production and hosting by Elsevier

and Arctic Ocean (e.g. Polyakov et al., 2012; Stroeve et al., 2012). In the last two decades, the summer sea ice extent has shrunk dramatically together with a strong decline of its thickness and volume (Serreze and Stroeve, 2015). While many complex feedback processes contribute to the enhanced warming of the Arctic region called Arctic amplification, it is largely driven by the loss of the sea ice cover, allowing for strong heat transfers from the ocean to the atmosphere. By exposing larger dark open areas, where the ocean can absorb more of the sun's energy and in consequence warm further, the loss of sea ice in the Arctic Ocean also has the potential to accelerate global warming trends and to change climate patterns (Overland, 2016).

Large oceanic exchanges between the North Atlantic and the Arctic Ocean result in the strong conversion of water masses when warm and salty Atlantic water (AW), transported through the Nordic Seas into the Arctic Ocean, undergo cooling, freezing and melting. As a result, it is transformed into freshened shelf waters over the shallow shelves, sea ice and dense (and highly saline) deep waters (e.g. Dickson et al., 2008). Southward transport of the Arctic origin and dense overflow waters is one of the main mechanisms of the global thermohaline circulation (THC, e.g. Mauritzen, 1996). A better understanding of the variability of volume and heat transports between the North Atlantic and Arctic Ocean as well as processes of water mass conversion is necessary for improved qualitative and quantitative estimation of the large-scale meridional overturning circulation and its role in shaping the climate change in the northern hemisphere on inter-annual to decadal time scales.

Fram Strait is the only deep passage linking the Nordic Seas and the Arctic Ocean. The northward transport of warm and salty Atlantic water, carried by the Norwegian-Atlantic Current and farther by the West Spitsbergen Current, has a significant impact on conversion and circulation of water masses in the Arctic Ocean (e.g. Rudels et al., 2015) as well as on sea ice and atmospheric fluxes in the Arctic. The complex bottom topography of the northern Greenland Sea and Fram Strait results in the splitting of both currents into several branches, located along the underwater ridges and the continental slope (e.g. Bourke et al., 1988; Quadfasel et al., 1987; Walczowski, 2014). The spatial extent and relative intensity of these branches to a great degree determine oceanic heat flux into the Arctic Ocean (e.g. Beszczynska-Möller et al., 2012; Schauer et al., 2008).

Understanding of Arctic climate processes is the main aim of the current oceanographic and atmospheric studies carried on in the polar region. The Institute of Oceanology PAN (IO PAN) contributes to this challenge with the strategic research initiative addressing the role of the ocean in changing climate and its effects on the European seas. Its core activity, the long-term monitoring program AREG, is focused on multidisciplinary observations in areas such as physical oceanography, air–ocean interactions, ocean biogeochemistry and ecology to study the long-term changes of abiotic and biotic Arctic environment. Every summer since 1987 the large-scale field measurements have been carried out in the Nordic Seas and European Arctic from the board of the IO PAN research vessel *Oceania*. These data, collected under the observational program AREG every year in the same way, provide time series of key ocean variables which allow monitoring changes of the Arctic environment and improving

numerical simulations of ocean, sea ice and climate in the Arctic region.

The main aim of the long-term AREG program and annual cruises, carried by r/v *Oceania* for the last 30 years in the Nordic Seas and Fram Strait, is to recognize and describe processes responsible for changing ocean climate and marine ecosystem in the sub-Arctic and Arctic region with a special focus on the European Arctic (Walczowski, 2014). To achieve this goal a large-scale study area, covering the poleward flow of Atlantic water in the eastern Nordic Seas and Fram Strait, has been selected for annually repeated ship-borne measurements on a regular grid. Most of the regularly repeated stations are distributed along several zonal sections, crossing the continental shelf break at the right angle and extending towards the deep basin. On the eastern side, the AREG oceanographic sections are limited by the Barents Sea shelf break and the shelf area west and north of Svalbard. To the west, the sections cross the Arctic Front, located above the system of underwater ridges (the Mohn and Knipovich ridges) and limiting the extent of Atlantic water in the Nordic Seas. The zonal sections following the Atlantic water inflow from the Norwegian Sea to the northern Fram Strait allow to assess transformation of water masses originating from the North Atlantic and advected northward. Two meridional sections, one from the northern Norway towards the Bear Island and one between the Bear Island and the southernmost tip of Svalbard (Sørkapp), cover the eastward flow of Atlantic water to the Barents Sea.

The AREG program and IO PAN field campaigns in the Arctic region are mainly based on statutory funding but since the early 90s they have also contributed significantly to several international projects, e.g. VEINS (Variability of Exchanges in the Nordic Seas, 1997–2000), ASOF-N (Arctic and subArctic Oceanic Fluxes – North, 2003–2005), and IP DAMOCLES (Developing Arctic Modelling and Observing Capabilities for Long-term Environment Studies, 2006–2009). The summer measurement campaigns of r/v *Oceania* and year-round observations with oceanographic moorings in the Nordic Seas, Fram Strait and, in recent years, in the southern Nansen Basin also provided crucial data for several projects under the Polish-Norwegian Research Program, including AWAKE-1 and -2, PAVE, CDOM-HEAT, POLNOR, and others. Last but not least, time series of ocean observations, collected in the last 30 years from r/v *Oceania*, have been employed by many IO PAN researchers and PhD students to carry on numerous studies of the Arctic climate and environment in the frame of IO PAN statutory research.

2. Oceanographic measurements during the AREG 2016 cruise

The AREG cruise of the IO PAN research vessel *Oceania*, repeated every summer over the same time period (June–August), in 2016 took place from June 14 to August 29. Two legs of the AREG 2016 cruise were devoted to the collection of oceanographic, meteorological, aerosol and ocean ecosystem observations in the open ocean regions, including the eastern Norwegian and Greenland seas, Fram Strait and the southern Nansen Basin of the Arctic Ocean.

The hydrographic survey carried out during the AREG 2016 cruise consisted of 11 sections extending from the outer

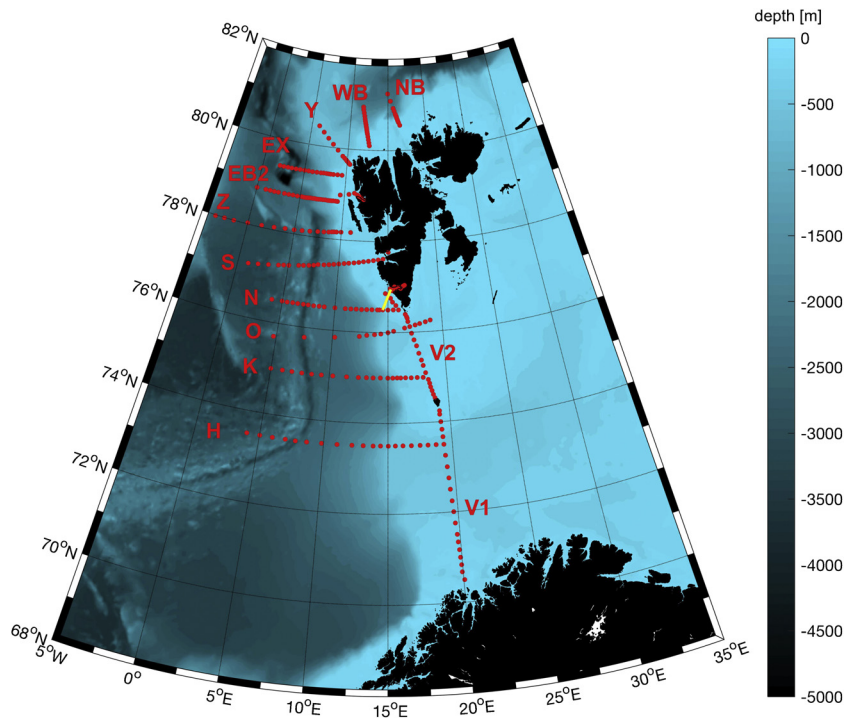


Figure 1 Location of CTD stations measured during the open ocean part of AREX 2016 (June 21–July 24, 2016). Red dots mark CTD stations and yellow line shows the high-resolution towed CTD section. (For interpretation of the references to color in this figure legend, the reader is referred to the web version of this article.)

shelf across the slope into the deep basin in order to sample the northward flow of Atlantic water and 2 meridional sections across the Barents Sea Opening and Storfjorden Trough to assess the exchange with the Barents Sea. A total of 270 conductivity-temperature-depth (CTD) full-depth stations within the geographical area $70^{\circ}30'–81^{\circ}15'N$ and $0–20^{\circ}E$ (with one section extending to $5^{\circ}W$) were carried out from June 21 to July 24, 2016, on board the r/v *Oceania* (Fig. 1). In addition to CTD casts, the ocean currents were measured with a Lowered Acoustic Doppler Current Profiler (LADCP) at each station and the upper ocean currents were continuously recorded during the whole survey with a Vessel-Mounted Acoustic Doppler Current Profiler (VMADCP). Water samples were collected at selected stations for calibration of conductivity sensor and biological and biogeochemical analyses.

Oceanographic measurements and collection of water samples during the AREX 2016 cruise contributed to several IO PAN statutory tasks and external research projects (national and international). Observations were carried on by three groups of scientists, focused on physical oceanography, meteorology and air–ocean interactions, and marine biology, but collaborating together during different shipborne measurements. A total of 10 scientists were supported on deck by two oceanographic instrumentation technicians and the ship crew for the heavy gear operations (e.g. carousel water sampler, multinet).

Following oceanographic measurements were carried on during the open ocean part of the AREX 2016 cruise:

- Full-depth measurements of temperature, salinity, dissolved oxygen and ocean currents in the Norwegian-Atlantic and West Spitsbergen currents (CTD, LADCP, VMADCP).
- High-resolution hydrographic measurements with a towed CTD system (scan-fish) at the section across the shelf and shelf break west of Svalbard (in the vicinity of the Hornsund outlet).
- A collection of water samples for calibration of conductivity and oxygen sensors and nutrient analysis.
- Deployment of two ARGO floats in the Norwegian Sea.

Additionally, the standard meteorological observations were carried out according to the SHIP standard and instantaneous values of wind components, air humidity and CO_2 concentration were measured separately. Concentration and distribution of marine aerosols, as well as aerosol optical thickness, were measured at selected stations. On selected stations, plankton samples were collected with various sampling gear (WP2 nets, Multiple Plankton Sampler) and preserved for different biological analyses in the laboratory.

The standard CTD system Seabird 9/11+ used during the AREX 2016 cruise was equipped with double pairs of temperature (SBE3) and conductivity (SBE4) sensors and Digiquartz pressure sensor 410K-105. Additionally, CTD system carried two dissolved oxygen sensors (one standard SeaBird sensor SBE43 and additional Rinko optode, connected directly to the CTD registration system), SeaPoint fluorescence sensor and Benthos altimeter Benthos PSA-916. The CTD system was mounted on the SeaBird bathymetric rosette (carousel) equipped with 9 large Nansen bottles (12 l each) and 3 small bottles (1.75 l each). Originally the rosette is designed to carry 12 large bottles but due to the mounting system for LADCP only 9 bottles can be used in the current configuration. RDI Teledyne Workhorse 300 kHz was used as Lowered Acoustical Doppler Profiler (LADCP), mounted in downward-looking configuration. The collected CTD data were registered on the

PC hard drive with a double backup on the external RAID array. The preliminary data processing was done in the near-real time while the final data set was available after the post-cruise calibration of sensors. The LADCP data were read out after each station and stored in single files for each cast. During the entire cruise, the underway measurements of ocean currents in the upper layer of about 300 m depth were continuously recorded with the Vessel Mounted Acoustic Doppler Current Profiler (RDI VM-ADCP 150 Hz).

3. Properties of Atlantic water in summer 2016 and their long-term variability

Since 2000, oceanographic measurements during the open ocean part of *r/v Oceania* cruise under the AREX program have been collected at the same stations, almost on the same day of the year. Collected time series of water properties are used to study long-term changes in the ocean climate in the

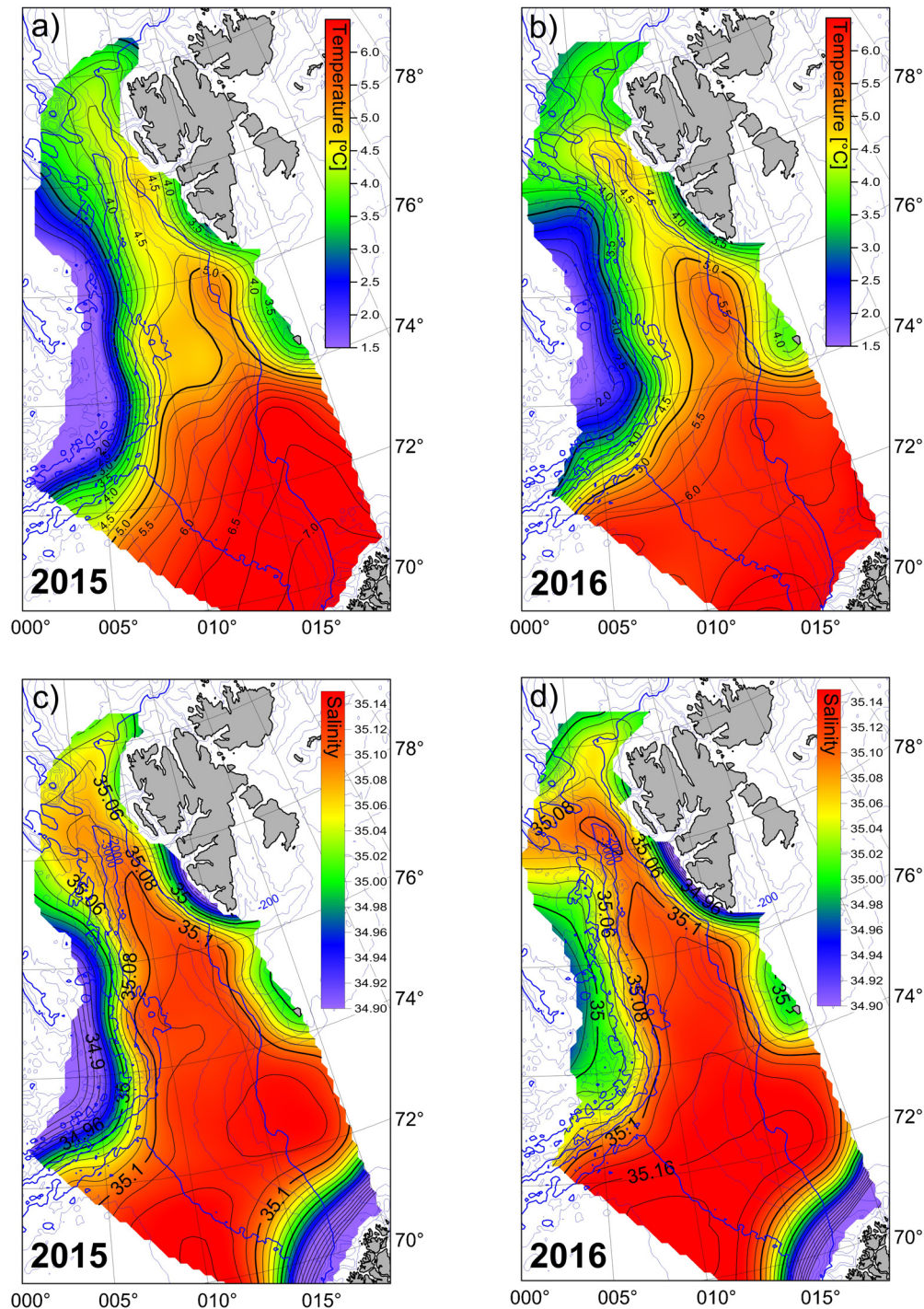


Figure 2 Spatial distribution of temperature measured in (a) 2015 and (b) 2016, and salinity measured in (c) 2015 and (d) 2016 at the depth of 100 m. Thick lines depict isotherms 5°C and 0°C (a and b) or isohalines 35.0 and 35.1 (c and d). Norwegian data from the Gimsøy section were used to extend the studied area towards the southwest.

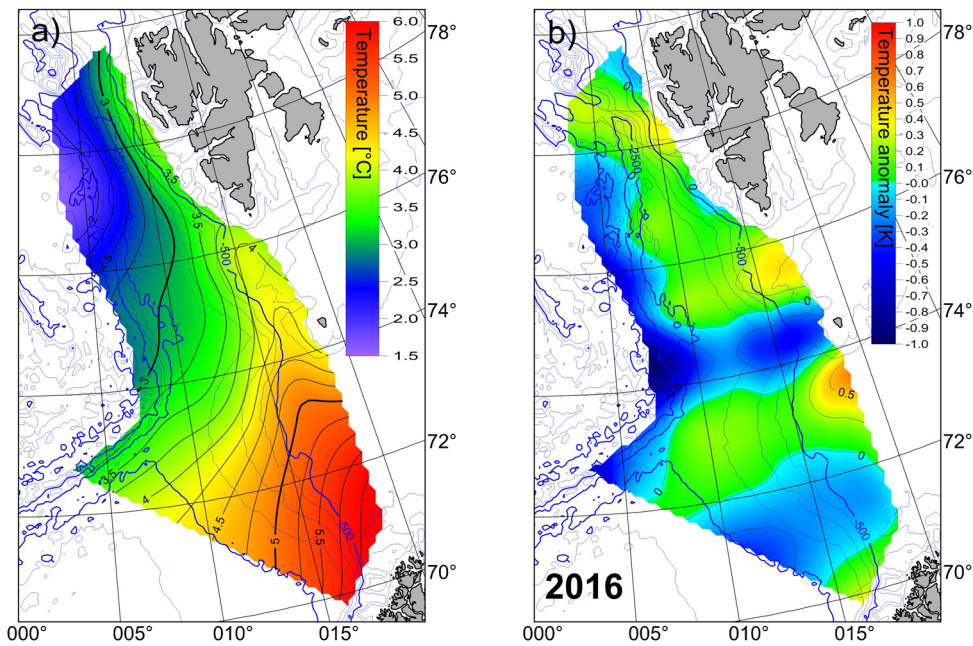


Figure 3 (a) The long-term mean field (2000–2016) of vertically averaged temperature in the Atlantic water layer and (b) anomaly of vertically averaged AW temperature measured in summer 2016 during the open ocean part of AREX 2016.

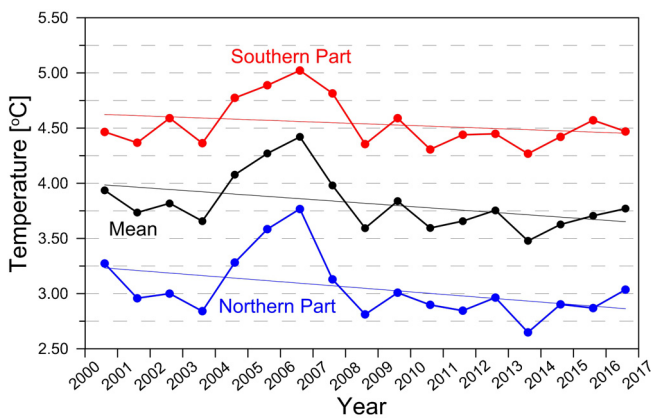


Figure 4 Vertically and spatially averaged temperature of the Atlantic water layer in the studied area. The black line depicts mean values for the whole area, the red line for the southern part (south of 74°N) and the blue line for the northern part (north of 74°N). Atlantic water is defined as warmer than 0°C and more saline than 34.92 (Walczowski, 2014). (For interpretation of the references to color in this figure legend, the reader is referred to the web version of this article.)

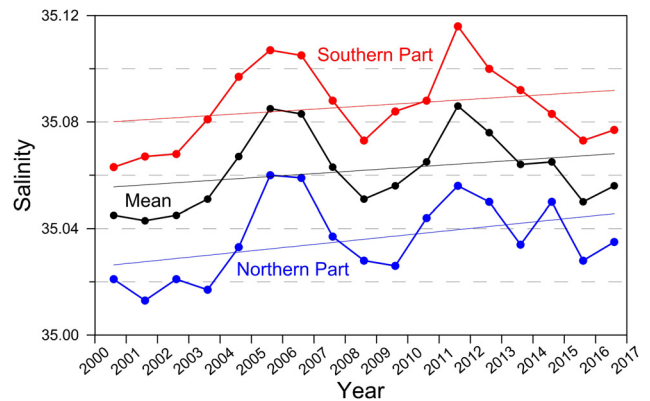


Figure 5 Vertically and spatially averaged salinity of the Atlantic water layer in the studied area. The black line depicts mean values for the whole area, the red line for the southern part (south of 74°N) and the blue line for the northern part (north of 74°N). Atlantic water is defined as warmer than 0°C and more saline than 34.92 (Walczowski, 2014). (For interpretation of the references to color in this figure legend, the reader is referred to the web version of this article.)

Table 1 Vertically averaged temperature (T) and salinity (S) in the Atlantic water layer, calculated for the whole studied area (T_{whole} and S_{whole}) and separately for its northern (T_{northern} and S_{northern}) and southern (T_{southern} and S_{southern}) parts.

Parameter	Long-term mean (LTM), 2000–2016	STD, 2000–2016	2015	2016	Difference, 2016–2015	Difference, 2016–LTM
T_{whole}	3.82	0.25	3.71	3.77	0.06	–0.05
S_{whole}	35.06	0.01	35.05	35.06	0.01	0.00
T_{southern}	4.36	0.22	4.57	4.47	–0.10	0.11
S_{southern}	35.09	0.02	35.07	35.08	0.01	–0.01
T_{northern}	3.05	0.29	2.87	3.04	0.17	–0.01
S_{northern}	35.04	0.02	35.03	35.04	0.01	0.00

Nordic Seas and Fram Strait. The AREX 2016 cruise extended all time series to 17 years. However, the longest time series collected at the section N along 76°30'N started already in 1996 and covers 21 years of summer observations. Due to its length, this time series is used as representative for temporal variability of the Atlantic water properties. Methods of calculating the spatially averaged properties of Atlantic water are presented in detail by Walczowski (2014).

Oceanographic conditions observed in summer 2016 in the studied region were close to the long-term mean situation. Similar as in 2015, the meridional extent of water warmer than 5°C observed at the depth of 100 m slightly exceeded the latitude of 76°N (Fig. 2a and b). The Arctic Front, depicted by the isotherm 3°C, was located at the same position as in 2015. Only in the northern Fram Strait, the westward deflection of isotherms can indicate stronger

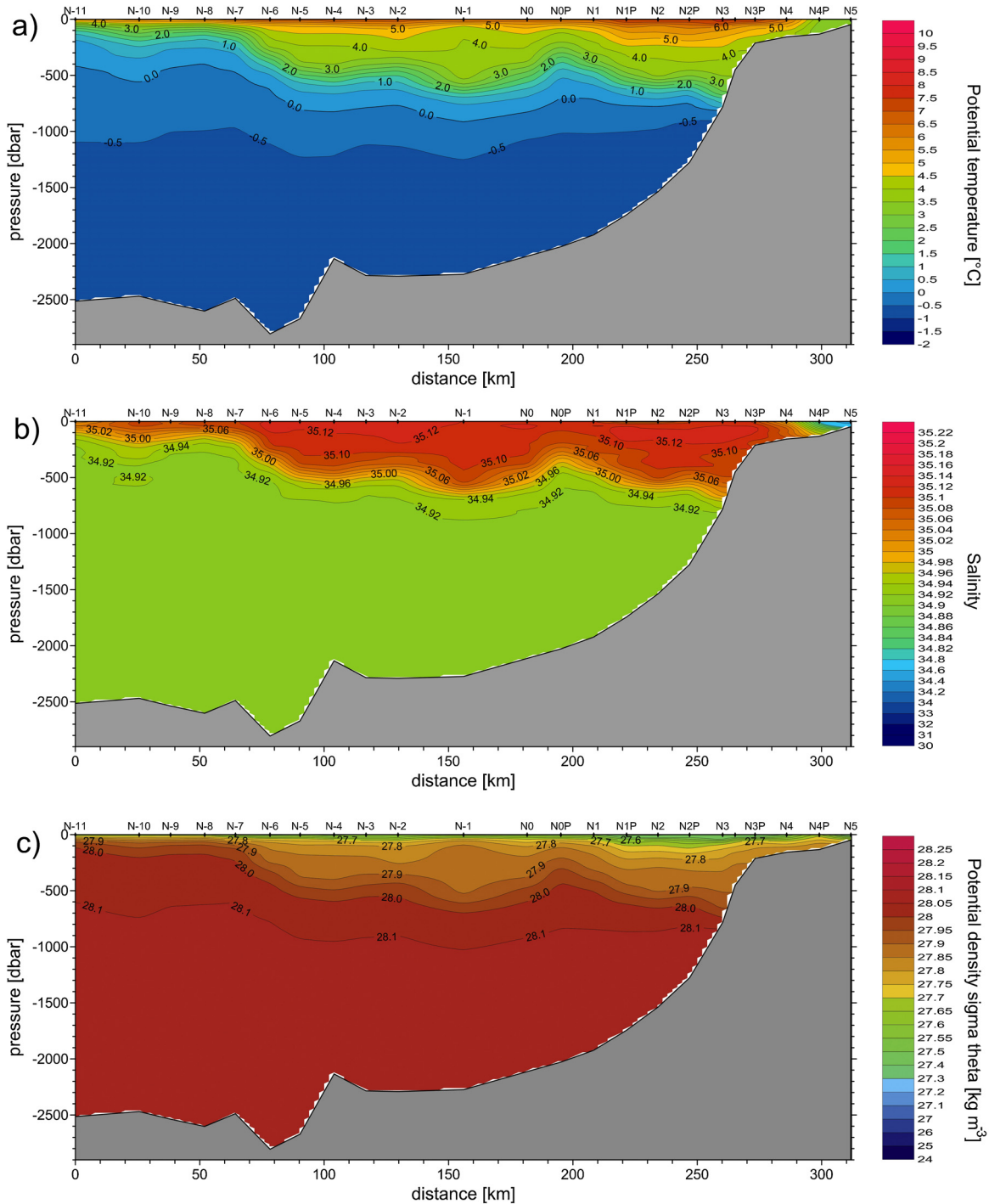


Figure 6 Vertical distributions of (a) potential temperature, (b) salinity and (c) potential density at the section N along 76°30'N observed in summer 2016.

westward recirculation of Atlantic water in 2016, concurrent with the weaker flow in the West Spitsbergen Current towards the Arctic Ocean. Spatial distribution of salinity at the depth of 100 m was also similar in 2015 and 2016 in the studied area (Fig. 2c and d).

The long-term mean field (2000–2016) of vertically averaged temperature in the Atlantic water layer is shown in Fig. 3a. Anomalies of vertically averaged AW temperature, presented in Fig. 3b, reveal slightly positive signal close to the Barents Sea Opening and in the eastern Fram Strait.

Time series of the vertically averaged temperature and salinity in the Atlantic water layer (defined as water with $T > 0^{\circ}\text{C}$ and $S > 34.92$), calculated for the whole studied area and separately for its northern and southern parts confirm, that AW temperature and salinity observed in summer 2016 were close to their climatological mean values (Fig. 4 and Table 1). Anomalies of mean AW temperature and salinity in 2016, calculated with respect to the long-term mean 2000–2016, were all below their standard deviations. Mean AW temperature and salinity for the northern part of the studied area (north of the Bear Island) were 3.04°C and 35.04 in 2016 as compared to their values observed in 2015 (2.97°C and 35.04, respectively). Mean AW temperature calculated for the whole studied region in 2016 was higher than in 2015, mostly due to higher AW temperatures in its northern part. In the southern part of the measured area mean AW temperature in 2016 was lower than in 2015 but still higher than its climatological mean 2000–2016 (Table 1). Mean AW salinity reached the maximum in 2011 and since then a steady decrease has been observed until 2015. In 2016 a small increase of AW salinity was observed in the whole studied area (Fig. 5).

Temperature and salinity distribution at the section N along $76^{\circ}30'\text{N}$ (Fig. 6) were also close to their long-term means. The eastern branch of the West Spitsbergen Current (the WSC core) is clearly visible between 12 and $14^{\circ}30'\text{E}$ (between stations N1 and N4P). On the eastern side the hydrographic front is visible on the shelf, separating warm Atlantic water carried by the West Spitsbergen Current from cold and freshened waters of the Sørkapp Current. To the west of the West Spitsbergen Current, the westward extent of Atlantic water is limited by the Arctic Front located about 7°E (station N-6). Farther westward the recirculating Atlantic water towards the Greenland Sea can be traced in the upper layer.

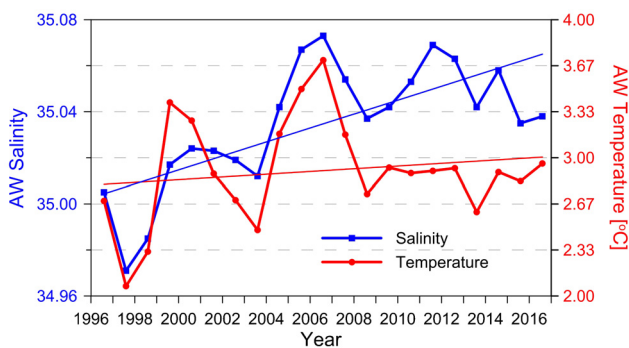


Figure 7 Time series of the vertically averaged temperature and salinity of the Atlantic water layer at the section N along $76^{\circ}30'\text{N}$ measured in summers of 1996–2016.

The longest observed time series of Atlantic water temperature and salinity, measured since 1996 at the section N along $76^{\circ}30'\text{N}$ are shown in Fig. 7. The Atlantic water layer was defined with $T > 0^{\circ}\text{C}$ and $S > 34.92$ and mean values were calculated only for the part of the section limited to the west by $6^{\circ}33'\text{E}$ to exclude the recirculating Atlantic water. A slight increase of AW mean temperature and salinity was found for 2016 as compared to 2015. Mean AW temperature at the section N was 2.96°C in 2016 and exceeded the 2015 value by 0.13°C . Mean AW salinity of 35.04 observed in 2016 was higher by 0.03 than measured in 2015. The long-term trends of AW temperature and salinity are both positive for the period 1996–2016.

Since a definition of the Atlantic water layer is based on temperature and salinity (or density) criteria, it strongly influences the temporal variability of AW mean temperature and salinity, calculated according to different parametrizations. Therefore mean temperature in the central part of section N (limited by 9°N and 12°N , laying between 130 and 210 km) was also calculated for selected depth levels (Fig. 8). The maximum temperature is visible between 2004 and 2006 depending on the depth level. The temperature trend reaches $0.058^{\circ}\text{C year}^{-1}$ in the upper layer between 0 and 400 m and decreases with depth to $0.015^{\circ}\text{C year}^{-1}$ observed at the depth of 1000 m. Temperature trends are positive and statistically significant (with p -values less than 0.01) for all depth levels. Observed trends at the section N confirm positive temperature trend observed overall in the eastern Nordic Sea and accompanied by positive salinity trend (Larsen et al., 2016).

While the 21-year-long time series of observations captures significant changes in water mass properties, it is still too short to separate the effect of trends caused by the ongoing climate change from multidecadal variability. The Atlantic meridional thermohaline circulation and associated fluctuations of poleward oceanic fluxes are strongly linked to the Atlantic Multidecadal Oscillation, which has been identified as a coherent mode of natural variability with an estimated period of 60–80 years (Delworth and Mann, 2000). Those multidecadal changes have been recently supported with strong observational evidence (e.g. McCarthy et al., 2015; O'Reilly et al., 2016). In-depth discussion of observed changes in relation to large-scale variability is out of the scope of this short communication and will be addressed in a separate paper.

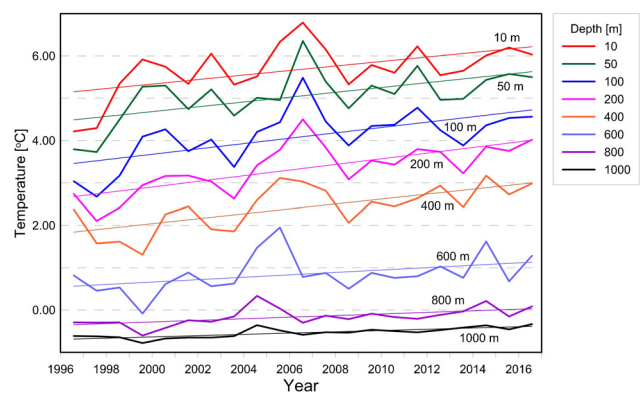


Figure 8 Time series of temperature at the selected depths observed in the central part of the section N (between 9 and 12°E , i.e. between 130 and 210 km of the section).

Oceanographic data collected under the AREX long-term monitoring program during the 30th cruise of *r/v Oceania* were used to extend time series of Atlantic water properties and analyze long-term changes observed along the Atlantic water inflow in the Nordic Seas and Fram Strait towards the Arctic Ocean. Based on the results of a preliminary analysis, summer hydrographic conditions observed in the Atlantic water domain in 2016 were close to their long-term averages. Atlantic water salinity reveals a clear positive trend while its temperature trend depends strongly on used definition of the Atlantic water layer. However spatially averaged temperature at different depths, calculated for the longest time series, indicates a clear increase of Atlantic water temperature in the whole layer from the surface down to 1000 m.

Acknowledgements

The 2016 field campaign of *r/v Oceania* in the Nordic Seas and Fram Strait was carried out under the IO PAN long-term program AREX and contributed to the IO PAN statutory research areas I.3, I.4 and I.5 and to activities of the Center for Polar Studies. The fieldwork was also supported by the projects PAVE and AWAKE-2 under the Polish-Norwegian Research Program. CTD data from the Gimsøy section were kindly provided by Kjell-Arne Mork from the Institute of Marine Research in Bergen. The captain and crew of *r/v Oceania* are gratefully acknowledged for extensive help and support provided over many years during the challenging field measurements in the harsh Arctic conditions.

Appendix A. Supplementary data

Supplementary data associated with this article (a station list, a cruise itinerary) can be found, in the online version, at [doi:10.1016/j.oceano.2016.12.003](https://doi.org/10.1016/j.oceano.2016.12.003).

References

- Beszczynska-Möller, A., Fahrbach, E., Schauer, U., Hansen, E., 2012. Variability in Atlantic water temperature and transport at the entrance to the Arctic Ocean, 1997–2010. *ICES J. Mar. Sci.* 69 (5), 852–863.
- Bourke, R.H., Weigel, A.M., Paquette, R.G., 1988. The westward turning branch of the West Spitsbergen Current. *J. Geophys. Res.* 93 (C11), 14065–14077.
- Cohen, J., Screen, J.A., Furtado, J.C., Barlow, M., Whittleston, D., Coumou, D., Francis, J., Dethloff, K., Entekhabi, D., Overland, J., Jones, J., 2014. Recent Arctic amplification and extreme mid-latitude weather. *Nature Geosci.* 7, 627–637, <http://dx.doi.org/10.1038/ngeo2234>.
- Delworth, T.L., Mann, M.E., 2000. Observed and simulated multi-decadal variability in the Northern Hemisphere. *Clim. Dynam.* 16 (9), 661–676.
- Dickson, R.R., Meincke, J., Rhines, P. (Eds.), 2008. Arctic–Subarctic Ocean Fluxes – Defining the Role of the Northern Seas in Climate. Springer, Dordrecht, 736 pp.
- Larsen, K.M.H., Gonzalez-Pola, C., Fratantoni, P., Beszczynska-Möller, A., Hughes, S.L. (Eds.), 2016. ICES Report on Ocean Climate 2015. ICES Coop. Res. Rep. No. 331. 79 pp.
- Mauritzen, C., 1996. Production of dense overflow waters feeding the North Atlantic across the Greenland-Scotland Ridge. Part 1: evidence for a revised circulation scheme. *Deep-Sea Res. Pt. I* 43 (6), 769–806.
- McCarthy, G.D., Haigh, I.D., Hirschi, J.J.-M., Grist, J.P., Smeed, D.A., 2015. Ocean impact on decadal Atlantic climate variability revealed by sea-level observations. *Nature* 521 (7553), 508–510, <http://dx.doi.org/10.1038/nature14491>.
- O'Reilly, C.H., Huber, M., Woollings, T., Zanna, L., 2016. The signature of low-frequency oceanic forcing in the Atlantic Multidecadal Oscillation. *Geophys. Res. Lett.* 43 (6), 2810–2818, <http://dx.doi.org/10.1002/2016GL067925>.
- Overland, J.E., 2016. Is the melting Arctic changing midlatitude weather? *Phys. Today* 69 (3), p. 38, <http://dx.doi.org/10.1063/PT.3.3107>.
- Polyakov, I.V., Walsh, J.E., Kwok, R., 2012. Recent changes of Arctic multiyear sea ice coverage and the likely causes. *Bull. Am. Meteorol. Soc.* 93 (2), 145–151.
- Quadfasel, D., Gascard, J.-C., Koltermann, K.P., 1987. Large-scale oceanography in Fram Strait during the 1984 Marginal Ice Zone Experiment. *J. Geophys. Res.* 92 (C7), 6719–6728.
- Rudels, B., Korhonen, M., Schauer, U., Pisarev, S., Rabe, B., Wisotzki, A., 2015. Circulation and transformation of Atlantic water in the Eurasian Basin and the contribution of the Fram Strait inflow branch to the Arctic Ocean heat budget. *Prog. Oceanogr.* 132, 128–152, <http://dx.doi.org/10.1016/j.pocean.2014.04.003>.
- Schauer, U., Beszczynska-Möller, A., Walczowski, W., Fahrbach, E., Piechura, J., Hansen, E., 2008. Variation of measured heat flow through the Fram Strait between 1997 and 2006. In: Dickson, R.R., Meincke, J., Rhines, P. (Eds.), *Arctic-Subarctic Ocean Fluxes*. Springer, Dordrecht, 65–85.
- Serreze, M.C., Barrett, A.P., Stroeve, J.C., Kindig, D.N., Holland, M.M., 2009. The emergence of surface-based Arctic amplification. *The Cryosphere* 3 (1), 11–19.
- Serreze, M.C., Stroeve, J., 2015. Arctic sea ice trends, variability and implications for seasonal ice forecasting. *Philos. T. R. Soc. A* 373 (2045) 16 pp.
- Stroeve, J.C., Serreze, M.C., Holland, M.M., Kay, J.E., Maslanik, J., Barrett, A.P., 2012. The Arctic's rapidly shrinking sea ice cover: a research synthesis. *Clim. Change* 110 (3), 1005–1027.
- Walczowski, W., 2014. *Atlantic Water in the Nordic Seas*. Springer, Heidelberg, New York, London, 300 pp.